

The Shallow Crustal Structure of the Chicxulub Impact Crater from Surface Wave Dispersion Studies.

Thesis submitted for the degree of
Doctor of Philosophy

by

Graeme Douglas Mackenzie

Department of Geology



University of Leicester

March, 1999

UMI Number: U123501

All rights reserved

INFORMATION TO ALL USERS

The quality of this reproduction is dependent upon the quality of the copy submitted.

In the unlikely event that the author did not send a complete manuscript and there are missing pages, these will be noted. Also, if material had to be removed, a note will indicate the deletion.



UMI U123501

Published by ProQuest LLC 2013. Copyright in the Dissertation held by the Author.
Microform Edition © ProQuest LLC.

All rights reserved. This work is protected against
unauthorized copying under Title 17, United States Code.



ProQuest LLC
789 East Eisenhower Parkway
P.O. Box 1346
Ann Arbor, MI 48106-1346

ABSTRACT

The Shallow Crustal Structure of the Chicxulub Impact Crater from Surface Wave Dispersion Studies

Graeme D. Mackenzie

A surface wave dispersion study has been conducted on high frequency (0.5–5 Hz) crustal Rayleigh waves propagating across the 65 Ma. Chicxulub impact structure in Mexico. These were recorded on a 20 station seismic array deployed along 4 radial arms across the region and originated from nearby quarries within the array. Events originating from the same quarry were stacked prior to the application of a multiple filter technique to produce group velocity dispersion curves. Using a genetic algorithm several one dimensional shear wave velocity–depth models have then been obtained through the optimization of the fundamental and higher mode dispersion curves.

The models provide information on the velocity structure of the upper few kilometres of the crust and suggest an infilling of the crater from the crater rim inwards. An inverted velocity gradient is modelled over the upper few hundred metres across most of the region with the exception of a central radial area. This inverted velocity zone may be connected to dolomitization during a late Miocene regression. The base of the Tertiary sequence is modelled at c. 1–1.5 km depth and shows increased velocities compared to the overlying sediments. This velocity increase may imply some form of hydrothermal alteration of the sediments caused by a thermal blanket effect created by the underlying crater breccia and melt. Immediately below the Tertiary sediments a c. 200 m thick low velocity zone is interpreted as a layer of suevitic impact breccia. Models obtained at c. 35–45 km radius from the crater centre are consistent with the existence of a peak ring as a topographic high above the crater floor.

The results from the velocity models provide fresh information on the sedimentation of the region and some constraints on the crater morphology.

Acknowledgments

The Chicxulub experiment was a result of lots of hard work by a large number of individuals. The project was funded by a fieldwork grant from the Royal Society of London and supported by the NERC grant to the British Institutes Reflection Profiling Syndicate (BIRPS) and Imperial College. I was funded by a NERC research studentship (reference number GT4/95/156/E). The equipment was provided by Leicester University, the NERC equipment pool, GeoForschung Zentrum, the British Antarctic Survey and IRIS Passcal. The field work was conducted by members of the Chicxulub Working Group and many willing volunteers.

Special thanks to my supervisor Dr Peter Maguire for allowing me the chance to conduct this PhD, for all his assistance, advice and support throughout the project. Also for not objecting when I took extended holidays following “strenuous” fieldwork and overseas conferences.

Thanks to all who helped in the field work especially Geoff for the 5 months work. Muchos gracias to Alberto and Francisco without whom much of the work would have never have received permission from locals, Chucha for keeping the house relatively clean and not giving us food poisoning despite her inventive cooking involving chicken feet! Also Hamish, John, Dr Edward King, Professor Aftab Khan and everyone else who at some point or another tested their bricklaying, joinery and electrical skills. Most of all thanks to the people of the Yucatan for their friendliness and assistance.

I am extremely grateful to Paul Denton who aided me greatly both in the field and back at Leicester. In Mexico his calm and laid back attitude (though infuriating at times) helped remind me fieldwork is also about having fun, his margaritas also helped in this respect. His assistance with computing, data processing and general geophysical information was invaluable and much appreciated.

A big thanks also to Dr Andy Myers and Chris Beckett for keeping the computers and printers running and for answering my innumerable “How do you do this ?” questions.

My work benefited from advice from discussion with Dr Max Meju, Dr Trevor Williams and Professor John Hudson at Leicester and I received ideas and suggestions from the other members of the Chicxulub working group. Thanks to both Dr Mark Pilkington and Dr Jo Morgan who provided diagrams of the potential field data for me.

Dr Colin Macbeth and Dr Philip Wild of the BGS Global Seismology Group in Edinburgh helped me greatly with several processing routines. Alex Brisbourne at Leeds assisted me in getting started with surface wave analysis and Sarah Buchanan of Edinburgh aided me greatly with relearning L^AT_EX 2_ε.

Many thanks to my fellow postgraduates who were always willing to discuss problems over a coffee or beer. Marion for the interpretations of papers and for the Spanish and salsa lessons. Fellow writing up students Roz, for founding the self-help group FRUSTRATE (Fiendishly Riting Up STudents Require Alcohol To Excel), Tiff and Kate for the chocolate chip cookies, support and for helping collate pages at the end. Vassilis provided advice and friendship and reassured me that I wasn't the only one to get easily lost in the quagmire of inversion theory! My office mates - Kim who kept me amused with her paper models of the jaws of Jamoytius, I never could decide if she was trying to get a PhD or a Blue Peter badge and Emin for his valiant and patient attempts to explain inversion theory to me and his knowledge of Fortran.

Thanks to the various members of the canoe club for helping me forget it all on many weekends in Wales and also not letting me drown. In particular Juy, Dave and Phil who fished me out at the bottom of many a grade IV and could be relied on to spend a Thursday evening at HPP.

Finally thanks to my parents for all their help and support throughout my studies. Mum maybe now you can simply answer "He's a Doctor" when asked what I do, and Dad you'll be pleased to know that I still read the question, check the units and don't panic!

Contents

1	The Chicxulub Impact Structure	1
1.1	Introduction	1
1.2	Impact cratering	1
1.2.1	Cratering mechanics	2
1.2.2	Crater morphology	6
1.2.3	Crater identification	11
1.2.4	Impact effects and relation to extinctions	14
1.3	Geology of the Yucatan	16
1.3.1	Stratigraphy	17
1.3.2	Structural geology	21
1.4	Studies of the Chicxulub impact crater	22
1.4.1	Geochemistry and petrology	23
1.4.2	Gravity and magnetics	24
1.4.3	Electrical and electromagnetic methods	27
1.4.4	Topography and hydrogeology	29
1.4.5	Previous seismology	30
1.4.6	Summary of previous models	31
1.4.7	1996 Seismology and model	31
1.5	Thesis outline	35
2	The Chicxulub Seismic Experiment	37
2.1	Objectives	37
2.2	The passive seismic array	38
2.3	Controlled source experiment	41

3	Event Location	44
3.1	Site location	44
3.2	Qualitative descriptions of seismograms	45
3.3	Hypocentral location	49
3.3.1	Phase-picking	52
3.3.2	Velocity model	52
3.3.3	Station corrections	54
3.3.4	Hypocentral depth	56
3.3.5	Vp/Vs ratio	56
3.3.6	Distribution of events and identification of quarry blasts	60
3.4	Determination of errors	66
3.5	Conclusions	70
4	Surface Wave Analysis	73
4.1	Introduction	73
4.1.1	Surface wave observations in Mexico	75
4.2	Processing	76
4.3	Multiple filter technique	77
4.4	Interstation calculation of phase velocity	80
4.5	Phase-matched filtering	86
4.6	Multiple station calculation of γ	89
4.7	Description and implications of dispersion and γ curves	93
4.7.1	Group velocities	93
4.7.2	Phase velocities	98
4.7.3	Amplitude spectra and γ curves	101
4.8	Conclusions	103
5	Surface Wave Inversion: Theory & Method	105
5.1	Inversion using a genetic algorithm	105
5.2	Theory	108
5.2.1	Coding	109
5.2.2	Reproduction	109

5.2.3	Crossover	111
5.2.4	Mutation	112
5.2.5	Schema theorem	113
5.3	Selection of genetic algorithm parameters	115
5.3.1	GA encoding	117
5.3.2	Population size	118
5.3.3	Selection of reproduction, crossover and mutation parameters	119
5.3.4	Further refinements of the genetic algorithm	120
5.4	Forward modelling of synthetic dispersion curves	128
5.5	Inversion for Q_β^{-1}	130
5.6	SVD theory	131
5.6.1	Error analysis	133
5.7	Summary	134
6	Velocity Inversion and Modelling Results	135
6.1	Inversion using fundamental mode	135
6.1.1	Group 1 curves	135
6.1.2	Group 2 curves	137
6.1.3	Resolution	139
6.1.4	Averaging effects	141
6.1.5	Summary of fundamental mode models	144
6.2	Inversion of higher modes	144
6.2.1	Flamboyanes blasts	147
6.2.2	Dzitya blasts	149
6.2.3	Airport blasts	149
6.2.4	Mode identification	151
6.2.5	Resolution	151
6.2.6	Mode sensitivity	155
6.2.7	Summary of higher mode models	155
6.3	Phase velocities	158
6.4	Q_β inversion results	158
6.5	Waveform modelling	161

6.6	Summary	166
7	Discussion and Conclusions	169
7.1	Cenozoic sedimentation	169
7.2	Crater structure and models	175
7.2.1	Impact breccia	175
7.2.2	Central uplift	176
7.2.3	Peak ring	179
7.2.4	Outside the peak ring	185
7.3	Conclusions	186
7.4	Further work	188
A	Recording Schedule	190
B	Teleseismic and Regional Events	194
C	Local Event Locations	199
D	Instrument Details	202
D.1	Seismometers	202
D.2	The PDAS recorder	203
E	Stacked MFT Plots	205
E.1	Flamboyanes Quarry	205
E.2	Dzitya Quarry	208
E.3	Airport Quarry	210
E.4	Near D26	212
F	Models	214
F.1	Fundamental mode models	214
F.2	Higher mode models	220

List of Figures

1.1	Location of the Chicxulub impact structure. This figure and a number of others in this thesis have been produced with the GMT package (Wessel and Smith, 1995).	2
1.2	Schematic illustration of the excavation flow geometry. Dashed lines indicate the shock pressure contours with solid lines the excavation flow streamlines. Ejecta from nearest the impact site travel at the highest speeds whereas ejecta emerging farther from the impact point travel slower (after Melosh, 1989).	4
1.3	Regions of materials expelled from the crater. Material at the point of impact is vapourized and expands outwards as a vapour plume. Near surface material is expelled as spall plates whilst remaining material is either ejected or displaced downward by the excavation flow. H_e is the final excavation depth and H_t the resultant transient crater depth (after Melosh, 1989).	5
1.4	Formation of the transient crater. Its shape at any one time is given by the position reached by the innermost material within the excavation flow. The crater initially is hemispherical (a), expanding at a rate much slower than the impact velocity. Its rate of growth in depth slows and ceases (b) prior to the halt of its radial growth (c). The resultant crater (d) is known as the transient crater or cavity with a diameter D_t . The disruption cavity has diameter D_d . Throughout the formation the sides and base are lined with melt and highly shocked rocks (after Melosh, 1989).	7

1.5	Crater morphology of lunar impacts (a) Alfrancus C, 10 km diameter simple crater, (b) Tycho, 85 km diameter central peak crater, (c) Schrödinger, 320 km peak ring crater and (d) Orientale, 900 km diameter multi ring impact basin. Images reproduced permission of the Geological Survey of Canada, Natural Resources Canada.	8
1.6	Formation of a simple bowl crater. The unstable sides of the transient cavity collapse to form the breccia infill. A buried melt pool is trapped at the base, whilst the mixed partial melt and breccia that lined the transient crater walls is concentrated near the top (after Melosh, 1989).	8
1.7	Formation of a central peak crater. Gravitational rebound of the centre of the crater begins almost immediately and no true transient crater is formed. Large slumping of the edges occurs to form terraces (after Melosh, 1989).	9
1.8	Formation of a peak ring crater. The central peak overshoots gravitational stability and collapses to form the peak ring (after Melosh, 1989).	10
1.9	Terrestrial impact sites (source of data Geological Society of Canada).	12
1.10	Generalized stratigraphy of the Yucatan platform (after Lopez-Ramos, 1973).	18
1.11	Surficial geology of the NW Yucatan peninsula with the location of PEMEX and UNAM drill holes (data taken from the 1984 INGEI maps).	20
1.12	Geomorphological surfaces of the NW Yucatan. Q1: Holocene, Q2: Late Pleistocene, T1: Pliocene–Pleistocene, T2: Late Miocene–Pliocene, T3: Late Miocene, T4: Late Eocene–Oligocene, T5: Eocene, dashed blue line indicates the cenote ring. (after Pope et al, 1996).	20
1.13	Tectonic map of the Yucatan including physiographic regions. NP - northern pitted karst plain, SP - southern hilly karst plain, EFB - eastern fault block, MM - Mayan mountains, LA - Libertad Arch, SS - Sierra Madre del Sur, SC - Sierra del Chiapas, SCA - Sierra of North Central America (after Weidie, 1985).	21
1.14	(a) Bouguer anomaly map of the Chicxulub impact with locations of seismic lines (figure courtesy of J. Morgan, IC London) and (b) aeromagnetic data across the Chicxulub impact structure (figure courtesy of M. Pilkington, NSC Canada).	26

1.15	Three gravity model cross sections of the Chicxulub crater. Note that the depth and horizontal (distance from centre of crater) scales of all three models are different.	28
1.16	Location of previous geophysical surveys mentioned in text and drill wells where seismic data has been gathered.	29
1.17	The two principal geological models prior to the 1996 Chicxulub experiment.	33
2.1	Recording geometry of the passive array. The inner dashed circle represents the smaller crater diameter of 180 km, the outer one the larger 300 km diameter.	39
2.2	48 hour 3 channel broadband record a) prior to insulation showing variations due to temperature fluctuations b) after insulation, removing the fluctuations outside the recording band.	40
2.3	Geometry of the controlled source experiment showing location of reflection profiles, land receivers and OBS's. Dashed lines are as in Figure 2.1	42
3.1	Distribution of distances of individual GPS locations from the average location of site D13. Positive distances are North and East in the respective plots. The differential GPS location of the site obtained by the GSC is marked by the arrow.	45
3.2	Typical record section for one event recorded at multiple stations. Note that the traces have been high pass filtered above 0.4 Hz to remove low frequency noise and are individually normalized.	46
3.3	Body wave amplitude spectra for an 8 s window around the P arrival. . . .	47
3.4	Example record showing high amplitude Rg on the vertical and radial and Lg on the transverse component.	47
3.5	(a) Waveforms from two events recorded at the same station and (b) their corresponding frequency spectra.	48
3.6	Vertical records from two stations for the same event and similar path lengths exhibiting very different Rg dispersion characteristics.	49

3.7	(a) Unfiltered vertical trace recorded at station F05. (b) Vertical, radial and transverse components for F05 band-passed filtered at 1.5 Hz. Fundamental and higher mode Rg can clearly be seen on the vertical and radial components with a strong Lg on the transverse (note different time window from (a)). (c) Particle motions in the sagittal plane for 2 second windows from 15–17 seconds and 26–28 seconds confirming a retrograde motion for the fundamental mode and showing the higher mode has prograde motion. .	50
3.8	Record section along Line E for a quarry blast near the airport. Apparent P-wave velocity shows an increase towards the centre of the crater.	51
3.9	Velocity-depth model used for initial event location.	53
3.10	Initial event locations. Crosses indicate the axis of the 3-D error ellipsoid collapsed onto a 2-D plane.	53
3.11	Final event locations.	55
3.12	Average station travel time residuals for all events and event clusters. . . .	57
3.13	3-D view of hypocentral depths for all events following initial location and the same depths collapsed onto Line E. For clarity the vertical errors have not been shown.	58
3.14	Example Wadati plots.	59
3.15	Mean RMS against V_p/V_s ratio for (a) Flamboyanes cluster and (b) airport cluster.	61
3.16	Location of known and suspected quarries and local towns in the Merida area. Suspected quarries are based on information provided by locals. . . .	62
3.17	Temporal distribution of events (a) Daily distribution and (b) Hourly distribution.	64
3.18	(a) Three events recorded at station D08. The upper two are both believed to originate from Dzitya, the third from near station E12, 5 km to the south east. (b) Cross-correlation functions with the first event. The top trace is the auto correlation of the first event. The second trace shows a clear spike with a -0.04 second offset, confirming the source is the same as the first whilst the third shows no correlation.	65

-
- 3.19 Sonogram analysis of (a) an event from Dzitya and (b) an event near site E12. The Dzitya event is known to be a ripple blast and displays clear banding throughout the signal which is not visible in the latter event. The event near E12 is believed to be related to construction work and is unlikely to be rippled. The proximity of the two paths suggests that the banding is a source rather than propagation effect. 67
- 3.20 Effect of varying V_p/V_s on (a) the epicentral location of events near the airport and (b) the origin time of those events. 69
- 4.1 Schematic illustration of the depth dependence of the vertical displacement eigenfunction of the fundamental, first and second higher modes at a fixed frequency. The number of zero crossings determines the mode number with the relative excitation of each mode dependent on wavelength, source depth and structure (after Ewing et al. (1957)). 74
- 4.2 Frequency spectra of a typical quarry blast. The fundamental Rg phase has a maximum amplitude occurring around 2 Hz. 77
- 4.3 (a) FTAN plot of fundamental group velocity from MFT analysis of synthetic seismogram and the theoretical group velocities. (b) Error between the MFT analysis and theoretical group velocities. 79
- 4.4 FTAN plots for the same event but with different choices of filter central frequencies. (a) Filtering with a constant ΔT provides clearly seen low frequency data including higher mode information. (b) Filtering at a constant Δf , improves resolution of high frequency information but with decreased resolution at low frequencies. (c) Logarithmic sampling of central frequencies allows both high and low frequency information to be seen. 81

- 4.5 Typical FTAN map from an unstacked record of a quarry blast at Flamboyanes quarry, 28/02/96 recorded at Station D21 (path length is 21 km). The fundamental Rg mode can be seen between 0.5 and 0.8 kms^{-1} with a higher mode responsible for the modal interference seen around 2 Hz. Symbols indicate size of the spectral peaks (\square - largest, \circ - second largest, \triangle - third and $+$ - fourth largest). The original waveform is shown at the far right of the plot with a constant sampling interval and to the left of that the waveform is scaled to the group velocities of the contour plot. 82
- 4.6 FTAN map for a stacked record of blasts from Flamboyanes quarry recorded at Station D21. Lower frequencies show decreased noise and higher modes are now more distinct than in the unstacked plot. The second higher mode is the decreasing velocity trail in the centre of the plot with the first higher mode responsible for the modal interference. 83
- 4.7 FTAN map of residual waveform from Figure 4.6 after application of a phase-matched filter. First and second higher modes can now be clearly identified between 0.4–4 Hz and 0.6–2.5 Hz with group velocities decreasing from 1.1–0.8 kms^{-1} and 1.5–1.1 kms^{-1} . Note a remnant of the fundamental mode energy is still visible between 1–3 Hz. 84
- 4.8 Station–event paths used for MFT analysis. 85
- 4.9 Map showing paths used for interstation phase velocity calculation. 86
- 4.10 The phase-matched filter technique (a) Original waveform, (b) Cross correlation with mode of interest concentrated about zero-lag, the lower plot is the cross-correlation windowed around the mode of interest (vertical bars indicate window), (c) Fundamental Rg waveform, and (d) Residual waveform after removal of the fundamental mode. Note the difference in maximum amplitudes (shown on the right) of the wavetrains. 88
- 4.11 Comparison of (a) dispersion and (b) amplitude spectra before and after the application of the PMF. 90
- 4.12 Amplitude reduction with distance for an event originating at the airport and propagating southwards. 92
- 4.13 Calculation of γ by linear regression. 93

4.14	Fundamental mode dispersion curves recorded at nine sites for a source at Flamboyanes. Group 1 is the dispersion to sites D5b, D08, D13, E18 and E12. Group 2 the dispersion to F05, F10, D26 and E04.	94
4.15	(a) Histograms of group velocity values at 1.0 Hz and 2.36 Hz for a quarry blast at Flamboyanes recorded during the controlled source experiment. (b) Station-event paths for the same quarry blast. Type of line indicates whether the dispersion at 2.36 Hz is of Group 1 or 2.	95
4.16	The region where the fundamental dispersion changes from being Group 2 to Group 1 type. Radius are from the crater centre marked by the + symbol.	96
4.17	Fundamental mode curves for an event at the airport.	97
4.18	Higher mode dispersion curves for events at (a) Flamboyanes, (b) Dzitya and (c) near airport.	99
4.19	Fundamental phase curves obtained from interstation analysis.	100
4.20	Attenuation coefficient γ curves from interstation analysis: (a) propagating southward from the crater, (b) across central crater area (c) outside central area and (d) all three without errors for comparison.	102
5.1	An objective function for a non-linear problem is irregular and can contain several local minima. Using an iterative method such as steepest descent only starting model 1 will converge to the global minimum (A), whilst model 2 will converge to the local minima (B) (adapted from Sen and Stoffa, 1995).	106
5.2	An example of binary coding for shear-wave velocity model parameters If the velocity is allowed to vary between 1–2.5 kms ⁻¹ with a resolution of 0.1 kms ⁻¹ then there are 16 possible velocity values which can each be represented by four bits. When all four bits are off (i.e., 0) then the velocity is 1 kms ⁻¹ ; when all four bits are on (1) then the velocity is 2.5 kms ⁻¹ . If the shear wave velocity was the only model parameter then each four bit code would form one chromosome, if another parameter existed then the chromosomes would be formed by joining them one after the other. The other parameters need not be represented by four bits but could be more or less, depending on the resolution required.	110

- 5.3 An example of crossover between two strings. The couple (a) are cut at a randomly chosen point (b) and the segments transposed to create two new strings(c). 112
- 5.4 A 4-dimensional space represented by two cubes, one within the other. Corners are labelled by 4 bits representing which cube and which three faces intersect at the corner. The schema (10**) defines the hyperplane representing the front face of the inner cube (after Whitley, 1994). 114
- 5.5 Convergence of a GA and Monte Carlo method showing alternation between rapid and slow convergence 117
- 5.6 Two examples of binary coding of the decimal parameters (24,10) and (14,25). (a) Regular binary coding creating two binary strings of length 10 (grey blocks represent 1 and white 0) with the first 5 bits the binary code of the first decimal value and the second 5 bits the binary code for the second decimal value. (b) The same two sets of decimal parameters now encoded by binary magnitude, again creating two strings of length 10 but where the first two bits represent whether the two decimal values are of order 2^4 , the second two bits, order 2^3 and so on. 118
- 5.7 The performance of a basic GA with varying population sizes (Q). It should be remembered that the $Q=10$ curve contains 22 times the number of iterations than the $Q=250$ curve. 119
- 5.8 On-line and off-line performance for (a) different methods of reproduction and varying values of P_{TS} and (b) various P_c 121
- 5.9 On-line and off-line performance for varying mutation probability. Note that whilst $P_m=0.001$ gives best convergence (off-line) the on-line performance indicates that this convergence is premature. 122
- 5.10 Model results from testing of the GA by this author for two values of mutation probability. (a) $P_m=0.1$, (b) $P_m=0.001$. The grey area indicates the model space searched with the dark grey being the best 5% of models. The darkness is logarithmically proportional to the number of models. Dashed line is the true model, white the average of the best 5% and black the best model from the GA (after Shibutani et al, 1996) 123

5.11	Off-line and on-line performance for a variety of refinements to the basic GA	125
5.12	An example of two point crossover between two strings. The pair (a) are cut at two randomly chosen points (b) and the segments between each point exchanged to create two new strings(c).	126
5.13	Test results of the GA chosen for surface wave inversion. (a) Velocity model results, (b) synthetic (circles) and modelled (diamonds) R_g dispersion curves for fundamental and second higher mode (including synthetic errors used for weighting).	127
6.1	1-D shear wave models for Group 1 fundamental dispersion curves. Paths are from Flamboyanes to station E04 and Dzitya to D21. Stippled area is the model space with the top 5% models in grey.	136
6.2	1-D shear wave models from Group 2 fundamental dispersion curves. Paths are from Flamboyanes to D13 and Dzitya to E18.	138
6.3	1-D shear wave models from the Airport to stations (a) E18 and (b) D13. The southward propagating path shows an increased surficial shear wave velocity of 1.2 kms^{-1} compared to 1 kms^{-1} for the northward path. Note the group velocity dispersion curves have a slightly different scale.	140
6.4	Range of dispersion curves generated by the top 5% models for F-D13. With the exception of a small region above c. 4 Hz the modelled curves fall within the limit of the observed errors.	141
6.5	Layer misfit surfaces for the fundamental group dispersion curve recorded at E04 and corresponding to model F-E04.	142
6.6	Layer misfit surfaces for the fundamental group dispersion curve recorded at E18 and corresponding to model D-E18.	143
6.7	Illustration of the averaging effect in the 1-D model caused by lateral variations in velocity structure. The first three models (a-c) together cross approximately the same path as the final model (d). It can now be seen that the apparent thick low velocity zone from 0.6–1.2 km depth in D-E18 is in fact most likely an artifact caused by significant velocity variations along the path.	145

- 6.8 Synthetic fundamental mode group dispersion curves for two velocity models. (a) Normal velocity gradient and (b) inverted velocity gradient over the top 300 m. Bar the variation in velocities over the top 300 m the model parameters are identical in both situations. 146
- 6.9 1-D shear wave velocity models and modelled dispersion curves for joint inversion of fundamental and higher mode data for paths from Flamboyanes to stations F05 and D13. 148
- 6.10 1-D shear wave velocity models and modelled dispersion curves for joint inversion of fundamental and higher mode data for paths from Dzitya to stations E7b and E12. 150
- 6.11 1-D shear wave velocity models and modelled dispersion curves for joint inversion of fundamental and higher mode data for paths from the airport to stations E12 and E18. 152
- 6.12 Best fitting dispersion curves for path F-D13. (a) Higher mode inverted as 1st higher mode, (b) higher mode inverted as 2nd higher mode. The observed higher mode data can not be adequately modelled as the 1st higher mode. 153
- 6.13 Range of dispersion curves generated by the top 5% velocity models for A-E18. 153
- 6.14 Layer misfit surfaces obtained from varying the parameters of model F-F05 using fundamental and second higher mode dispersion curves. Two ranges of layer thicknesses have been investigated for layer 9. 154
- 6.15 Variation of normalized vertical displacement eigenvalues, U_z , and phase velocity partial derivatives, $\partial c/\partial\beta$ with depth for the fundamental and first two higher Rayleigh wave modes at 0.45 and 5.1 Hz. Velocity model is F-F05. 156
- 6.16 1-D velocity models collapsed radially onto Line E. The velocity scale of all models is $0-5 \text{ kms}^{-1}$ with the midpoint of each station-event path at 0 kms^{-1} . Fl - Flamboyanes, Dz - Dzitya and Ai - airport. 157
- 6.17 Interstation phase observations and modelled phase velocity dispersion curves (red) from 1-D velocity models derived from group velocity dispersion. . . . 159

- 6.18 Q_β^{-1} models from SVD inversion of γ values using a range of Marquardt damping values (red = 1, orange = 5, black = 10, green = 25, blue = 50). Horizontal bars are the standard deviations for a damping value of 5. Observed and calculated γ curves are shown on the right. 160
- 6.19 Synthetic seismograms using velocity model F-D13 with no attenuation and two different source time functions. (a) Delta function (b) step function (c) actual waveform. 163
- 6.20 Synthetic (green) and observed (red) waveforms using Q_β model 1. 164
- 6.21 Synthetic (green) and observed (red) waveforms. The lower two (F-F05 and F-D26) are modelled with Q_β model 1 the top waveform (A-E21) with Q_β model 2. 165
- 6.22 Effect on the synthetic waveform (green) of changing the Q_β values for each layer in Model 1 by $\pm 50\%$. Also shown is the synthetic waveform generated with no attenuation model. The observed (red) seismogram is for path F-D21. 168
- 7.1 Well logs of wells C-1, S-1, Y-6 and T-1 arranged in radial distance from the crater centre (modified from Sharpton et al, 1996). 170
- 7.2 Models of dolomitization. (a) Evaporative model where storm recharge followed by evaporation induces an upward flow of Mg rich groundwater. Changes in pore water chemistry occur due to the evaporation and mixing of tidal and fresh water. The seepage-reflux (b) and evaporative drawdown (c) models are an extension of this with dolomitizing fluids generated through evaporation of lagoonal waters and then descending through the underlying carbonates. Mixing zone dolomitization (d & e) is based on the principle that dolomite is precipitated more easily from a dilute solution e.g., a mix of fresh water and sea water. The sea water provides the Mg^{2+} whilst the groundwater pumps the solution through the carbonates. Burial dolomitization (f) relies on the compactional dewatering of basinal mudrocks and the expulsion of Mg rich fluids into adjacent carbonates. Finally seawater dolomitization (g) relies purely on an efficient pumping mechanism to drive seawater that is chemically unchanged through the carbonate (after Tucker and Wright, 1990). 172

7.3	Eustatic sea level changes during the Tertiary (modified from Kennett, 1982).	174
7.4	Schematic models of the central crater area by (a) Sharpton et al, 1996 and (b) Hildebrand et al, 1998.	177
7.5	1-D velocity models collapsed radially onto a transect parallel to the coast across the central crater area. Location of model paths are shown in Figure 7.6.	178
7.6	Location of central model paths shown in Figure 7.5 and the paths across the peak ring shown in Figure 7.8.	179
7.7	Gravity anomaly over the central area of the crater. The gravity high associated with the central uplift is split into two maxima with a southwest trending trough between. Location of path averaged by model F-D13 is shown.	180
7.8	1-D velocity models along Line E from 30-60 km radius.	182
7.9	Line drawing of the offshore normal incidence reflection data across the peak ring with a possible explanation for its formation. The outward collapsing central jet interacts with the inward collapsing transient cavity to produce an inward dipping low angle transition zone. Interior velocities are higher than those outside the transition zone (after Morgan and Warner, 1998). . .	183
7.10	Expected 1-D velocity models arising from the structure proposed by Brittan et al, 1998. The dipping high-low velocity interface will produce a transition in models from those with high velocities to those with lower velocities below the breccia layer.	183
7.11	Comparison of models D-E12 and MD-D21. MD-D21 is centred at c. 25 km from the crater centre whilst D-E12 is c. 35 km suggesting asymmetries in the location of the peak ring, possibly consistent with an oblique impact from the southwest.	184
7.12	Formation of an off-centre peak ring from an oblique impact. The central jet rebounds up and towards the impact direction before collapsing to form the peak ring. The resultant crater has a peak ring centred at R_c , offset uprange from the overall crater centre, C_c	184
B.1	Locations of teleseismic and regional events.	198

D.1	Amplitude and phase response for the Teledyne Geotech S13.	202
D.2	Amplitude and phase response for the Guralp CMG-40T. The response of the CMG-3T is similar but with a flat response over a wider frequency range.	203
D.3	Observed and true P arrival showing precursor generated by the internal FIR filter (after Scherbaum, 1996).	204

List of Tables

1.1	(a) Examples of laboratory measured compressional and shear velocities of rocks likely to be found in the Yucatan (¹ Press, 1966, ² Carmichael, 1982). (b) Summary of velocities obtained from previous seismic studies of the Chicxulub crater.	32
1.2	Summary of crater models	34
3.1	Parameters for final locations giving a minimum RMS residual. Z is the depth to the top of the layer. Parameters (a) were used for the Flamboyanes and south Flamboyanes cluster (< 25–30 km radius of the crater centre), (b) for events at Dzitya and near site E12 (between 25 km and 45 km radius) and (c) for the airport events (> 45 km radius).	54
3.2	Effect of varying model parameters on hypocentral locations of events near Merida airport.	71
4.1	Simple two layer models calculated from the interstation phase curves using the modified half space equations (equation 4.19).	101
6.1	Model space used in the GA for optimization of the fundamental mode. N possible values within the limits are allowed providing an incremental value of Δ	137
6.2	Model space used in the GA for optimization including higher modes. . . .	147
6.3	Q_β models used to generate synthetic waveforms in Figures 6.20 and 6.21. .	162
A.1	Recording schedule Julian days 39–90.	191
A.2	Recording schedule Julian Days 91–140.	192
A.3	Summary of station recording statistics.	193

D.1 Gain settings for the seismometers used and their associated maximum read- ing.	203
--	-----

Chapter 1

The Chicxulub Impact Structure

1.1 Introduction

The Chicxulub impact structure is located on the NW edge of the Yucatan peninsula in Mexico (Figure 1.1) lying partly offshore and buried under approximately 1 km of post-impact sediments. It is now widely recognized as a bolide impact site on the Cretaceous–Tertiary (K–T) boundary and has been linked to the mass extinctions of that time. Through the use of gravity, magnetics, drill hole and topographic data previous researchers (e.g., Hildebrand et al., 1991; Sharpton et al., 1993) have attempted to determine the size and morphology of the crater but these remained poorly constrained, ranging from 180–300 km in diameter, still making it one of the largest craters on the Earth. The impact occurred in a shallow marine environment and subsequent rapid burial, combined with the tectonic stability of the region has resulted in one of the best preserved impact structures on Earth.

Through the use of high frequency surface wave dispersion, 1-D shear wave velocity models have been obtained across the region and used to infer the shallow structure of the crater, its formation and its influence on the post-impact Tertiary sedimentation.

The remainder of this chapter will focus on the mechanics of cratering and provide a review of previous exploration and modelling of the Chicxulub structure.

1.2 Impact cratering

Impact cratering has been one of the dominant influences on planetary evolution and yet its importance has only been realized over the last few decades. It is now being

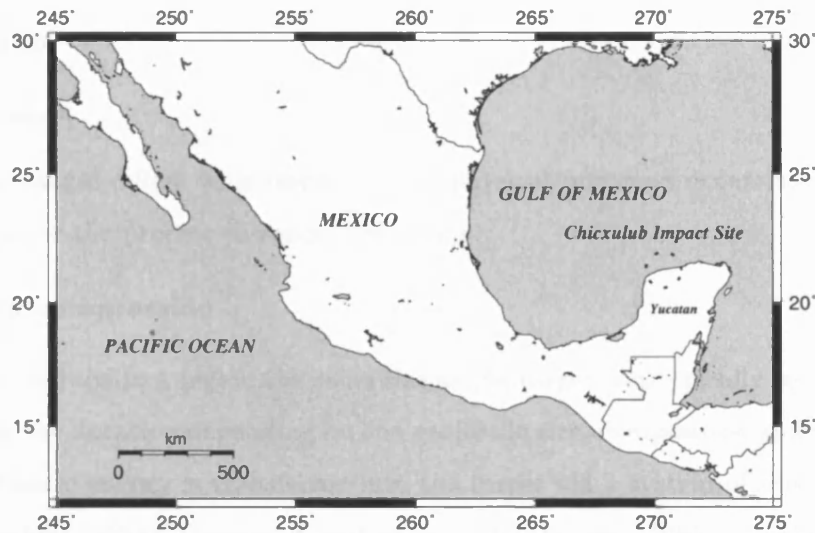


Figure 1.1: Location of the Chicxulub impact structure. This figure and a number of others in this thesis have been produced with the GMT package (Wessel and Smith, 1995).

recognized as a fundamental geological process; the formation of the moon (Stevenson, 1987), outgassing of the crust to form the primordial atmosphere (Lange and Ahrens, 1982), development and evolution of life (Alvarez et al., 1980), major tectono/thermal events (Glikson, 1995) and formation of economic deposits (e.g., Donofrio, 1981) all being suggested as results of large impact events. Whilst major advances have been made in the understanding of impact processes and effects there remain several unanswered questions and poorly understood areas. One of the major restrictions on that research has been the lack of well preserved terrestrial craters, thus requiring the extrapolation of information from deformed and eroded structures or from lunar and Venusian impact sites.

The Chicxulub crater provides an ideal opportunity to study one of the largest terrestrial impacts and develop an understanding of the processes occurring during crater formation and also the effects such an impact will have.

1.2.1 Cratering mechanics

The formation of craters from impacting bodies forms a rapid but ordered sequence of events. Although these are a continuous series, in order to understand the process better, they can be divided into three main stages (Gault et al., 1968):

- contact and compression
- excavation
- modification

Each of these stages differs with respect to the physical processes occurring and the time scale required for the process to reach completion.

Contact and compression

This stage is confined to a region the same size as the target and typically lasts from 10^{-3} –1 second with the duration depending on the projectile size, composition and velocity. The projectile's kinetic energy is transferred into the target via a system of shock waves with pressures reaching 1000 GPa (e.g., Gault et al., 1968; Melosh, 1989). As the front of the projectile hits the target, target material is compressed and accelerated away from the projectile whilst the target's resistance to penetration decelerates the projectile (Melosh, 1989). Initially a small high pressure region develops at the interface, encompassing a shocked region of both target and projectile. Both projectile and target are compressed and begin to distort. A torus of extra high pressure is formed by the oblique impact of the curved sides of the projectile and the initially flat target area. Jets of highly shocked, molten or vapourized material are squirted out of this region at high speeds several times faster than the projectile velocity. This jetting last only for a very short time, finishing before the projectile is fully compressed and involves only a small amount of material, but becomes more important for oblique impacts (e.g., Kieffer, 1977; Miller, 1998). The shock wave generated at the interface propagates into both target and projectile with the projectile material being compressed and decelerated whilst the target material is similarly compressed and accelerated. Shock pressures vastly exceed material strengths and this stage is hydrodynamic. Once the shock wave reaches the back of the projectile it is reflected as a rarefaction wave which travels back through the compressed material at the speed of sound, further decelerating it and unloading it to near zero pressure. The shock wave in the target is now approximately hemispherical, centred a projectile diameter below the pre-impact surface. This initial stage is considered to have ended when the rarefaction has unloaded the projectile by which point the majority of the projectile has been vapourized and a detached shock wave is developing in the target (Melosh, 1989).

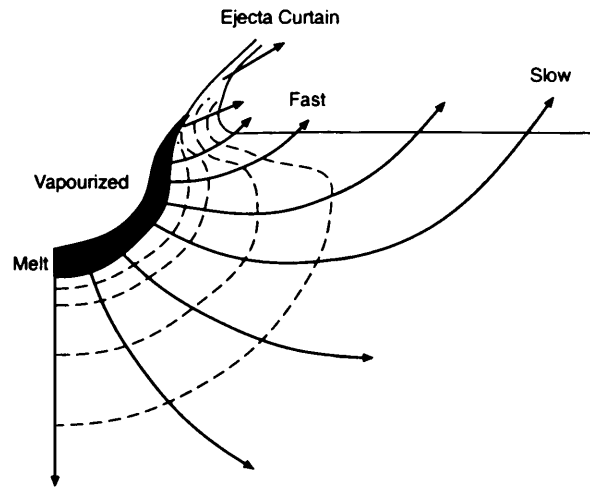


Figure 1.2: Schematic illustration of the excavation flow geometry. Dashed lines indicate the shock pressure contours with solid lines the excavation flow streamlines. Ejecta from nearest the impact site travel at the highest speeds whereas ejecta emerging farther from the impact point travel slower (after Melosh, 1989).

Excavation

The excavation stage is characterized by two processes. The earliest of these is the expansion of the hemispherical shock wave initiated during the contact and compression stage. The second of these processes is the excavation flow which is responsible for the opening of the crater. The two processes, although responsible for different physical effects, occur on overlapping time scales, are closely related and governed by one complex law making it impossible to truly separate them (Melosh, 1989).

The shock wave initiated by the compression stage propagates radially outwards distributing the kinetic energy from the projectile. As it expands, the material behind the shock wave is left with a motion radially away from the impact point. To fulfill the boundary condition of zero stress at the free surface a series of rarefaction waves are initiated by the movement of the shock wave along the face of the target. Particle motions near the surface are predominantly horizontal with the interaction of the rarefactions and the shock wave compression ejecting thin spall plates at high speed. At deeper depths the rarefactions deflect the particle motions from the outward radial motion upwards towards the surface establishing an upward and outward excavation flow (Gault et al., 1968). The geometry of the excavation flow is illustrated in Figure 1.2. Streamlines begin on the inner

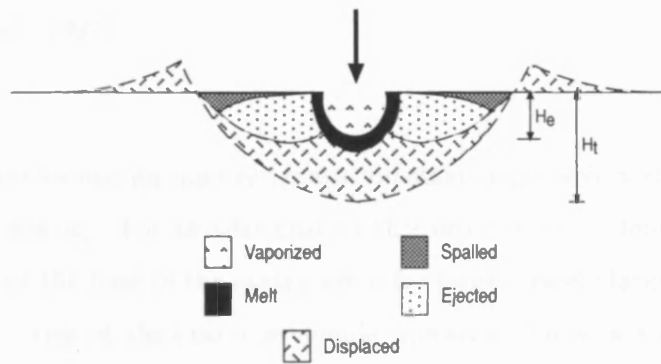


Figure 1.3: Regions of materials expelled from the crater. Material at the point of impact is vaporized and expands outwards as a vapour plume. Near surface material is expelled as spall plates whilst remaining material is either ejected or displaced downward by the excavation flow. H_e is the final excavation depth and H_t the resultant transient crater depth (after Melosh, 1989).

surface of the crater and progress outwards along curved paths cutting through pressure contours so that material following the path of the streamlines contain a range of shock levels. When material rises above the pre-impact surface it is considered to be ejected and begins to follow ballistic trajectories. Streamlines originating at the base of the crater indicate the path of displaced material that is not ejected (Figure 1.3). The excavation flow is responsible for the growth of the crater, opening the hemispherical cavity initially created during the contact and compression stage to its final stage known as the transient crater (Figure 1.4).

It should be noted that the term transient crater has been defined differently by various authors, leading to confusion and inaccuracies in scaling laws and energy estimates. Melosh (1989) defines the transient crater as the cavity lined with breccia and melts whilst Dence et al. (1977) define it as being the cavity that is bounded by the interface between the impacted rock and the breccias and melt, larger than the transient cavity of Melosh. Hildebrand et al. (1998) differentiated between the two by redefining the transient crater of Dence et al. as the disruption cavity (Figure 1.4d). Whilst it is possible to theoretically reconstruct the disruption cavity of large craters by moving slump blocks back to their original locations, the transient crater can only be reconstructed with knowledge of the

melt and breccia volumes, hence discussion of the transient crater of most large craters (including Chicxulub) has in fact referred to the disruption cavity (e.g., Hildebrand et al., 1991; Morgan et al., 1997).

Modification

The transient crater formed during the excavation stage is unstable and immediately begins to collapse under gravity. For smaller craters this involves loose debris sliding down the crater walls forming the base of the crater while for larger craters large slump blocks form terraces and the centre of the crater rebounds upwards. These are discussed further in Section 1.2.2. The time period over which these modifications occur is remarkably short, c. 10 seconds for smaller craters up to c. 10 minutes for larger craters. The resultant crater has an interior that is mass deficient but with a mass excess around the rims. True gravitational stability only occurs once the interior rebounds and the rim subsides to produce a plain. This occurs over a much longer time period generally through the long term viscous flow of the substrate or by erosion and infilling.

1.2.2 Crater morphology

The final morphology of a crater following the gravity driven modification stage goes through a series of transitional stages. As the crater increases in size the form of the crater graduates from a simple bowl shape to a series of more complex structures (Figure 1.5). Being gravity driven these morphological transitions occur at varying diameters on the different planets.

Simple craters

Simple craters are characterized by their bowl shape with overturned rims. They resemble the transient crater differing only in that their floor is covered with breccia and a pool of melt and shocked debris. Their formation from collapse of the transient crater and sliding of breccia back into the crater is relatively well understood (Figure 1.6) (e.g., Grieve et al., 1977; Melosh, 1989).

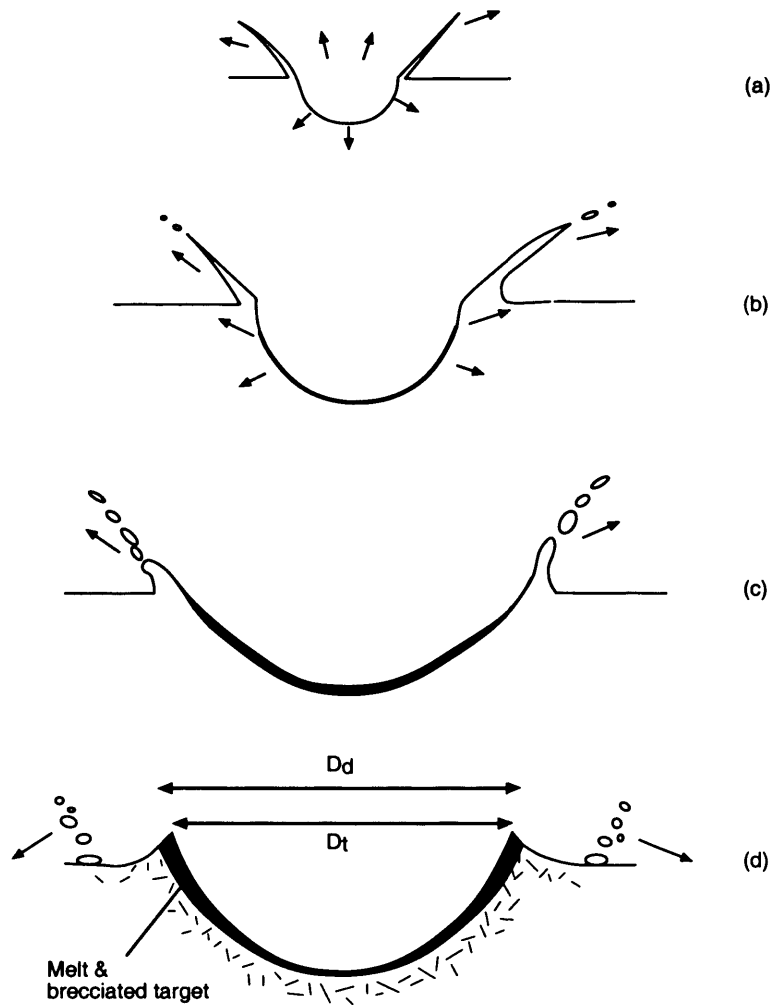


Figure 1.4: Formation of the transient crater. Its shape at any one time is given by the position reached by the innermost material within the excavation flow. The crater initially is hemispherical (a), expanding at a rate much slower than the impact velocity. Its rate of growth in depth slows and ceases (b) prior to the halt of its radial growth (c). The resultant crater (d) is known as the transient crater or cavity with a diameter D_t . The disruption cavity has diameter D_d . Throughout the formation the sides and base are lined with melt and highly shocked rocks (after Melosh, 1989).

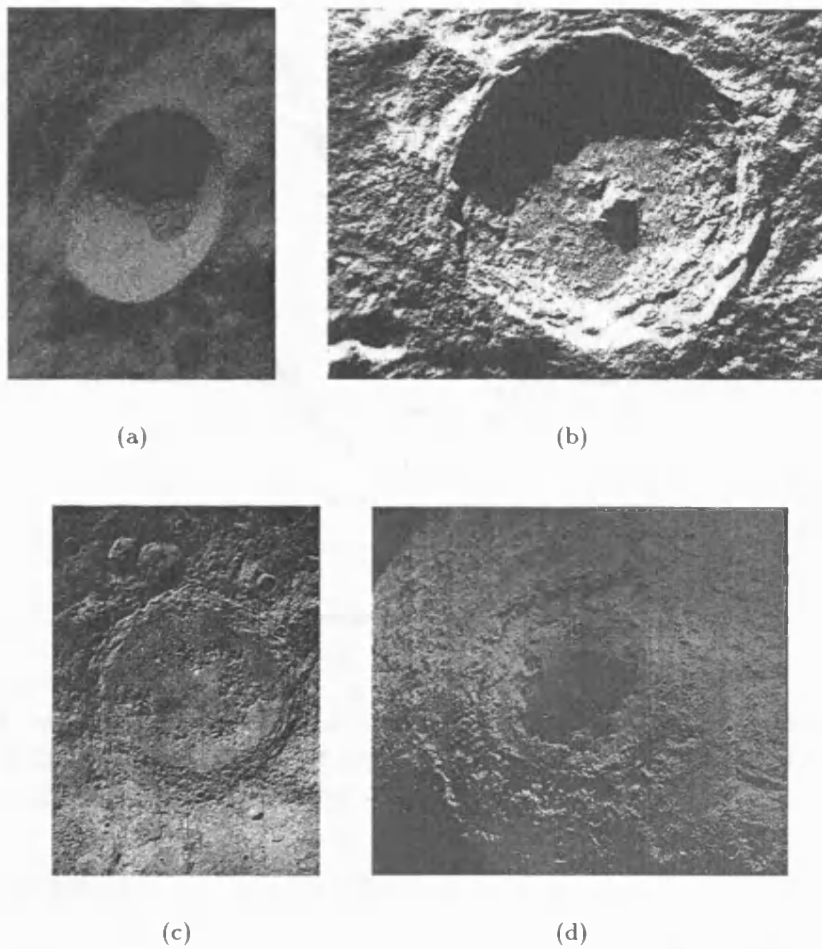


Figure 1.5: Crater morphology of lunar impacts (a) Alfrancus C, 10 km diameter simple crater, (b) Tycho, 85 km diameter central peak crater, (c) Schrödinger, 320 km peak ring crater and (d) Orientale, 900 km diameter multi ring impact basin. Images reproduced permission of the Geological Survey of Canada, Natural Resources Canada.

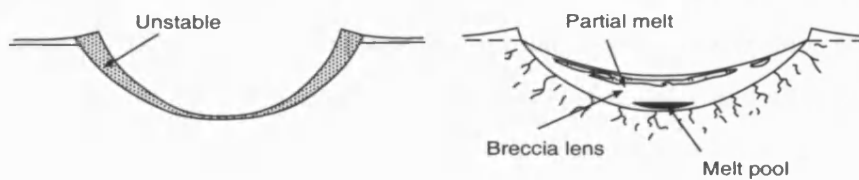


Figure 1.6: Formation of a simple bowl crater. The unstable sides of the transient cavity collapse to form the breccia infill. A buried melt pool is trapped at the base, whilst the mixed partial melt and breccia that lined the transient crater walls is concentrated near the top (after Melosh, 1989).

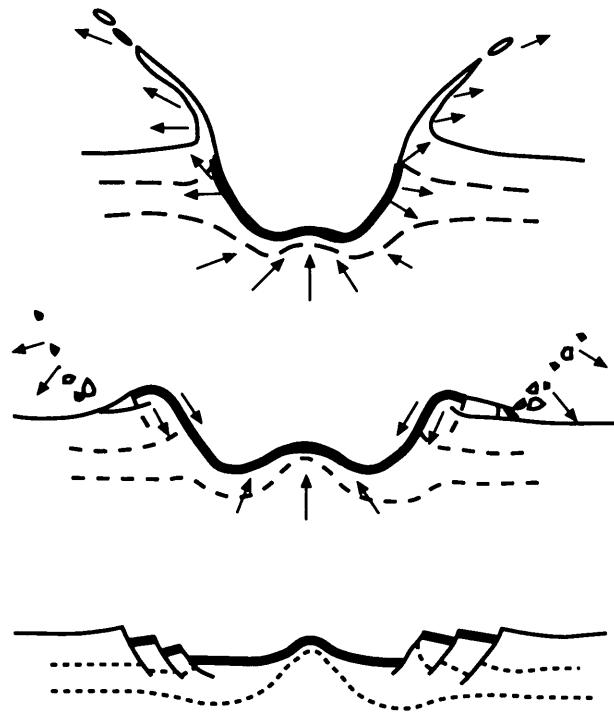


Figure 1.7: Formation of a central peak crater. Gravitational rebound of the centre of the crater begins almost immediately and no true transient crater is formed. Large slumping of the edges occurs to form terraces (after Melosh, 1989).

Complex craters

The formation of complex craters is less well understood with debate over the nature and origin of many of their features and the validity of the transient crater concept (Grieve, 1987). The transition from simple to complex form is abrupt occurring once the crater exceeds a few kilometres in diameter; the exact diameter depending on the target rock. Gravity driven modifications result in slumping of the crater sides to form terraced walls. The central floor of the transient crater rebounds rapidly upwards to form a peak in the centre of the crater (Figure 1.7) surrounded by a relatively flat crater floor (e.g., Melosh, 1989). The central uplift is composed of the original stratigraphy and although fractured and deformed is not a breccia or melt. Motion of basement rocks in the crater centre is inwards and upwards with the amount of uplift generally 10–15% of the final crater diameter (Dence et al., 1977). Nearer the rim, motion is inward and downward.

At around 25 km diameter on the Earth, a transition is seen from a central peak to a peak ring. The formation of a peak ring crater is widely believed to be a natural

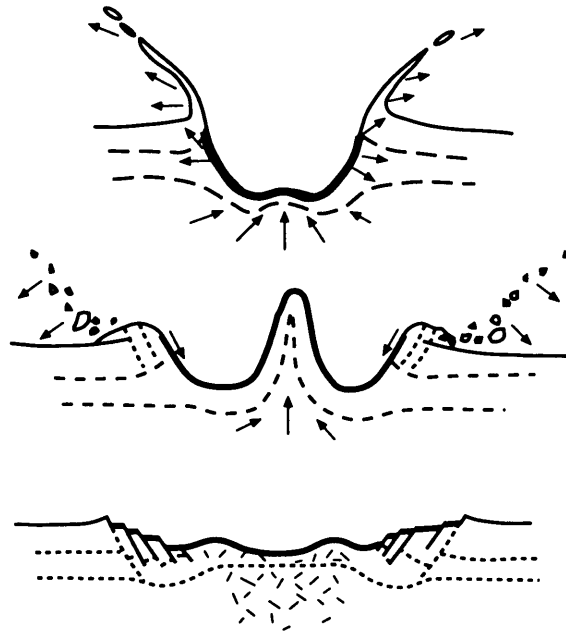


Figure 1.8: Formation of a peak ring crater. The central peak overshoots gravitational stability and collapses to form the peak ring (after Melosh, 1989).

progression from a central peak as the crater size increases. The peak ring is thought to form when the central uplift overshoots gravitational stability and collapses in on itself (Figure 1.8), analogous to the way in which a liquid droplet will form a central jet before collapsing and creating a ripple around its initial location. In the case of the droplet this ripple will expand outwards, however, in the crater situation the ripple ‘freezes’ to form the peak ring.

The mechanics of the formation of complex craters contravene generally held ideas concerning geological material strengths. Conventional rock and debris strength cannot explain the rim collapse to form terraced walls which instead requires the rocks to behave as perfectly plastic materials (Melosh, 1977). The formation of the central peak and peak ring requires the material to behave as a Bingham fluid with hydrodynamic behaviour that ceases when the shear stresses driving the central jet fall below its cohesion strength (Melosh, 1982). Whilst the phenomenology is understood, the physics remain debatable. Several ideas have been proposed including a melt-solid slurry, fluidization by water and acoustic fluidization (Melosh, 1983, 1989).

The largest craters form multi-ring basins which differ from peak ring craters in that several asymmetric ring scarps exist outside the crater rim. Possibly due to the lack of any unequivocal well preserved terrestrial example, multi-ring basins remain extremely controversial with debate on whether their formation is simply the next stage in the size-morphology progression or the result of a completely different process (Melosh, 1989). Several researchers have proposed that the diameter of successive rings form a $1:\sqrt{2}$ ratio (Pike and Spudis, 1987) whilst others have doubted the existence of such a ratio or whether it has any significance.

1.2.3 Crater identification

Whilst cratering on the moon is easily visible, identification of impact sites on the Earth has been more difficult. The high level of geological activity on the Earth hinders the recognition and discovery of terrestrial impacts. Although the increase in understanding of the processes of cratering and their effect on source geology has led to more discoveries the terrestrial impact record is still heavily biased towards stable cratonic areas and where active programmes to search for impact sites exist e.g., North America and Australia (Figure 1.9).

To date, approximately 156 impact sites have been identified on the Earth through their geological or geophysical signatures (Grieve, 1998).

Geological

Sediments can contain evidence of impact events in the form of shocked minerals, impact glass, soot and ash layers, impact breccias and impact induced tsunami deposits (Claeys, 1995). Geochemical and mineralogical studies of these layers may prove that they have an impact origin.

Some of the strongest geological evidence for impacts are a variety of shock features. On a megascopic scale, conical striated structures known as shatter cones have been shown to be impact related (Dietz, 1968) whilst on a smaller scale the high pressures and temperatures involved in impact events result in the shock metamorphism of most minerals (Bunch, 1968). The most commonly cited evidence of shock metamorphism is planar deformation features in tectosilicates such as quartz. Evidence of all carbon allotropes can be found in impact related deposits due to the wide range of temperature and pressure

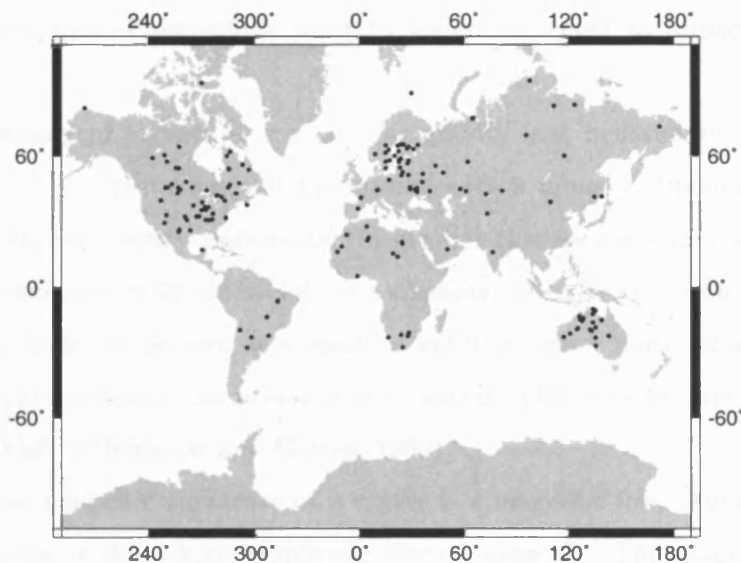


Figure 1.9: Terrestrial impact sites (source of data Geological Society of Canada).

conditions (Gilmour, 1998). These include micro-diamonds which under the P-T conditions of terrestrial volcanism would have reverted back to graphite or have been oxidized to form CO_2 . Geochemical studies of impact deposits show that they are enriched in rare earth elements such as iridium and osmium and indicate chemical relations in melt rocks and glass that are incompatible with a volcanic source. Spinels enriched in Mg, Al, Ni and Cr have been reported in impact related sediments worldwide and from meteorite fusion crusts (Bohor, 1990). These spinels have no terrestrial counterparts.

Small rounded silicate glass particles, often aerodynamically shaped, known as tektites are formed from the melting of terrestrial sediments during hyper velocity impacts (Glass, 1990). Geochemical and petrological evidence e.g., high $\text{FeO}/\text{Fe}_2\text{O}_3$ ratios and the existence of lechatelierite support an impact origin as opposed to a volcanic one. Tektites have been found over large regions of the Earth in areas called “strewn fields”, several of which have been linked to known impact events.

Geophysical

Approximately 35% of known impact structures on the Earth are buried by post impact sediments (Grieve, 1998) leaving geophysically based investigative methods as the pri-

mary tool for their investigation. The majority of terrestrial craters are initially identified through their geophysical signatures prior to being confirmed as impact structures by geological study.

The most prominent signature is a circular gravity low, believed to be the result of density contrasts from fracturing and brecciation with a minor component from infilling of the crater with low density sediments. In general this anomaly increases with crater diameter to a maximum of 20–30 mGal for a diameter of c. 30 km. Above this diameter a central gravity high can be seen as a result of uplift of denser material and compression in the central uplift although the presence of a central uplift does not necessarily imply a central gravity high (Pilkington and Grieve, 1992).

The dominant magnetic signature of a crater is a magnetic low. Again larger craters (> 40 km diameter) show a high amplitude central anomaly. The magnetic anomaly is generally more complex than the gravity and as with the gravity signature there is not a direct correlation between the character of the anomaly and crater morphology. The magnetic anomaly is believed to be a result of a combination of shock demagnetization and remagnetization, production of magnetic minerals through shock metamorphism and thermoremanent magnetization of impact melt rocks (Pilkington and Grieve, 1992).

Impact induced brecciation and fracturing can result in relatively large changes in seismic properties and both reflection and refraction methods have been used to provide detailed models of impact structures (e.g., Green and Chetty, 1990; Wu et al., 1995). Low velocities corresponding to the fracture zone extend at least one crater diameter beyond the crater rim with the velocity anomaly decreasing with distance as fracture density decreases. The low velocity zone correlates with a low density region and the potential field anomalies. In the centre of large craters, high velocities can be expected from uplifted deep crustal material. Crater features can be imaged by disruption of reflectors and incoherency of the seismic signal.

Although few examples exist of electrical methods being utilized in crater study, changes in electrical properties would occur indirectly from fracturing and brecciation resulting in changes in fluid volume and distribution. Recently Pilon et al. (1991) showed that ground penetrating radar could be utilized to provide detailed shallow (tens of metres) subsurface information of small impact craters.

1.2.4 Impact effects and relation to extinctions

Several researchers have raised the possibility of mass extinction events being related to impacts (e.g., De Laubenfels, 1956; Urey, 1973), but it was not until the suggestion by Alvarez et al. (1980) that the K–T extinction was the result of a bolide impact, that the idea was accepted by some sections of the science community. Alvarez et al. suggested that such an impact would result in a shut down of photosynthesis from dust in the atmosphere blocking out sunlight with a subsequent collapse of the food chain. The effects and possible kill mechanisms of impacts have since been examined by several researchers and are reviewed by Toon et al. (1997). They include:

Dust loading Dust would be ejected by an impact into the stratosphere with resultant effects on climate, photosynthesis and visibility. A large enough impact would blow ejecta out of the atmosphere allowing global distribution in under an hour. A layer of dust in the atmosphere will scatter sunlight back into space reducing or stopping photosynthesis and cause global cooling. An additional climatic effect to cooling could be a reduction in rainfall through changes in the thermal structure of the atmosphere reducing cloud formation.

Fires Several means exist of igniting global wildfires. Initially radiation is emitted from the bolide as it passes through the atmosphere followed by a fireball at the impact site. Impact debris will be heated both by the impact and, for larger impacts, atmospheric re-entry. Ivany and Salawitch (1993) proposed that as much as 25% of the Earth's biomass had to be burned at the K–T boundary to account for the reversal of the oceanic $\delta^{13}\text{C}$ gradient. Soot released by fires is extremely effective at reducing sunlight reaching the Earth's surface through back-scattering and absorption.

Nitric acid rain Strong shock waves in the atmosphere will produce nitric oxide from atmospheric nitrogen and oxygen. The reaction could occur during the initial transit of the bolide, the movement of the ejecta plume through the atmosphere or the re-entry of ejecta into the atmosphere (if the plume is large enough to punch through it). It is unlikely however that enough nitric acid would be produced to have serious effects on the acidity of the Earth's ocean.

Ozone depletion Nitrous oxide, dust and smoke particles and heating of the atmosphere would all cause severe depletion of the Earth's ozone level. This could result in a significant increase in ultraviolet radiation reaching the Earth's surface.

Water injections For an oceanic impact massive amounts of water vapour would be released into the atmosphere resulting in an increased greenhouse effect and higher surface temperatures.

Sulphate aerosol formation SO_2 and SO_3 can be generated by an impact into evaporites. Once in the atmosphere these would react with atmospheric water or water vapour released by the impact to create sulphuric acid resulting in surface water acidification (e.g., D'Hondt et al., 1994). Sulphur opacity could also result in long term global cooling from the presence of a persistent aerosol cloud.

Seismicity and volcanism A 10 km diameter impactor would generate at least 10^{24} J with $\sim 0.01\%$ of this being converted instantaneously into seismic energy. This compares with a yearly release of terrestrial seismic energy of 10^{18} J and the rate of energy input would be $\sim 10^7$ times the rate of global heat flow (Melosh, 1989). This amount of seismic energy has been estimated to be equivalent to that released by a magnitude 10–11 earthquake (McKinnon, 1982). It has been proposed that this energy could have induced volcanism both at the impact site (Rampino, 1987) and at the antipode due to seismic focussing (Boslough et al., 1996), although the possibility of Chicxulub triggering the Deccan traps has been precluded due to the timing and exact position of India at the time (Sutherland, 1994).

Tsunami An impact into an ocean would induce a tsunami which whilst not a global kill mechanism would probably result in local extinctions around continental margins. The exact size and effect of the tsunami would be variable depending upon local conditions.

Interactions between the various effects will affect their “efficiency” e.g., atmospheric sulphur will reduce the affect of ozone loss by back scattering ultraviolet radiation. The time scales can also vary depending on these interactions and the size of impact.

Subsequent to the linking of the K–T extinctions to an impact, several attempts have been made to relate impacts to the remainder of the “Big Five” extinctions (end Ordovi-

cian, late Devonian, end Permian, end Triassic and end Cretaceous), where over 75% of species were lost (e.g., Rampino et al., 1997). These lack compelling evidence and are often the result of an attempt to relate a periodicity of a single mechanism to all extinctions.

Chicxulub and the K–T extinctions

The K–T extinction remains highly controversial amongst researchers with debates over most aspects of it. Stratigraphic sections have been interpreted as representing both a geologically instantaneous or a gradual extinction by various groups. Bolide impact, volcanism, marine regression, anoxia or climatic changes are all advocated as causes of the extinction. This debate is reviewed elsewhere (e.g., Hallam and Wignall, 1997) and it is not the aim of this thesis to enter into it.

Whether or not it was linked to mass extinctions, there can be little doubt that the Chicxulub impact would have had a severe effect on the environment. The size of the impact and the Cretaceous stratigraphy of the Yucatan platform (a shallow marine carbonate platform with an anhydrite layer) are such that probably all of the previously mentioned effects would have played a role.

1.3 Geology of the Yucatan

The Yucatan peninsula is a large limestone platform that extends into the Gulf of Mexico as the Campeche bank. The peninsula is bounded by the Sierra Madre del Sur, the Sierra de Chiapas and the Maya mountains of Belize to the south. Geological knowledge of the platform is limited due to the heavy vegetation, poor access, limited outcrops and low relief combined with approximately horizontal strata. Much of the reliable information is known only through the wells that have been drilled by the Mexican state oil company, PEMEX and more recently the Universidad Nacional Autonoma de Mexico, UNAM. This lack of data make interpretations of the depositional environment and tectonics of the region difficult. In addition the majority of geological interpretation was prior to the correct identification of the Chicxulub crater making much of the understanding of the Cenozoic for the northwest corner of the peninsula suspect or incorrect. Data and analysis since 1991 have been focused on the crater itself and provided little further information on overlying geology.

The surficial geology of the platform is primarily Tertiary to Holocene carbonates and sediments which exhibit a range of physiographic features. The peninsula can be split into 4 regions (Weidie, 1985): the northern pitted karst plain, the Sierrita de Ticul, the southern hilly karst plain and the eastern block fault district (Figure 1.13). The northern part is characterized by low relief with a gentle increase in topography rising to c. 45 m over its 150 km inland extent. The Sierrita de Ticul is a narrow region around the Ticul fault scarp rising 50–100 m above the northern plain. Extending southward from the Sierrita lies the third province with maximum elevations of c. 300 m and gently undulating topography. The eastern fault block along the Caribbean coast is characterized by NNE trending ridges and depressions related to horst and graben faulting.

Throughout the northern and central Yucatan there is effectively no surface drainage and the area is a karstic surface. Numerous cenotes (sinkholes) have been formed in the limestone surface by the infiltration of rainwater.

1.3.1 Stratigraphy

The stratigraphy of the peninsula is one of slow, steady deposition and sinking from the Cretaceous through to the Pliocene when its present shape was attained. The general stratigraphy across the peninsula is indicated in Figure 1.10. Only a few wells have penetrated basement which generally consists of palaeozoic sediments or metasediments. There is no evidence of precambrian rocks. Precambrian rocks however are documented in Oaxaca and parts of Guatemala and Honduras and it has been suggested that this Precambrian belt may extend eastwards below the peninsula and scarcity of data is the reason for its apparent absence (Weidie, 1985).

Overlying the palaeozoic rocks is an unconformable red bed sequence, the Trodos Santos formation, whose age has been placed from Triassic to Cretaceous by various researchers but is most probably early Jurassic (Viniegra, 1981). An extensive sequence of lower Cretaceous evaporites named the Yucatan Evaporites by Lopez Ramos (1975) overlies this.

A marine transgression occurred during the Jurassic and throughout the early Cretaceous shallow marine conditions extended across the Yucatan platform with evaporite and carbonate deposition. Periodic intense evaporation producing magnesium carbonate concentrations gave rise to some dolomitization (Viniegra, 1981). During the late Creta-

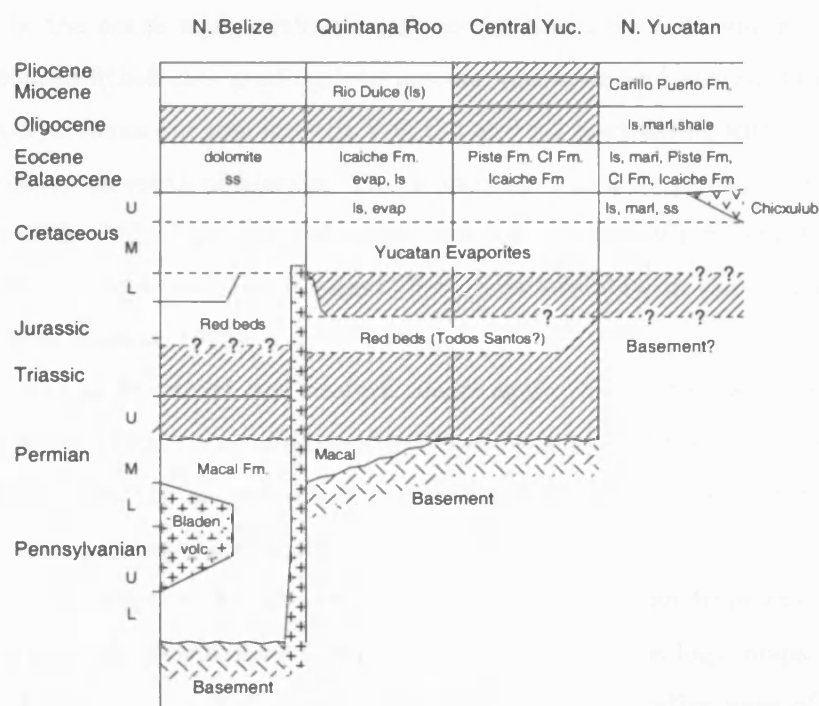


Figure 1.10: Generalized stratigraphy of the Yucatan platform (after Lopez-Ramos, 1973).

ceous the east central portion of the peninsula underwent substantial uplift and deeper water sedimentation took place towards the northwest (Weidie, 1985). Wells Y-6, C-1 and S-1 encountered an andesitic type rock which was initially interpreted as being of volcanic origin (Lopez Ramos, 1975).

Throughout the Tertiary sequences thicken to the northwestern corner of the peninsula and sediments appear to derive from a shallow water depositional environment with the exception of the Upper Oligocene in the northwest corner (Weidie, 1985). Lower Tertiary rocks are predominantly interbedded marls and limestones, with some dolomites and anhydrites. In the north and northwest Palaeocene and Lower Eocene rocks are of an evaporite-dolomite lithofacies grading into marine limestone and shales. Oligocene sediments of a bathyal fauna are seen in wells Y-6, C-1 and S-1 contrasting with the sub-littoral fauna of the outcrops south of Merida. This is indicative of a deepening of a basin to the north. South of 20° 30', Oligocene sediments have been partially removed due to erosion and the Carillo Puerto formation (Neogene) lies unconformably on Eocene and Oligocene sediments (Lopez Ramos, 1975).

Neogene rocks on the north and eastern coasts again thicken to the northwest. These are primarily shallow water carbonates which have been named the Mio-Pliocene Carillo Puerto formation. On the margins of the peninsula Quaternary rocks outcrop consisting primarily of beach and lagoon deposits (Pope et al., 1993).

The surficial geology of the northwest corner of the Yucatan from the 1984 INGEI (Instituto Nacional de Estadística Geografía e Informática) geology maps is shown in Figure 1.11. Pope et al. (1996) used soil analysis to infer relative ages of geomorphic surfaces within the northern Yucatan (Figure 1.12). This varies from the surficial geology from the INGEI with the Neogene–Eocene boundary more radial and a distinction of the Miocene and Pliocene surfaces within the Neogene. A complex pattern of emergence from mid Eocene to early Miocene was inferred with the oldest surfaces being the first to emerge. A two phase emergence pattern during the Neogene was implied from differences in late Tertiary geomorphic surfaces. Along the coastline the formation of a 2–20 km wide calcite cement aquitard (known as *tsekel* in Mayan) is an ongoing process (Perry et al., 1989). The cement is formed by the precipitation of calcium and carbonate ions from ground water evaporation. This zone continues offshore confining the aquifer and possibly producing a

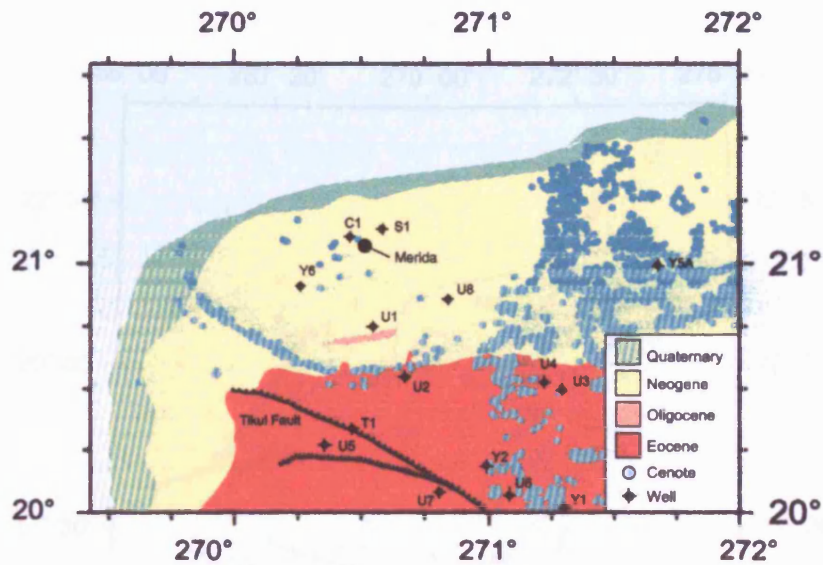


Figure 1.11: Surficial geology of the NW Yucatan peninsula with the location of PEMEX and UNAM drill holes (data taken from the 1984 INEGI maps).

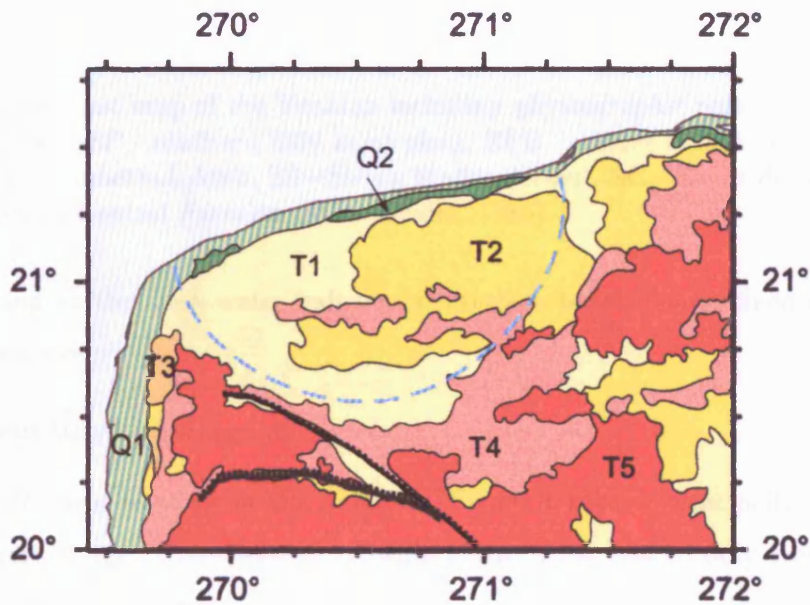


Figure 1.12: Geomorphological surfaces of the NW Yucatan. Q1: Holocene, Q2: Late Pleistocene, T1: Pliocene–Pleistocene, T2: Late Miocene–Pliocene, T3: Late Miocene, T4: Late Eocene–Oligocene, T5: Eocene, dashed blue line indicates the cenote ring. (after Pope et al, 1996).

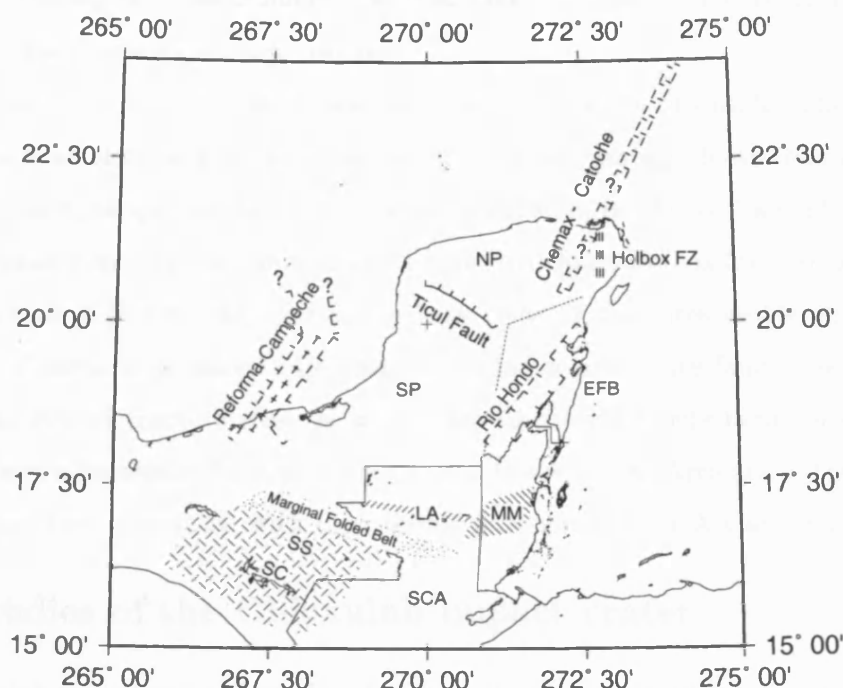


Figure 1.13: Tectonic map of the Yucatan including physiographic regions. NP - northern pitted karst plain, SP - southern hilly karst plain, EFB - eastern fault block, MM - Mayan mountains, LA - Libertad Arch, SS - Sierra Madre del Sur, SC - Sierra del Chiapas, SCA - Sierra of North Central America (after Weidie, 1985).

zone of mixing at the fresh-water/salt-water interface below the confined section where dolomitization occurs.

1.3.2 Structural geology

The known tectonic features in the Yucatan (Figure 1.13) are principally Mesozoic and early Cenozoic in age. Pre-Mesozoic information is vague due to only two wells having been drilled into basement.

The Reforma-Campeche fault zone is a generally north-south trending series of step faults running from onshore Tabasco to offshore Campeche (Viniegra, 1981). The normal faults are offset by some left lateral northwest trending faults. The age of faulting is uncertain but was probably associated with salt doming and diapirism during the Late

Cretaceous. In the northwest of the peninsula the Ticul fault is visible as a c. 160 km long southwest trending fault escarpment. Normal faulting down to the northeast occurred during the Late Cretaceous–Early Tertiary.

Three main zones are seen in the east and northeast of the peninsula. The Rio Hondo fault zone is a series of normal faults bounding horst and graben blocks trending approximately northeast, subparallel to the Caribbean coast from Belize northward for c. 350 km. In the northeast corner of the peninsula is the poorly defined Holbox fracture zone. Weidie (1985) describes a 50 km long zone of northern trending fractures visible on the surface as a series of linear depressions. He also postulated a subsurface fault zone believed to antedate the Holbox fracture zone. Known as the Chemax–Catoche fault zone this trends northeast from a Palaeozoic basement high known as the X-Can Arch across the Campeche bank and has been associated with taphrogenic movement of the X-Can Arch.

1.4 Studies of the Chicxulub impact crater

The Chicxulub structure was first identified from its circular gravity and magnetic anomalies. These potential field anomalies were associated with what were initially interpreted as andesitic rocks of a volcanic origin (Lopez Ramos, 1975).

Penfield and Camargo-Zanoguera (1981) first suggested that the Merida andesite volcanic field could, in fact, have an impact origin, but the significance of this was not realized despite the controversial theory of Alvarez et al. (1980) and it was not until a decade later that interest in the crater re-arose.

Hildebrand et al. (1991) on the basis of geophysical, petrological, geochemical and stratigraphical evidence repropounded a crater origin and suggested that the crater was on the K–T boundary. Impact shocked quartz was found within the andesitic rocks which were reinterpreted as impact melt and breccias. A thickening of ejecta layers towards Chicxulub and a similarity in composition of melt rocks and K–T boundary tektites made it a strong candidate as the K–T impact site. Since then the crater has been extensively investigated.

1.4.1 Geochemistry and petrology

Sharpton et al. (1992) conducted geochemical analysis of samples from wells Y-6 and C-1 finding evidence of planar deformation of quartz and feldspar and a high iridium content in the melt rocks. $^{40}\text{Ar}/^{39}\text{Ar}$ dating of several samples of melt rock from Y-6 gave an average age of 65.2 ± 0.4 Myr and palaeomagnetic analysis showed a reversed remanent magnetization believed to be chron 29R, spanning the K-T boundary. A K-T age for the melts was also reported by Swisher et al. (1992) who obtained a $^{40}\text{Ar}/^{39}\text{Ar}$ date of 64.98 ± 0.05 Myr from melt from C-1. This agreed with ages they obtained from tektite fields in Beloc, Haiti and NE Mexico. The composition of the melt was within the same range as that of the tektites.

Premo and Izett (1992) conducted isotopic analysis of Haiti black tektites concluding that the isotopic signature was consistent with the stratigraphy of either the Chicxulub or Manson impact sites. The Manson site in Iowa was ruled out as being a source of K-T boundary ejecta following the examination of U-Pb isotope data in shocked zircons (Krogh et al., 1993). Zircons from the K-T sections in Haiti and Colorado provided a primary source age of 545 Ma. with varying degrees of lead loss and isotopic resetting at the time of impact at 65 Ma. A 545 Ma. primary age was also obtained from a sample from well Y-6 but is inconsistent with the mid Proterozoic age of the material beneath the Manson impact. Other isotope studies of K-T boundary impact glasses have also proved to be indistinguishable from samples from Chicxulub cores (e.g., Blum et al., 1993).

Elevated iridium concentrations and a low $^{187}\text{Os}/^{188}\text{Os}$ ratio, incompatible with continental crust, have been obtained through examination of the Re-Os isotope signature of melt samples from Chicxulub cores (Koeberl et al., 1994). These are consistent with a meteoritic component and particles of almost pure iridium have also been discovered (Schuraytz et al., 1996) with possible implications for the impactor's size, composition, velocity and the energy release involved.

Evidence of extensive hydrothermal alteration of melt-rock including enriched sulphides was discovered from whole rock major and trace element chemical analysis. Schuraytz et al. (1994) suggested that the similarity of these to the Sudbury complex in Canada raised the possibility of ore deposits at Chicxulub but no evidence of these have yet been discovered.

As part of a drilling program by UNAM two wells c. 700 m deep were cored to the SE

of the crater centre at 125 km and 150 km radius. The inner well, U-7 had a two breccia sequence typical of the suevite-bunte breccia sequence observed at other craters (e.g., Hörz, 1982). Magnetic susceptibility measurements showed distinct contrasts between the Tertiary carbonates and the two breccia layers (Urrutia-Fucugauchi et al., 1996a). The upper suevitic breccia unit was not observed at U-6, its absence interpreted as a result of erosion occurring outside the crater rim.

The opinion that the stratigraphy of Y-6 was consistent with a volcanic and not an impact origin was restated by Meyerhoff et al. (1994). They also reported Maastrichtian fauna above the melt indicating a pre K-T age. Whilst there is no continued support for a volcanic origin, a pre K-T age was also suggested by Ward et al. (1995) following examination of biostratigraphic data and lithology of PEMEX wells. However other studies of Y-6 place a Tertiary age to lithologies immediately above the breccia from the identification of several species with a lowest stratigraphic age in the lower Danian (Sharpton et al., 1996). A non-volcanic or non-impact source for the breccia layer was suggested by Friedman (1996, 1997) who proposed that rapid dissolution and withdrawal of sulfates formed a dissolution-collapse breccia but admitted to not taking into account the evidence for impact shocked minerals. The composition of the breccia containing fragments of melt rock, metamorphic basement and unaltered anhydrite clasts is also incompatible with solution collapse (Ward, 1996).

1.4.2 Gravity and magnetics

Large amounts of potential field data have been recorded across the crater and used to produce several models of crater structure. Both the gravity anomaly and aeromagnetic data (Figure 1.14) show a striking circular structure.

The gravity anomaly shows a c. 180 km diameter low which is disrupted to the north forming a U shape. A central high is surrounded by several concentric maxima and minima. A southward trough is seen in the gravity anomaly, believed to be related to crustal thinning and rifting during opening of the Gulf of Mexico during the Jurassic (Sharpton et al., 1993).

The aeromagnetic data is elongated slightly in a NNW-SSE direction and has a central single high amplitude anomaly surrounded by short wavelength high amplitude anomalies. Neither the disruption to the north or the south trending trough in the gravity field are

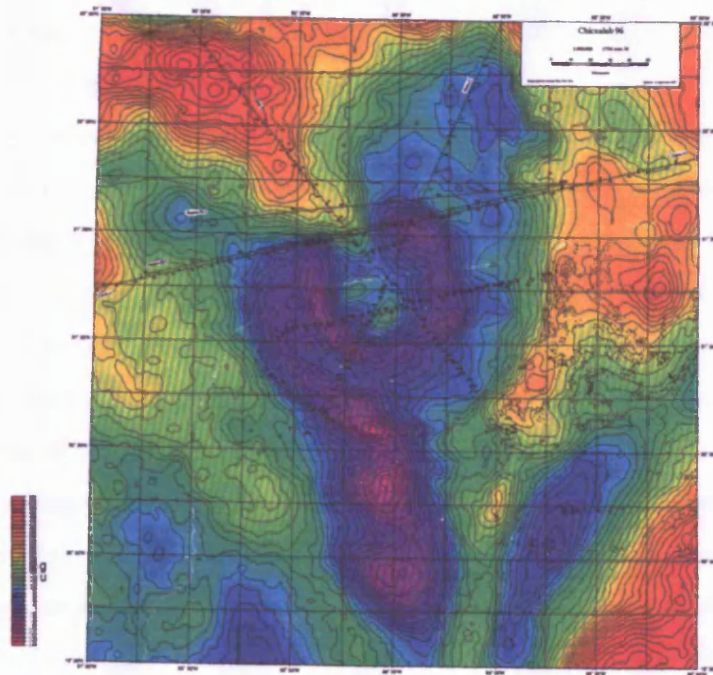
visible in the magnetic data.

Hildebrand et al. (1991) initially proposed a 180 km diameter crater with the crater rim corresponding to the boundary of a negative gravity anomaly. Two concentric lows at c. 25 km and c. 65 km were reported within this negative anomaly. The crater diameter was revised downward to 170 km diameter (Hildebrand et al., 1994) following 2-D gravity and magnetic modelling (Figure 1.15a) and constraints from borehole and cenote distribution. Assuming a 90 km radius Pilkington et al. (1994) estimated a mass deficiency for the crater of c. 1.2×10^{16} kg. The magnetic anomalies were interpreted in terms of the presence of a central melt pool and the central uplift.

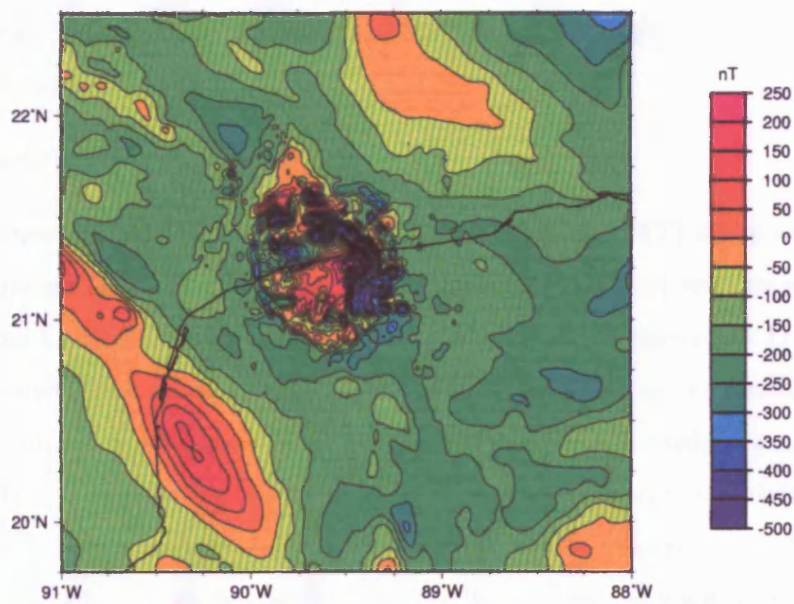
Sharpton et al. (1993) reinterpreted the gravity data (Figure 1.15b), proposing a multi-ring basin of c. 300 km diameter on the basis of three concentric maxima within the gravity anomaly and claims of a fourth fragmented ring corresponding to the crater rim. A peak ring was inferred from the inner gravity maxima at c. 52 km radius with the inner and outer limit of the transient crater related to the second (c. 77 km radius) and third (c. 99 km) maxima. They argued that steep gravity gradients inside the third ring were inconsistent with terrace and rim morphology and more suited to the outer limit of excavation and deformation. The diameter of the rings proposed by Sharpton et al. also followed the $\sqrt{2}$ relationship proposed by Pike and Spudis (1987) for lunar multi-ring basins.

A 180 km diameter crater was again advocated by Hildebrand et al. (1995) using the horizontal gravity gradient to emphasize lateral density changes and to suppress regional gradients. Six radial gradient maxima were reported with the outer four gradient maxima (c. 55 km–90 km radii) interpreted as a result of faulting in the crater slump zone. The outermost maximum also corresponded to the ring of cenotes, suggesting they were formed by slump faults near the crater rim. The inner maxima were interpreted as the central uplift (c. 25 km radius) and a peak ring (c. 45 km radius). Radial features extending over the central 40 km were explained by structural “puckering” on the central uplift.

On the basis of gravity and magnetic 2.5-D modelling, Espindola et al. (1995) (Figure 1.15c) proposed a central structural high surrounded by only one ring with its diameter constrained to c. 200 km. Campos-Enríquez et al. (1998) also advocated a 180–200 km diameter from calculations of the mass deficiency of the crater. Using Gauss’s theorem,



(a)



(b)

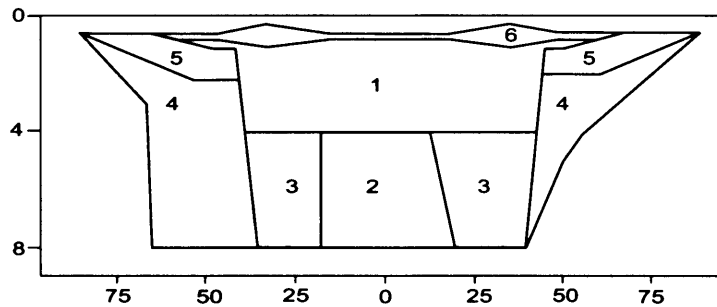
Figure 1.14: (a) Bouguer anomaly map of the Chicxulub impact with locations of seismic lines (figure courtesy of J. Morgan, IC London) and (b) aeromagnetic data across the Chicxulub impact structure (figure courtesy of M. Pilkington, NSC Canada).

mass deficiency values were obtained which corresponded closely to values obtained from the gravity models of Pilkington et al. (1994) and Espindola et al. (1995). In contrast the model of Sharpton et al. (1993) has a mass excess.

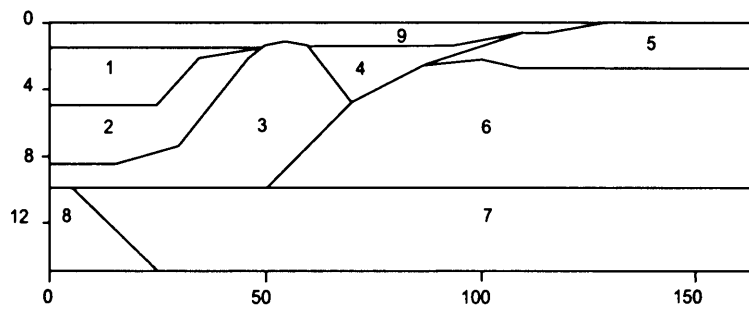
The asymmetries in the gravity anomaly have been explained by the poorer resolution obtained in marine gravity surveys compared to land surveys and also to an inferred northeast-southwest lineament. Schultz and D'Hondt (1996) advocated that the elongated central high encircled by the horseshoe shaped gravity low was a result of an oblique impact angle from the southeast. An oblique impact could explain the greater maximum size of grains and a two layer sequence seen in impact ejecta in North America. The lower layer represents fall out of a high velocity down range ballistic vapour cloud created by jetting during the early stages of penetration with the upper layer the fall out from a spherical vapour cloud created during the excavation stage. Laboratory experiments also revealed that oblique impacts allow a greater probability of survival of parts of the impactor which would be consistent with the recovery of a meteorite fragment from DSDP hole 576 (Kyte, 1998). However, it is more likely that the gravity high seen to the north is a result of a Palaeozoic basement high (J. Morgan, pers. comm. 1997). An oblique impact, this time from the southwest, was also proposed by Hildebrand et al. (1997) on the basis of an off-centre location of the central uplift that would be formed by rebound up and towards the impact direction.

1.4.3 Electrical and electromagnetic methods

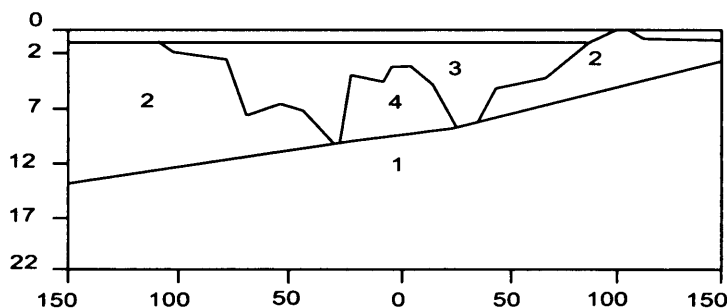
Campos-Enríquez et al. (1997) conducted a magnetotelluric (MT) study along two radial arms, one running south from Merida (line MT-A in Figure 1.16 and the second running southeast from Chicxulub Pueblo (line MT-B Figure 1.16). Preliminary 1-D results suggest a 190 km diameter structure with a region of high resistivity at the southern end of the profiles to a radius of c. 100 km. This decreases smoothly northwards to a zone of constant low resistivity from c. 70 km to c. 40 km radius before a high resistivity zone in the centre. This pattern has been interpreted as representing the transition from unaltered rock (associated with the resistivity high) to highly fractured rock within the impact basin reaching down to the lower crust and a central structural uplift again of relatively intact rock. No evidence was seen for a regional Moho uplift, providing isostatic compensation, which many cratering models suggest.



(a) Gravity model by Pilkington et al, 1994. Density contrasts are relative to surrounding rocks or Tertiary sediments (2550 kgm^{-3}): 1 - Melt sheet (-100 kgm^{-3}), 2 - uplifted basement (40 kgm^{-3}), 3 - megabreccia (-90 kgm^{-3}), 4 - Cretaceous stratigraphy (90 kgm^{-3}), 5 - outer breccia (-220 kgm^{-3}), 6 - upper breccia (-320 kgm^{-3})



(b) Gravity model by Sharpton et al, 1993. Density contrasts are relative to the Tertiary sediments ($9, \rho=1800-2000 \text{ kgm}^{-3}$): 1 - melt sheet (370 kgm^{-3}), 2 - inner breccia (250 kgm^{-3}), 3 - fracture uplifted crystalline basement (310 kgm^{-3}), 4 - outer breccia (230 kgm^{-3}), 5 - Cretaceous sediments (180 kgm^{-3}), 6 - upper basement (400 kgm^{-3}), 7 - intermediate basement (600 kgm^{-3}), 8 - uplifted deep basement (800 kgm^{-3})



(c) Gravity model by Espindola et al, 1995. Density contrasts are relative to the Tertiary sediments (2700 kgm^{-3}): 1 - Basement (40 kgm^{-3}), 2 - Mesozoic sediments (20 kgm^{-3}), 3 - breccias (-100 kgm^{-3}), 4 - uplifted basement (40 kgm^{-3})

Figure 1.15: Three gravity model cross sections of the Chicxulub crater. Note that the depth and horizontal (distance from centre of crater) scales of all three models are different.

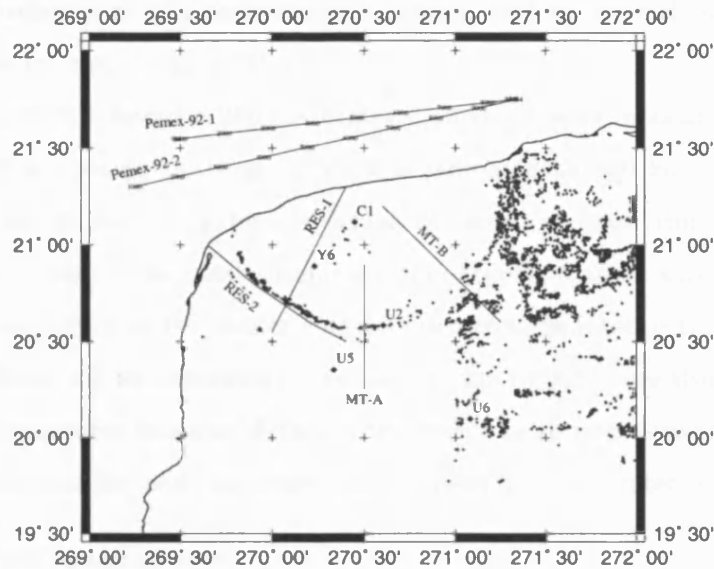


Figure 1.16: Location of previous geophysical surveys mentioned in text and drill wells where seismic data has been gathered.

A resistivity survey (Steinich and Marín, 1996) was conducted over the crater region to study the Yucatan karst aquifer associated with the cenote ring. Variations in cenote density were related to changes in permeability; high cenote density corresponding with low resistivities and high permeability. Electrical anisotropy calculations were used to determine the direction of aquifer discharge.

1.4.4 Topography and hydrogeology

Pope et al. (1991) proposed that the cenote ring visible at c. 80 km radius from the crater centre was related to post impact subsidence of the crater rim. This created fracturing of the limestone outwith the ring creating a boundary between fractured and unfractured rock with an increased flow of groundwater along the boundary causing dissolution and collapse. The ring also corresponds to a 5–10 m depression in topography and fresh water springs where the ring meets the coast (Pope et al., 1993). Connors et al. (1996) also advocated faulting of the outer slump zone as a formation mechanism for the cenote ring although an alternative origin from Oligocene reactivation along an arcuate shoreline of a

pre-existing fault system has also been proposed (Perry et al., 1995). Whilst they suggest that this may outline part of a hydrothermal system cooling the melt sheet they do not provide an origin for the initial faulting.

Pope et al. (1993) inferred a 240 km crater diameter from the location of the Cenote ring and fracturing outside the ring. This was increased to 260 km after examination of the topography of the region by extraction of elevation data from PEMEX gravity files (Pope et al., 1996). The most prominent topographic feature was the semi-circular depression corresponding to the cenote ring but two troughs interior to this (at c. 41 km and c. 62 km radius) and an outer ridge crest (at 129 km radius) were also observed. These were related to structural features of the crater with a peak ring between the location of the two innermost troughs and the ridge crest representing the crater rim.

1.4.5 Previous seismology

The first seismic data available for the area was obtained by Cué (1953) who conducted a shallow refraction survey adjacent to well C-1 and compared the results with the geological profile obtained from the core. Velocities of $<3 \text{ kms}^{-1}$ were obtained for the Tertiary section with higher velocities in what was interpreted to be the breccia layer. Slightly higher velocities were also suggested for the Palaeocene sediments than for the later Tertiary.

In 1992 PEMEX shot two offshore normal incidence reflection profiles along two chords across the northern portion of the crater (Camargo-Zanoguera and Suárez-Reynoso, 1994) (Figure 1.16). They interpreted three main sequences of reflectors. Firstly c. 1.25 km of Tertiary sediments with a relatively constant velocity of 2.5 kms^{-1} . Two topographic highs at c. 85 km radius were imaged at the base of the Tertiary and interpreted as a peak ring. The second sequence was interpreted as a melt sheet with a velocity of 5.5 kms^{-1} . A strong reflector at 1.5–1.8 seconds two way travel time (TWTT) was interpreted as the base of the melt sheet. Offsets of up to 2 seconds TWTT were imaged in the Cretaceous stratigraphy (the third sequence). These were interpreted as collapse slumping of the transient crater and used to infer a transient crater diameter of c. 170 km giving a final crater diameter of c. 300 km using appropriate scaling laws.

Seismic velocities have also been measured from samples gathered from well Y-6 and UNAM boreholes U-2, U-5, U-6 and U-7 (Urrutia-Fucugauchi et al., 1997). In U-7 a two layered breccia sequence with a higher V_p in the lower breccias is observed, consistent with

interpretations from magnetic susceptibilities measurements. Well U-5 shows an inverted velocity sequence between the Tertiary carbonates and breccias; V_p in the carbonates range from 3.5–6.3 kms^{-1} and in the breccias from 1.5–2.8 kms^{-1} .

A summary of previous seismic measurements at Chicxulub and seismic velocities of rocks similar to those found in the region is shown in Table 1.1.

1.4.6 Summary of previous models

Prior to the 1996 Chicxulub experiment several models, mostly based on gravity and magnetic data, had been proposed for the crater. The principal differences between them were the crater diameter and morphology. The two main models, a 180 km diameter peak ring (e.g., Hildebrand et al., 1991; Pilkington et al., 1994; Hildebrand et al., 1995; Kring, 1995; Connors et al., 1996) and a 300 km multi-ring (e.g., Sharpton et al., 1993; Camargo-Zanoguera and Suárez-Reynoso, 1994; Sharpton et al., 1996; Urrutia-Fucugauchi et al., 1996b) are summarised in Table 1.2 and Figure 1.17.

1.4.7 1996 Seismology and model

As part of this project normal incidence offshore and wide angle onshore and offshore refraction data was gathered. The geometry of this experiment is outlined in Chapter 2.

Two normal incidence reflection profiles (Morgan et al., 1997) indicate a multi-ring morphology with a peak ring at c. 40 km radius, an inner ring at c. 65 km and an outer ring at c. 97 km radius. An additional ring at c. 120 km radius was also suggested from disruptions in stratigraphy and continued deep deformation. This outermost ring was confirmed and the diameters of the inner rings slightly adjusted following analysis of an additional two profiles (Morgan and Warner, 1998). A low angle whole crustal fault was observed offsetting the Moho, believed to correspond to ring formation and analogous to pseudotacholyte zones observed at Sudbury (Spray and Thompson, 1996). Asymmetries in the location of the Moho offset would be consistent with a southwest oblique impact proposed by Hildebrand et al. (1997).

Analysis of refraction data recorded on ocean bottom seismometers (Christeson et al., 1998) indicates a regional deepening of the Moho to the east, opposite to the trend observed from gravity data. This contrast between gravity and seismics would imply considerable topography on the Moho, some indication of which was observed near the centre of the

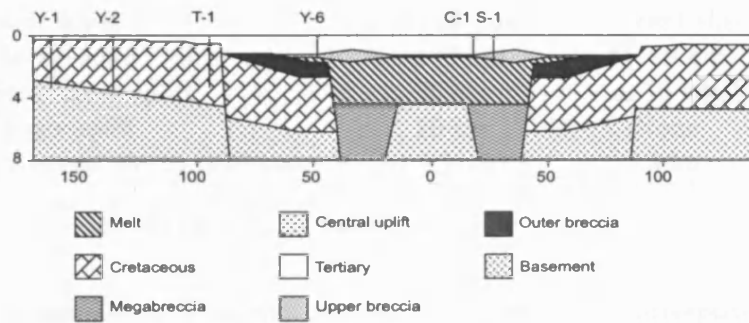
Rock	Location	V _p (kms ⁻¹)	V _s (kms ⁻¹)
Limestone (soft) ¹		1.7–4.2	
Limestone (hard) ¹		2.8–6.4	
Limestone ²	Germany	5.68	3.09
Marly limestone ²	CO, USA	2.38	
Well cemented limestone ²	PTT, USA	5.33	
Dolomitic limestone ²	CO, USA	1.86	
Dolomitized limestone ²		6.58	
Dolomite ²		6.68	3.41
Marl ²	CO, USA	3.20	
Dolomitic marl ²	CO, USA	1.86	
Gypsum ²		4.95	
Anhydrite ²		6.00	
Calcite ²		6.53	3.36
Volcanic Breccia ²	CO, USA	4.22	2.49
Lunar Breccia ²		2.88	1.80
Lunar Breccia ²		4.38	3.28
Tektites ²		5.92	3.63
Gneiss ¹	USA	6.71	
Marble ¹		3.75–6.94	2.02–3.86
Schist ¹	USA	4.89	3.27

(a)

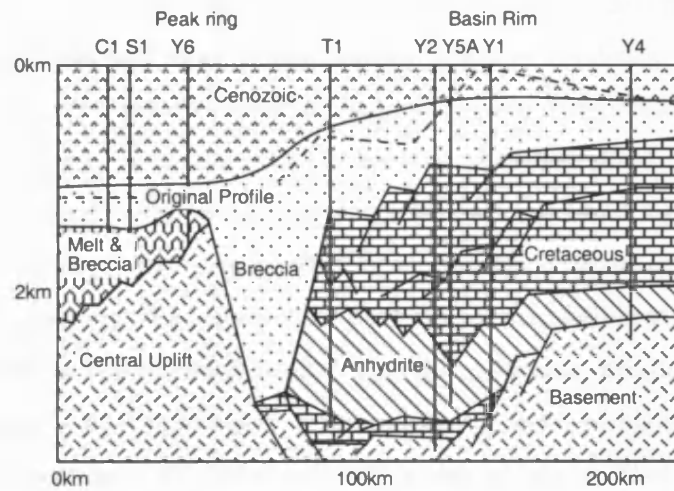
Lithology	Cue, 1953 (C-1) V _p kms ⁻¹	Camargo-Zanoguera, 1994 V _p kms ⁻¹	Urrutia-Fucugauchi, 1997		
			U-5 V _p kms ⁻¹	U-7 V _s kms ⁻¹	U-7 V _p kms ⁻¹
Tertiary	2.16–3.64	2.5	3.5–6.3	2.1–3.4	
Breccia	3.83		1.5–2.8	1.0–1.8	2.8–4.0 (Upper) 4.7–5.8 (Lower)
Melt sheet		5.5			

(b)

Table 1.1: (a) Examples of laboratory measured compressional and shear velocities of rocks likely to be found in the Yucatan (¹ Press, 1966, ² Carmichael, 1982). (b) Summary of velocities obtained from previous seismic studies of the Chicxulub crater.



(a) Simplified geological cross section of a 180 km diameter peak ring Chicxulub crater (after Pilkington et al, 1994).



(b) Geological model of the Chicxulub crater based on a 300 km diameter multi ring morphology (after Sharpton et al, 1996).

Figure 1.17: The two principal geological models prior to the 1996 Chicxulub experiment.

Feature	Sharpton 1996	Hildebrand 1994
Crater size	295 km	180 km
Crater morphology	Multi-ring	Peak ring
Transient crater diameter	170 km	90 km
Peak ring composition	Basement	Breccia
Melt sheet	Localized pods	Coherent sheet
Slump zone radius	85–105 km	45–90 km
Structural uplift	c. 30 km	c. 18 km
Moho uplift	c. 20 km	None
Proximal ejecta thickness	1.5 km	0.5 km

Table 1.2: Summary of crater models

profile where a deepening of 4 km was observed. Low velocities corresponding to the Tertiary infilling of the crater showed evidence of a progressive migration of shelf facies from the flanks to the centre of the basin. Slightly higher velocities were imaged at the base of the Tertiary with overlying younger unconsolidated sediments showing lower velocities. The lowest Tertiary velocities were imaged in the centre of the basin. Beneath the Tertiary section several large negative velocity anomalies were interpreted as representing a discontinuous melt sheet. A comparison of observed and theoretical travel times to on-shore stations using the velocity model from the OBS data indicated higher velocities were required within the crater centre, corresponding to the region of the central gravity high.

Brittan et al. (1998) report a topographic peak ring clearly visible at c. 80 km diameter, above the inner edge of the transient crater. Significant lateral variations are seen in the peak ring suggesting that it consists of a discontinuous series of highs, several hundred metres above the crater floor and consistent with observations at other large craters. The material composing it has comparable velocities with the lowest Tertiary sediments and the material immediately beneath the impact basin (Brittan et al., 1998) implying that there is no simple relationship between the gravity anomaly and peak ring as proposed by previous models. Formation of the ring from uplifted basement (Sharpton et al., 1993) is incompatible with its location above slumped blocks (Morgan et al., 1997) and the lack of density contrast between the ring and surrounding material. Similarly, formation from a low density breccia floating on a melt sheet (Pilkington et al., 1994) is also excluded. Shallow inward dipping reflectors are observed from below the peak ring to the inner edge

of the slumped block. These are believed to indicate the meeting of outwardly moving material from the collapsing uplifted central jet acting as a Bingham fluid and inwardly moving material from the collapse of the transient cavity. The surface manifestation of this meeting is the peak ring. This variation in materials is also believed to be visible in the wide angle refraction data as a 200–300 ms offset in first arrival times (J. Morgan pers. comm. 1998).

Three independent formation methods for the crater rim, peak ring and outer rings were proposed by Morgan and Warner (1998). The crater rim is the head scarp from the collapse of the transient crater to form the terrace zone; the peak ring from the interaction outlined above; and the outer rings by whole crustal collapse inwards. The exterior rings are believed to have been formed by low angle thrust faulting probably caused during the initial compression stage. During collapse, the outer rings then reactivated to accommodate some of the inward and downward motion. This would be consistent with observations at Sudbury of thick pseudotacholytes implying large scale motion, but with minimal stratigraphic offset.

1.5 Thesis outline

This Chapter has dealt with the mechanics of impact cratering with particular reference to the Chicxulub impact structure. Previous models of the structure and their failings have been discussed. The remaining Chapters deal with the seismic work conducted during the spring of 1996 and the analysis of surface waves in terms of crater structure and post impact sedimentation patterns.

- Chapter 2 outlines the main period of data acquisition in Spring 1996 and the controlled source experiment conducted in October of that year.
- The hypocentral location of local events is described in Chapter 3.
- Chapter 4 gives an introduction to surface wave analysis and its development. The chapter then outlines the theory and methodology used to obtain group velocity dispersion curves and attenuation coefficient (γ) values prior to inversion for Earth structure. Initial hypotheses of geology from the nature of the surface wave dispersion are discussed.

-
- Chapter 5 explains the theory of genetic algorithms used to invert for velocity and the choice of parameters to maximize the efficiency of the algorithm. The theory of singular value decomposition and its application to inversion for the attenuation quality factor, Q_β , is also presented.
 - The 1-D velocity models obtained from inversion of group velocity using a genetic algorithm are displayed in Chapter 6. These are combined with attenuation models obtained from linear inversion of γ to produce synthetic seismograms.
 - Chapter 7 presents the conclusions of this thesis. The results of this study are summarized and possible interpretations of the crater structure and overlying sediments are discussed.

Chapter 2

The Chicxulub Seismic Experiment

The field work associated with this study was conducted in two stages during 1996. Four months passive seismic recording of local, regional and teleseismic events from February–May 1996 (Section 2.2) was followed later in September by a controlled source onshore-offshore experiment (Section 2.3).

These two projects produced a number of seismic datasets which were studied by four institutions, University of Leicester, Imperial College, London, University of Texas Institute of Geophysics (U.T.I.G.), Austin and the British Institutes Reflection Profiling Syndicate (B.I.R.P.S.), Cambridge.

2.1 Objectives

The research aims of the studies reported in this thesis were to:

- Produce 1-D shallow crustal velocity and attenuation models of the crater and overlying sediments through the analysis of crustal Rayleigh wave (R_g) dispersion along solely onshore paths. These would complement the controlled source onshore-offshore interpretations and help constrain the shallower structure including the breccia layer and any melt sheet
- Utilize these models to infer crater structure especially across the crater centre where reflection data is not available. This is especially valuable for efforts to map the extent of any central uplift

- Investigate any influence the crater formation has had over post-impact sedimentation patterns and study changes in sediment depth in relation to topography of the crater floor and possible crater morphology.

These were chosen in order to aid in the combined objective of all the institutions studying the Chicxulub seismic datasets to investigate the crustal and upper mantle structure of the Chicxulub crater. In particular this included:

- the amount and extent of basement uplift
- the position and size of the melt sheet
- the position of slumped blocks and mega-terraces
- the position and formation mechanism of any peak ring
- the degree of radial asymmetry of crater features
- the radial extent of the crater
- the classification and morphology of the structure.

2.2 The passive seismic array

A temporary seismic array was deployed across the impact structure by the University of Leicester during early 1996 (Maguire et al., 1998). The array geometry consisted of 20 sites with a nominal spacing of 25 km, deployed along 4 radial arms extending from the centre of the structure, covering an area of approximately 100 x 200 km² (Figure 2.1). All of the stations bar two were deployed within a radius of 90 km from the approximate crater centre and thus within the smaller estimate of the crater size (Hildebrand et al., 1991). The remaining two stations were only just outside this radius and so well within the larger estimate of 150 km (Sharpton et al., 1993). Initially it had been intended to place these stations well outside the structure on “undisturbed crust”, however, budget and logistic constraints necessitated their being sited at a closer distance to the field base at Chicxulub Puerto. A denser deployment of instruments was used over the crater centre as offshore reflection profiles would be unable to image this area during the controlled source project (Section 2.3).

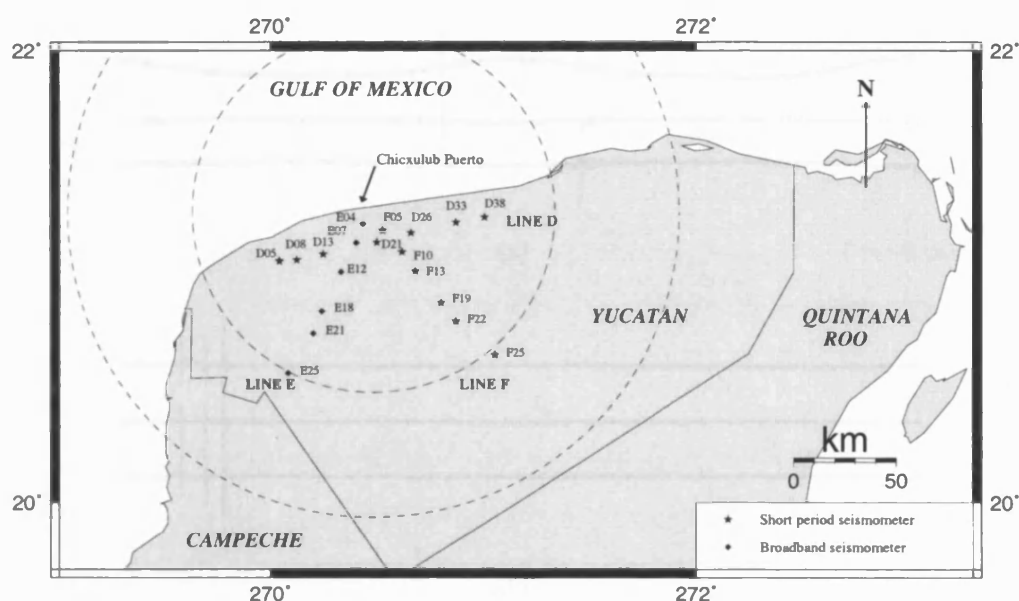


Figure 2.1: Recording geometry of the passive array. The inner dashed circle represents the smaller crater diameter of 180 km, the outer one the larger 300 km diameter.

The equipment used consisted of 15 x 3-component Teledyne Geotech S13 short period (1 Hz) seismometers, 5 x 3-component Guralp CMG-40T broadband seismometers (on loan from GeoForschung Zentrum, G.F.Z.) and 1 x 3 component Guralp CMG-3T broadband seismometer (on loan from the British Antarctic Survey). The seismometers recorded continuously to Teledyne PDAS (Portable Digital Acquisition System) recorders which wrote to 540 Mb external disks. These and the short period S13 seismometers belonged to the University of Leicester or were on loan from the Natural Environment Research Council (N.E.R.C.). An external GPS receiver connected to each PDAS controlled timing and recorded station location every 2 hours.

The broadband seismometers were deployed along Line E (Figure 2.1) with the short-period instruments along Lines D and F. One station (E07) recorded from both broadband and short-period instruments allowing for signal comparison during later processing.

The initial period of the field work season was spent gaining permission from local authorities and landowners to deploy instruments and in building the structures and digging the pits to locate the instruments in.

The seismometers were buried in shallow brick lined pits where possible, but the lack of topsoil in many locations made this difficult and often they had to be deployed on

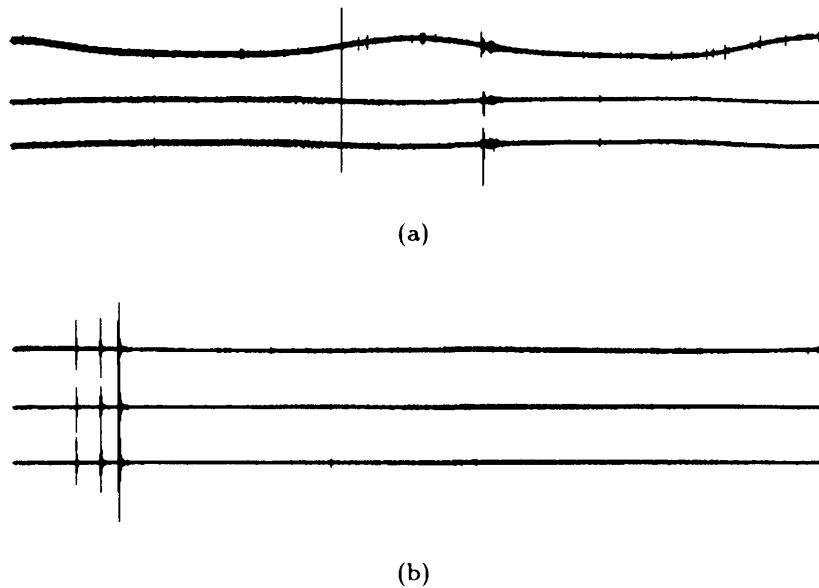


Figure 2.2: 48 hour 3 channel broadband record a) prior to insulation showing variations due to temperature fluctuations b) after insulation, removing the fluctuations outside the recording band.

the surface enclosed in small brick huts (c. $1 \times 1 \times 0.5 \text{ m}^3$). The recording instruments were located in a similar structure c. 12 m from the seismometers. An initial problem with the broadband instruments was the recording of the expansion and contraction of the instrument due to daily temperature fluctuations (Figure 2.2). This was solved by insulation of the instruments, filling the pits with sand and then mounding sand and gravel across the top.

Recording took place from the 8th February (Julian day 39) to the 18th May (day 139). During this time two sites were moved due to problems with instrument security. Individual instrument recording schedules are given in Appendix A. The sites were visited using an 8 day rotation cycle, whereby approximately 4 to 5 sites were visited every second day. This visit was used to replace the external disk and battery, the disks then being returned to the base at Chicxulub Puerto for down loading to computer and tape. The intervening day between site visits was used for this down loading, checking data quality, cataloguing of events dependent on signal to noise ratio and revisiting any sites to fix problems that had been noticed.

The most common problems that occurred were:

- Interference, disturbance by animals and people
- Failure of the digital to analogue conversion link within the PDAS
- Problems with the link to the GPS.

Where possible these were corrected in the field but when necessary the PDAS was replaced by a spare recorder and brought back to the base. In addition to the above list one Guralp had a mechanical problem which resulted in its replacement by a set of S13's and one of the PDAS's developed an electrical fault.

Data recording was continuous as the external disk size and the ability to look at all the data in the field and catalogue events negated the need to employ any form of triggering on the PDAS's. This maximized the recording time available as no time was spent testing triggering and it also meant that no events were missed.

Despite the majority of seismometers being deployed above ground, signal to noise was in general extremely good, with the worst levels occurring along Line E which was close to the main Merida–Campeche highway. However, during periods of high winds, signal to noise did deteriorate slightly due to the seismometer siting.

In addition to running the array this field season was also used for preparatory work for the controlled source experiment conducted later that year. Permissioning and building of the sites to be used was completed and as many of these stations as possible had a RefTek recorder and single component vertical seismometer deployed for a few days to check their suitability for recording. The principal concerns were the ambient noise level and the possibility of siting an instrument over a cenote which would have caused severe distortion of the signal.

2.3 Controlled source experiment

The second stage of the project was conducted in September and October of 1996, primarily by Imperial College, London, B.I.R.P.S. and U.T.I.G. (Morgan et al., 1997; Christeson et al., 1998).

This experiment consisted of c. 650 km of deep reflection normal incidence profiles recorded by B.I.R.P.S. along 4 radial offshore lines, the closest being c. 26 km from the crater centre. The crater centre lies approximately on the coastline and the shallow offshore

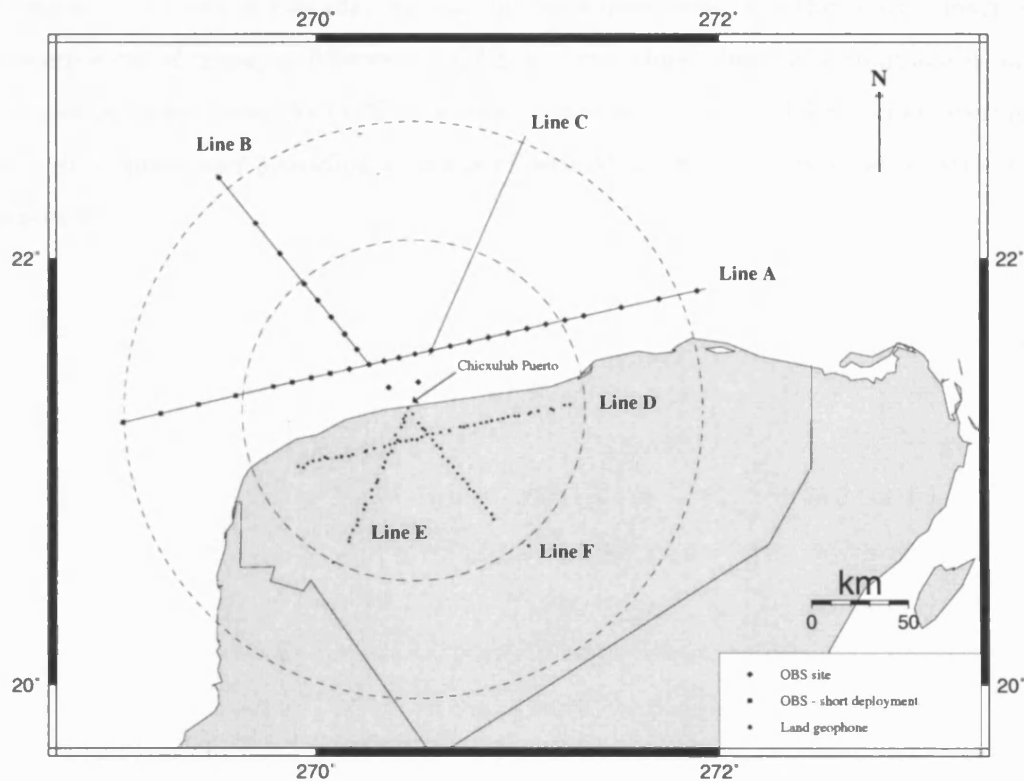


Figure 2.3: Geometry of the controlled source experiment showing location of reflection profiles, land receivers and OBS's. Dashed lines are as in Figure 2.1

conditions precluded the shooting of a marine crater centre profile. Wide angle seismic refraction data was recorded simultaneously on 34 Ocean Bottom Seismometers (OBS's) along 3 of these lines (A, A1 and B) with a station spacing of 10–20 km and 91 land receivers (Figure 2.3).

The land instruments were deployed along the 4 radial arms used for the passive array and consisted of 3 component Mark geophones connected to RefTek recorders on loan from IRIS Passcal. The geophones had a station spacing of c. 5 km again with a denser spacing over the crater centre. Continuous operation of the receivers during the experiment allowed the recording of several quarry blasts from local quarries, identified during the passive experiment. These quarries were also visited to obtain shooting information and GPS locations.

During this project a concurrent marine and onshore gravity survey was conducted by

the Geological Survey of Canada. As part of this survey several of the seismic instrument sites were located using a differential GPS system, thus allowing a comparison of site locations calculated from the GPS receivers connected to the PDAS recorders during the passive experiment and providing a means of estimating the single receiver location errors (Chapter 3).

Chapter 3

Event Location

Whilst in Mexico, the recorded data was downloaded from disk to tape as disks were retrieved from the field. This produced an archive where one tape contained several days data from three or four sites. On return to Leicester, this resulted in a complex and disorganized event retrieval system so, prior to any processing, the data was re-archived. Tapes were re-written on a daily basis with one tape containing all data for one 24 hour period. At the same time known events from the cataloguing completed in the field were copied to separate event tapes. The regional and teleseismic data has since been converted to SEED format and archived on the IRIS DMC catalogue.

Regional and teleseismic event locations were obtained from the catalogues issued by the USGS and NEIC and are listed in Appendix B. This chapter describes the location and distribution of recorded local events.

3.1 Site location

All the sites were connected to a GPS system which recorded time and position every two hours. This controlled drift of the recorders internal clocks which never exceeded 4 ms. Site locations were calculated by a simple averaging of the two hourly location measurements (in general an average of over 1000 locations). These all occur within a c. 300 m radius of the average and no jumps or drifts occurred over the recording period, indicating that the need for anything more complex than a simple average is not called for (Figure 3.1). Differential GPS positions using dual frequency and carrier phase were recorded at many of the sites in October by members of UNAM and the GSC during a gravity survey. In each of these situations the average and differential locations differ by

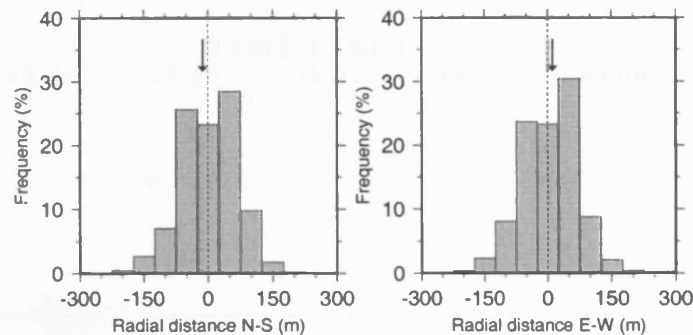


Figure 3.1: Distribution of distances of individual GPS locations from the average location of site D13. Positive distances are North and East in the respective plots. The differential GPS location of the site obtained by the GSC is marked by the arrow.

not more than 15 m.

3.2 Qualitative descriptions of seismograms

A typical local event is shown in Figure 3.2. It can be seen that there are variations in dispersion characteristics of the traces and the arrival times of phases are path dependent, suggesting there is significant variation in the geology across the region. All events were characterized by several distinctive features:

- High frequency (> 10 Hz) body wave spectra often exhibiting spectral modulations (Figure 3.3).
- High amplitude, well dispersed fundamental Rg phase with a 1–3 Hz spectra (Figure 3.4).
- Clearly defined complex Lg phase showing little dispersion on the transverse component (Figure 3.4).

In addition several of the events show almost identical waveform and spectral content, implying identical (or near identical) source functions (Figure 3.5).

The large amplitude fundamental Rg phase which can be seen to propagate across the network to over 55 km, is generally indicative of a shallow source (Sakia, 1992). Unusually, the fundamental Rg mode on the majority of seismograms exhibits reversed dispersion,

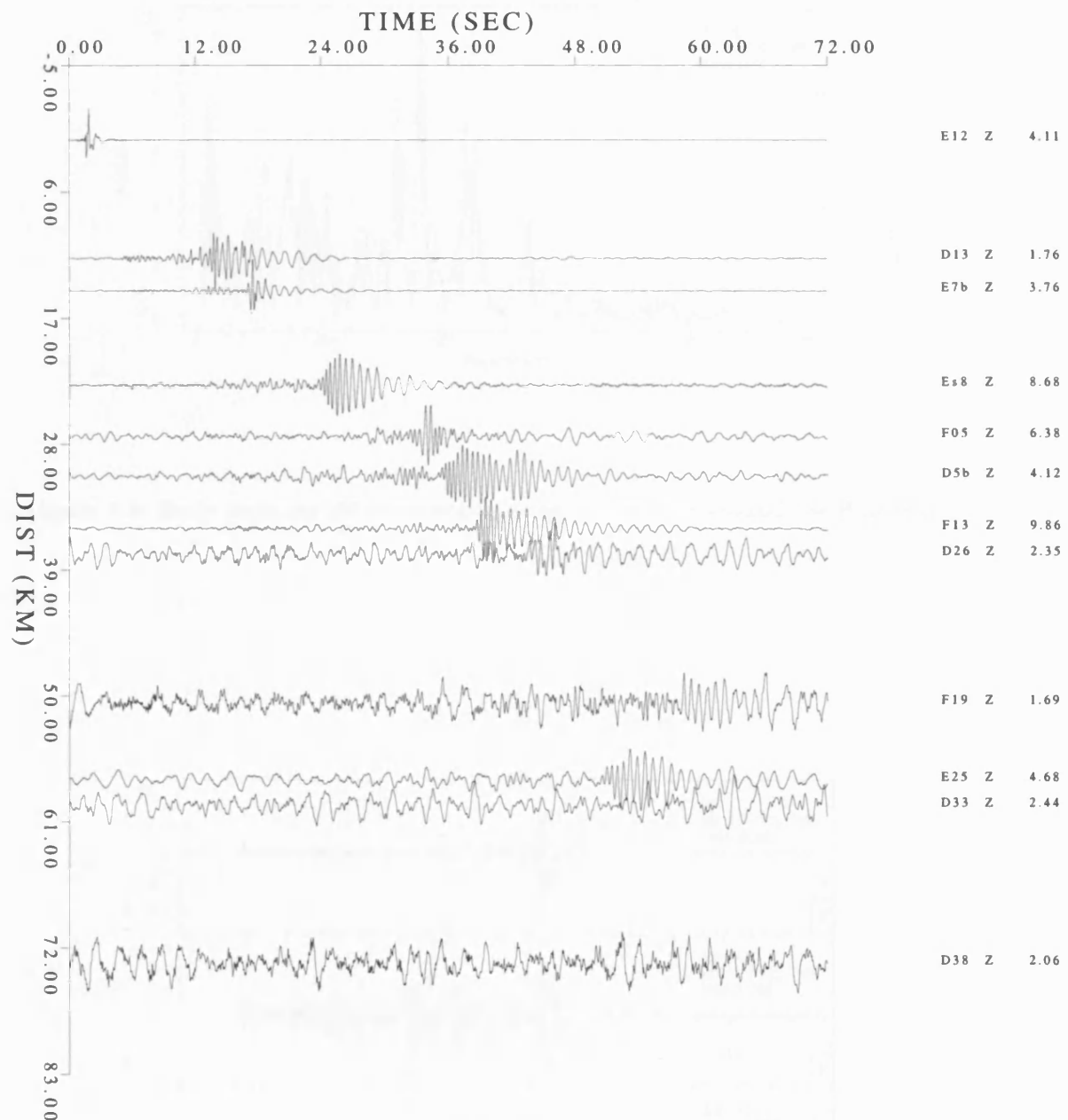


Figure 3.2: Typical record section for one event recorded at multiple stations. Note that the traces have been high pass filtered above 0.4 Hz to remove low frequency noise and are individually normalized.

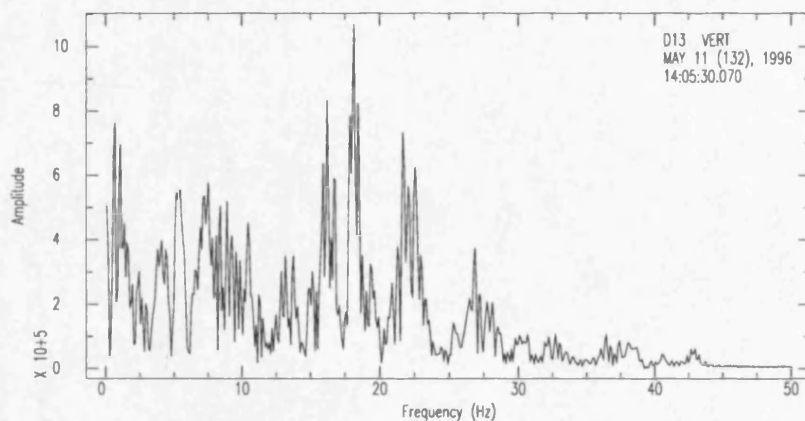


Figure 3.3: Body wave amplitude spectra for an 8 s window around the P arrival.

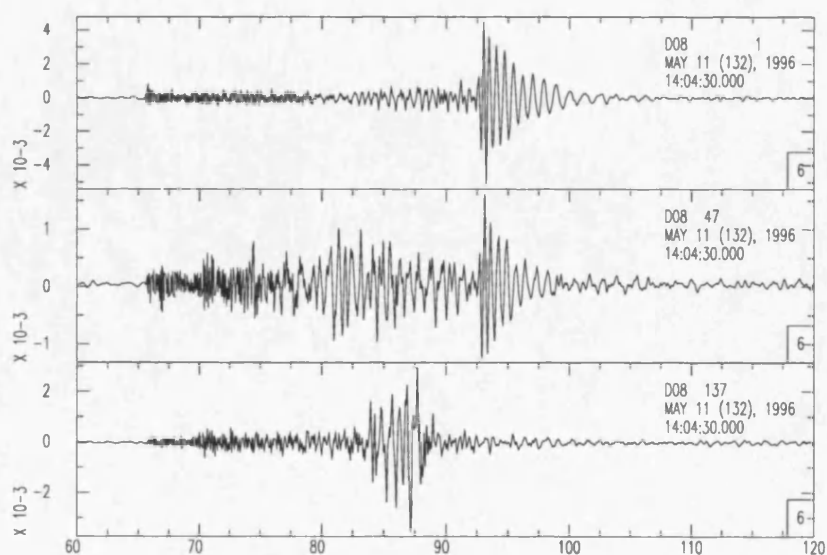
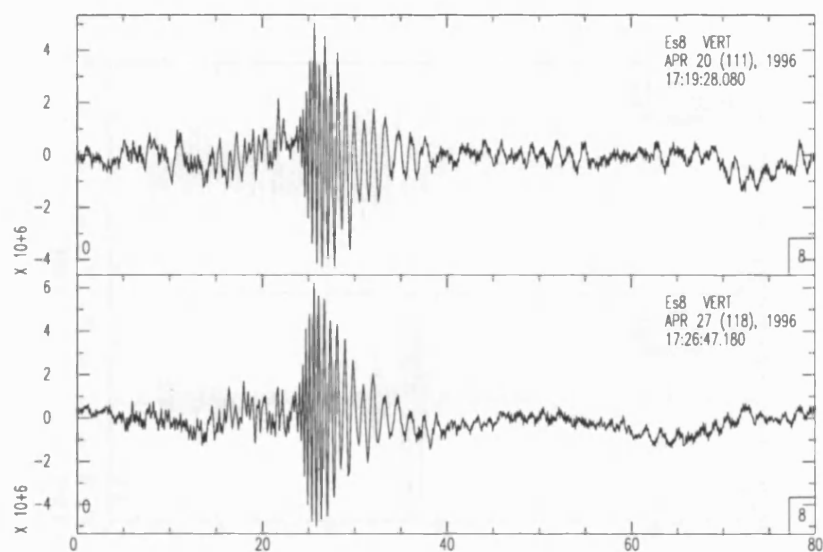
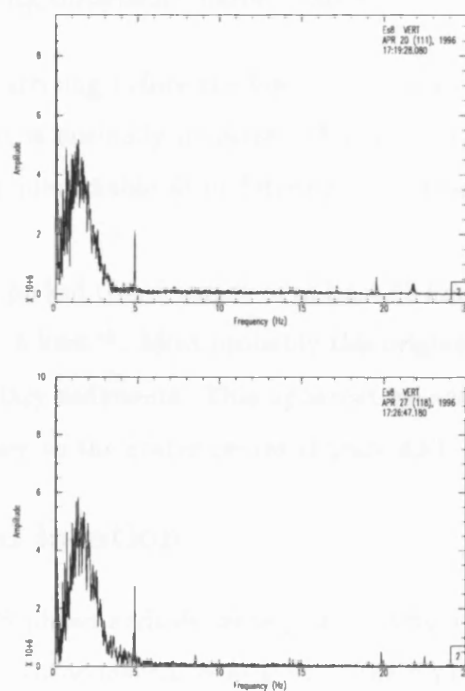


Figure 3.4: Example record showing high amplitude Rg on the vertical and radial and Lg on the transverse component.



(a)



(b)

Figure 3.5: (a) Waveforms from two events recorded at the same station and (b) their corresponding frequency spectra.

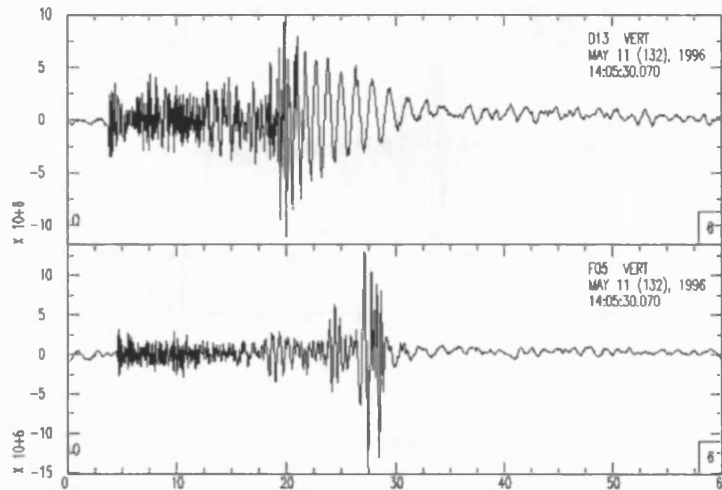


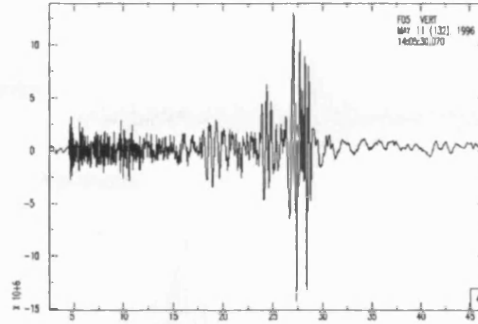
Figure 3.6: Vertical records from two stations for the same event and similar path lengths exhibiting very different Rg dispersion characteristics.

with the high frequency arriving before the lower frequencies. The minority show a much less dispersive phase that is normally dispersed (Figure 3.6). Probable higher modes are also visible, more clearly identifiable after filtering and through particle motion analysis (Figure 3.7).

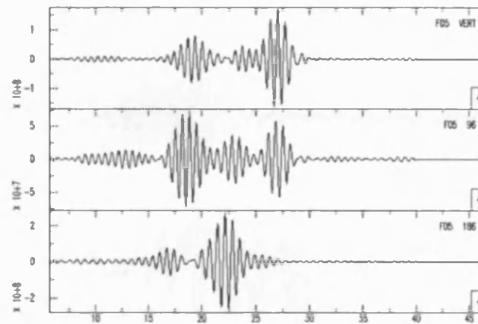
P-wave onsets can be picked to a distance of at least 40 km from the source and provide an apparent velocity of c. 5 kms^{-1} . Most probably this originates from brecciated material and melt below the Tertiary sediments. This apparent velocity can be seen to increase to c. 6 kms^{-1} for paths closer to the crater centre (Figure 3.8).

3.3 Hypocentral location

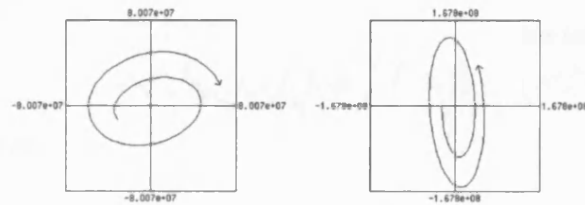
P and, where possible, S phase arrivals were picked using the seismic package SEISAN (Haskov, 1995) and events subsequently located using the HYPOINVERSE program (Klein, 1990). The accuracy of the final locations obtained from this program depend upon the validity of the various input parameters and assumptions made. These are the number and precision of picked arrival times, the accuracy of the timing, location of stations, the



(a)



(b)



(c)

Figure 3.7: (a) Unfiltered vertical trace recorded at station F05. (b) Vertical, radial and transverse components for F05 band-pass filtered at 1.5 Hz. Fundamental and higher mode Rg can clearly be seen on the vertical and radial components with a strong Lg on the transverse (note different time window from (a)). (c) Particle motions in the sagittal plane for 2 second windows from 15–17 seconds and 26–28 seconds confirming a retrograde motion for the fundamental mode and showing the higher mode has prograde motion.

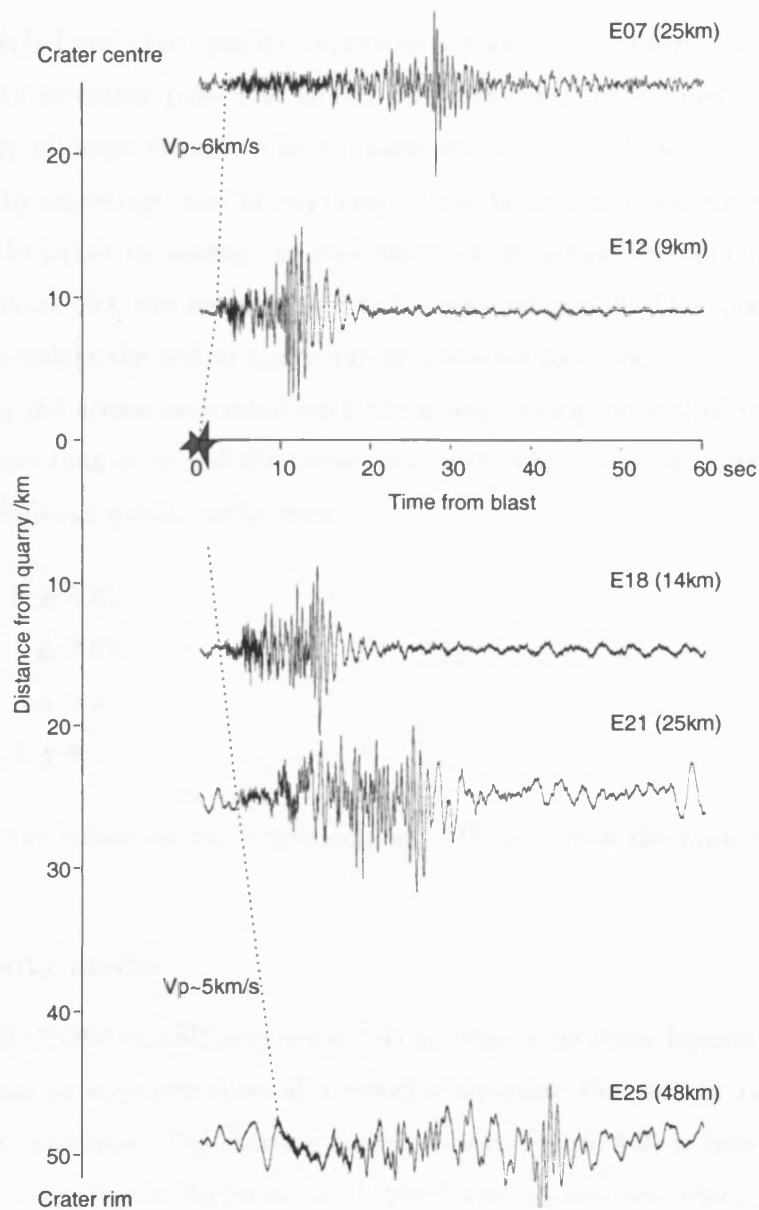


Figure 3.8: Record section along Line E for a quarry blast near the airport. Apparent P-wave velocity shows an increase towards the centre of the crater.

input model and V_p/V_s ratio.

3.3.1 Phase-picking

Phases were picked and their quality judged on a scale of 0–3, where 0 is the best (clear pulse onset with no earlier pulse and almost zero error) and 3 the worst (very poor onset with possibility of large error). The S phase arrives in the P wave coda and is also more affected by anisotropy and attenuation. These latter effects can cause splitting and shadowing of the phase, increasing the uncertainty of the arrival time (Thurber, 1993). As a result an S phase pick was never judged to have a quality of 0. This quality assessment is then used to weight the arrival times during the event location.

To evaluate the errors associated with the phase picking, several of the seismograms were picked more than once and the times compared. The maximum difference in arrival times for the different quality picks were:

Quality 0 \pm 0.01

Quality 1 \pm 0.07

Quality 2 \pm 0.2

Quality 3 \pm 0.4.

In general the difference was approximately 75% less than the maximum differences listed here.

3.3.2 Velocity model

The program HYPOINVERSE requires a 1-D homogeneous plane layered velocity model which represents an approximation of a velocity structure that will in reality show significant lateral variations. The starting model chosen (Figure 3.9) is from a summary of shallow seismic velocities by Brittan et al. (1998) based on offshore reflection data (Ewing et al., 1970) and borehole data (Cué, 1953). During the initial location, V_p/V_s was set to an arbitrary value of 1.74. The event locations using this initial model are shown in Figure 3.10. The distribution of the events is discussed further in Section 3.3.6.

Each event cluster was then studied independently to investigate model suitability, event depth (Section 3.3.4), station residuals (Section 3.3.3) and V_p/V_s ratios (Sec-

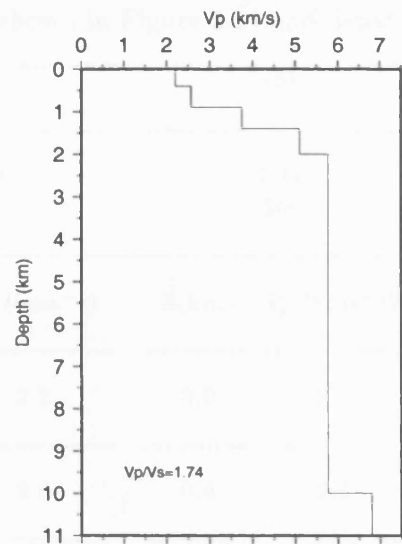


Figure 3.9: Velocity-depth model used for initial event location.

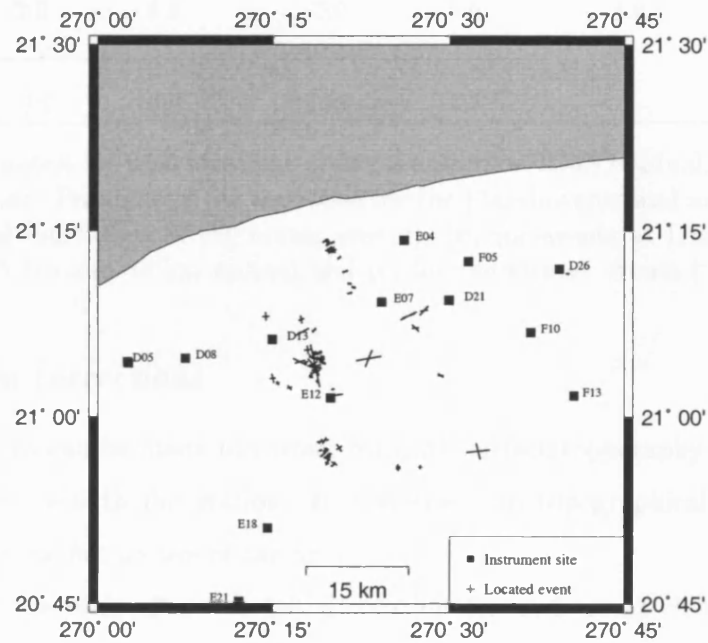


Figure 3.10: Initial event locations. Crosses indicate the axis of the 3-D error ellipsoid collapsed onto a 2-D plane.

tion 3.3.5). They were then relocated using the best values for these parameters (Table 3.1) to give the final locations shown in Figure 3.11 and listed in Appendix C.

	(a)		(b)		(c)	
V_p/V_s Depth	1.75 10m		1.77 5m		1.73 5m	
	Z(km)	V_p (kms ⁻¹)	Z(km)	V_p (kms ⁻¹)	Z(km)	V_p (kms ⁻¹)
	0.0	2.2	0.0	2.2	0.0	2.2
	0.4	2.6	0.4	2.6	0.0	2.55
	0.9	3.7	0.8	3.7	0.8	3.65
	1.4	5.1	1.5	5.0	1.5	5.1
	2.0	5.8	2.0	5.6	1.9	5.79
	10.0	6.8	10.0	6.7		

Table 3.1: Parameters for final locations giving a minimum RMS residual. Z is the depth to the top of the layer. Parameters (a) were used for the Flamboyanes and south Flamboyanes cluster (< 25–30 km radius of the crater centre), (b) for events at Dzitya and near site E12 (between 25 km and 45 km radius) and (c) for the airport events (> 45 km radius).

3.3.3 Station corrections

Station corrections can be made to correct for both surface topography and for any local velocity anomaly beneath the station. In this study no topographical corrections were necessary due to the flat nature of the area.

The average residuals after the initial location for each event cluster are shown in Figure 3.12. If a local velocity anomaly exists beneath a station then that station should have an abnormally large travel time residual for all events. If on the other hand a velocity anomaly occurs along a source–station path then the residual would only be atypical for the events from one particular source region.

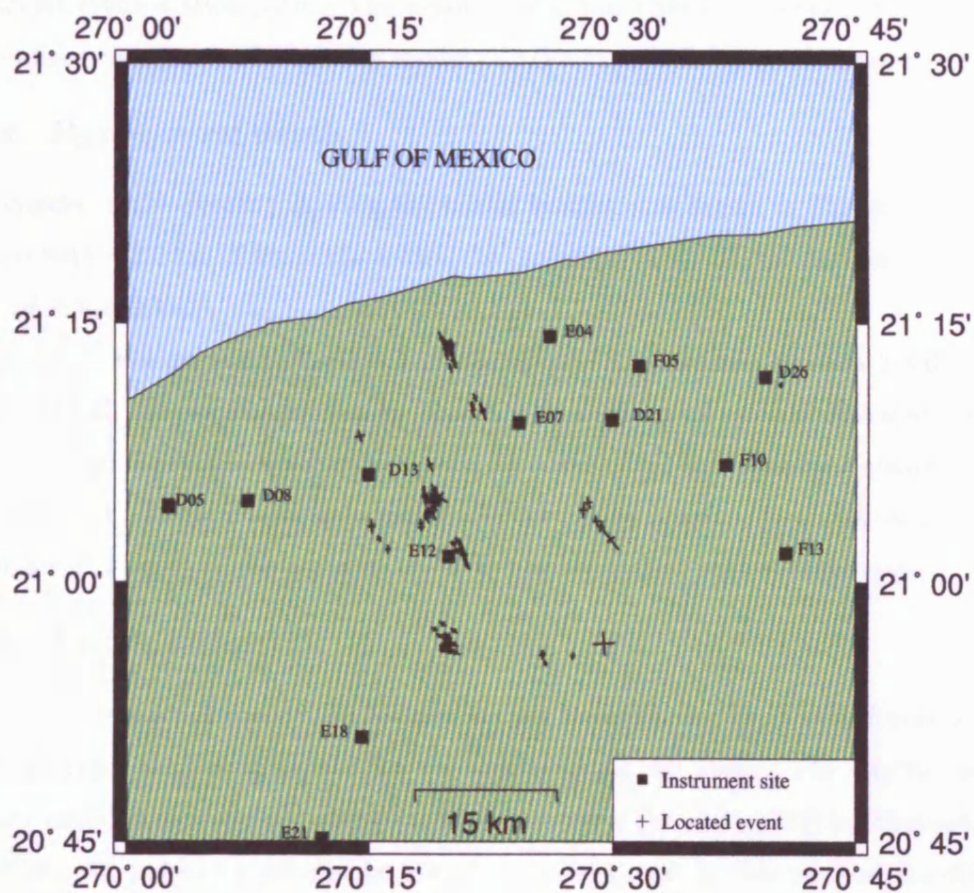


Figure 3.11: Final event locations.

It can be seen from Figure 3.12 that there appear to be no obviously different residual values with the possible exceptions of stations D33 and D38. Closer examination of the data for these sites revealed that the average was calculated over a small number of residuals, only one of which was very large. As the quality of the picks at these sites was very poor the residual is more probably a result of this than local geology. It was concluded that there was no evidence to suggest any local velocity anomalies near stations or along particular event-station paths. The negative bias was removed following relocation after some minor changes to the velocity model, V_p/V_s ratio and fixing of the event depths.

3.3.4 Hypocentral depth

The depths of the events following the initial location are shown in Figure 3.13. All are located within 2.5 km of the surface with the majority within 0.5 km and having a vertical error of ± 0.3 –2 km.

Based on the event distribution and the shape of waveforms (Section 3.3.6), it is believed that all the events are quarry blasts or some form of surface explosion. Prior to relocation the depth was fixed at 5 m or, in the case of the northernmost cluster at Flamboyanes, 10 m. These depths were based on information obtained from two of the quarries in the area. This produced a reduction in the residual RMS values and errors.

3.3.5 V_p/V_s ratio

In order to make full use of the S-wave arrival times in the hypocentral determination a V_p/V_s ratio must be provided for the area beneath the array. The V_p/V_s ratio was initially calculated using the traditional Wadati method (Wadati, 1933) for 40 events which had 6 or more pairs of good quality P and S arrival times. In this method the difference between the P and S-wave arrival times ($t_s - t_p$) is plotted against the P-wave arrival time (t_p). Assuming a constant Poisson's ratio along the travel path and that the P and S paths are identical then the graph will have a slope of $V_p/V_s - 1$ (Kisslinger and Engdahl, 1973). The ratio will be the average for the area covered by the stations used in the plot. Following the initial location Wadati plots were made for selected events and although linear (Figure 3.14) gave a large variation in slope. Slopes were calculated using a least squares fit and varied from 1.54–1.97.

This variation in V_p/V_s is to be expected as it is known to change over relatively small

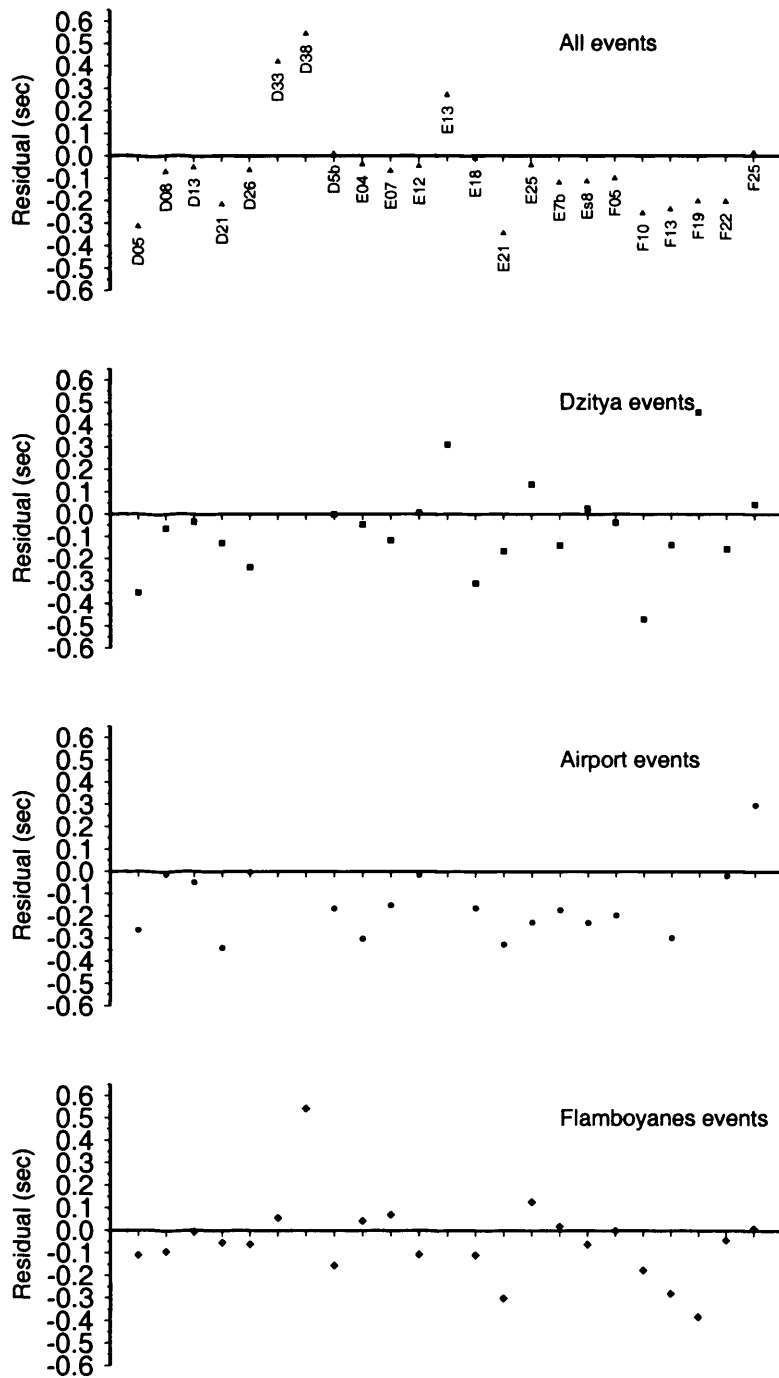


Figure 3.12: Average station travel time residuals for all events and event clusters.

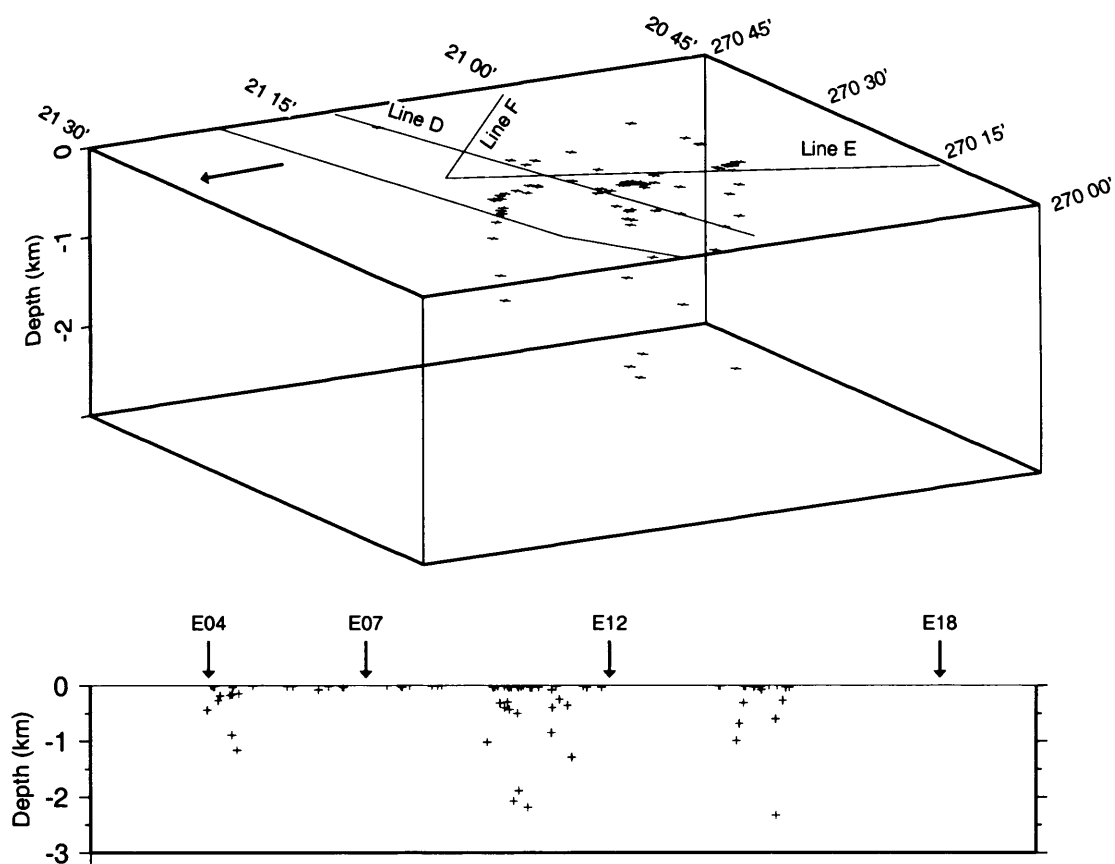
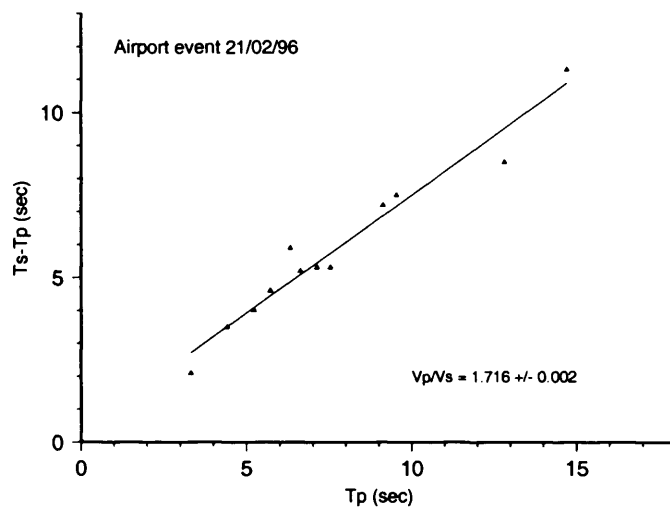
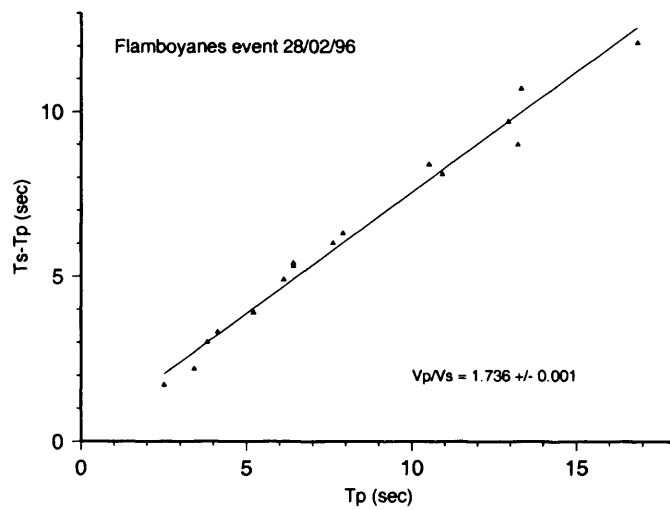


Figure 3.13: 3-D view of hypocentral depths for all events following initial location and the same depths collapsed onto Line E. For clarity the vertical errors have not been shown.



(a)



(b)

Figure 3.14: Example Wadati plots.

areas (Young, 1989). Local inhomogeneities, pore spaces and anisotropy have all been shown to affect the ratio (e.g., Winkler and Murphy, 1995). Åström (1998) also found large variations in V_p/V_s across the 121 Ma. Lake Mien impact crater in Sweden. This was believed to be a result of the thermal effects of the impact. The energy release from a thermal blanket was sufficient to sustain hydrothermal flow for a long period depositing quartz and thereby lowering the V_p/V_s ratio.

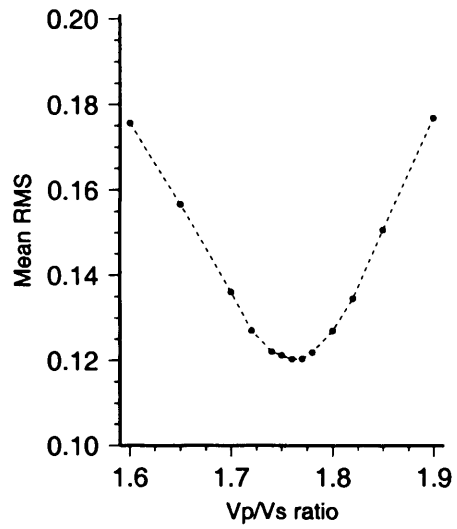
Laboratory measurements of quartz give a V_p/V_s ratio of 1.48 compared to the 1.7–2.0 of carbonates (Carmichael, 1982) and so varying levels of quartz deposition could explain the lower ratios. However, increasing dolomitization also results in a reduction of the V_p/V_s ratio with the reduction dependent upon the degree of dolomitization (Winkler and Murphy, 1995). Lack of geological control prevents any definitive reason for the variation to be given and the effectiveness of any further study into this is limited due to the small number of events and their distribution and so was not attempted.

Due to the large distribution of ratios obtained by this method it was decided that for the hypocentral analysis a best fitting V_p/V_s ratio would be obtained for each cluster by repeatedly relocating the subset of events and modifying the ratio each time to minimise the RMS residual (Marrow and Walker, 1988). The results of this for the event clusters at the quarries at Flamboyanes and near Merida airport are shown in Figure 3.15.

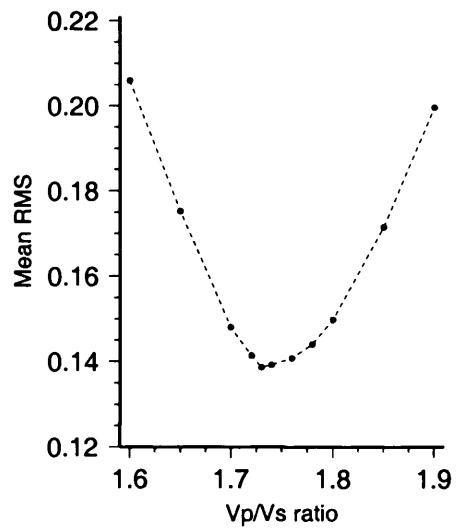
3.3.6 Distribution of events and identification of quarry blasts

The majority of the events fall into several distinct spatial clusters. Figure 3.16 shows the locations of suspected or known quarries within the Merida area based on site visits or local communication and it can be seen that most of these correlate with the located events. Two of these, at Flamboyanes and Dzitya, were visited and dates of blasts obtained (although unfortunately no times) and again these correlate with the recorded events in these regions.

The remaining events are also believed to be related to surface blasts. Their distribution around the outskirts of Merida most likely indicates either blasting associated with construction which was observed during the fieldwork or small local quarrying that we were informed did occur around the outskirts. The other option would be blasting associated with farming practices, possibly in order to sink wells, which again was observed during the fieldwork. The single event by station D26 may be an example of the latter as



(a)



(b)

Figure 3.15: Mean RMS against Vp/Vs ratio for (a) Flamboyanes cluster and (b) airport cluster.

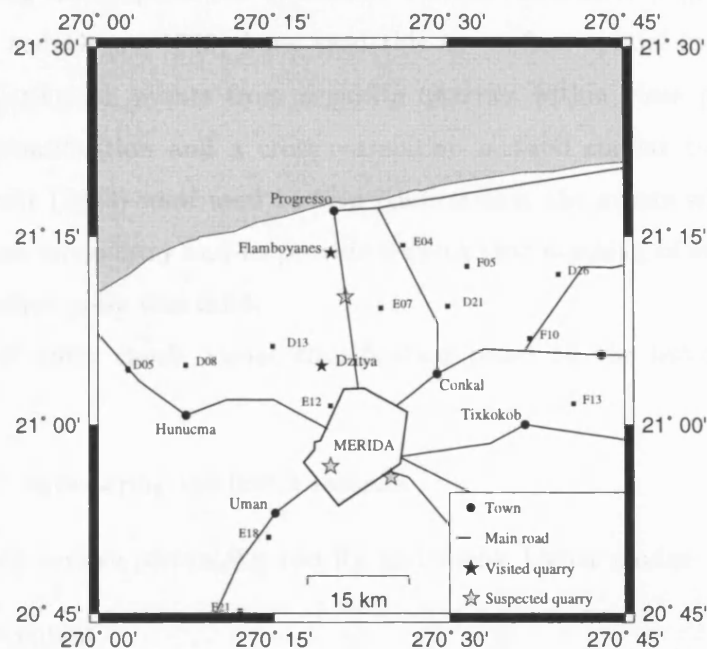


Figure 3.16: Location of known and suspected quarries and local towns in the Merida area. Suspected quarries are based on information provided by locals.

this is largely an agricultural area.

The temporal distribution of the events (Figure 3.17) agrees with the supposition of man-made as opposed to natural sources. No events occur on a Sunday and all the events fall between 14:00 and 00:30 GMT (07:00am - 17:30 local time). Each cluster never has more than one event per day and in general show a gap of three or four days before the next event.

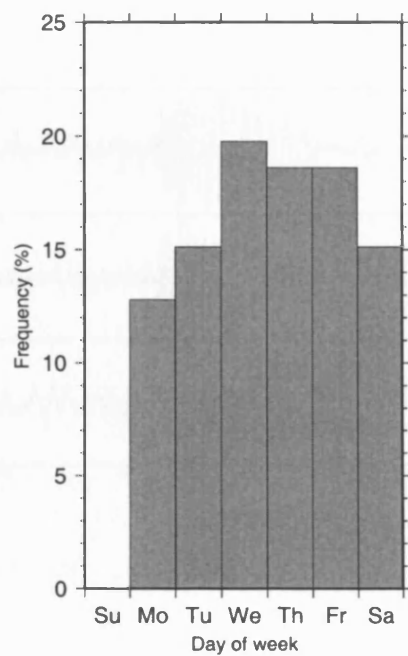
Burkhardt and Vees (1976) reported that quarry blasts can be regarded as approximately reproducible signal sources with path and secondary effects in the vicinity of the quarry dominating the shape of the waveform. Various researchers (e.g., Israelsson, 1990; Rivière-Barbier and Grant, 1993) have used this to confirm spatial locations of quarry blasts and to distinguish events from separate quarries within close proximity of each other. Visual identification and a cross-correlation method similar to that of Rivière-Barbier and Grant (1993) were used to help confirm that the events within each cluster did originate from one quarry and to provide a check that stacking of events during later processing to reduce noise was valid.

For an initial quick check, visual classification based on the following criteria was conducted:

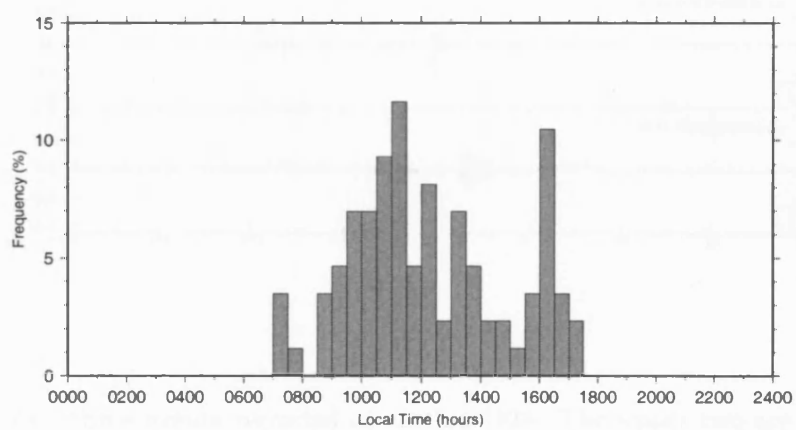
- shape of P wave during the first 3 seconds
- shape of the surface phases, Lg and Rg and visible higher modes
- frequency content.

Cross-correlation of the data then provided a further check and the time shifts necessary for stacking of the different events. Cross-correlation of two similar events should produce a spike with the peak offset by the time shift (Figure 3.18). Prior to the correlation the data was high-passed filtered above 0.1 Hz to remove low frequency noise. The correlation was then carried out on a 60 second envelope of the entire trace

Quarries generally employ several sub-explosions staggered in time in order to enhance rock fracture and reduce ground motion in the vicinity of the blasts (ripple blasting). Superposition of the sub-events can result in the modulation of the spectrum of the overall shot, suppressing some frequencies and reinforcing others to form time independent frequency bands visible through the seismic signal (Smith, 1989; Hedlin et al., 1989). Whilst

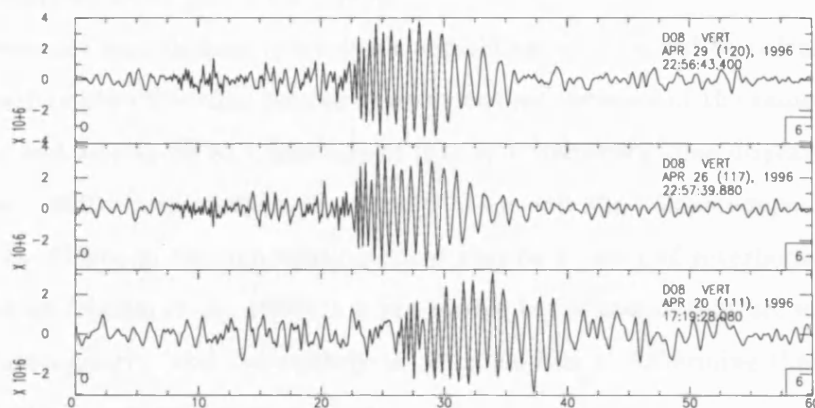


(a)

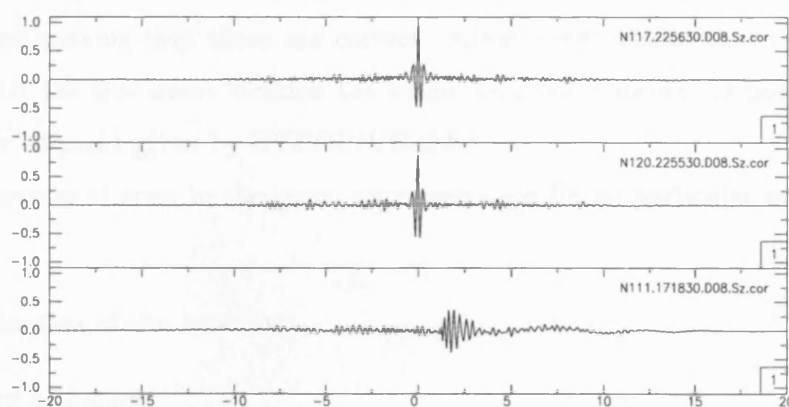


(b)

Figure 3.17: Temporal distribution of events (a) Daily distribution and (b) Hourly distribution.



(a)



(b)

Figure 3.18: (a) Three events recorded at station D08. The upper two are both believed to originate from Dzitya, the third from near station E12, 5 km to the south east. (b) Cross-correlation functions with the first event. The top trace is the auto correlation of the first event. The second trace shows a clear spike with a -0.04 second offset, confirming the source is the same as the first whilst the third shows no correlation.

in theory the spacing of these bands should allow calculation of the delay time employed, in reality the delay times can vary both between and along rows of the shot sometime by as much as 34% from the intended time (Hedlin et al., 1989) introducing a scatter that may disrupt the organization of the bands.

High frequency modulations in a seismic signal can be enhanced by calculating a spectrogram equal to the difference between two smoothed versions of the same spectrogram of the signal and displaying as a function of time in a frequency-time display or sonogram (Hedlin et al., 1989). Such analysis of several of the events show time independent banding (Figure 3.19). Although this modulation could also be a result of reverberations in a low velocity horizon (Hedlin et al., 1989) it is not visible in the events that are not believed to originate from a quarry (and are unlikely to be ripple blasts) confirming that the banding is a source rather than propagation effect.

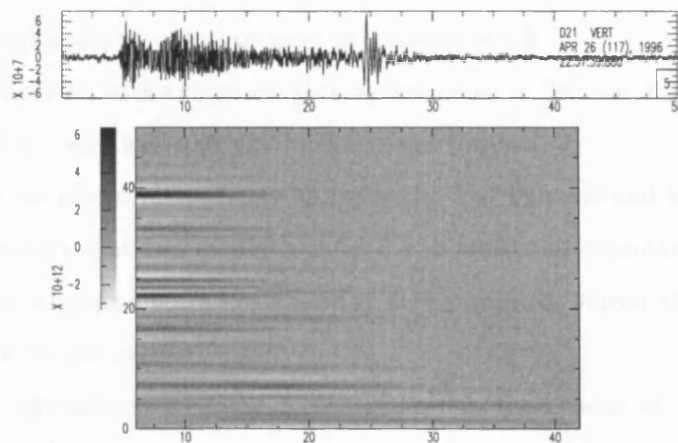
3.4 Determination of errors

The errors given by the location program do not account for errors within the input parameters and assume that these are correct. Klein (1990) states that there is a 95% probability that the true event location lies within an error ellipsoid 2.4 times that of the standard error ellipsoid given by HYPOINVERSE.

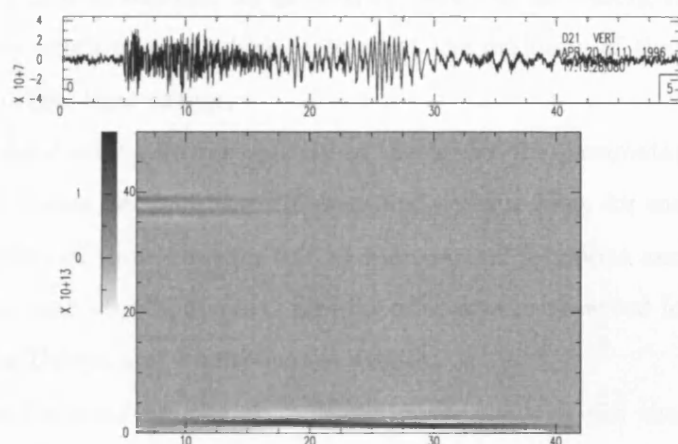
Possible sources of error in the input parameters are (in no particular order of preference):

- Determination of site location
- Accuracy of timing
- Accuracy of phase picking
- Number of stations and phases used
- Selection of V_p/V_s ratio
- Choice of velocity model.

Site location errors were mentioned briefly in Section 3.1 and compared to the other errors are considered negligible. A location error of 20 m for a wave with an average velocity



(a)



(b)

Figure 3.19: Sonogram analysis of (a) an event from Dzitya and (b) an event near site E12. The Dzitya event is known to be a ripple blast and displays clear banding throughout the signal which is not visible in the latter event. The event near E12 is believed to be related to construction work and is unlikely to be rippled. The proximity of the two paths suggests that the banding is a source rather than propagation effect.

of 5 kms^{-1} corresponds to a change in travel time of only 4 ms. Timing errors have also been ignored as the drift on the internal PDAS clocks was, with only two exceptions, less than 4 ms. The exceptions to this were where the GPS cable was damaged and in both cases this was noted and the data not used in location work.

The errors associated with the phase picking are given in Section 3.3.1. Any event that had phases picked at less than four stations was not located.

The main sources of errors are likely to be in the V_p/V_s ratio and the velocity model. This is due to the fact that the model is only a 1-dimensional representation of the true earth and these input parameters are assumed to be uniform across the area, which has been shown to not be the case.

To investigate the influence of the choice of V_p/V_s the cluster of 20 events near the airport was relocated with a range of ratios from 1.65–1.85. The effect of this on the hypocentral location is shown in Figure 3.20 and can be seen to be quite small with the maximum RMS variation in epicentral location of 0.83 km. The effect on the origin times was a maximum of ± 0.31 seconds. In general the effect of increasing the ratio is to move these events to the north or east which is towards the majority of the recording stations and to make the origin time earlier.

To gain an understanding on the validity of the model the parameters were changed by the maximum variations between the well logs and seismic lines for each layer. Table 3.2 summarizes the effect of these changes on the hypocentral locations and travel time residuals for the events near Merida airport. Similar effects were observed for variations in the parameters for the Dzitya and Flamboyanes events.

To investigate the need for the sixth layer in the models, the changes in individual station residuals with and without the layer were examined. Addition of the layer showed a reduction in travel time residuals for stations near the crater centre (e.g., E04, D21, F05 and D26) or for stations with station-event paths predominantly within the crater centre, but an increase for the outer stations (F22, F25, E21 and E25). An F-test (Davis, 1973) was conducted to confirm that the improvement in the RMS residuals was not simply a result of overmodelling and that the models were significantly different at a 5% significance level.

The observed improvement would be consistent with a high velocity zone beneath the

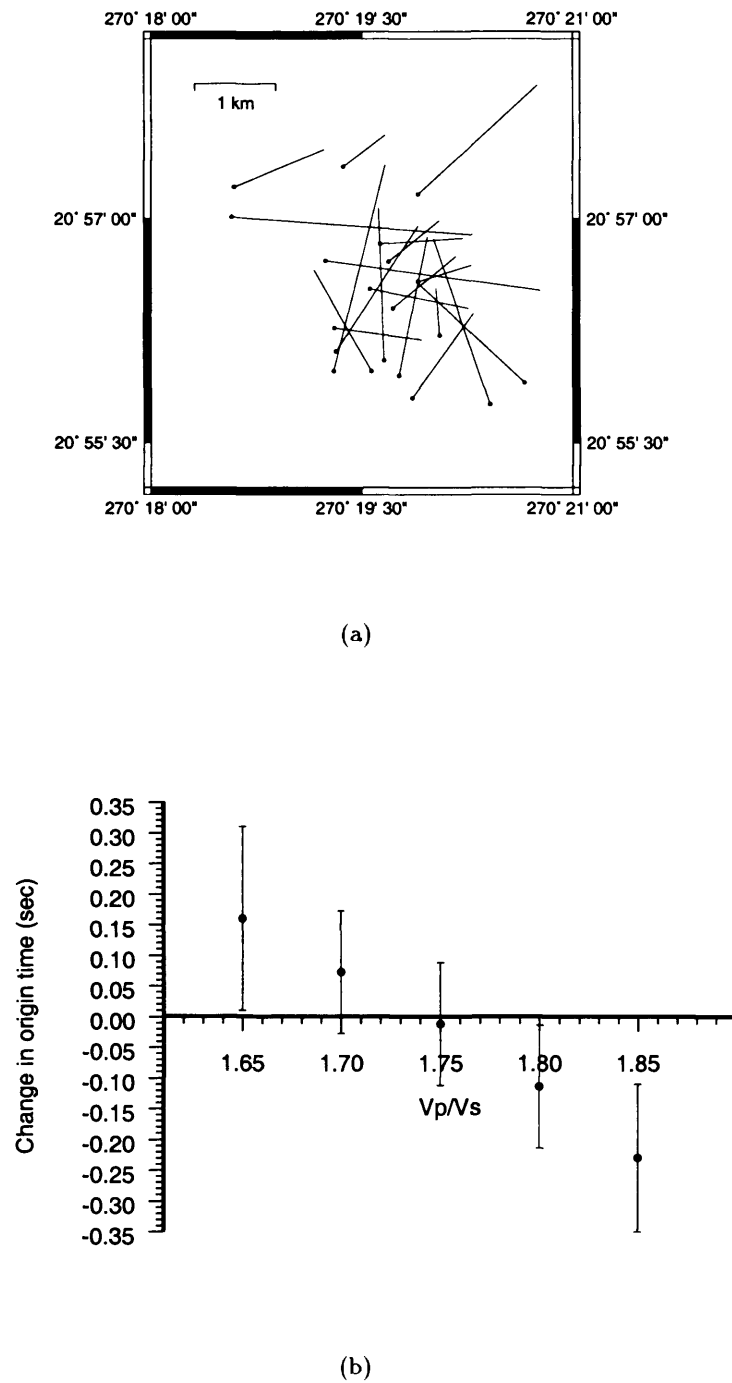


Figure 3.20: Effect of varying V_p/V_s on (a) the epicentral location of events near the airport and (b) the origin time of those events.

crater centre. The velocity model giving the minimum total RMS residual will be that which best represents the area sampled. In the case of events near Flamboyanes and Dzitya few of the picked phases used in the location are from the outer sites compared to the central area which is well sampled. The best model for use in the location of these events therefore requires the sixth layer. By contrast the events near the airport have a high proportion of phases picked at the outer sites and so the model must represent a 1-dimensional average of a larger area which, in this case, does not require the sixth layer.

Given these variations and that the locations of the events at Flamboyanes and Dzitya have an RMS variation of 1.1 km from the GPS readings taken at these quarries it is probable that the overall horizontal location error is of the order of ± 1.5 km with an origin time error of ± 0.2 seconds. Although considered, it was decided that fixing the hypocentre based on the GPS readings at these two quarries to improve the origin time solution could not be justified. Given the error in the GPS measurement (the GPS reading was made with a hand held GPS and did not use differential methods), the size of the quarries (c. 1 km) and that up to 8 months had elapsed between the blasts in question and the GPS measurement during which time blasting may have moved to the opposite region of the quarry raises doubt as to whether this would produce a reliable improvement.

3.5 Conclusions

The distribution of events is dominated by five clusters which correspond to the locations of known or suspected quarries in the region. Events at two of these locations agree with dates of blasts provided by the quarries. The remaining events are believed to be the result of blasting for agricultural or construction work.

The properties of the seismic signals recorded are consistent with the conclusion that the northwestern Yucatan peninsula is seismically quiet and local seismicity is a result of man-made explosive sources rather than natural ones. The strong surface wave phases are consistent with a shallow or surface source and waveform analysis suggest events from within each cluster are a result of a reproducible source function. Sonogram analysis shows clearly defined time independent frequency bands consistent with ripple fired quarry blasts.

Initial analysis of the signal waveforms and phase arrival times suggests significant

Velocity variation of Layer 1 by $\pm 0.04 \text{ kms}^{-1}$ to 2.16 kms^{-1} and 2.24 kms^{-1}	
RMS variation in epicentral location	$= 0.22 \text{ km}$
RMS variation in origin time	$= 0.03\text{s}$
Variation in residual RMS	$= 0$
Velocity variation of Layer 2 by $\pm 0.1 \text{ kms}^{-1}$ to 2.45 kms^{-1} and 2.65 kms^{-1}	
RMS variation in epicentral location	$= 0.21 \text{ km}$
RMS variation in origin time	$= 0.03\text{s}$
Variation in residual RMS	$= + 3.25 \times 10^{-3}$
Velocity variation of Layer 3 by $\pm 0.18 \text{ kms}^{-1}$ to 3.47 kms^{-1} and 3.83 kms^{-1}	
RMS variation in epicentral location	$= 0.11 \text{ km}$
RMS variation in origin time	$= 0.04\text{s}$
Variation in residual RMS	$= + 3.75 \times 10^{-3}$
Velocity variation of Layer 4 by $\pm 0.2 \text{ kms}^{-1}$ to 4.9 kms^{-1} and 5.3 kms^{-1}	
RMS variation in epicentral location	$= 0.14 \text{ km}$
RMS variation in origin time	$= 0.04\text{s}$
Variation in residual RMS	$= + 2.5 \times 10^{-3}$
Velocity variation of Layer 5 by $\pm 0.2 \text{ kms}^{-1}$ to 5.59 kms^{-1} and 5.99 kms^{-1}	
RMS variation in epicentral location	$= 0.62 \text{ km}$
RMS variation in origin time	$= 0.03\text{s}$
Variation in residual RMS	$= + 2.175 \times 10^{-2}$
Depth variation to top of Layer 2 by $\pm 0.1 \text{ km}$ to 0.3 km and 0.5 km	
RMS variation in epicentral location	$= 0.15 \text{ km}$
RMS variation in origin time	$= 0.19\text{s}$
Variation in residual RMS	$= + 3.5 \times 10^{-3}$
Depth variation to top of Layer 3 by $\pm 0.15 \text{ km}$ to 0.65 km and 0.95 km	
RMS variation in epicentral location	$= 0.21 \text{ km}$
RMS variation in origin time	$= 0.03\text{s}$
Variation in residual RMS	$= + 4 \times 10^{-3}$
Depth variation to top of Layer 4 by $\pm 0.2 \text{ km}$ to 1.3 km and 1.7 km	
RMS variation in epicentral location	$= 0.24 \text{ km}$
RMS variation in origin time	$= 0.06\text{s}$
Variation in residual RMS	$= + 3.25 \times 10^{-3}$
Depth variation to top of Layer 5 by $\pm 0.25 \text{ km}$ to 1.65 km and 2.15 km	
RMS variation in epicentral location	$= 0.22 \text{ km}$
RMS variation in origin time	$= 0.06\text{s}$
Variation in residual RMS	$= + 3.75 \times 10^{-3}$
Adding Layer 6, $v = 6.8 \text{ kms}^{-1}$, $Z = 10 \text{ km}$	
RMS variation in epicentral location	$= 0.29 \text{ km}$
RMS variation in origin time	$= 0.09\text{s}$
Variation in residual RMS	$= + 9.5 \times 10^{-3}$
Depth freed (trial depth = 5 km)	
RMS variation in epicentral location	$= 1.12 \text{ km}$
RMS variation in origin time	$= 0.37\text{s}$
Variation in residual RMS	$= + 3.6 \times 10^{-2}$

Table 3.2: Effect of varying model parameters on hypocentral locations of events near Merida airport.

3-dimensionality of the seismic structure of the area.

Wadati plots show that the V_p/V_s ratio varies across the area from 1.54–1.97 (corresponding to a change in Poisson ration of 0.14–0.325). This may be due to the thermal effects of the impact, varying degrees of dolomitization in the carbonates or simply the complex geology of the structure but lack of suitable data prevents any further analysis of this change.

Examination of schematic models of the crater (Pilkington et al., 1994; Sharpton, 1997) can give an indication of the likely stratigraphy represented by the velocity models used in the location of the local events. These suggest a relatively homogeneous layer of approximately 1 km thick Tertiary sediments with a velocity of 2.2–2.6 kms^{-1} . These values are consistent with sonic data obtained from well logs (Urrutia-Fucugauchi et al., 1997) and previous seismic work in the region (Cué, 1953). Beneath this a 500–700 m layer with a 3.7 kms^{-1} velocity which is likely to represent a combination of melts and upper breccias. The 5.1 kms^{-1} underlying layer is probably a result of ejecta and mega breccias with the pre-existing Cretaceous stratigraphy producing a velocity of 5.8 kms^{-1} below 2 km depth. An increase in apparent P-wave velocity can be seen towards the centre of the structure and a layer of 6.8 kms^{-1} is required at depth for paths mainly within the crater centre. This high velocity material may be uplifted basement which is consistent with the interpretation of the gravity and magnetic anomalies observed within a 20–25 km radius of the crater centre (Pilkington et al., 1994).

Chapter 4

Surface Wave Analysis

4.1 Introduction

For seismicity excited by shallow earthquakes and explosions, surface waves are the longest and strongest portion of the record. Over their path they absorb information on the elastic and anelastic properties of the Earth dependent on their frequency content, which is reflected in their dispersion and attenuation characteristics. As a result they have become important in the modelling of crustal structure.

Following the theoretical work of Rayleigh (1885), Lamb (1903) and Love (1911) surface waves were observed and used for studies of the Earth's structure throughout the first half of the 20th century (e.g., Jeffreys, 1925; Stoneley, 1931; Bullen, 1939). Early research focused on the determination of crustal thickness and the modelling of two or three layered crustal structure. Differences in oceanic and continental crust were inferred through the variation of dispersion curves.

From 1950 onwards, rapid progression was made as improvements were made in seismological instrumentation and analysis methods were developed. The measurement of longer periods (20–500 s) became possible allowing determination of 1-D mantle structure (e.g., Ewing and Press, 1954). Dispersion studies displayed the lateral heterogeneity of the upper mantle and allowed the delineation of major tectonic regions within the crust (e.g., Brune and Dorman, 1963; Brune, 1969). Higher modes were identified (Oliver and Ewing, 1957) which sample different depth extents than the fundamental mode (Figure 4.1). The velocity structure influences different portions of each mode independently thus providing additional information which could be used to gain more reliable and accurate models. Better definition of crustal structure was also obtained through the measurement of dis-

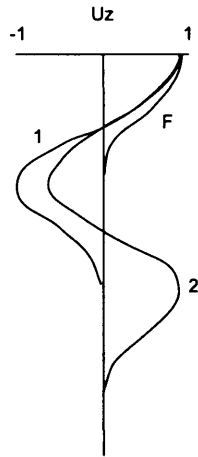


Figure 4.1: Schematic illustration of the depth dependence of the vertical displacement eigenfunction of the fundamental, first and second higher modes at a fixed frequency. The number of zero crossings determines the mode number with the relative excitation of each mode dependent on wavelength, source depth and structure (after Ewing et al. (1957).

persion at higher frequencies (e.g., Bache et al., 1978).

As the observation of surface waves increased so to did the analysis and processing methods. Dziewonski et al. (1969) developed the multiple filter technique of calculating group velocities; the seismogram being filtered and windowed in the frequency domain then transformed back to the time domain to determine the velocity from the maximum energy content. Herrmann (1973) and Denny and Chin (1976) developed the method further and investigated the effects of using different filters determining that a Gaussian filter has the smallest, if any, side lobes that could be misidentified as higher modes and was therefore preferred for the technique. Herrin and Goforth (1977) introduced a method of isolating modes from higher modes and multi-path effects to improve group velocity measurements.

The importance of the 0.5–5 Hz frequency range in upper crustal studies was recognized by McEvelly and Stauder (1965). Their analysis of stripmine blasts highlighted the sensitivity of this frequency of Rayleigh wave to sedimentary structure. Marked differences in group velocities for several propagation paths across the Illinois basin were modelled in terms of sedimentary sequences within the basin. The combination of stripmines and single stations produced an inexpensive and simple technique, a fact highlighted again by Herrmann (1969). Utilizing sources from stripmines, quarries and highway construction sites, the sediment cover of the Cincinnati Arch was modelled to a depth of 2 km, includ-

ing identification of a low velocity zone that would be difficult to resolve in a refraction study. In large scale refraction studies, surface wave dispersion has been used to model the shallow crustal structure and identify low velocity zones that the body wave data provides little information on (e.g., Berry and Fuchs, 1973). Quarry blasts are now widely recognized as providing an excellent data base for high frequency Rg studies which have been used to model crustal structure to maximum depths of 10 km (e.g., Kafka and Dollin, 1985; Sakia et al., 1990; Hutchenson, 1994).

Whilst velocity dispersion provides information on the elastic properties of the Earth, anelastic structure can be obtained by investigation of the amplitude attenuation of the surface wave. Surface wave measurements are more reliable than body wave measurements (Knopoff, 1964) and the analysis of the surface wave attenuation factor, Q_β , has developed in step with that of velocity dispersion. Firstly long period measurements were made from single stations as the wave propagated several times around the Earth (e.g., Toksöz and Ben-Menahem, 1963) and then shorter periods using several stations (e.g., Burton, 1974). Expressions relating surface measurements to the anelastic parameters of the Earth were developed by Anderson et al. (1965) and refined by Mitchell (1975). Single station methods for short paths were developed and used to determine crustal Q_β across Scotland by Macbeth (1983). Detailed knowledge of near surface attenuation values was recognized as being important for ground motion studies and in particular seismic risk assessment (Jongmans and Demanet, 1993). As with velocity studies, quarry blasts have often been used as a high frequency source to obtain measurements of shallow crustal attenuation often via waveform modelling techniques (e.g., Sakia et al., 1990).

4.1.1 Surface wave observations in Mexico

Surface wave studies in Mexico have concentrated primarily on surface waves excited by earthquakes along the subduction zones of the Central American Trench. Fix (1975) inverted group velocity dispersion curves for an average crustal and upper mantle structure of north and south Mexico. Gomberg et al. (1988) inverted fundamental mode long period Rayleigh and Love phase velocities to model the crust and mantle of North Mexico. Using synthetic waveform modelling Gomberg and Masters (1988) found significant differences in lithospheric structure between northern and southern Mexico. A very low shear wave velocity zone was imaged at the base of the lithosphere in the region of the trans-Mexico

volcanic belt (TMVB) and no evidence of a 400 km mantle discontinuity was found, interpreted as a result of high heat flow and partial melting, consistent with active volcanism. This low velocity zone was also seen by Alsina et al. (1996) using phase velocity tomography of long period Rayleigh waves. They also imaged a high velocity mantle anomaly to a depth of ≥ 300 km under the Yucatan and northward through the Gulf of Mexico into Florida believed to be a result of subduction.

Upper crustal studies have focused on the region of the Mexico Valley (e.g., Sanchez-Sesma et al., 1993; Singh et al., 1995) to understand the large amplification of seismic waves that occurs there. This was attributed to the resonance of trapped waves in soft clays and a complex low velocity structure in the upper layers of the volcanic rocks. To aid in the seismic risk evaluation for Mexico City, shallow crustal velocity and Q_β estimates from high frequency Rayleigh waves excited during shallow refraction experiments over the lake bed zone NE of Mexico City (Ramos-Martinez et al., 1997) have been combined with deeper structure from longer period earthquake data (e.g., Chavez-Garcia et al., 1995; Shapiro et al., 1997).

4.2 Processing

All data used in this surface wave study underwent several stages of processing. Firstly the locations of local events were determined (Chapter 3) and several quarries identified. Individual waveforms were selected for the surface wave analysis and processed using the Seismic Analysis Code (SAC) developed at Lawrence Livermore National Laboratory and Computer Programs in Seismology (Herrmann, 1987) developed by St. Louis University. These processing steps included: removal of dc-offsets, removal of instrument effects (Appendix D), stacking of events from the same source, cutting to 80 second length, decimation to 2048 points (bringing the sample rate to 25 Hz) and conversion to the EXSPEC format (Herrmann, 1987). All but the last of these initial processing steps were completed using SAC.

The stacking of signals was based on the analysis conducted during quarry identification (Chapter 3). Time shifts for each stack were determined by cross-correlation with a master signal. The choice of the master signal was arbitrary as no one signal had a significantly better location than the others. The waveforms were then shifted with respect to the mean

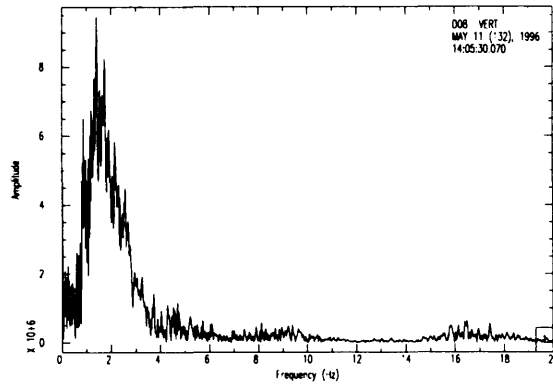


Figure 4.2: Frequency spectra of a typical quarry blast. The fundamental Rg phase has a maximum amplitude occurring around 2 Hz.

time shift obtained to produce a signal with an averaged travel time and distance.

The decimation to 2048 points was completed using an FIR anti-alias filter and was felt to have no adverse effects for the purpose of this study. Although the body wave spectra includes energy of > 10 Hz the spectra of the Rg phase lies predominantly between 1–3 Hz (Figure 4.2).

Following the conversion to the EXSPEC format, the processing sequence was as listed below. These steps were implemented using the computer code developed at St. Louis University occasionally with some slight modifications.

- Obtain group velocity values using the multiple filter technique (MFT).
- Interstation calculation of fundamental phase dispersion curves.
- Isolation of fundamental mode dispersion curves using phase-matched filtering (PMF)
- Multiple station calculation of the attenuation coefficient, γ .

The basic theory of these techniques and the methods used are summarised in the following sections.

4.3 Multiple filter technique

Initial estimates of group velocity were obtained using a multiple filter technique (MFT) originally developed by Dziewonski et al. (1969) and later refined by others (e.g., Her-

rmann, 1973; Denny and Chin, 1976).

Assuming a laterally homogeneous media, Aki and Richards (1980) give the complete normal mode solution in the time domain for a propagating dispersed surface wave with M modes at time t and distance r as

$$f(t, r) = \frac{1}{2\pi} \int_{-\infty}^{\infty} \sum_{j=0}^M A_j(\omega, r) e^{i(\omega t - k_j(\omega)r)} d\omega \quad (4.1)$$

where ω is the angular frequency, k_j is the wavenumber of the j^{th} mode and A_j is the complex amplitude of the j^{th} mode which is dependent upon the instrument response, source spectrum, path response, attenuation and geometric spreading.

Filtering the signal with a symmetric Gaussian band-pass filter, $H(\omega)$, centered at $\omega = \omega_o$ and cutoffs at $\omega = \omega_o \pm \omega_c$ where $H(\omega)$ is defined by

$$H(\omega) = \begin{cases} 0 & |\omega| > \omega_c \\ \exp\left(\frac{-\alpha\omega^2}{\omega_o^2}\right) & |\omega| \leq \omega_c \end{cases} \quad (4.2)$$

gives the resultant filtered signal

$$g(t, r) = \frac{\omega_o}{2\pi} \sqrt{\frac{\pi}{\alpha}} \sum_{j=0}^M A_j(\omega_o, r) e^{i(\omega_o t - k_{oj}r)} \exp\left[-\frac{\omega_o^2}{4\alpha} \left(t - \frac{r}{U_{oj}}\right)^2\right] \quad (4.3)$$

where U_{oj} is the group velocity of the j^{th} mode at $\omega = \omega_o$. The modulus of equation 4.3 gives the envelope of the signal and individual maxima of the envelope correspond to the arrival of the group velocities of each mode.

The duration of the Gaussian envelope is defined in terms of the filter parameter α and filter centre frequency T_0 as (Herrmann, 1973),

$$t_d = T_0 \sqrt{\frac{\alpha}{\pi}} \quad (4.4)$$

For accurate determination of group velocities of each mode the maxima of the envelope must be well separated or interference between the modes will occur.

When the modal maxima are separated by less than $2t_d$, modal interference will occur, and the maxima of the envelope will be a result of the summation of two or more overlapping envelopes and not represent the actual maxima of the individual modes. For maxima separated by more than $2t_d$, then the two modes will not interfere. For this study $\alpha = 16\pi$ was chosen, giving $2t_d = 4$ sec for a filter centre frequency of 2 Hz. Thus for

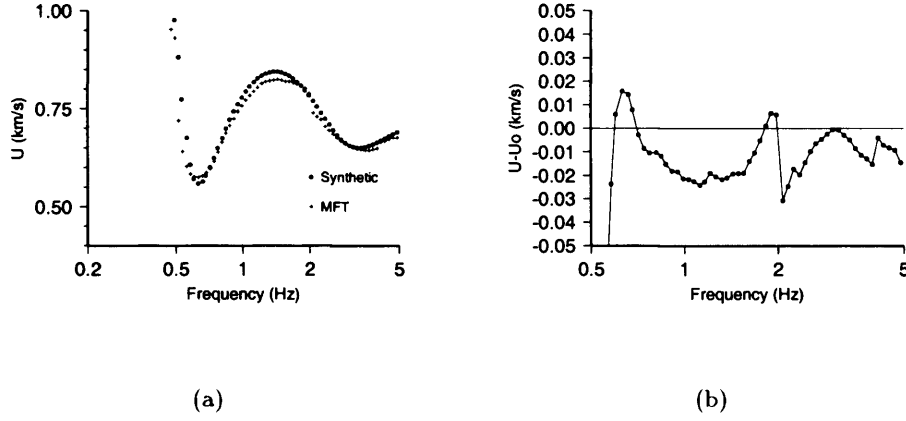


Figure 4.3: (a) FTAN plot of fundamental group velocity from MFT analysis of synthetic seismogram and the theoretical group velocities. (b) Error between the MFT analysis and theoretical group velocities.

typical velocities in this study of 0.7 km s^{-1} and 0.85 km s^{-1} for the fundamental and first higher mode a minimum station distance of 16 km is required. Whilst narrowing the filter width would reduce contamination from higher mode energy this results in an increase in inaccuracies in group arrival times (Bache et al., 1978) and 16π has been used with success by previous researchers for similar distances and velocities to those in this study (e.g., Hutchenson, 1994).

Other inaccuracies arise from the hypocentral location and intrinsically within the MFT process. Hypocentral location errors are discussed in Chapter 3. To constrain the intrinsic errors within the MFT process a synthetic seismogram was calculated and analyzed. Figure 4.3 shows the difference between the theoretical and calculated group velocities. For the 0.5–5 Hz frequency range the MFT in general underestimates the group velocity with the an average error of -0.015 seconds. The largest errors are predominantly around the maxima in the dispersion curve and arise from the first order expansion of $k(\omega)$ to obtain equation 4.3 with the assumption that higher order terms can be neglected (Herrmann, 1973). Below 0.5 Hz the errors increase. However the majority of observations are within the 0.5–5 Hz range, and are not seriously contaminated by this property of the technique.

A logarithmic range of filter central frequencies was chosen between 0.2–5 Hz. Due to

the frequency range of interest, central frequencies chosen with a constant Δf or ΔT (in the time domain) are either biased towards the high frequency range or the low frequency range respectively (Figure 4.4). For frequencies below 0.2 Hz, noise makes any dispersion indistinguishable and above 5 Hz the signal is principally body wave energy.

The amplitude maxima for each given frequency are recorded and contoured on an FTAN (Frequency-time analysis) map (Figure 4.5) with the four largest spectral peaks shown. The original waveform is shown at the far right of the plot with a constant sampling interval and to the left of that the waveform is scaled to the group velocities of the contour plot. This enables an easier correlation between group velocity maxima and time series peaks. The fundamental Rg mode is the most dominant contour showing an increase in group velocity with frequency between 0.5 Hz and 1.8 Hz before slightly decreasing. The dominance of this mode makes identification of higher modes difficult.

Figure 4.6 shows the FTAN plot for the stacked record for the same source station path as Figure 4.5. It can be seen that the stacking has reduced some of the low frequency noise content of the signal and improved the identification of possible higher modes.

By using a phase-matched filter (Section 4.5) it is possible to isolate and remove the fundamental mode before performing the MFT on the residual waveform. This allows better definition of the higher modes as they are no longer hidden by the high amplitude contours of the fundamental mode. This is shown in Figure 4.7, where now two higher modes can be seen between 0.4–4 Hz and 0.6–2.5 Hz with group velocities decreasing from 1.1–0.8 kms^{-1} and 1.5–1.1 kms^{-1} .

Three main source regions were used during the MFT analysis: the quarries at Flamboyanes, Dzitya and near Merida airport. In addition a single event near station D26 was used to help constrain the eastern region (Figure 4.8). The FTAN plots for all the selected paths are shown in Appendix E.

4.4 Interstation calculation of phase velocity

Interstation phase velocity are calculated via the correlation of Rayleigh wave crests between stations (Bloch and Hales, 1968). In order for this to be achieved without errors arising from azimuthal variations in initial phase (Knopoff and Schwab, 1968) and lateral refraction (Evernden, 1953, 1954) it is necessary that the source lies within a small az-

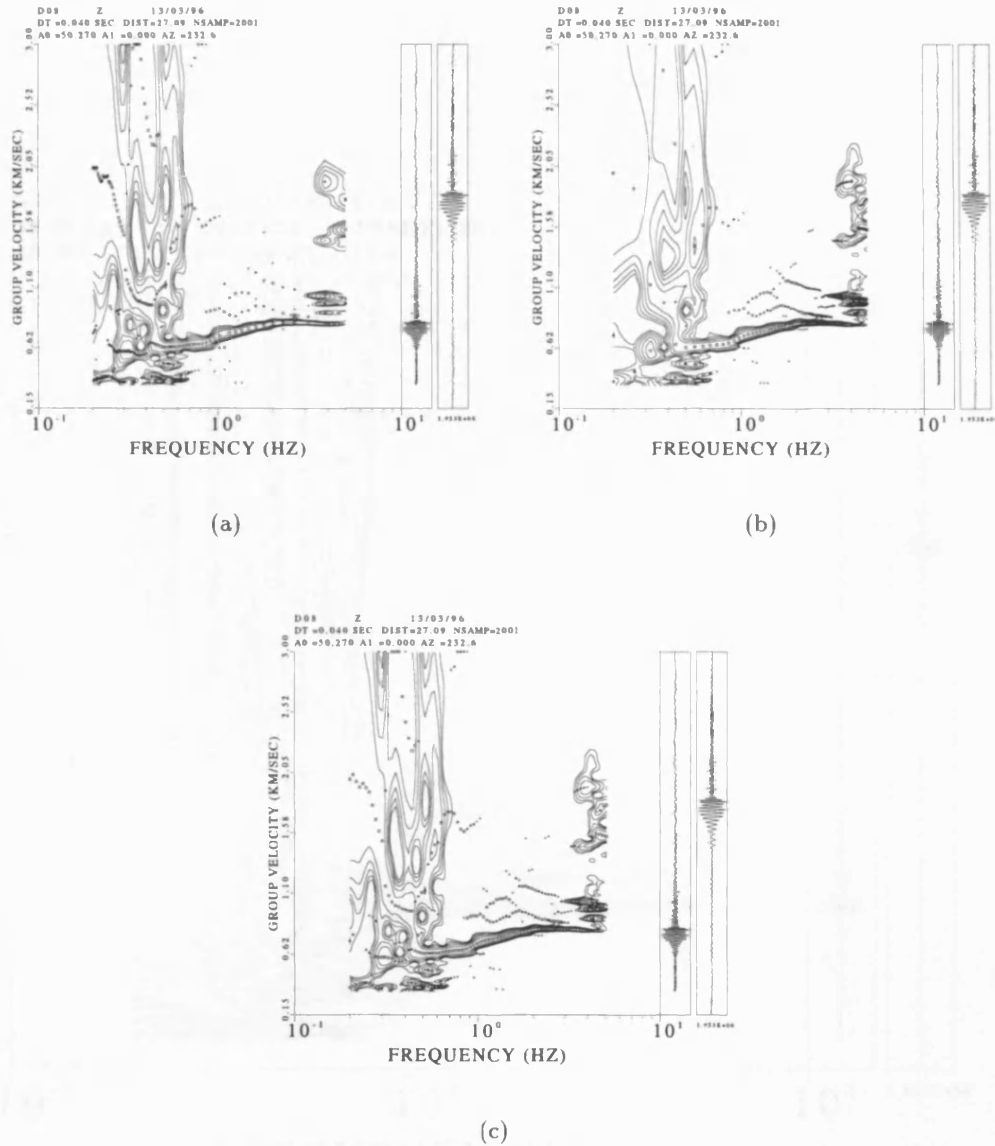


Figure 4.4: FTAN plots for the same event but with different choices of filter central frequencies. (a) Filtering with a constant ΔT provides clearly seen low frequency data including higher mode information. (b) Filtering at a constant Δf , improves resolution of high frequency information but with decreased resolution at low frequencies. (c) Logarithmic sampling of central frequencies allows both high and low frequency information to be seen.

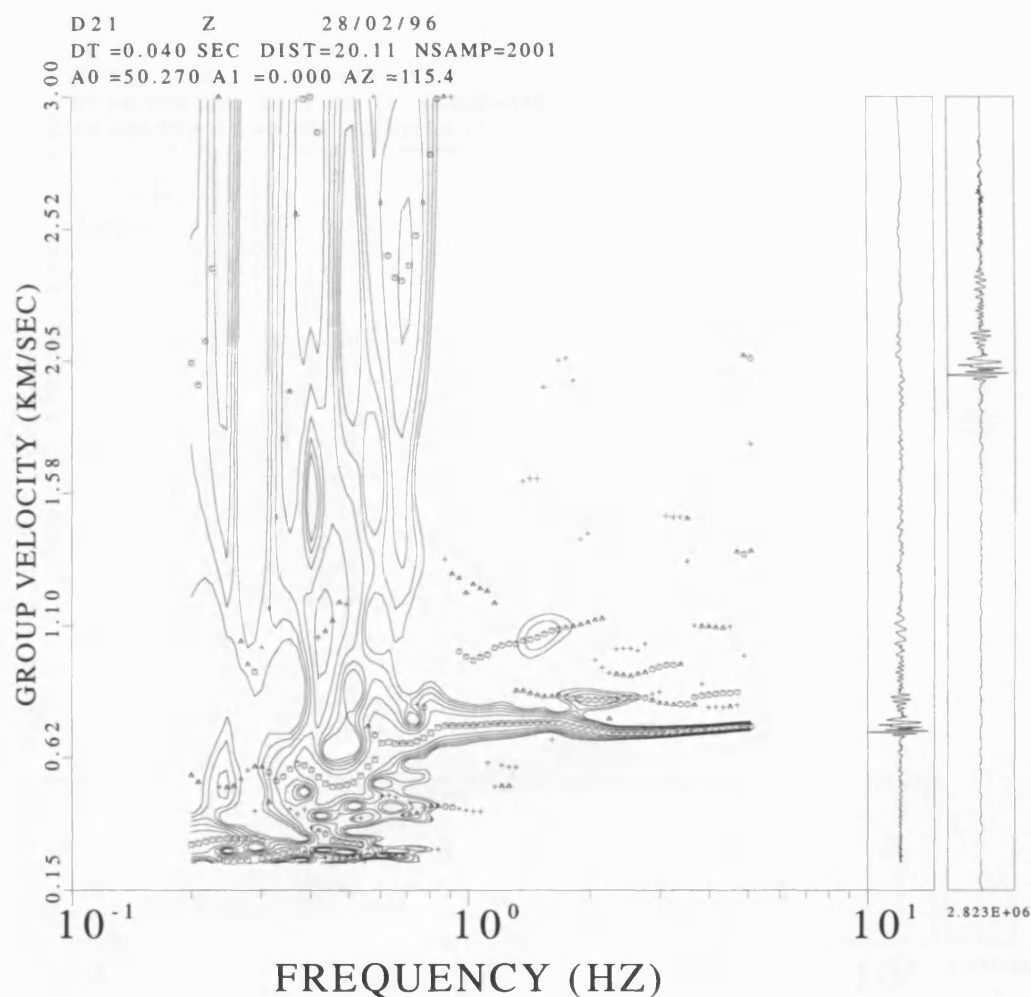


Figure 4.5: Typical FTAN map from an unstacked record of a quarry blast at Flamboyanes quarry, 28/02/96 recorded at Station D21 (path length is 21 km). The fundamental R_g mode can be seen between 0.5 and 0.8 kms^{-1} with a higher mode responsible for the modal interference seen around 2 Hz. Symbols indicate size of the spectral peaks (\square - largest, \circ - second largest, \triangle - third and $+$ - fourth largest). The original waveform is shown at the far right of the plot with a constant sampling interval and to the left of that the waveform is scaled to the group velocities of the contour plot.

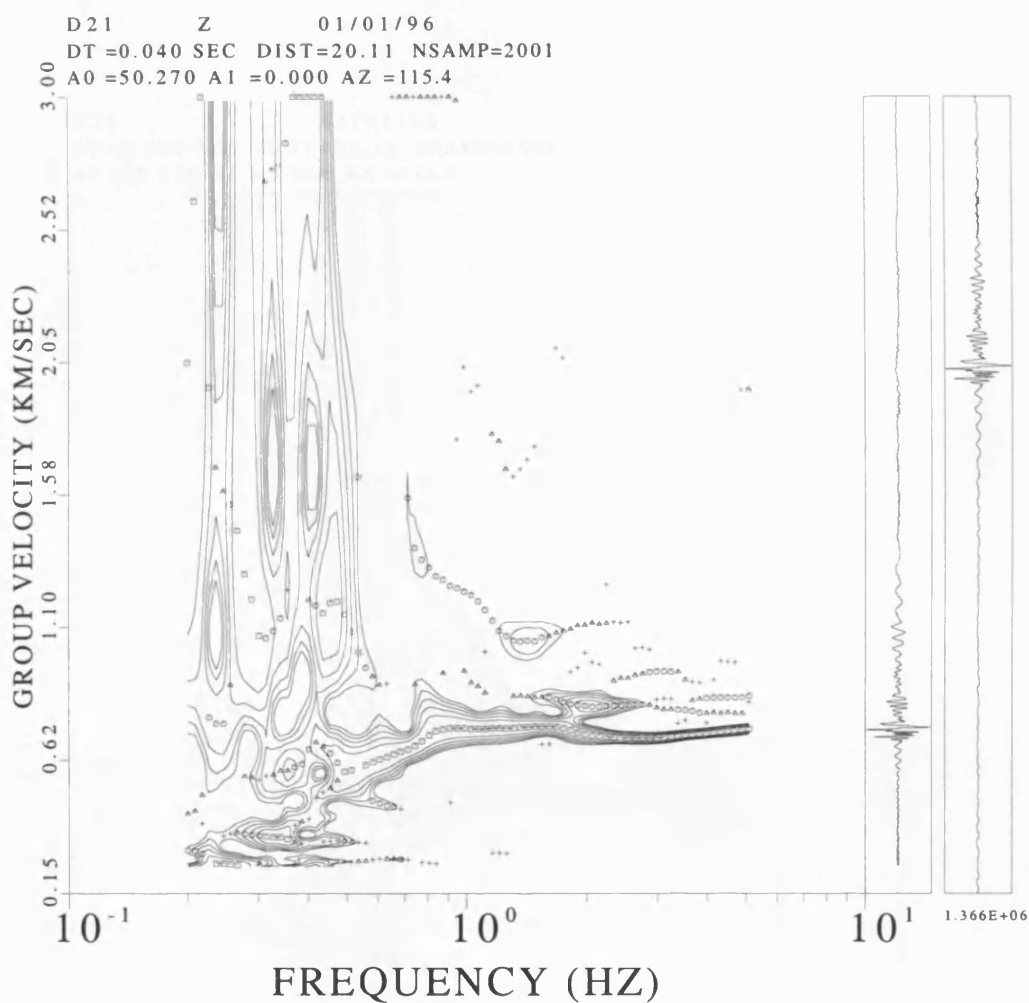


Figure 4.6: FTAN map for a stacked record of blasts from Flamboyanes quarry recorded at Station D21. Lower frequencies show decreased noise and higher modes are now more distinct than in the unstacked plot. The second higher mode is the decreasing velocity trail in the centre of the plot with the first higher mode responsible for the modal interference.

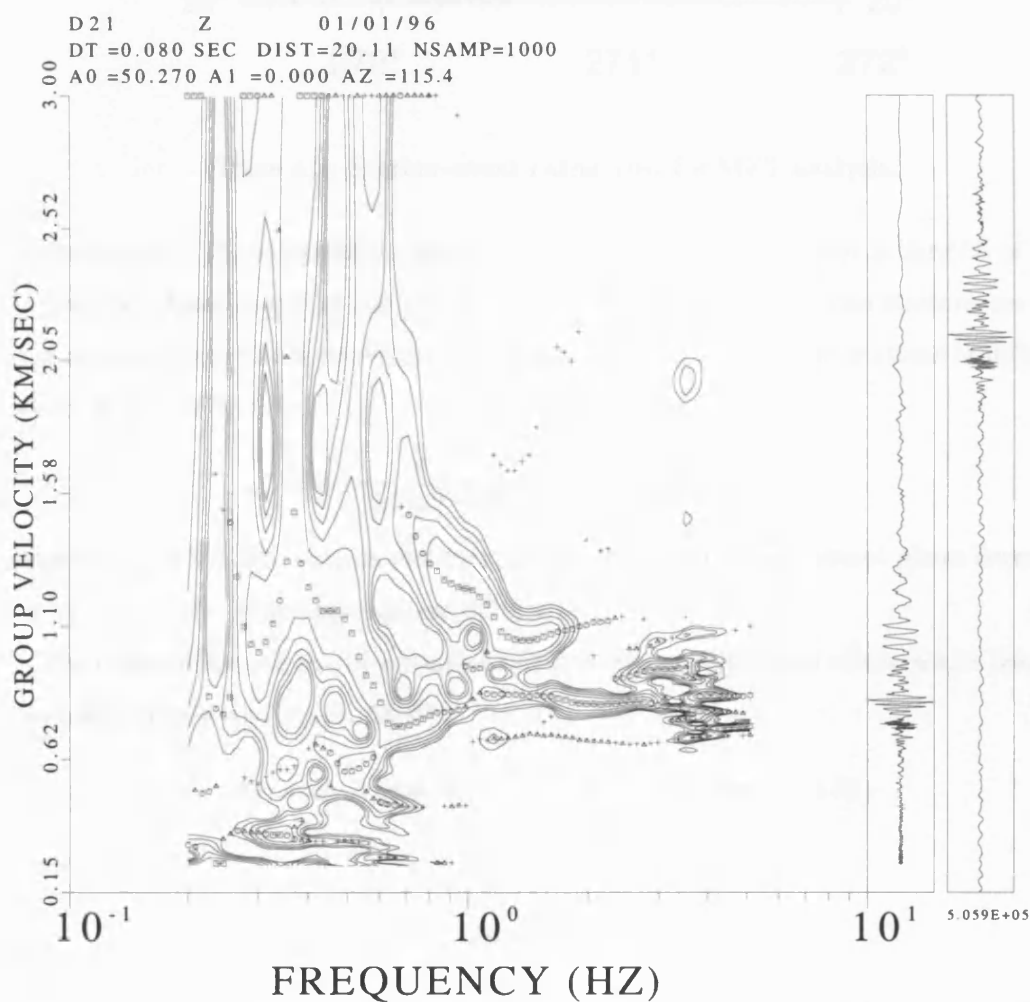


Figure 4.7: FTAN map of residual waveform from Figure 4.6 after application of a phase-matched filter. First and second higher modes can now be clearly identified between 0.4–4 Hz and 0.6–2.5 Hz with group velocities decreasing from 1.1–0.8 kms^{-1} and 1.5–1.1 kms^{-1} . Note a remnant of the fundamental mode energy is still visible between 1–3 Hz.

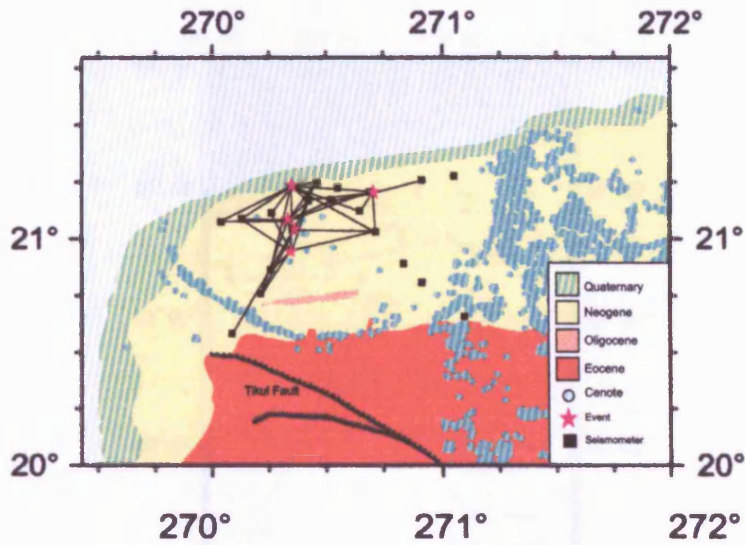


Figure 4.8: Station–event paths used for MFT analysis.

imuthal range of the interstation path. This restricts the data to only a handful of events (Figure 4.9). Assuming that the source phase shift is constant and two stations are at the same azimuth from the source then the phase velocity between the stations is defined as (Stuart et al., 1976)

$$C(\omega) = \frac{\omega}{k(\omega)} = \frac{\omega(r_2 - r_1)}{\phi_2 - \phi_1 - \phi_{i2} + \phi_{i1} + 2n\pi} \quad (4.5)$$

where $r_2 - r_1$ is the interstation distance, ϕ_{i1} and ϕ_{i2} are the instrument phase corrections and $\phi_2 - \phi_1$ is the interstation phase difference.

The phase difference can be obtained by the cross-multiplication of two single frequency wavetrains (Bloch and Hales, 1968)

$$A_1 \cos \omega t . A_2 \cos \omega t = \frac{A_1 A_2}{2} (\cos(2\omega t + \delta\phi) + \cos \delta\phi) \quad (4.6)$$

where

$$\delta\phi = \phi_2 - \phi_1 \quad (4.7)$$

This cross product represents a wavetrain with twice the original frequency and a DC shift proportional to $\cos \delta\phi$. When the DC shift is at a maximum the two wavetrains are in phase. Other maxima will occur at each additional 2π phase shift and so the correct n must be identified.

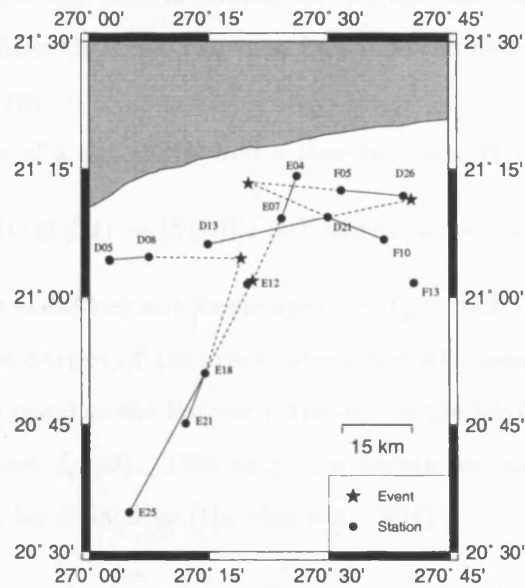


Figure 4.9: Map showing paths used for interstation phase velocity calculation.

The technique similar to that developed by Stuart et al. (1976) was used to calculate the interstation phase velocities for the chosen paths. The seismograms were windowed around the group arrival time of the period of interest calculated from the group velocity, and then narrow band-pass filtered with a Gaussian filter to produce the single frequency wavetrains. These were then cross correlated to produce a signal with a maximum amplitude at a time shift when the phase difference is zero.

The interstation distance is then divided by the time shift to produce the phase velocities. The resultant phase velocity curves were then used as a constraint during the phase matched filter stage.

4.5 Phase-matched filtering

The group velocity dispersion curves derived from the MFT technique can be further refined to isolate the fundamental (or higher) mode using a phase-matched filter (Herrin and Goforth, 1977). The phase-match filter (PMF) is one whose Fourier phase is the same as that of the component of interest of the signal. The cross correlation of the two produces a time series in which the energy of the signal is compressed. The mode of interest

is concentrated about zero lag, and, assuming the arrival times between the fundamental and higher modes is sufficiently large, can then be windowed and isolated from the rest of the spectrum (Figure 4.10).

The cross correlation of a signal $s(t)$ and a time function $f(t)$ can be represented as

$$s(t) \otimes f(t) \rightarrow |S(\omega)||F(\omega)| \exp i[\sigma(\omega) - \phi(\omega)] \quad (4.8)$$

The phase matched filter is defined as a linear operator $f_p(t)$ such that $\sigma(\omega) = \phi(\omega)$ (Herrin and Goforth, 1977). The output of the cross-correlation will then have Fourier transform $|S(\omega)||F(\omega)|$ and will be equal to the Fourier transform of the convolution of the signal and the time reversed function $f_p(-t)$. This output is known as the pseudo-autocorrelation function (PAF) and can be defined as (Hutchenson, 1994)

$$\psi_j(t, r) = \frac{1}{2\pi} \int_{-\infty}^{\infty} [e^{i\tilde{k}_j(\omega)r}] \sum_{m=0}^j A_m(\omega, r) e^{i(\omega t - k_m(\omega)r)} d\omega \quad (4.9)$$

where $e^{i\tilde{k}_j(\omega)r}$ is the PMF and $\tilde{k}_j(\omega)$ is an estimate of the wavenumber dispersion of the j^{th} mode.

This can be re-written as

$$\begin{aligned} \psi_j(t, r) = & \frac{1}{2\pi} \int_{-\infty}^{\infty} A_j(\omega, r) e^{i(\tilde{k}_j(\omega) - k_j(\omega))r} e^{-i\omega t} d\omega \\ & + \frac{1}{2\pi} \int_{-\infty}^{\infty} \sum_{m \neq j} A_m(\omega, r) e^{i(\omega t - (k_m(\omega) - k_j(\omega))r)} d\omega \end{aligned} \quad (4.10)$$

where the first integral is the mode to be isolated. The PAF in equation 4.10 will be approximately zero-phase if $\tilde{k}_j(\omega) \neq k_j(\omega)$ and concentrated about zero-lag. Windowing the isolated mode by a symmetric, zero-phase window, removes higher modes and noise to give

$$\phi(r, t)w(t) \approx w(t) \frac{1}{2\pi} \int_{-\infty}^{\infty} A_j(\omega, r) e^{i(\delta k_j r)} e^{-i\omega t} d\omega \quad (4.11)$$

where $\delta k_j r$ is the estimate of phase difference and $w(t)$ is the real part of $\omega(t)$. The amplitude spectra of the isolated mode of interest is then obtained by taking the Fourier transform.

In practice the PMF is derived from the signal and an initial estimate of the group velocity (the output from the MFT) using an iterative technique to identify the correct phase of the signal.

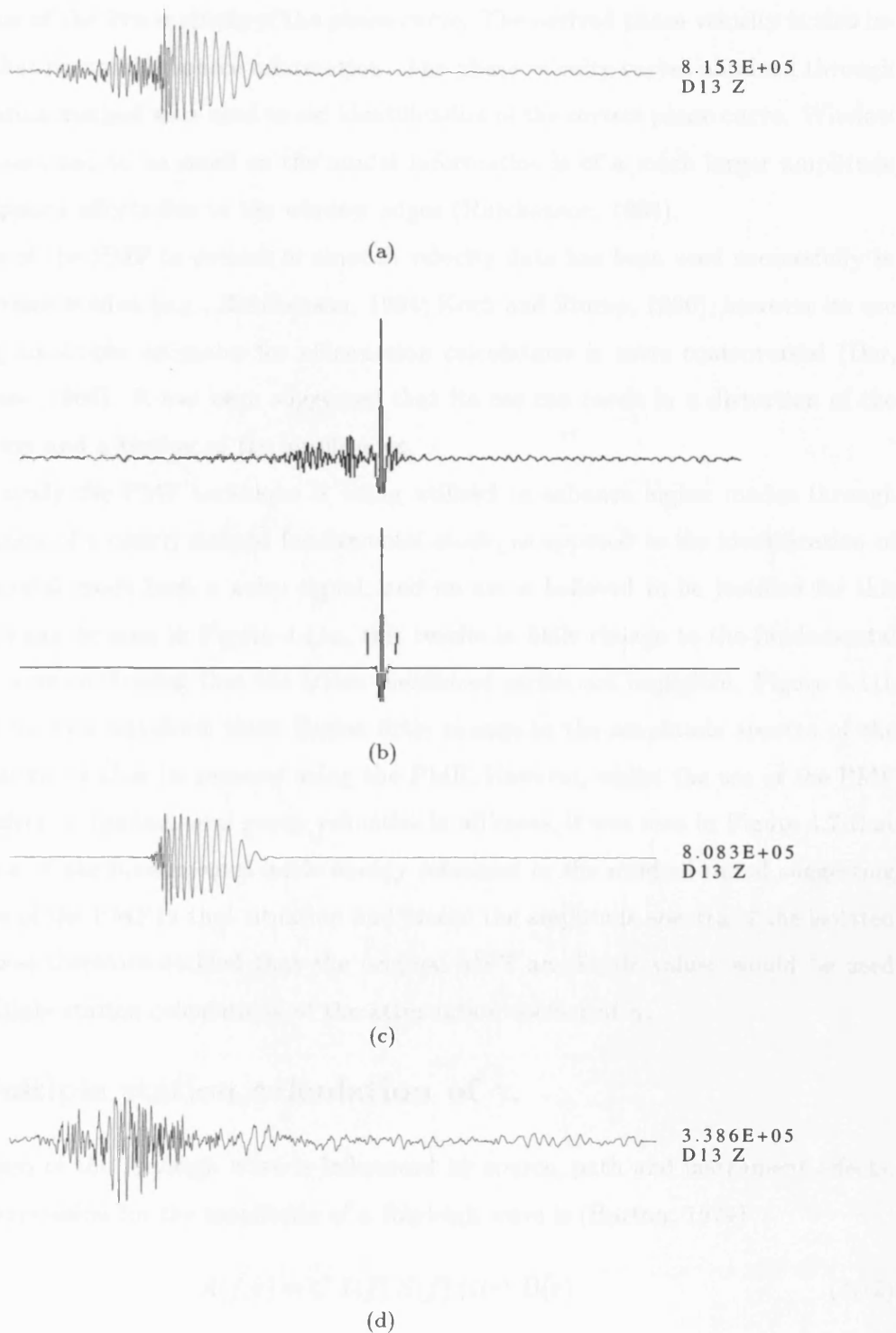


Figure 4.10: The phase-matched filter technique (a) Original waveform, (b) Cross correlation with mode of interest concentrated about zero-lag, the lower plot is the cross-correlation windowed around the mode of interest (vertical bars indicate window), (c) Fundamental Rg waveform, and (d) Residual waveform after removal of the fundamental mode. Note the difference in maximum amplitudes (shown on the right) of the wavetrains.

The final amplitude spectrum will have errors due to window biasing and the correct identification of the $2\pi n$ multiple of the phase curve. The derived phase velocity is also incorrect in that it contains source information. The phase velocity curves obtained through the interstation method were used to aid identification of the correct phase curve. Window effects are assumed to be small as the modal information is of a much larger amplitude than the rippling effects due to the window edges (Hutchenson, 1994).

The use of the PMF to extract or smooth velocity data has been used successfully in several previous studies (e.g., Hutchenson, 1994; Koch and Stump, 1996), however its use for refining amplitude estimates for attenuation calculations is more controversial (Der, 1986; Stevens, 1986). It has been suggested that its use can result in a distortion of the true spectrum and a biasing of the amplitudes.

In this study the PMF technique is being utilized to enhance higher modes through the elimination of a clearly defined fundamental mode, as opposed to the identification of the fundamental mode from a noisy signal, and its use is believed to be justified for this purpose. As can be seen in Figure 4.11a, this results in little change to the fundamental dispersion curve confirming that the errors mentioned earlier are negligible. Figure 4.11b shows that for this waveform there is also little change to the amplitude spectra of the fundamental mode after its removal using the PMF. However, whilst the use of the PMF had little effect on fundamental group velocities in all cases, it was seen in Figure 4.7 that some portion of the fundamental mode energy remained in the residual signal suggesting that the use of the PMF in that situation had biased the amplitude spectra of the isolated signal. It was therefore decided that the original MFT amplitude values would be used for the multiple station calculations of the attenuation coefficient γ .

4.6 Multiple station calculation of γ .

The spectrum of the Rayleigh wave is influenced by source, path and instrument effects. A general expression for the amplitude of a Rayleigh wave is (Burton, 1974)

$$A(f, r) = C I(f) S(f) G(r) D(r) \quad (4.12)$$

where

$C = \text{constant},$

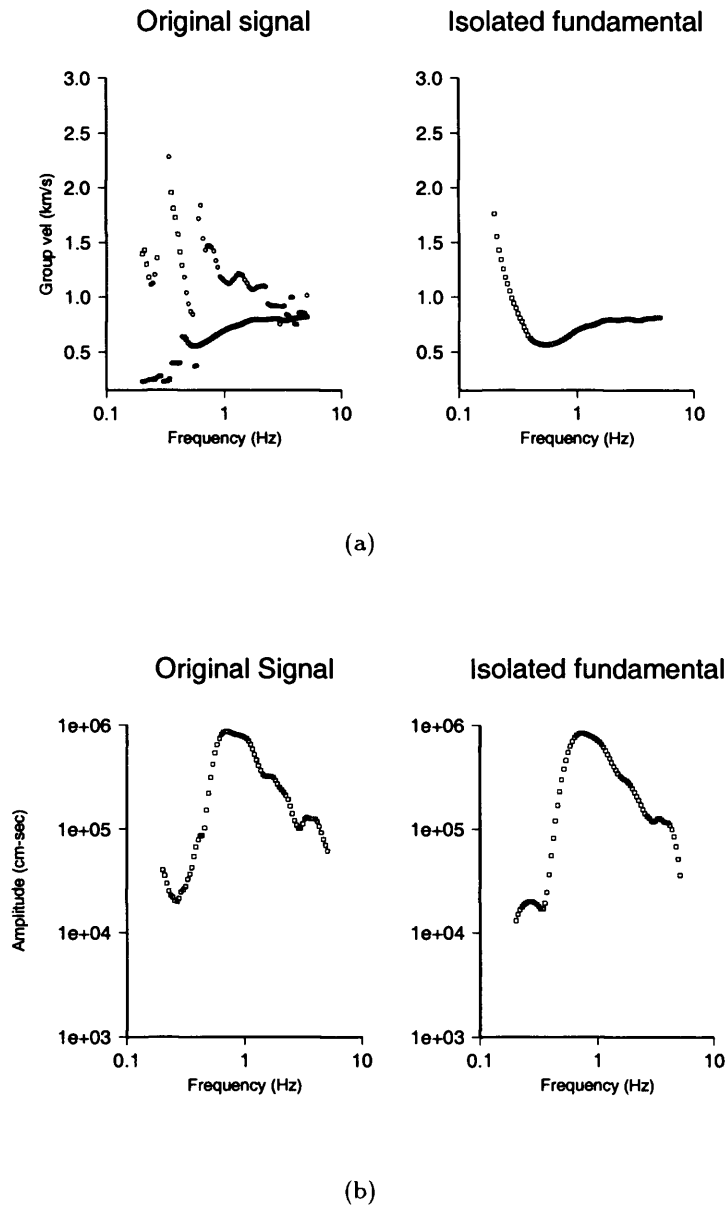


Figure 4.11: Comparison of (a) dispersion and (b) amplitude spectra before and after the application of the PMF.

$I(f)$ = instrument effect,
 $S(f)$ = source time function,
 $G(r)$ = geometrical spreading correction,
 $D(r)$ = absorption term

and it is assumed that $A(f, r)$ is independent of azimuth and that lateral variations in the source medium do not introduce a non-circular radiation pattern. The geometrical spreading is entirely a function of distance and is independent of frequency (Burton, 1974).

Removing the instrument effect and combining the source amplitude term with the constant gives the variation of amplitude with distance at a particular frequency f as

$$A(f, r) = K_1 r^{-1/2} \exp \frac{-\pi f r Q_\gamma^{-1}}{U} \quad (4.13)$$

Burton (1974) showed that a linear amplitude-distance dependence of the form $y = Q_\gamma^{-1}x + b$ can be obtained by taking the logarithm of equation 4.13 to give:

$$\ln(A\sqrt{r}) = -Q_\gamma^{-1} \frac{\pi f r}{U} + K_2 \quad (4.14)$$

The relationship between the attenuation coefficient, $\gamma(f)$, and the specific dissipation factor, $Q_\gamma^{-1}(f)$ is

$$Q_\gamma^{-1} = 2 \frac{U\gamma}{\omega}$$

By substitution into equation 4.14 the relation

$$\ln(A\sqrt{r}) = -\gamma r + K_2$$

is obtained.

The multiple filter technique described in section 4.3 calculates the spectral amplitudes for the dispersed wave train. This routine corrects for geometrical spreading so the \sqrt{r} term in equation 4.16 can be dropped.

Although a two-station calculation of γ is possible, Herrmann and Mitchell (1975) showed that for this calculation very long spreads are required to minimise the inherent errors arising from random noise and propagation effects. Evans (1981) suggested that for

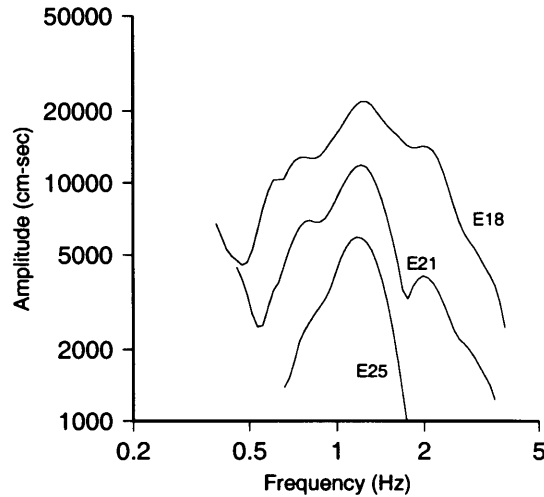


Figure 4.12: Amplitude reduction with distance for an event originating at the airport and propagating southwards.

smaller spreads a minimum of four stations is required using a linear regression technique to calculate γ .

Due to the small number of stations and their distribution in this study it was not possible to obtain four stations for the multiple station method. It was therefore decided to use a lesser number of stations to obtain γ curves and calculate an estimate of anelastic structure which would then be refined using a trial and error method during waveform modelling (e.g., Mokhtar et al., 1988; Malagnini et al., 1995)(Chapter 6). Prior to calculating γ , amplitude spectra obtained from the MFT process were checked to confirm a reduction in amplitude with distance (Figure 4.12) as often on short paths local site effects, scattering and lateral lithological changes can result in a breakdown of the assumption made in equation 4.12 of a circular propagating wavefront (Evans, 1981). Differences arising from different instrument sensitivities and pre-amp gain settings were also corrected for. Prior to the corrections the amplitude spectra of data recorded on the S13 seismometers were 1/30th of those recorded on the Guralp 40T instruments.

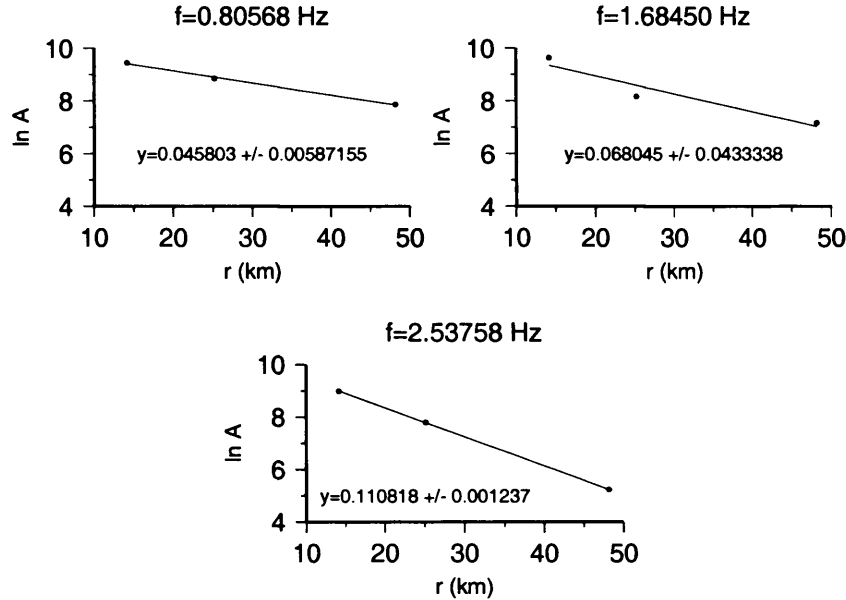


Figure 4.13: Calculation of γ by linear regression.

4.7 Description and implications of dispersion and γ curves

4.7.1 Group velocities

In most case two modes could be clearly seen following MFT analysis. The dominant higher mode is believed to be the second higher mode which agrees with observations of surface waves from quarry blasts from previous studies (e.g., Hutchenson, 1994).

Plotting of all the fundamental modes from a source at Flamboyanes (Figure 4.14) shows a distinct bimodal dispersion pattern with a change occurring above 1.5–2 Hz. Group 1 curves show a gradual continuation in the increase of group velocity with frequency, whilst Group 2 curves show a slight reduction in the group velocities. The station-event paths for these groups would suggest that the change occurs for paths travelling outwith a central area of the crater.

To further investigate this change, and to constrain this central area the dispersion curves were calculated for a quarry blast from Flamboyanes recorded during the controlled source experiment on 92 instruments across the whole structure. Figure 4.15 shows histograms of the group velocities of these at 1.0 Hz and 2.36 Hz and their corresponding paths. Again the clear bimodal distribution at the higher frequencies is visible with those

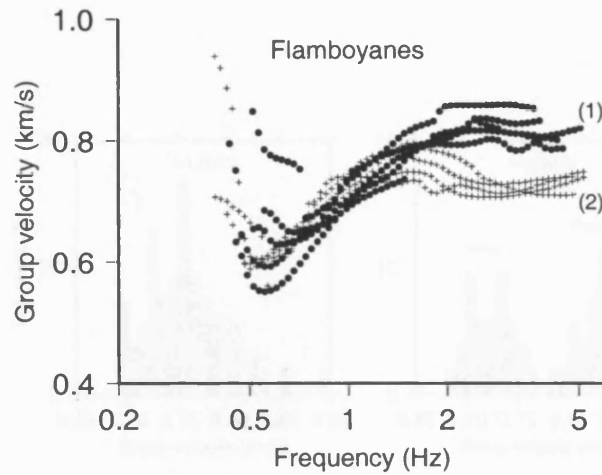
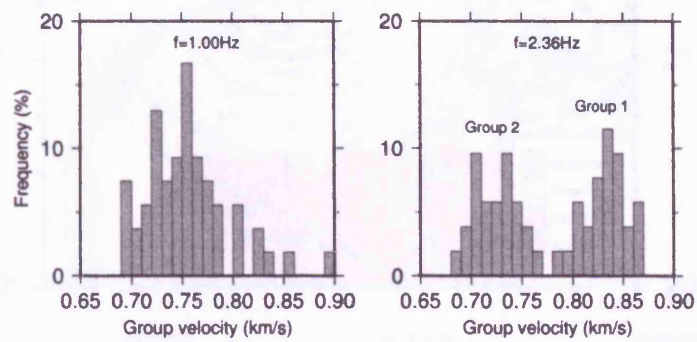


Figure 4.14: Fundamental mode dispersion curves recorded at nine sites for a source at Flamboyanes. Group 1 is the dispersion to sites D5b, D08, D13, E18 and E12. Group 2 the dispersion to F05, F10, D26 and E04.

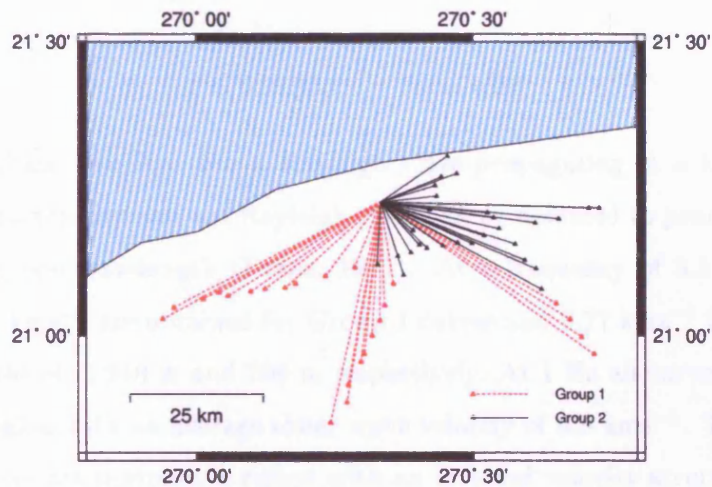
showing a lower group velocity (Group 2) related to paths limited to the crater centre (within a c. 30 km radius of the crater centre). These two types of dispersion can also be seen in the records from other events and it is possible to approximately demarcate the region of the change (Figure 4.16). It can be seen that this change, although unconstrained in the east, is very probably elliptical, with a radius between 20–30 km from the crater centre. Whilst this does not correspond to any visible change in the surficial geology it is similar in shape to the change in Neogene geomorphic surfaces reported by Pope et al. (1996). The high frequency makes it extremely unlikely that it is a result of crater geology but is probably due to a change within the top few hundred metres of the infilling sediments. If this is the case then its radial nature suggests that the crater has influenced sedimentation patterns throughout the Tertiary.

At the lower frequencies (< 1.0 Hz) the Group 2 curves are relatively tightly gathered compared to those in Group 1 suggesting a fairly homogeneous geology at the base of the Tertiary or upper crater within the crater centre. The scatter of the Group 1 curves at these frequencies is to be expected as these paths are likely to be crossing a variety of lithologies.

Simple half space calculations can be made assuming a Poisson solid using (Ewing



(a)



(b)

Figure 4.15: (a) Histograms of group velocity values at 1.0 Hz and 2.36 Hz for a quarry blast at Flamboyanes recorded during the controlled source experiment. (b) Station-event paths for the same quarry blast. Type of line indicates whether the dispersion at 2.36 Hz is of Group 1 or 2.

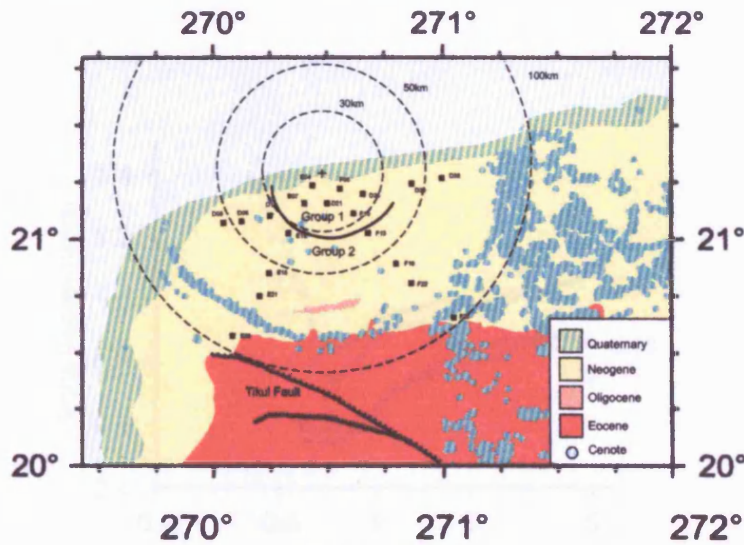


Figure 4.16: The region where the fundamental dispersion changes from being Group 2 to Group 1 type. Radius are from the crater centre marked by the + symbol.

et al., 1957)

$$c = 0.9194\beta \quad \alpha = \sqrt{3}\beta \quad (4.18)$$

where c is the phase velocity. For a Rayleigh wave propagating in a half space this is equal to the group velocity and the Rayleigh wave can be assumed to penetrate to a depth of approximately one wavelength (Evans, 1981). At a frequency of 3.5 Hz, shear wave velocities of 0.87 kms^{-1} are obtained for Group 1 curves and 0.77 kms^{-1} for Group 2 with penetration depths of c. 240 m and 200 m respectively. At 1 Hz all curves are sampling a c. 700 m deep region with an average shear wave velocity of 0.8 kms^{-1} . This implies that the Group 1 curves are sampling a region with an inverted velocity structure.

The curves from the airport events show higher group velocities for waves travelling southward away from the crater centre than those towards it (Figure 4.17). Again using equation 4.18 gives shear wave velocities of 1.12 kms^{-1} propagating southwards with a penetration depth of c. 300 m, and northwards a shear wave velocity of 0.94 kms^{-1} with a penetration depth of c. 250 m, at 3.5 Hz.

Both first and second higher modes are visible (Figure 4.18) but in most cases the second higher mode is dominant. The first higher mode is often visible on the residual FTAN plots as several regions of energy between the fundamental and second higher

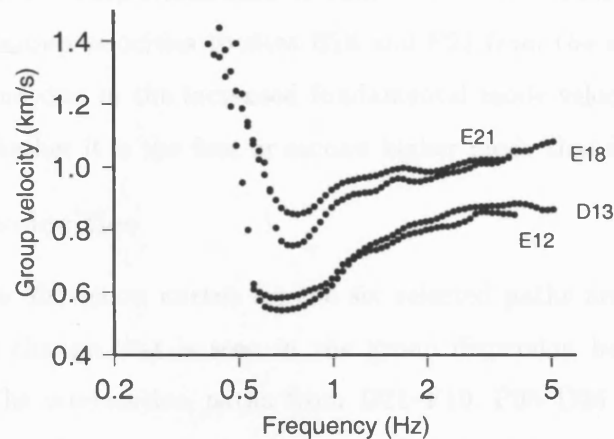


Figure 4.17: Fundamental mode curves for an event at the airport.

mode, but only in a few situations is it clear enough to be confidently identified. When identifiable, the first higher mode is consistent with normal dispersion with a decrease in velocity from c. $1.2\text{--}0.8\text{ km s}^{-1}$ for $0.5\text{--}1.5\text{ Hz}$ before flattening off above 1.5 Hz . There are several possible explanations for the first higher mode being easily visible on certain paths. In the situations where it can be positively identified the source is Flamboyanes and the path lies across the central area. This area is also highlighted by the change in higher frequency fundamental mode curves. One possibility is that the larger shot size and greater shot depths involved in Flamboyanes blasts are more efficient at exciting the first higher mode than the other sources. This is unlikely as it fails to explain paths from Flamboyanes to other stations e.g., D13, where the first higher mode can only be seen as several distinct areas of dispersed energy between the fundamental and second higher mode. A second possibility is that the reduced fundamental mode velocities across the central area allow the MFT to correctly distinguish between the fundamental and first higher modes, whilst the inverted velocity structure outside the central area reduces the time difference between the modes. Finally a change in anelastic parameters could result in greater attenuation of the first higher mode outside the central area, resulting in the dominance of the second higher mode.

The second higher modes also show normal dispersion with velocities decreasing from c. 1.7–1.0 kms⁻¹. Several minima in the dispersion curves are visible. In most cases modal interference above 3.5–4 Hz makes reliable identification of modes difficult.

Higher mode group velocities to sites E18 and E21 from the airport are greater than for other paths and due to the increased fundamental mode velocities to these sites it is difficult to say whether it is the first or second higher mode that is seen in these cases.

4.7.2 Phase velocities

Interstation phase dispersion curves for the six selected paths are shown in Figure 4.19. These reflect the change that is seen in the group dispersion between central and non central paths. The interstation paths from D21–F10, F05–D26 and E7b–E04 all show normal dispersion with a decrease in phase velocity with increasing frequency. The paths farther from the crater centre show the opposite pattern, although the frequency range for E18–E21 is very limited and the errors could permit either normal or reversed dispersion.

Higher phase velocities are seen between E18–E21 and E18–E25. This area also showed higher group velocities from events from the airport.

A modified form of equation 4.18 can be used to approximate simple two layer models of intrinsic shear wave velocity (Evans, 1981). The equations are obtained by assuming that at the lowest frequency the wave is averaging over a region one wavelength deep. This average includes a top layer whose parameters are calculated from the highest frequency group velocity which is allowed for in calculating the second layer velocity and thickness.

$$\begin{aligned}
 \beta_1 &= \frac{c(f_m)}{0.9194} \\
 d_1 &= \frac{c(f_m)}{f_m} \\
 \beta_2 &= \frac{1}{0.9194} \cdot \frac{f_m c(f_m)^2 - f_1 c(f_1)^2}{c(f_1) f_m - c(f_m) f_1} \\
 d_2 &= \frac{c_1}{f_1} - \frac{c_m}{f_m}
 \end{aligned} \tag{4.19}$$

where

β_1 = shear wave velocity in upper layer,

d_1 = thickness of upper layer,

f_m = maximum frequency,

$c(f_m)$ = phase velocity at maximum frequency,

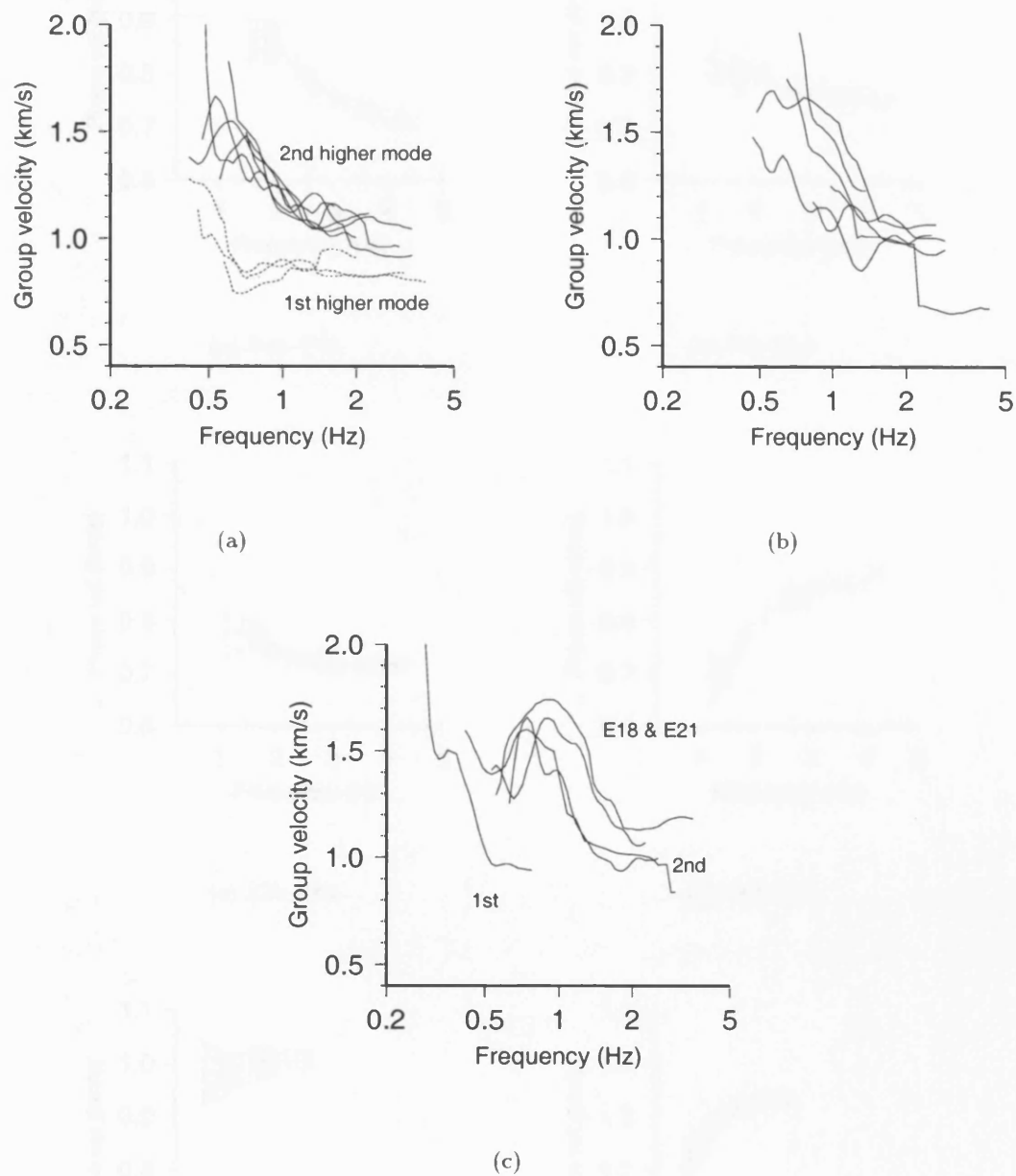
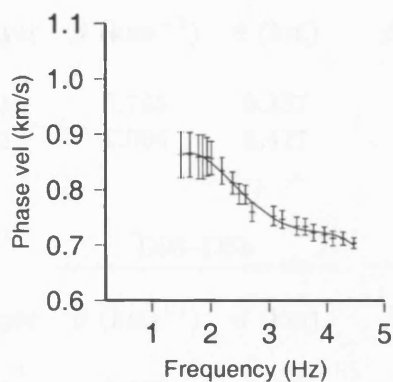
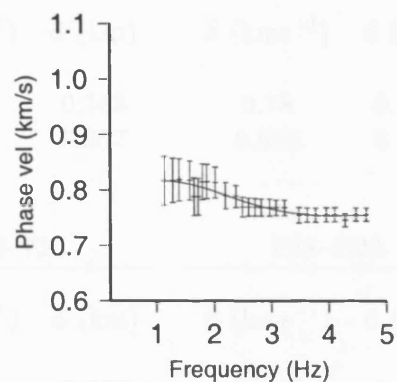


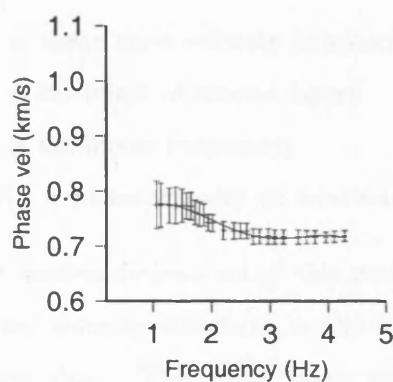
Figure 4.18: Higher mode dispersion curves for events at (a) Flamboyanes, (b) Dzitya and (c) near airport.



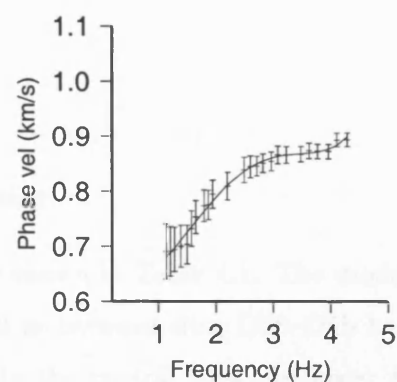
(a) D21-F10



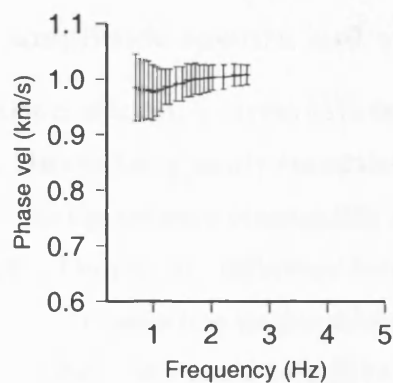
(b) F05-D26



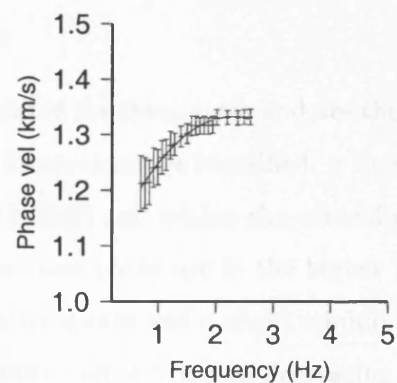
(c) E7b-E04



(d) D08-D5b



(e) E18-E21



(f) E18-E25

Figure 4.19: Fundamental phase curves obtained from interstation analysis.

Layer	D21–F10		F05–D26		E7b–E04	
	β (kms ⁻¹)	d (km)	β (kms ⁻¹)	d (km)	β (kms ⁻¹)	d (km)
1	0.765	0.157	0.822	0.163	0.78	0.168
2	1.004	0.417	0.908	0.557	0.868	0.562

Layer	D08–D5b		E18–E21		E18–E25	
	β (kms ⁻¹)	d (km)	β (kms ⁻¹)	d (km)	β (kms ⁻¹)	d (km)
1	0.972	0.209	1.096	0.387	1.448	0.512
2	0.636	0.40	1.06	1.027	1.270	1.264

Table 4.1: Simple two layer models calculated from the interstation phase curves using the modified half space equations (equation 4.19).

β_2 = shear wave velocity in second layer,

d_2 = thickness of second layer,

f_1 = minimum frequency,

$c(f_1)$ = phase velocity at minimum frequency

The four models derived using this method are shown in Table 4.1. The models confirm an inverted velocity structure in the upper 400 m between sites D08–D5b but not over the central sites. The upper layer velocities in the central area are lower than those outside. Significantly higher velocities are calculated for the paths E18–E21 and E18–E25 with those to E25 the highest, possibly corresponding to the change to Eocene sediments. These results agree in general with the half space values obtained from the group velocities.

4.7.3 Amplitude spectra and γ curves

Attenuation coefficient, γ curves have been calculated for three areas and are shown in Figure 4.20. Despite being poorly constrained some features can be identified. γ increases with frequency for the outward propagating path (E18–E25) and within the central crater area (E04–D26). The primary difference between these two paths are in the higher (> 1.5 Hz) frequencies with lower frequencies exhibiting similar values and a slight minimum at 1 Hz. The path outside the central area (D13–D5b) shows higher γ values decreasing to a minimum at c. 2 Hz and then increasing to values similar to those of the other paths.

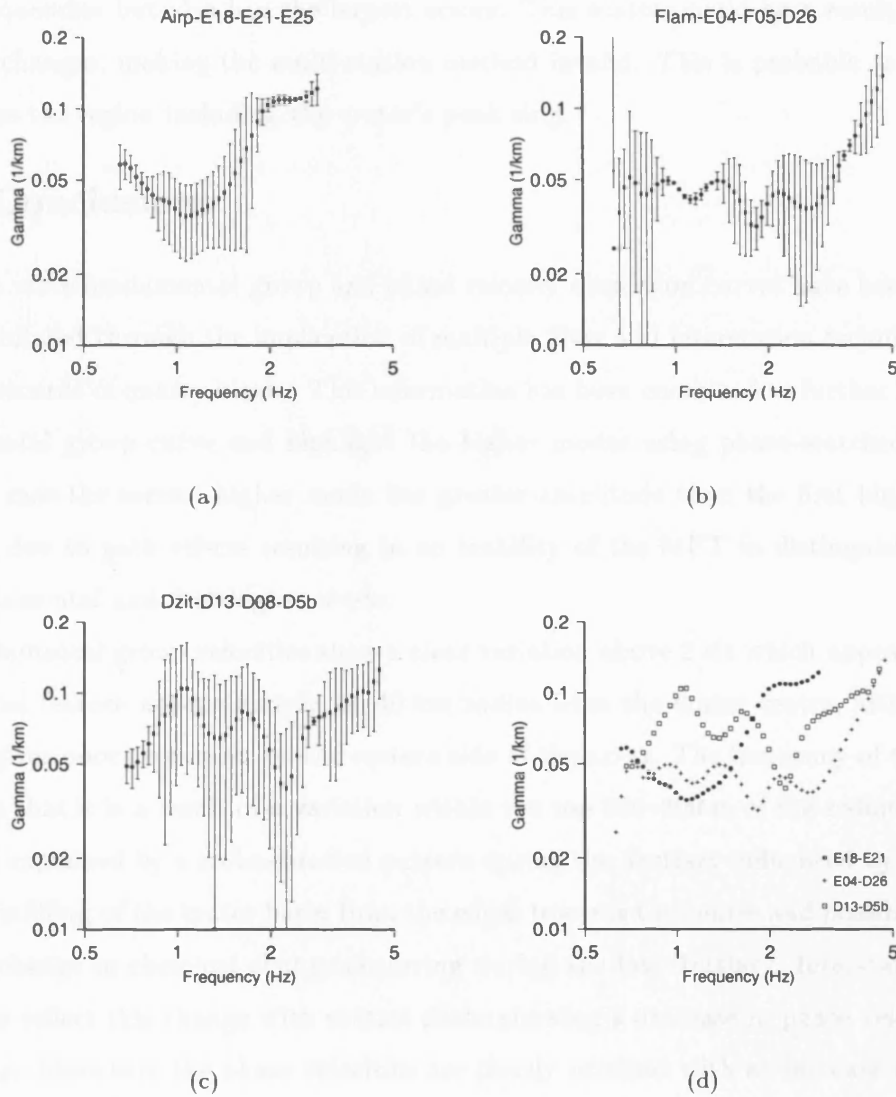


Figure 4.20: Attenuation coefficient γ curves from interstation analysis: (a) propagating southward from the crater, (b) across central crater area (c) outside central area and (d) all three without errors for comparison.

The increase in γ with frequency relates to higher attenuation at shallow depths, which would be expected for poorly consolidated surface sediments. The continuation of the high attenuation to lower frequencies for path E18–E25 may relate to the cenote ring and corresponding increased fracture density. The path D13–D5b shows high attenuation at most frequencies but also has the largest errors. This scatter could be a result of lateral velocity changes, making the multi-station method invalid. This is probable as this path may cross the region including the crater's peak ring.

4.8 Conclusions

Rayleigh wave fundamental group and phase velocity dispersion curves have been successfully calculated through the application of multiple filter and interstation techniques from stacked records of quarry blasts. This information has been combined to further isolate the fundamental group curve and highlight the higher modes using phase-matched filtering. In most case the second higher mode has greater amplitude than the first higher mode, possibly due to path effects resulting in an inability of the MFT to distinguish between the fundamental and first higher mode.

Fundamental group velocities show a clear variation above 2 Hz which appear to relate to a radial feature approximately 20–40 km radius from the crater centre, although lack of data gives poor constraint on the eastern side of the array. The frequency of the change indicates that it is a result of a variation within the top 200–300 m of the sediments. This could be explained by a sedimentation pattern during the Tertiary influenced by the crater with an infilling of the crater basin from the edges towards the centre and possibly a depositional change or chemical change occurring during the late Tertiary. Interstation phase velocities reflect this change with central paths showing a decrease in phase velocity with frequency. Elsewhere the phase velocities are clearly reversed with an increase in velocity with frequency. Simple half space models of shear wave velocity have been calculated from the group and phase velocities which confirm this velocity inversion. Increasing velocities are modelled progressing outward from the crater centre, corresponding firstly with the change to an inverted velocity gradient and then probably older Tertiary sediments. The change to Eocene geology may also be imaged by increased velocities.

At lower frequencies the group velocities appear to be consistent across the crater

centre but outside show some differences. These relate to geological variations at depth, most likely within the upper sections of the crater. The first higher modes also show little variation across the central area. Higher mode curves to sites E18 and E21 are significantly different from those closer to the crater centre.

Curves of the attenuation coefficient, γ , have been calculated using a multiple station technique, although these are not well resolved. High attenuation is seen at high frequencies which would be expected for near surface sediments. For two paths, E18–D25 and E04–D26, the attenuation decreases with depth, although this decrease takes place at deeper depths for E18–E25, possibly corresponding to the increased fracture density related to the cenote ring. The remaining path D13–D5b shows an initial decrease followed by increasing attenuation. Whilst this may reflect the true anelastic structure the very high errors could indicate that lateral velocity boundaries are resulting in a breakdown of the assumptions used in the multiple station method.

Chapter 5

Surface Wave Inversion: Theory & Method

Following the initial processing described in Chapter 4 to obtain velocity dispersion curves and γ values these results were inverted to produce shallow crustal velocity and attenuation (Q_β^{-1}) models.

A genetic algorithm was used to invert dispersion curves for 1-D velocity models whilst Q_β^{-1} was obtained using a linear singular value decomposition (SVD) method based on a routine of Meju (1994a). In reality the group velocity has a causal relationship with Q_β^{-1} (O'Neill and Hill, 1979) and ideally they should be inverted simultaneously. However previous studies have suggested that simultaneous inversion whilst increasing the accuracy of the Q_β^{-1} determination can result in a decreased accuracy in the determination of shear wave velocity (Lee and Solomon, 1978). For this reason and also due to the large errors involved in the measurement of γ it was decided to keep the inversions independent.

5.1 Inversion using a genetic algorithm

Optimization methods can be classed within two broad groups. The first group is where the model parameters are linear with respect to the data and use linear algebra to solve for a model, or where the data is quasi-linear and an iterative method, relying on local gradient information to update the model, is used. In this situation it is assumed that the minimum misfit can be found by several linear approximations at each iteration and derivatives calculated at each iteration are used to update the model. One disadvantage with this type of inversion is that it produces a single solution which can be heavily biased

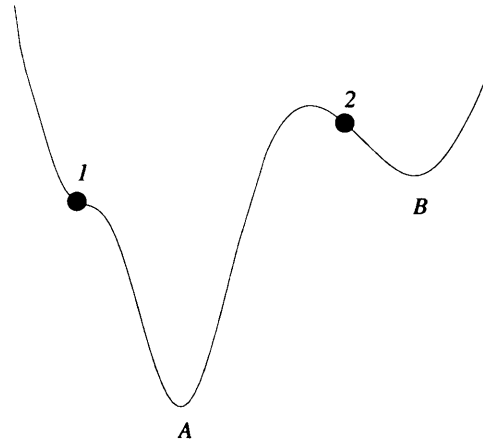


Figure 5.1: An objective function for a non-linear problem is irregular and can contain several local minima. Using an iterative method such as steepest descent only starting model 1 will converge to the global minimum (A), whilst model 2 will converge to the local minima (B) (adapted from Sen and Stoffa, 1995).

by the starting model (e.g., Menke, 1984; Sandvol et al., 1998). Most geophysical problems are non-linear and as a result have irregular objective (misfit) functions with several local minima. The effectiveness of the inversion is therefore very dependent upon the starting model with the method only finding the minima closest to it (Figure 5.1). This can especially be a problem for inversion of short period surface waves (Yamanaka and Ishida, 1996) which are affected greatly by near-surface layers which can be very variable both laterally and vertically, thus making it difficult to have a good initial model. Where *a priori* information is available this can be used to help define the starting model but where it is not available often the optimization will find a local rather than the global minimum. By only producing a single solution, these methods also provide little information on the model space.

The second group use a random method to search the model space to find acceptable solutions e.g., the Monte Carlo method. Using a method such as the Monte Carlo can be computationally expensive as it involves searching large areas of the model space that have no relevance to the problem. During the last two decades advances have been made in guided random methods e.g., genetic algorithms (GA) and simulated annealing (SA). These methods are still random but are iterative, operating on populations of possible solutions and using them to constrain the sample area of the model space. The scatter

of acceptable solutions gives an indication of the resolution and non-uniqueness of the model. Sen and Stoffa (1995) provide a review of these methods and their application to geophysical problems.

Genetic algorithms are based on evolution and the principle of natural selection and genetics (Holland, 1992; Forrest, 1993). By emulating the processes of selection, mating and mutation, genetic algorithms search a model space for acceptable solutions, and evolve to focus the search on the most promising areas of the model space. They have the ability to be tailored for a variety of different problems giving them applications across a wide range of disciplines.

It is only within the last decade that interest in the applications of the GA has been generated within earth sciences. Since then it has been successfully utilized in many areas especially seismology. Shibutani et al. (1996) used the method for receiver function inversion; it has been used in both hypocentral location (e.g., Sambridge and Gallagher, 1993; Xie et al., 1996) and determination of source parameters (e.g., Hartzell and Liu, 1995; Sileny, 1998); Stoffa and Sen (1991) fitted synthetic waveforms to obtain 1-D depth dependent seismic profiles and Drijkoningen and White (1995) applied a GA to the inversion of marine refraction data. The method has also been successfully applied to infer thermal histories from apatite fission trails (Gallagher, 1995), 2-D magnetotelluric inversion (Everett and Schultz, 1993; Schultz et al., 1993) and mantle dynamics (King, 1995; Kido et al., 1998).

Lomax and Snieder (1994, 1995) investigated a GA's ability to find sets of acceptable solutions and their applicability to Rayleigh wave dispersion. They then used the method to investigate differences in upper mantle shear wave velocities beneath the stable East European platform and tectonically active regions of central and western Europe. Utilizing a modified GA, Yamanaka and Ishida (1996) produced a shear-wave profile of sedimentary layers within the top 4 km of the crust across Sagami Bay, Japan from short and medium period Lg dispersion curves. Shapiro et al. (1997) confirmed the existence of an anomalously low velocity layer associated with active volcanism in the southern section of the Mexican Volcanic Belt by inverting fundamental Rg dispersion curves using a two step inversion method. They firstly obtained a model using a gradient inversion method and then explored the model space and obtained a range of acceptable methods through

a guided random method.

These studies have shown that the genetic algorithm is an effective method of optimizing surface wave data to obtain crustal and mantle shear wave velocity models.

5.2 Theory

In nature organisms evolve through two processes, selection and reproduction. Selection determines which survive by means of some form of test; failing the test results in death. Reproduction allows evolution of the organism through the mixing and recombination of genes. Evolution is more rapid if the offspring contain a mixture of their parents' genes than if they simply contained a copy of a single parent's genes (Holland, 1992).

Genetic algorithms are a form of search methods based on these processes. They encode a random population of potential solutions to chromosome type structures, evaluate them and then create a new population, with the same size as the original, through the application of recombination operators such that the chromosomes representing a better solution have an increased chance of survival over those with poorer solutions.

The principal differences between genetic algorithms and other more traditional optimization methods are (Goldberg, 1989)

- GAs operate on some form of encoded parameters rather than the parameters themselves
- GAs begin their search from a population of random starting points across the model space rather than one single point
- GAs do not require derivative information or assume any linearization (and hence do not operate using a deterministic transition) but work solely on the objective function information.

The basic GA is composed of four stages

- coding
- reproduction
- crossover

- mutation.

The first stage codes the model parameters into an analog of a chromosome which the next three stages operate on. The combination of the latter three stages results in taking an input population (“parent”) and producing an output population (“offspring”). The aim of the three steps is to allow the more successful characteristics of the parent to be passed down to the offspring, whilst “killing off” the less desirable components. These steps are repeated with each iteration (or generation) thus optimizing the initial problem.

5.2.1 Coding

The initial stage of using a GA is the discretization of the model parameters into a bit-string (or chromosome). The most common method of this is binary encoding although other methods do exist using higher order and real values (e.g., Davis, 1996).

In simple binary (regular) encoding, each bit corresponds to a gene which can take the value of 0 or 1 and each model parameter is represented by several genes, which are then concatenated to form an individual bit string or chromosome representing the model. The coding scheme for each model parameter can be individually defined thus limiting the search space and resolution of each parameter independently. In a geophysical situation the model parameters would be the physical properties of the Earth controlling the measured response. These would be encoded by defining an upper and lower limit for each parameter and the desired resolution or number of intervening values. Each possible value would then be represented by a binary code (Figure 5.2).

5.2.2 Reproduction

From the randomly selected initial population (with size Q) a new population is selected with the probability of selection being determined by some measure of the objective (misfit) functions, $\phi(i), i = 1, Q$. The two most common forms of determining the probability are linear (equation 5.1) and exponential (equation 5.2).

$$P_r(m_k) = a - b\phi_k \quad (5.1)$$

$$P_r(m_k) = A \exp(-B\phi_k) \quad (5.2)$$

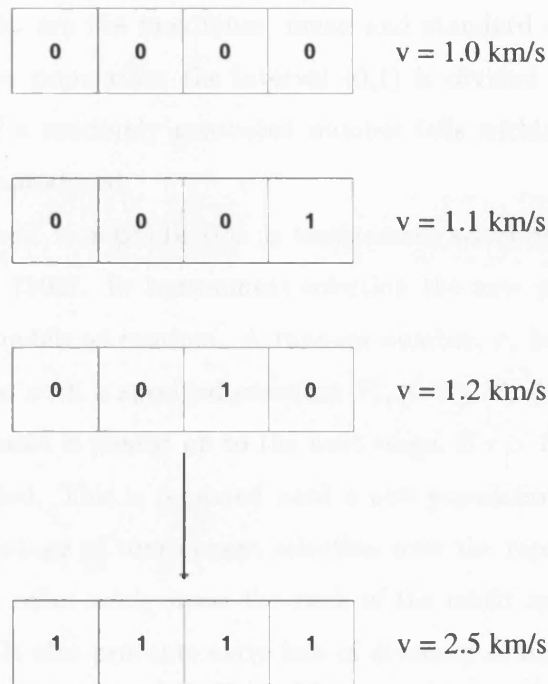


Figure 5.2: An example of binary coding for shear-wave velocity model parameters. If the velocity is allowed to vary between $1\text{--}2.5 \text{ km s}^{-1}$ with a resolution of 0.1 km s^{-1} then there are 16 possible velocity values which can each be represented by four bits. When all four bits are off (i.e., 0) then the velocity is 1 km s^{-1} ; when all four bits are on (1) then the velocity is 2.5 km s^{-1} . If the shear wave velocity was the only model parameter then each four bit code would form one chromosome, if another parameter existed then the chromosomes would be formed by joining them one after the other. The other parameters need not be represented by four bits but could be more or less, depending on the resolution required.

where $P_r(m_k)$ is the probability of string m_k being selected and constants a, b, A and B are determined by the misfit distribution (equation 5.3) (Sambridge and Gallagher, 1993)

$$\begin{aligned} b &= Q^{-1}(\phi_{max} - \phi_{avg})^{-1} & a &= b\phi_{max} \\ A &= 1 / \sum_{j=1}^Q \exp(-B\phi_j) & B &= \phi_{\sigma}^{-1} \end{aligned} \quad (5.3)$$

where ϕ_{max} , ϕ_{avg} and ϕ_{σ} are the maximum, mean and standard deviation of the misfit values. To select a new population the interval (0,1) is divided into Q segments with lengths equal to P_r . If a randomly generated number falls within a segment then that string is chosen to be reproduced.

An alternative method to reproduction is tournament selection (e.g., Sambridge and Gallagher, 1993; Riolo, 1992). In tournament selection the new population is generated by selecting a pair of models at random. A random number, r , between 0 and 1 is then generated and compared with a specified constant P_s , ($0.5 \leq P_s \leq 1$). If $r \leq P_s$ then the model with the lower misfit is passed on to the next stage. If $r > P_s$ then the model with the higher misfit is copied. This is repeated until a new population containing Q models is generated. The advantage of tournament selection over the reproduction methods described above is that it relies solely upon the rank of the misfit and is unaffected by the range of misfit values. It also prevents early loss of diversity reducing the chance of premature convergence, however Booker (1987) argues that using a rank based reproduction method and ignoring the relative fitness violates the theories of GAs.

5.2.3 Crossover

The new population generated after the reproduction stage consists solely of models that existed in the original population. The crossover stage modifies the population by changing individual strings. Pairs of strings are selected at random to produce $Q/2$ couples. Again a random number, r ($0 \leq r \leq 1$), is generated and compared to a constant P_c . If $r \leq P_c$ then a position is chosen at random on the bit-strings and two new strings are created by cutting and transposing the segments (Figure 5.3). If $r > P_c$ then the pair are passed through to the next stage unchanged. This is repeated for each pair to produce a new population of Q models.

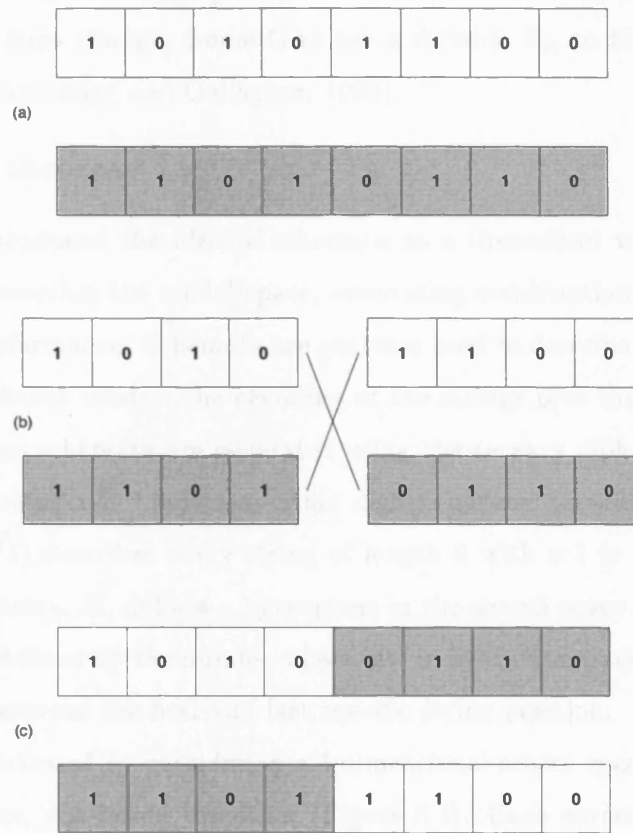


Figure 5.3: An example of crossover between two strings. The couple (a) are cut at a randomly chosen point (b) and the segments transposed to create two new strings(c).

5.2.4 Mutation

The final stage of the GA is the mutation of randomly chosen bits. This in general affects only a tiny proportion of the bits, either flipping the parity from 0 to 1 (or vice versa) or replacing the bit with a randomly generated a new bit. In the second case, mutation will only change the bit value 50% of the time. The probability of mutation of individual bits is determined by a constant P_m , which is typically chosen to be $< 1\%$ (Whitley, 1994). The aim of this stage is to prevent the development of a uniform population that can not evolve further (premature convergence if a satisfactory solution has not been found) and thus retain some degree of diversity. In general it does not advance the search for a solution. By increasing the value of P_m the GA will resemble a Monte Carlo method. With a constant value of P_m , mutation affects all bits equally. Thus a mutation of a low order

bit, causing a relatively small change, is just as probable as the mutation of a high order bit, resulting in a large change. Some GAs use a variable P_m to bias mutation towards lower order bits (Sambridge and Gallagher, 1993).

5.2.5 Schema theorem

Holland (1975) introduced the idea of schemata as a theoretical way to explain how a genetic algorithm searches the model space, associating combinations of model attributes with improving performance. Schemata are patterns used to describe subsets of bit strings defined by the alphabet used in the encoding of the strings plus the * symbol. Thus for binary coded strings schemata are generated using the ternary alphabet (0,1,*), where 0 and 1 define a bit value and * indicates either digit is allowed (a wild card). For example, the schema (1****1) describes every string of length 6 with a 1 in the first and last bit positions. Each schema, H , defines a hyperplane in the search space with the order of the hyperplane $o(H)$, defined by the number of set bits in the schema and the defining length, δH , the distance between the first and last specific string position.

This can be illustrated by considering a 4-dimensional search space represented by two 3-dimensional cubes, one inside the other (Figure 5.4). Each corner is labelled with a 4 bit string, where the first bit defines the inner or outer cube and the next three bits define the face; front/back, top/bottom and left/right. The schema (0***), with defining length $\delta H = 0$, defines the order-1 hyperplane corresponding to the outer cube and schema (1*1*), $\delta H = 2$, defines the order-2 hyperplane corresponding to the top of the inner cube. Every bit of a chromosome of length, L , is a member of 2^{L-1} hyperplanes and the entire search space contains 3^{L-1} hyperplanes (the string containing only wild cards is not considered a portion of the space). Therefore each time the GA evaluates a string it also evaluates numerous hyperplanes, suggesting that a GA exhibits implicit parallelism (Holland, 1975).

The schema theorem is the fundamental theorem of genetic algorithms. Through various operators the number of schemata in the population will increase or decrease depending on the fitness of the strings representing that schemata. This occurs for every schema within a population in parallel.

It is possible to track the sampling rate of a hyperplane and indicate whether its representation in a population will increase or decrease over a generation. Let $P(H, t)$ be the proportion of strings sampling a hyperplane, H , at the current generation, t . Let

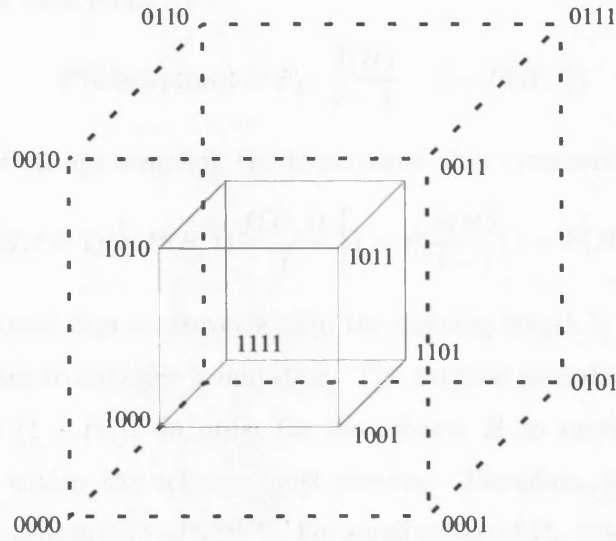


Figure 5.4: A 4-dimensional space represented by two cubes, one within the other. Corners are labelled by 4 bits representing which cube and which three faces intersect at the corner. The schema (10**) defines the hyperplane representing the front face of the inner cube (after Whitley, 1994).

the generation after reproduction but before crossover and mutation be represented by the index ($t + intermediate$), and the next generation after crossover and mutation represented by ($t + 1$). The change in representation according to fitness associated with strings after reproduction is expressed as

$$P(H, t + intermediate) = P(H, t) \frac{f(H, t)}{\bar{f}} \quad (5.4)$$

where $f(H, t)$ is the objective function of each string and \bar{f} is the average misfit of all the strings in the population.

To calculate the proportion of strings sampling the hyperplane at the next generation, the effects of crossover must be considered. Crossover is applied probabilistically to a portion of the population. The representation due to reproduction of the portion that does not undergo crossover remains as in equation 5.4. Where crossover does occur, then its disruptive effects must be taken into consideration. Disruption of the hyperplane depends on three events; (1) that crossover occurs, (2) that it will fall within the defining length of the hyperplane and (3) that the mate of the parent is not also a member of the same hyperplane. As these events are independent, the probability of disruption is the product

of the probability of each event

$$P(\text{disruption}) = P_c \cdot \frac{\delta(H)}{l-1} \cdot (1 - P(H, t)) \quad (5.5)$$

so the proportion of strings sampling the hyperplane after crossover is

$$P(H, t+1) \geq P(H, t) \frac{f(H, t)}{\bar{f}} \left[1 - P_c \frac{\delta(H)}{l-1} (1 - P(H, t)) \right] \quad (5.6)$$

where we have assumed that crossover within the defining length is always disruptive.

The final operator to consider is mutation. The survival probability of each individual bit in the string is $(1 - P_m)$. In order for the schema H to survive, each of the $o(H)$ specified positions within the schema must survive. Therefore, the probability of the schema surviving mutation is $(1 - P_m)^{o(H)}$. For small values of P_m this can be approximated by $P_m(1 - o(H))$. Including this term in equation 5.6 gives the expression for the proportion of strings sampling a particular schema in the next generation as;

$$P(H, t+1) \geq P(H, t) \frac{f(H, t)}{\bar{f}} \left[1 - P_c \frac{\delta(H)}{l-1} (1 - P(H, t)) \right] P_m(1 - o(H)) \quad (5.7)$$

Although the schema theorem does show how short, low-order, above average schemata receive increasing trials in the next population, it does not prove that these will combine to build optimal solutions or that convergence will occur. However, Goldberg (1987) showed that even for deceptive problems (where short, low-order blocks can build sub-optimal longer blocks), surprisingly the GA usually converges on the global optimum.

5.3 Selection of genetic algorithm parameters

Previous research (e.g., Gallagher and Sambridge, 1994) has suggested that although it is relatively easy to implement a genetic algorithm, its efficiency is dependent upon several parameters

- encoding method
- population size, Q
- reproduction method
- crossover probability, P_c

- mutation probability, P_m

Poor choice of these parameters will result in too slow convergence and a failure to find the global minimum, or too rapid convergence resulting in the algorithm sticking in a local minimum. In addition, several changes can be made to the basic GA to improve optimization e.g., elite selection (e.g., Yamanaka and Ishida, 1996) and hybridization (e.g., Sen and Stoffa, 1992; Chunduru et al., 1997). In order to maximize the efficiency of the GA, it is best to experiment with several parameters and choose the most effective. In order to achieve this, synthetic dispersion curves were calculated using the forward modelling method described in Section 5.4 and then inverted several times, varying the parameters each time. The exception to this was the encoding method which was left as binary, although some exploration of regular and magnitude based binary encoding was made (section 5.3.1). The initial GA used for the velocity inversion is that of Sambridge and Drijkoningen (1992).

An rms misfit (equation 5.8) was used in order to determine the misfit between the observed and theoretical values

$$\phi(i) = \sqrt{\frac{\chi^2}{ND}} \quad (5.8)$$

where ND is the number of data and χ^2 is defined by

$$\chi^2(i) = \sum_{i=1}^{ND} [y_{calc}(i) - y_{obs}(i)]^2 / W(i)^2 \quad (5.9)$$

$W(i)$ is a weighting function determined by the observational errors, $\xi(i)$

$$W(i) = \frac{y_{obs}(i) + \xi(i)}{y_{obs}(i)} \quad (5.10)$$

In a matrix method such as SVD, a stopping criterion is generally given, either when the misfit goes below an acceptable value, when the convergence slows (i.e. the change in misfit between two iterations drops below an acceptable value) or after a set number of iterations. Whilst it is possible to introduce these criteria to the GA it was decided to use only the number of iterations as a stopping criteria. Whilst this results in a computationally longer process it provides the highest probability of finding the best model and also allows a more thorough investigation of the model space. The use of a convergence criteria is advised

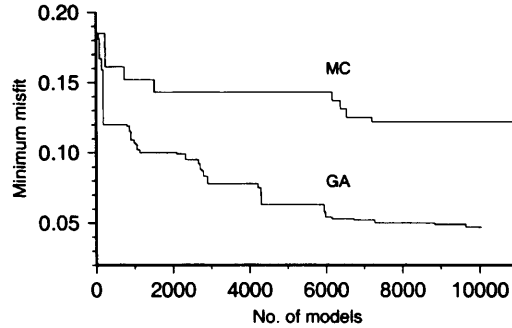


Figure 5.5: Convergence of a GA and Monte Carlo method showing alternation between rapid and slow convergence

against, as it can be seen, both in this study (Figure 5.5) and others (e.g., Sambridge and Drijkoningen, 1992) that the convergence of a GA occurs in steps varying between rapid convergence and relatively slow convergence. This change has been explained in two ways. Either all available information from the population has been gained and the algorithm needs a new injection of information from a random model to proceed; or the algorithm switches from conducting a local search to a global search, allowing it to jump out of a local minima in the misfit surface. Therefore, using a convergence stopping criteria could result in the failure of the global optimization of the GA.

5.3.1 GA encoding

As mentioned above, genetic algorithms operate on a bit-string representation of the model parameters and several different techniques, known as encoding, are available to map between the bits and decimal numbers. The traditional method is the use of binary encoding. The advantages of using a binary bit string are that they maximize the number of schemata per bit of information giving more chance of matching similarities among strings with a high fitness value.

An alternative to regular binary encoding is magnitude binary encoding. In magnitude binary encoding the bits are organized by binary magnitude, thus the first n bits would be determined by the 2^x digits of the binary values, the second set of n bits by the 2^{x-1} digits and so on. For example, coding the decimal parameters (24,10) to binary gives (11000, 01010) producing the bit string (1100001010) using regular binary encoding. Using

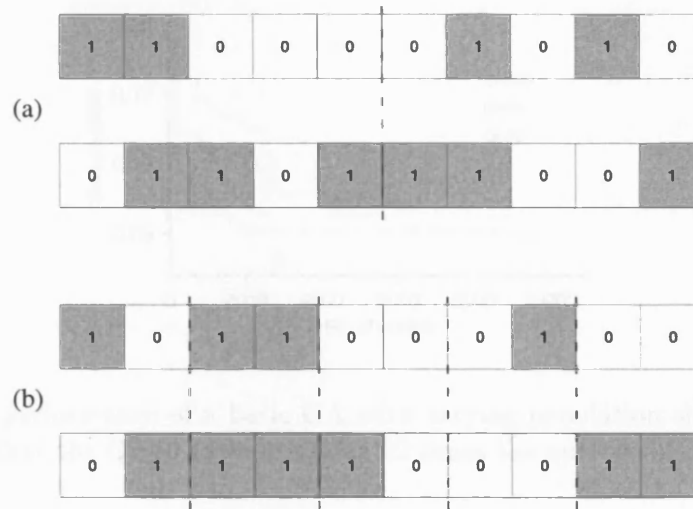


Figure 5.6: Two examples of binary coding of the decimal parameters (24,10) and (14,25). (a) Regular binary coding creating two binary strings of length 10 (grey blocks represent 1 and white 0) with the first 5 bits the binary code of the first decimal value and the second 5 bits the binary code for the second decimal value. (b) The same two sets of decimal parameters now encoded by binary magnitude, again creating two strings of length 10 but where the first two bits represent whether the two decimal values are of order 2^4 , the second two bits, order 2^3 and so on.

magnitude based encoding the first two bits are determined by the 2^4 values (1,0), the third and fourth bits by the 2^3 values (1,1) etc., thus producing the string (1011000100) (Figure 5.6).

The differences in these two methods of encoding only affect the crossover stage, since the reproduction is determined by the objective functions and mutation is a random process.

Testing by this author of these two methods showed that for a velocity–depth optimization normal binary encoding gave improved performance over magnitude based encoding.

5.3.2 Population size

The initial population size can be extremely important. Whereas in a Monte Carlo method increasing the population generally results in an improved misfit, the same is not necessarily true for the GA. Too large a population can degrade the usefulness of the crossover and mutation stages by introducing too many poor model parameters and slowing down the convergence (Sambridge and Drijkoningen, 1992; Gallagher and Sambridge, 1994). Too

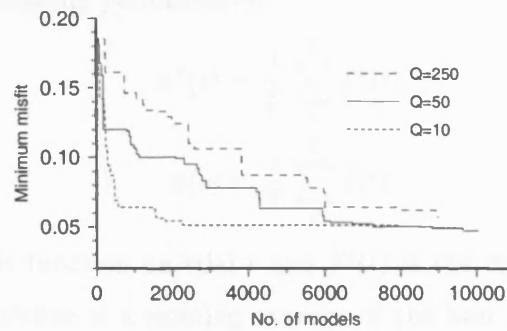


Figure 5.7: The performance of a basic GA with varying population sizes (Q). It should be remembered that the $Q=10$ curve contains 22 times the number of iterations than the $Q=250$ curve.

small a population will result in there being too little information on the model space and cause only a local optimization of the data.

Several runs of the GA were conducted starting with the same initial model space but varying the population size, Q . Figure 5.7 shows how the minimum misfit reduces against increasing number of models sampled for each choice of Q . It can be seen that the smallest population ($Q=10$) has a rapid reduction in misfit over the first 500 models before slowing down and stalling through a lack of information. Increasing the population to 50 gives a better minimum misfit but a slower reduction as the model space is explored more. Further increasing the population to 250 causes the GA to slow down further and does not reach the minimum misfit of the lower population.

5.3.3 Selection of reproduction, crossover and mutation parameters

Once the size of the initial population had been chosen the method of reproduction and values for crossover and mutation probability were selected in a similar *ad hoc* manner. There were however some general guidelines that were followed (Sambridge and Gallagher, 1993). P_c was kept high (0.6–1.0) to ensure mixing whilst P_m kept low, equivalent to about one parity flip per string ($\sim 1/L$ or $1/2L$). To evaluate the effectiveness of the GA two measures were monitored, the off-line and on-line performance (DeJong, 1975). Off-line (equation 5.11) is an indication of the convergence of the GA whilst on-line (equation 5.12)

is an indication of its ongoing performance.

$$x^*(s) = \frac{1}{T} \sum_1^T f^*(t) \quad (5.11)$$

$$x(s) = \frac{1}{T} \sum_1^T f(t) \quad (5.12)$$

where $f(t)$ is the misfit function on trial t and $f^*(t)$ is the minimum misfit function for each iteration, hence off-line is a running average of the best misfits whilst on-line is an average of all misfits.

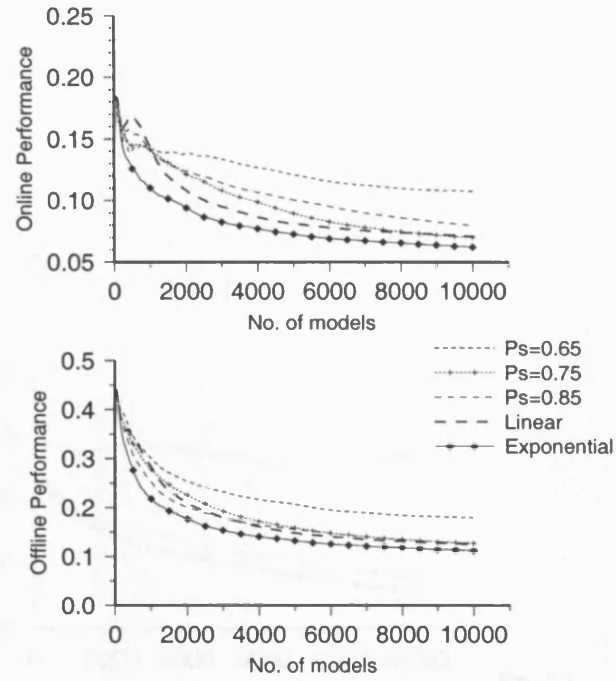
Both linear and exponential reproduction were tested as was tournament selection with varying values for P_{TS} . Figure 5.8 shows the performance of these and various crossover values. An exponential reproduction selection and crossover value of 0.85 are seen to give the best performance.

Having chosen P_{TS} and P_c the mutation probability, P_m , was varied from 0.001–0.1 and a linear and exponential ramped probability was tested. Figure 5.9 shows the change in online and offline performance against number of models sampled for a range of constant P_m s and a ramped P_m . The high value of P_m (0.1) shows little improvement for either, suggesting a fairly random process. Smaller values of P_m show much better performance. Figure 5.10 shows the model results of a high and low mutation rate. It can be seen that the high mutation rate provides a much wider search of the model space than the low mutation rate.

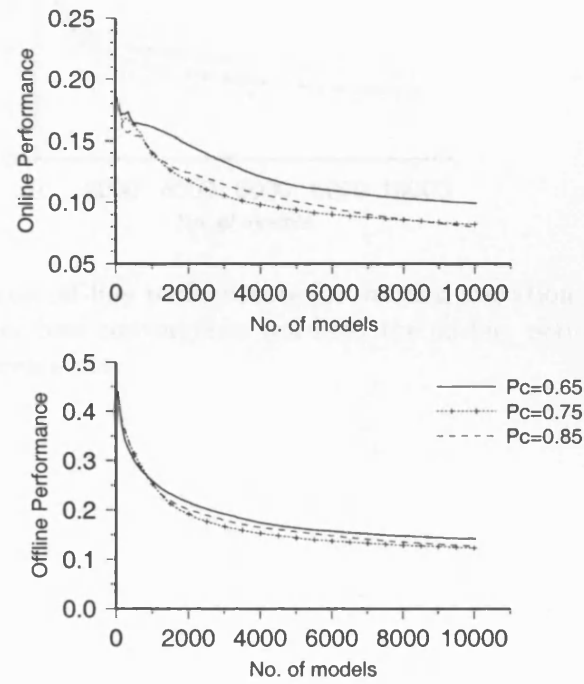
By using a constant P_m the probability of mutating high order bits (causing global changes) is the same as for low order bits (responsible for local changes). By varying the mutation depending on bit order it is possible to allow a higher mutation on the low order bits providing more local sampling and a lower mutation on high order bits helping to prevent too many global jumps which are not beneficial to the algorithm. Figure 5.9 shows that the introduction of an exponentially ramped mutation probability gives increased performance. Testing by this author showed that using an exponential ramp gave superior on-line and off-line performance than a linearly varying mutation.

5.3.4 Further refinements of the genetic algorithm

Several additional refinements to the basic GA, consisting of selection, crossover and mutation, to improve efficiency have been proposed by various authors and several of these



(a)



(b)

Figure 5.8: On-line and off-line performance for (a) different methods of reproduction and varying values of P_{TS} and (b) various P_c

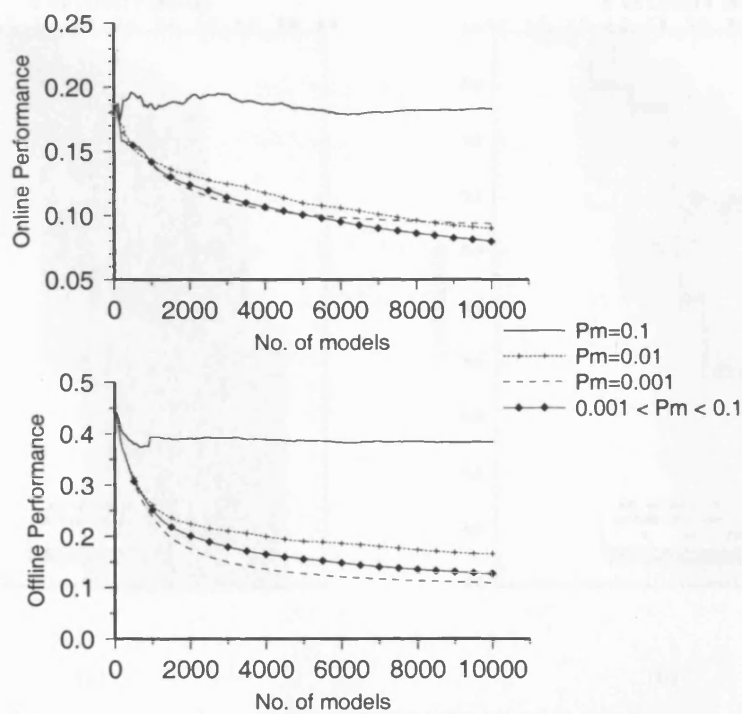


Figure 5.9: On-line and off-line performance for varying mutation probability. Note that whilst $P_m=0.001$ gives best convergence (off-line) the on-line performance indicates that this convergence is premature.

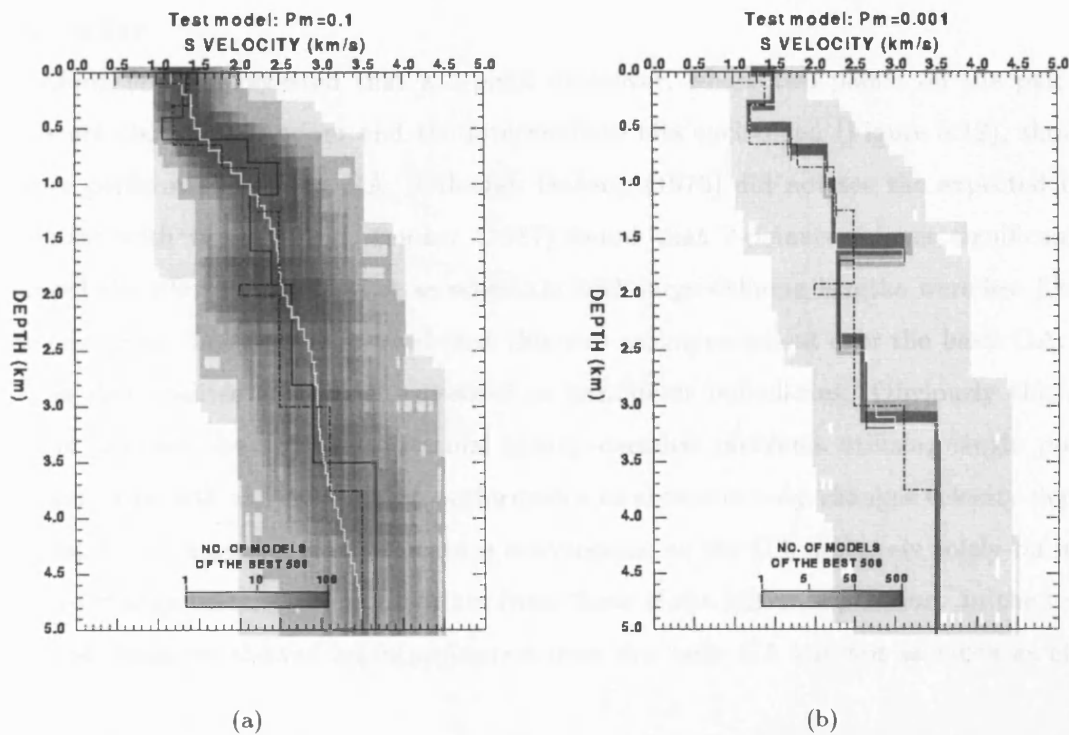


Figure 5.10: Model results from testing of the GA by this author for two values of mutation probability. (a) $P_m=0.1$, (b) $P_m=0.001$. The grey area indicates the model space searched with the dark grey being the best 5% of models. The darkness is logarithmically proportional to the number of models. Dashed line is the true model, white the average of the best 5% and black the best model from the GA (after Shibutani et al, 1996)

were tested. On-line and off-line performance of the GA with these refinements are shown in Figure 5.11.

Elitism ensures that the best fit model from each population will always survive to the next iteration although Lomax and Snieder (1995) suggested that this could produce premature convergence. Tests by this author showed that whilst this was a problem using exponential reproduction, it could be avoided by employing tournament selection. This resulted in both the on-line and off-line performance showing improvement, most markedly on the on-line.

DeJong (1975) suggested that a 2-point crossover, where two points on the pair of strings are chosen at random and the intermediate bits exchanged (Figure 5.12), should enhance performance of the GA. Although DeJong (1975) did not see the expected improvement with this method, Booker (1987) found that 2-point crossover significantly enhanced the efficiency of the GA as schemata with large defining lengths were less likely to be disrupted. Tests again showed that this was an improvement over the basic GA.

It is also possible to restrict crossover to parameter boundaries. Obviously this restriction can only be applied to normal binary encoded problems utilizing single point crossover. This will aid local search performance as crossover only changes velocity-depth relations, but it may result in premature convergence as the GA must rely solely on mutation to change velocity or depth values from those of the initial population. In the tests restricted crossover showed an improvement over the basic GA but not as much as elite selection.

Testing by this author of combinations of these refinements showed performance was always greater than the basic GA but could not improve over the performance of just one refinement alone.

The final parameters chosen for the GA were exponential reproduction, single point crossover with $P_c = 0.8$, exponentially ramped mutation ($0.001 < P_m < 0.1$) and elite selection. The results of this are shown in Figure 5.13.

It should be noted that despite the excellent correlation between the test and modelled dispersion curves the GA fails to model the top 100 m correctly or the thin low velocity layer at 2 km depth. The latter is due to the fact that the dispersion is not sensitive to such a thin layer at that depth. Closer examination of the dispersion curves shows that at

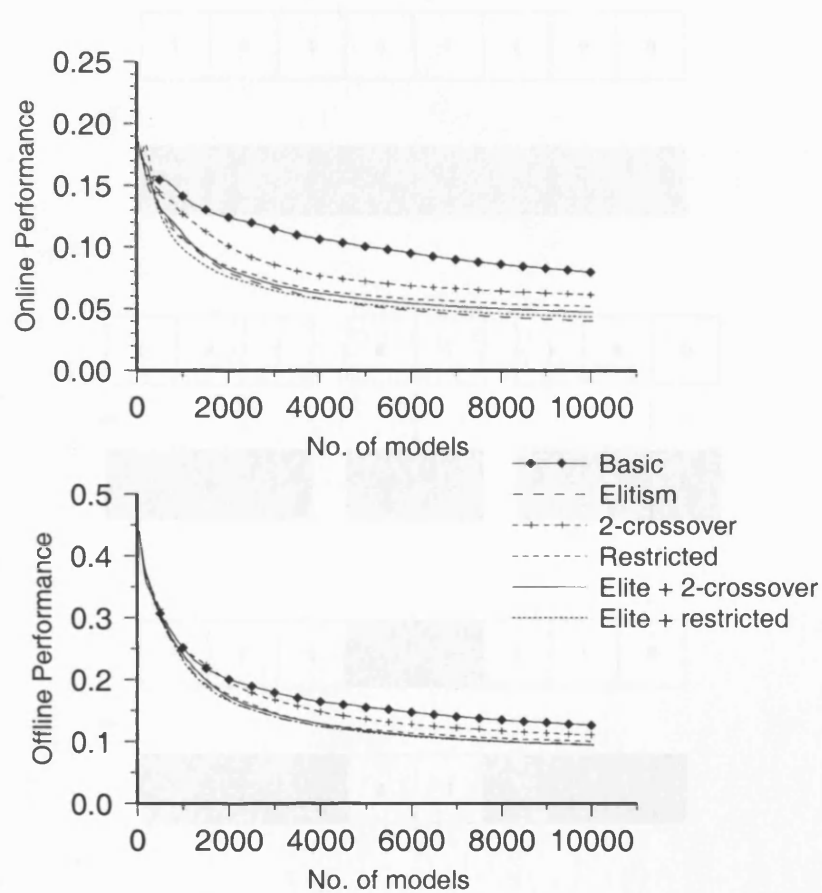


Figure 5.11: Off-line and on-line performance for a variety of refinements to the basic GA

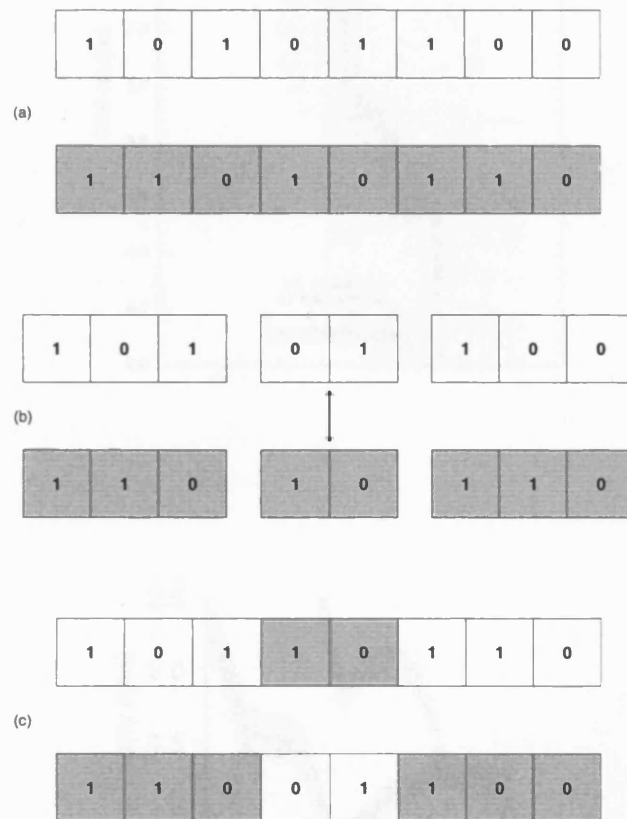
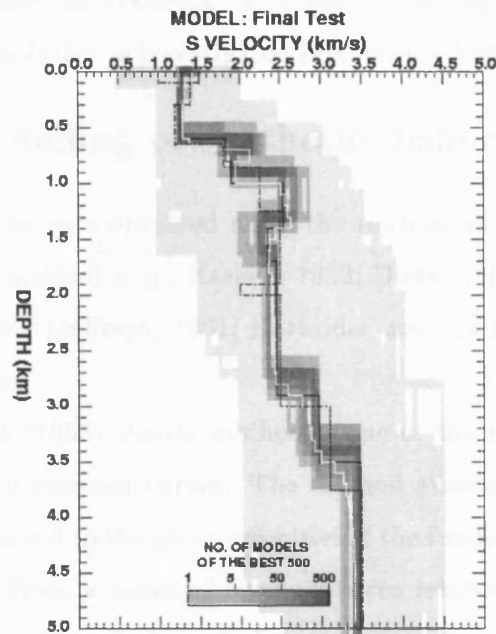
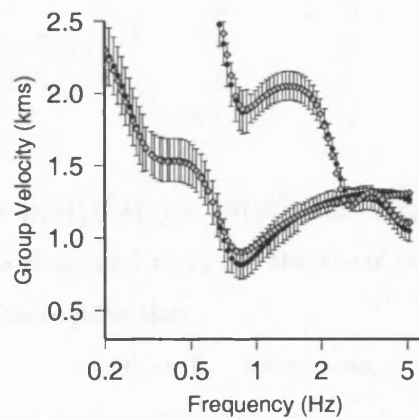


Figure 5.12: An example of two point crossover between two strings. The pair (a) are cut at two randomly chosen points (b) and the segments between each point exchanged to create two new strings(c).



(a)



(b)

Figure 5.13: Test results of the GA chosen for surface wave inversion. (a) Velocity model results, (b) synthetic (circles) and modelled (diamonds) R_g dispersion curves for fundamental and second higher mode (including synthetic errors used for weighting).

the higher frequencies, corresponding to the shallowest structure, the modelled curve does not show the slight decrease the synthetic curve has, explaining the misfit in the velocity of the top 100 m. The resolution is investigated further in Chapter 6.

5.4 Forward modelling of synthetic dispersion curves

Synthetic dispersion curves were obtained using the routines of Herrmann (1987). These use a propagator matrix method (e.g., Haskell, 1953; Dunkin, 1965; Gilbert and Backus, 1966) and energy integrals (Jeffreys, 1961; Harkrider and Anderson, 1966) to calculate phase and group velocities.

The Thomson-Haskell (1953) matrix method is one of the most common methods of calculating surface wave dispersion curves. The method evaluates a dispersion function, the zeroes of which correspond to the phase velocities of the fundamental and higher modes. The function is built up from a series of layer matrices relating motion and stresses on both sides of a boundary. The product of these matrices then relates these motion and stresses at the deepest interface to those at the surface.

The differential equations of the motion-stress vector for Rayleigh waves is given by (Aki and Richards, 1980)

$$\frac{d}{dz} \begin{pmatrix} r_1 \\ r_2 \\ r_3 \\ r_4 \end{pmatrix} = \begin{pmatrix} 0 & k & \mu^{-1}(z) & 0 \\ -k\lambda(z)[\lambda(z) + 2\mu(z)]^{-1} & 0 & 0 & [\lambda(z) + 2\mu(z)]^{-1} \\ k^2\zeta(z) - \omega^2\rho(z) & 0 & 0 & k\lambda(z)[\lambda(z) + 2\mu(z)]^{-1} \\ 0 & -\omega^2\rho(z) & -k & 0 \end{pmatrix} \begin{pmatrix} r_1 \\ r_2 \\ r_3 \\ r_4 \end{pmatrix} \quad (5.13)$$

where $\zeta(z) = 4\mu(z)[\lambda(z) + \mu(z)]/[\lambda(z) + 2\mu(z)]$ and r_1, r_2 are the displacements in the horizontal and vertical directions and r_3, r_4 are the shear and normal stresses.

The boundary conditions require that

$$\begin{aligned} r_1, r_2 &\rightarrow 0, \quad \text{as } z \rightarrow \infty, \\ r_3 = r_4 &= 0 \quad \text{at the free surface.} \end{aligned} \quad (5.14)$$

Nonvanishing solutions of equation 5.13 under these conditions exist only for certain $k = k_n(\omega)$ for a given ω . The phase velocity is given by $\omega/k_n(\omega)$ and the vertical dependence of the mode is given by the solution of equation 5.13.

The problem is of the form

$$\frac{d\mathbf{f}(z)}{dz} = \mathbf{A}(z)\mathbf{f}(z) \quad (5.15)$$

The propagator matrix \mathbf{P} generates the motion stress vector at a depth z by operating on the vector at depth z_o

$$\mathbf{f}(z) = \mathbf{P}(z, z_o) \mathbf{f}(z_o) \quad (5.16)$$

Problems with loss of precision are solved using the method of Dunkin (1965) which utilizes a delta matrix (Pestel and Leckie, 1963) to form the propagator.

The group velocity is then calculated using a variational technique suggested by Jeffreys (1961). By equating the kinetic and strain energies the equation

$$\omega^2 I_1 = k^2 I_2 + k I_3 + I_4 \quad (5.17)$$

is obtained, where

$$\begin{aligned} I_1 &= \int_0^\infty \rho(r_1^2 + r_2^2) dz \\ I_2 &= \int_0^\infty [(\lambda + 2\mu)r_1^2 + \mu r_2^2] dz \\ I_3 &= 2 \int_0^\infty \left(\lambda r_1 \frac{dr_2}{dz} - \mu r_2 \frac{dr_1}{dz} \right) dz \\ I_4 &= \int_0^\infty \left[(\lambda + 2\mu) \left(\frac{dr_2}{dz} \right)^2 + \mu \left(\frac{dr_1}{dz} \right)^2 \right] dz \end{aligned} \quad (5.18)$$

The r_1 and r_2 that satisfy these conditions are the eigenvalues of the Rayleigh waves. Perturbation of k and ω , such that $k = k_o + \delta k$ and $\omega = \omega_o + \delta \omega$, and substituting into equation 5.17 gives, to the first order

$$U = \frac{I_2 + \frac{I_3}{k}}{c I_1} \quad (5.19)$$

Partial derivatives of phase velocity with respect to the model parameters can also be calculated in this way.

Densities required in equation 5.13 were calculated from the shear wave velocities using the velocity to density conversion (Zelt and Smith, 1992)

$$\rho = -0.6997 + 2.2302\alpha - 0.598\alpha^2 + 0.07036\alpha^3 - 0.0028311\alpha^4 \quad (5.20)$$

where

$$\alpha = \frac{\beta}{\sqrt{(1 - 2\nu)/(2 - 2\nu)}} \quad \nu = 0.25 \quad (5.21)$$

5.5 Inversion for Q_β^{-1}

The attenuation of seismic waves can be described in terms of a quality factor, Q . Anderson et al. (1965) developed equations for the quality factor of both Love waves, Q_L , and Rayleigh waves, Q_R , in terms of the Q factor of body waves. For Rayleigh waves this is

$$Q_R^{-1} = \sum_{l=1}^N \left[\frac{\alpha_l}{c} \frac{\partial c}{\partial \alpha_l} \right]_{\rho k \beta} Q_{\alpha l}^{-1} + \sum_{l=1}^N \left[\frac{\beta_l}{c} \frac{\partial c}{\partial \beta_l} \right]_{\rho k \alpha} Q_{\beta l}^{-1} \quad (5.22)$$

where the subscript l is the layer number and the subscripts ρ, k, β and α refer to the quantities, density, wavenumber, shear and compressional wave velocity which are held constant whilst obtaining the partial derivatives.

For an isotropic material and assuming there are no losses due to compression the compressional wave factor, Q_α , can be related to the shear wave factor, Q_β , by (Anderson et al., 1965)

$$Q_\alpha^{-1} = \frac{4}{3} \left(\frac{\beta}{\alpha} \right)^2 Q_\beta^{-1} \quad (5.23)$$

The quality factor (Q) was related to the attenuation coefficient, γ by Mitchell (1975) as

$$\gamma = \frac{\pi}{UTQ} \quad (5.24)$$

where U and T are the group velocity and period. Equation 5.22 can then be re-expressed (Mitchell, 1975) as

$$\gamma = \frac{\pi}{T} \left[\sum_{l=1}^N \left(\frac{\alpha_l}{c^2} \frac{\partial c}{\partial \alpha_l} \right)_{\omega \rho \beta} Q_{\alpha l}^{-1} + \sum_{l=1}^N \left(\frac{\beta_l}{c^2} \frac{\partial c}{\partial \beta_l} \right)_{\omega \rho \alpha} Q_{\beta l}^{-1} \right] \quad (5.25)$$

where subscripts again indicate fixed parameters during calculation of the partial derivatives. It should be noted that the attenuation coefficient, γ , and phase velocity, c , in equation 5.25 relate solely to the Rayleigh wave (similar relations exist for Love waves but for simplicity have not been shown here). Substituting equation 5.23 into equation 5.25 removes the compressional quality factor, Q_α to give

$$\gamma = \frac{\pi}{T} \left[\sum_{l=1}^N \left(\frac{\alpha_l}{c^2} \frac{\partial c}{\partial \alpha_l} \right)_{\omega \rho \beta} \frac{4}{3} \left(\frac{\beta_l}{\alpha_l} \right)^2 Q_{\beta l}^{-1} \right] + \frac{\pi}{T} \left[\sum_{l=1}^N \left(\frac{\beta_l}{c^2} \frac{\partial c}{\partial \beta_l} \right)_{\omega \rho \alpha} Q_{\beta l}^{-1} \right] \quad (5.26)$$

This can then be expressed in vector matrix form as

$$\gamma(\omega) = \mathbf{A} \mathbf{Q}_{\beta l}^{-1} \quad (5.27)$$

where γ is now linear in Q_β .

This can now be inverted using a linear singular value decomposition (SVD) method described in Section 5.6.

5.6 SVD theory

This section is not intended to be a comprehensive review of the theory of SVD; there are numerous texts and papers for those wishing to delve further into the subject (e.g., Backus and Gilbert, 1967; Wiggins, 1972; Jackson, 1972; Twomey, 1977; Lines and Treitel, 1984; Parker, 1994; Meju, 1994b).

Many geophysical processes can be described mathematically in the form of a Fredholm integral (Twomey, 1977)

$$y_i = \int_0^r K_i(r)x(r)dr, \quad i = 1, 2, \dots, n \quad (5.28)$$

where y_i is the observed or measured response of the system (e.g. group velocity) with n the total number of observations, $x(r)$ is the desired physical property or model parameter (e.g. shear-wave velocity) as a function of depth and K_i is the data kernel relating the data to the model parameters.

Equation 5.28 can be approximated by

$$y_i = \sum_{l=1}^m K_{il}x_l \quad (5.29)$$

where it has been assumed that the structure is laterally homogeneous and varies vertically over m finite layers and x is a constant within each layer. This can now be expressed in vector matrix form as

$$\mathbf{y} = \mathbf{G}\mathbf{m} \quad (5.30)$$

where \mathbf{G} is the design matrix with dimension $n \times p$ and p is the number of model parameters.

The solution for model parameters \mathbf{m} , for perfect data, is given by

$$\mathbf{m} = \mathbf{G}^{-1}\mathbf{y} \quad (5.31)$$

However, in the general case, there is a mismatch between the idealized model and the actual earth due to observational errors or noise in the data, such that

$$\mathbf{y} = \mathbf{G}\mathbf{m} + \mathbf{e} \quad (5.32)$$

and the best way to obtain a solution is to minimize the sum of squares of the residuals, e_i . The minimization function is given by

$$q = \mathbf{e}^T \mathbf{e} = \sum_{i=1}^n \left(y_i - \sum_{j=1}^p G_{ij} m_j \right)^2 \quad (5.33)$$

Minimization is achieved by differentiating q with respect to the model parameters, \mathbf{m} and equating the result to zero. The resulting equations are then solved for \mathbf{m} to obtain a least squares solution for the parameter estimates, $\hat{\mathbf{m}}$ given by

$$\hat{\mathbf{m}} = [\mathbf{G}^T \mathbf{G}]^{-1} \mathbf{G}^T \mathbf{y} \quad (5.34)$$

One of the most efficient methods of solving this is by use of singular value decomposition (SVD)(Lawson and Hanson, 1974). This method is popular due to its mathematical robustness and stability and allows determination of model resolution and parameter bounds. Lanzcos (1961) factored an arbitrary matrix into a product of three other matrices

$$\mathbf{G} = \mathbf{U} \mathbf{\Lambda} \mathbf{V}^T \quad (5.35)$$

where for n data and p parameters, the orthogonal matrices $\mathbf{U}_{(n \times p)}$ and $\mathbf{V}_{(p \times p)}$ are the data and parameter space eigenvectors and $\mathbf{\Lambda}$ is a $p \times p$ diagonal matrix containing the non-zero eigenvalues of \mathbf{G} . The diagonal entries, λ_j , are known as the singular values of \mathbf{G} .

Equation 5.34 can be expressed in terms of the SVD of \mathbf{G} as

$$\begin{aligned} \mathbf{G}^T \mathbf{G} &= \mathbf{V} \mathbf{\Lambda} \mathbf{U}^T \cdot \mathbf{U} \mathbf{\Lambda} \mathbf{V}^T \\ &= \mathbf{V} \mathbf{\Lambda}^2 \mathbf{V}^T \end{aligned} \quad (5.36)$$

and the least squares generalized inverse is then

$$\begin{aligned} (\mathbf{G}^T \mathbf{G})^{-1} \mathbf{G}^T &= \mathbf{V} \mathbf{\Lambda}^{-2} \mathbf{V}^T \cdot \mathbf{V} \mathbf{\Lambda} \mathbf{U}^T \\ &= \mathbf{V} \mathbf{\Lambda}^{-1} \mathbf{U}^T \end{aligned} \quad (5.37)$$

so that the unconstrained least squares solution is given by

$$\begin{aligned} \hat{\mathbf{m}} &= (\mathbf{G}^T \mathbf{G})^{-1} \mathbf{G}^T \mathbf{y} \\ &= \mathbf{V} \mathbf{\Lambda}^{-1} \mathbf{U}^T \mathbf{y} \end{aligned} \quad (5.38)$$

If one or more of the singular values λ_j , are small the matrix \mathbf{G} is said to be ill-conditioned and instabilities may result in a magnification of the solution. One method to bypass

potential problems with the small singular values is by using a damped least squares method, or the Marquardt-Levenberg technique (Marquardt, 1963; Levenberg, 1944). This approach damps the absolute values of the parameter estimates by adding a bias β to the eigenvalues. Thus the diagonal matrix Λ^{-1} is replaced by

$$\Lambda_D^{-1} = \frac{\Lambda}{(\Lambda + \beta)^2} \quad (5.39)$$

giving the Marquardt formula

$$\begin{aligned} \mathbf{m}_D &= (\mathbf{G}^T \mathbf{G} + \beta \mathbf{I})^{-1} \mathbf{G}^T \mathbf{y} \\ &= \mathbf{V} \Lambda_D^{-1} \mathbf{U}^T \mathbf{y} \end{aligned} \quad (5.40)$$

As in the GA the data was weighted with the observational errors by multiplying the data vector \mathbf{y} and design matrix \mathbf{G} by the weighting matrix, \mathbf{W} defined in equation 5.10.

5.6.1 Error analysis

The quality of the model can be assessed by examining the parameter resolution matrix (Jackson, 1972). For the unconstrained least squares solution (equation 5.38) this is defined by

$$\begin{aligned} \mathbf{R} &= (\mathbf{G}^T \mathbf{G})^{-1} \mathbf{G} \\ &= [\mathbf{V} \Lambda^{-1} \mathbf{U}^T] [\mathbf{U} \Lambda \mathbf{V}^T] \\ &= \mathbf{V} \mathbf{V}^T = \mathbf{I} \end{aligned} \quad (5.41)$$

For the damped least squares solution given by equation 5.40, \mathbf{R} is given by (e.g., Meju, 1994b)

$$\begin{aligned} \mathbf{R} &= (\mathbf{G}^T \mathbf{G} + \beta \mathbf{I})^{-1} \mathbf{G} \\ &= [\mathbf{V} \Lambda_D^{-2} \mathbf{U}^T] [\mathbf{U} \Lambda^2 \mathbf{V}^T] \\ &= \frac{\mathbf{V} \Lambda^2 \mathbf{V}^T}{\Lambda_D^2} \end{aligned} \quad (5.42)$$

The resolution matrix \mathbf{R} is generally understood to give an indication of how well resolved the final model is with the deviation of \mathbf{R} from the identity matrix being a measure of the resolution (or lack of it). However, Meju (1994b) shows that a perfect resolution is not necessarily indicative of an accurate or reliable model and that \mathbf{R} will always be an identity matrix for unconstrained linear inversion or linear inversion with *a priori* data.

The determination of the parameter standard deviations from the covariance matrix \mathbf{C} provides a simple method of model error estimation. The covariance matrix is a $p \times p$ matrix defined as

$$\mathbf{C} = \sigma^2(\mathbf{G}^T \mathbf{G})^{-1} \quad (5.43)$$

for the undamped case and

$$\mathbf{C} = \sigma^2(\mathbf{G}^T \mathbf{G} + \beta \mathbf{I})^{-1} \mathbf{G}^T \mathbf{G} (\mathbf{G}^T \mathbf{G} + \beta \mathbf{I})^{-1} \quad (5.44)$$

for the damped situation assuming the data are uncorrelated and of equal variance σ^2 .

The off-diagonal elements of \mathbf{C} indicate the correlation between model parameters. Large off-diagonal elements C_{ij} indicate that the i^{th} and j^{th} model parameters are highly correlated. The square root of the diagonal elements are referred to as the standard deviations and give an estimation of the bounds of the model parameters (Meju, 1994a).

5.7 Summary

Through a series of tests a genetic algorithm has been shown to be successful in the optimization of surface wave dispersion for 1-D velocity–depth models. The best parameters for the algorithm operators have been chosen to enhance its performance. This final algorithm has then been applied to the observed dispersion data to produce the shear wave velocity models presented in the subsequent chapter.

Using a linear SVD method, γ curves can be inverted to produce attenuation–depth models which will be presented in the subsequent chapter.

Chapter 6

Velocity Inversion and Modelling Results

Fundamental and higher mode curves obtained using the methods described in Chapter 4 have been inverted using the GA to obtain 1-D shear wave velocity models. Attenuation models have been obtained from a linear inversion of γ values. This elastic and anelastic information has then been used in an attempt to model the waveforms.

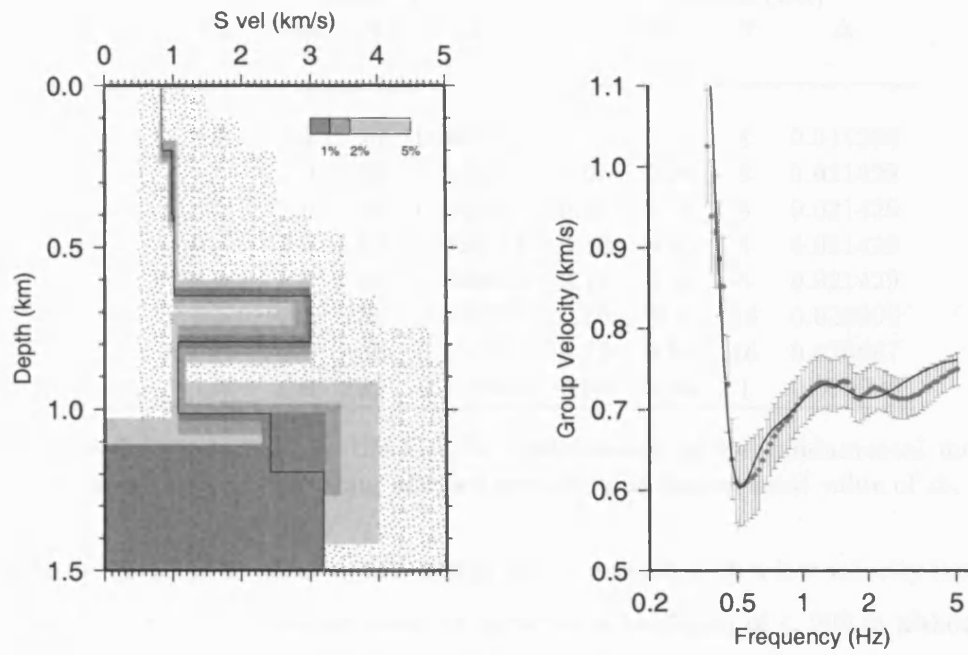
6.1 Inversion using fundamental mode

The model space used for inverting the fundamental mode is shown in Table 6.1. For each model parameter an upper and lower limit and N possible values are specified. Examples of the 1-D velocity models obtained from the fundamental mode optimization of both Group 1 and Group 2 curves are presented in the following sections. All the models are displayed in Appendix F.

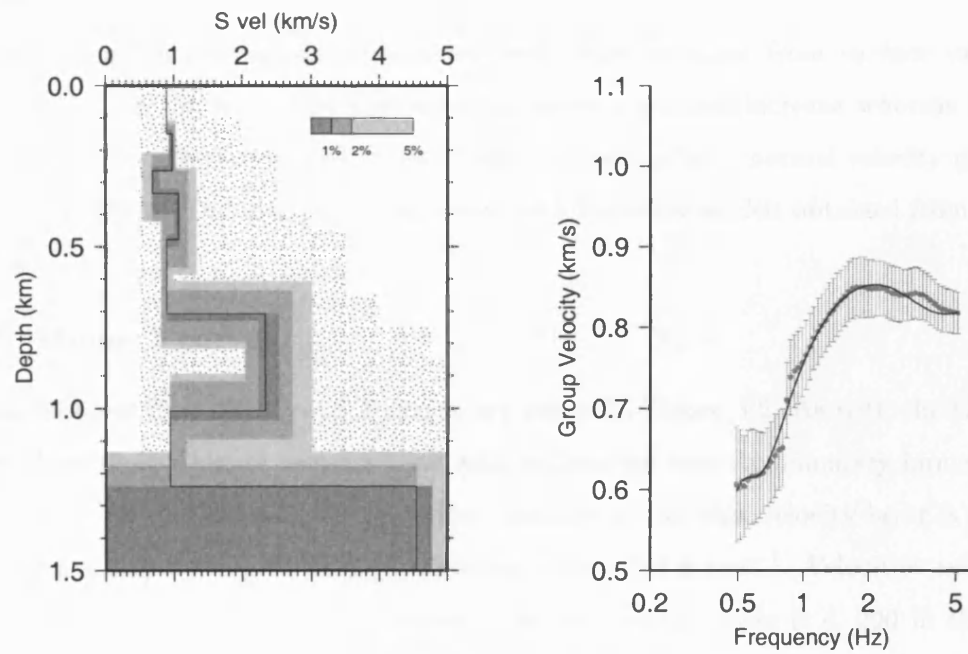
6.1.1 Group 1 curves

Two examples of the models from the Group 1 curves (F-E04 and D-D21) are shown in Figure 6.1. The model space is indicated by the light stippling and the top 5% models are shown in the grey shades with the best model in black. Variation between the top 5% models gives an indication of the resolution (Shibutani et al., 1996) which is discussed further in Section 6.1.3. The velocity models are shown on the left with the observed and modelled dispersion curves on the right.

The dominant feature of these models is an abrupt increase in velocities at c. 0.7 km depth. This boundary shows a velocity change from c. 1 kms^{-1} – c. 2.6–3 kms^{-1} . The high



(a) F-E04



(b) D-D21

Figure 6.1: 1-D shear wave models for Group 1 fundamental dispersion curves. Paths are from Flamboyanes to station E04 and Dzitya to D21. Stippled area is the model space with the top 5% models in grey.

Layer	β (kms ⁻¹)				Thickness (km)			
	Min	Max	N	Δ	Min	Max	N	Δ
1	0.5	1.5	16	0.066667	0.05	0.15	8	0.014286
2	0.5	2.0	32	0.048387	0.05	0.20	8	0.021429
3	0.5	2.0	32	0.048387	0.05	0.20	8	0.021429
4	0.5	2.5	32	0.064516	0.10	0.25	8	0.021429
5	0.5	3.0	32	0.080645	0.10	0.25	8	0.021429
6	0.5	3.5	32	0.096774	0.10	0.4	16	0.020000
7	0.5	4.0	32	0.112903	0.10	0.50	16	0.026667
8	1.5	5.0	32	0.112903	0.00	0.00	1	0.000000

Table 6.1: Model space used in the GA for optimization of the fundamental mode. N possible values within the limits are allowed providing an incremental value of Δ .

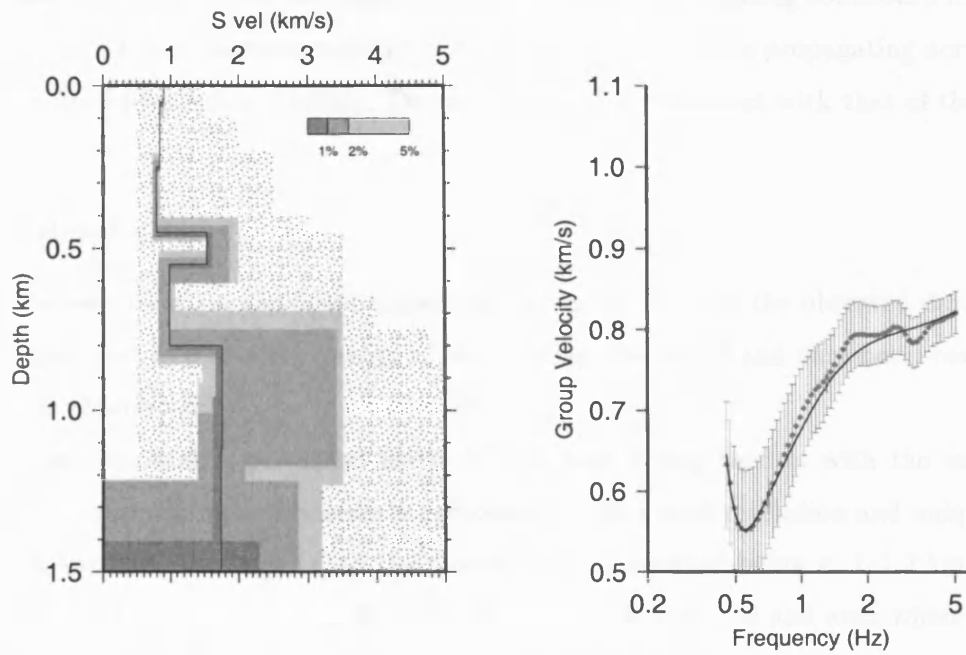
velocity layer has a thickness of c. 150–250 m and is underlain by a low velocity layer with a velocity of c. 1 kms⁻¹. This low velocity layer has a thickness of c. 200 m although the bottom of the layer is poorly constrained and so could be thicker. Similarly the velocity increase in the bottom layer is unconstrained and may be an artifact of the optimization process.

Over the upper 700 m velocities show very little variation from surface values of c. 0.8 kms⁻¹. In model F-E04 the velocities show a gradual increase whereas D-D21 shows a little more variation with 2 lower velocity layers after a normal velocity gradient over the top 300 m. This pattern is consistent with the other models obtained from Group 1 curves.

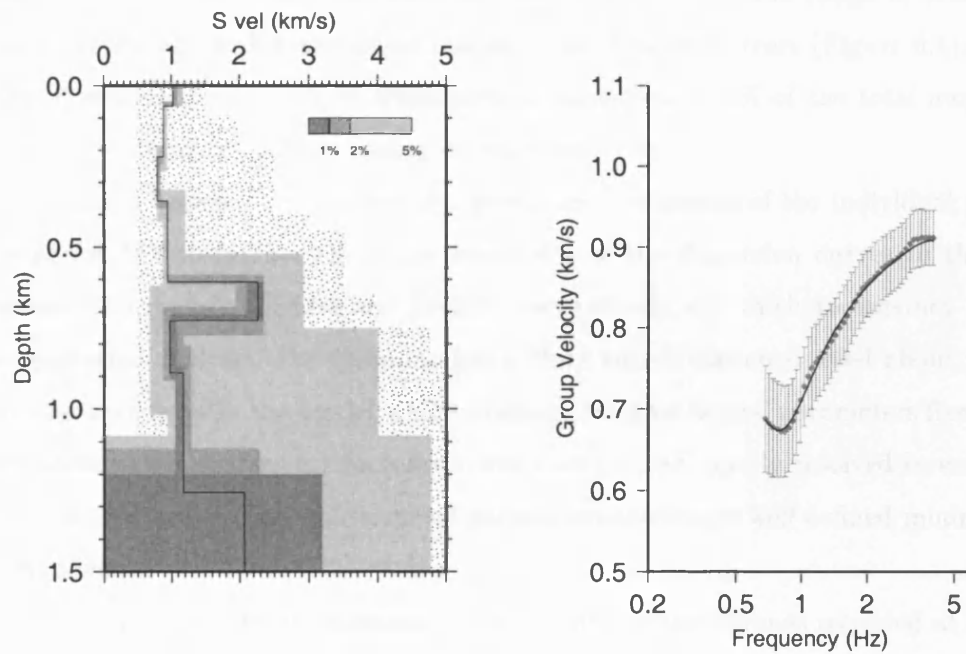
6.1.2 Group 2 curves

Models obtained from the Group 2 curves are shown in Figure 6.2. As with the Group 1 curves, these show a higher velocity zone with an inverted velocity boundary immediately below it at c. 0.5–0.7 km depth. Again the thickness of the high velocity layer is c. 150–250 m with a slightly larger range of velocities from 1.6–3.6 kms⁻¹. Velocities below are similar to those from the Group 1 curves. The low velocity layer is c. 200 m thick for model F-D13, which is consistent with most of the other models, however in model D-E18 it is clearly much thicker (> 500 m) although resolution is poorer in this model.

Surficial shear wave velocities are slightly higher than in the Group 1 curves (0.9–1 kms⁻¹) and show a decrease to c. 0.7 kms⁻¹ over the top 250–400 m.



(a) F-D13



(b) D-E18

Figure 6.2: 1-D shear wave models from Group 2 fundamental dispersion curves. Paths are from Flamboyanes to D13 and Dzitya to E18.

As was suggested by the half space modelling, events propagating southward from the airport show a higher surficial velocity of c. 1.2 kms^{-1} than those propagating northward (Figure 6.3) or from other stations. Deeper structure is consistent with that of the other models.

6.1.3 Resolution

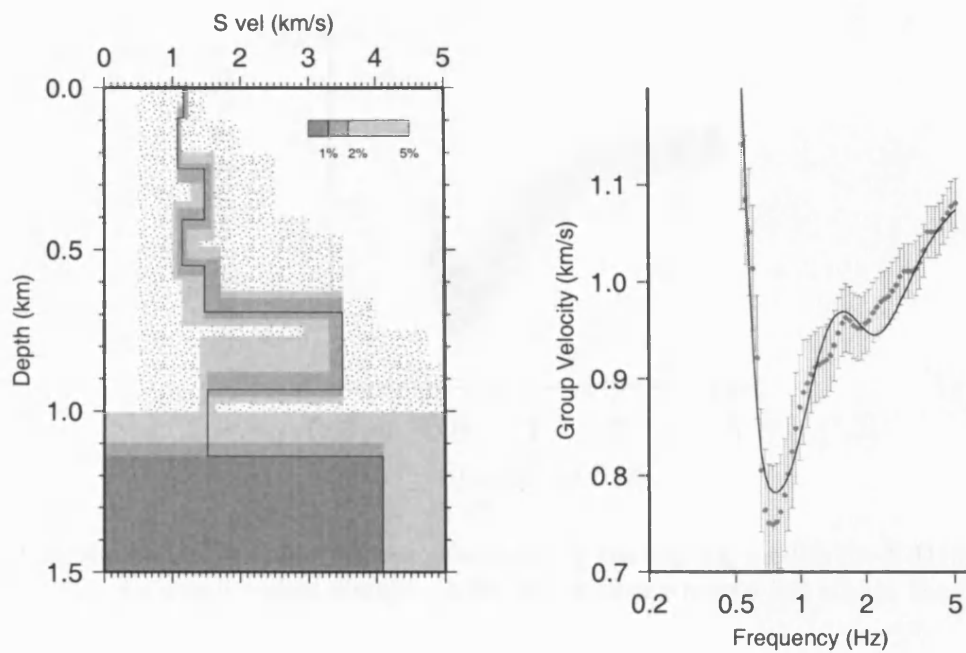
As can be seen from the modelled dispersion curves the fit with the observed data is extremely good but to assess the quality of the solution, the model and parameter resolution need to be considered.

The velocity models presented show the 5% best fitting models with the variation between these providing an immediate indication of the model resolution and uniqueness. From this variation it is clear that the models are not resolved below c. 1–1.2 km depth. In most cases this corresponds to the base of the low velocity zone and even where it does not (e.g., F–D13) resolution of the layer immediately below this remains poor.

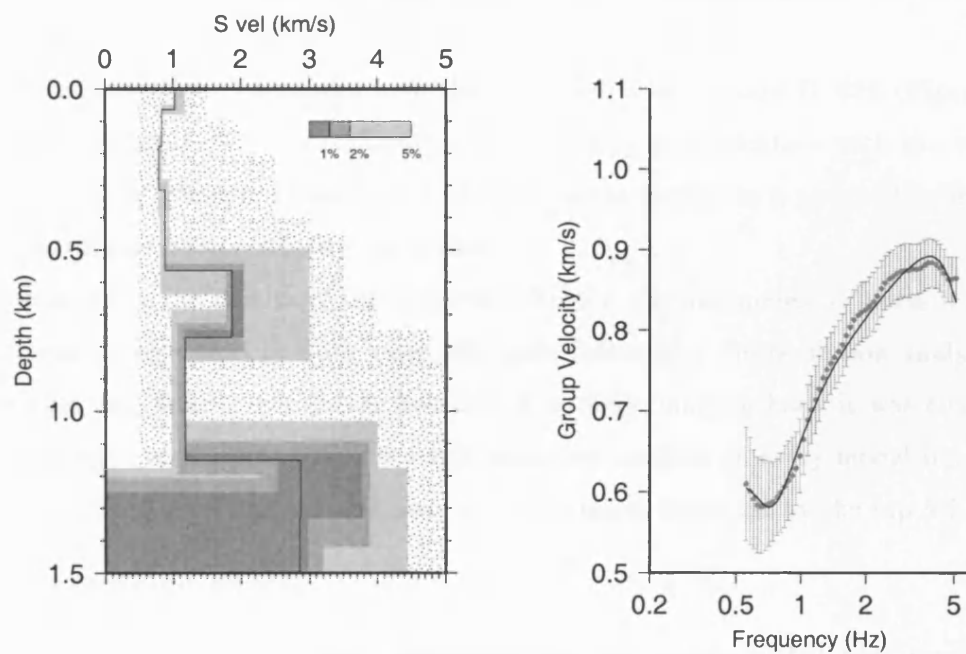
The number of acceptable models was chosen by the number of models whose misfit was less than the misfit from the observed data errors. Thus the range of acceptable dispersion curves falls within the limits placed by the observed errors (Figure 6.4). In the majority of models the number of acceptable solutions was c. 5% of the total number of solutions so for simplicity 5% was taken as standard.

The variation between the models also gives some indication of the individual parameter resolution but to further check the sensitivity of the dispersion curves to the layer parameters, two models (F–E04 and D–E18) were chosen on which to conduct a more precise resolution analysis. For these models a block search was conducted about the parameters for each layer in the model whilst holding the other layers' parameters fixed. The log normalized misfit surface for each layer was then plotted, poorly resolved layers showing flat misfit surfaces whilst well resolved parameters showing a well defined minimum in the misfit surface.

Figure 6.5 shows the layer resolution for an event at Flamboyanes recorded at station E04. As would be expected the upper layers are extremely well constrained in both thickness and velocity with a gradual degradation of resolution with depth. In all cases, bar layer 5, the shear-wave velocity is better resolved than layer thickness. The resolution of the high velocity layer (layer 5) is quite poor but is good enough to be able to confirm



(a) A-E18



(b) A-D13

Figure 6.3: 1-D shear wave models from the Airport to stations (a) E18 and (b) D13. The southward propagating path shows an increased surficial shear wave velocity of 1.2 km s^{-1} compared to 1 km s^{-1} for the northward path. Note the group velocity dispersion curves have a slightly different scale.

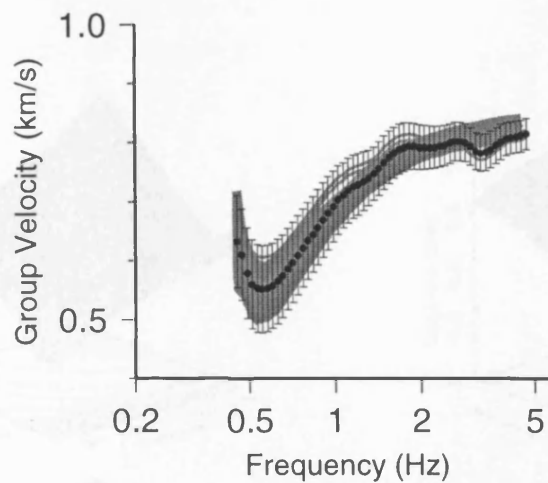


Figure 6.4: Range of dispersion curves generated by the top 5% models for F-D13. With the exception of a small region above c. 4 Hz the modelled curves fall within the limit of the observed errors.

that the velocity is higher than the other layers. Resolution of the velocity of the low velocity zone is extremely good but there is no thickness resolution, partly due to the lack of resolution of the layer below it.

A similar situation is observed with the misfit surfaces of model D-E18 (Figure 6.6). The upper 600 m are well constrained in both velocity and thickness with the velocity resolution slightly greater. From layer 5 downwards the resolution is poor with very little depth control and poorer velocity resolution.

By comparing the results of this analysis with the original models (Figures 6.1a and 6.2b) it can be seen that in both cases the main features of the resolution analysis are reflected by the variance within the best 5% of models. On this basis it was concluded that it was not necessary to conduct a full resolution analysis on every model but it was sufficient to judge resolution on the basis of the variation indicated by the top 5%.

6.1.4 Averaging effects

An important point to remember when examining the models is that they represent a 1-D average of the actual structure sampled over the station-event path. Given that the paths are predominantly along radial lines compared to the expected crater structure and assuming a radial symmetry for the crater then the actual structure is most likely to be

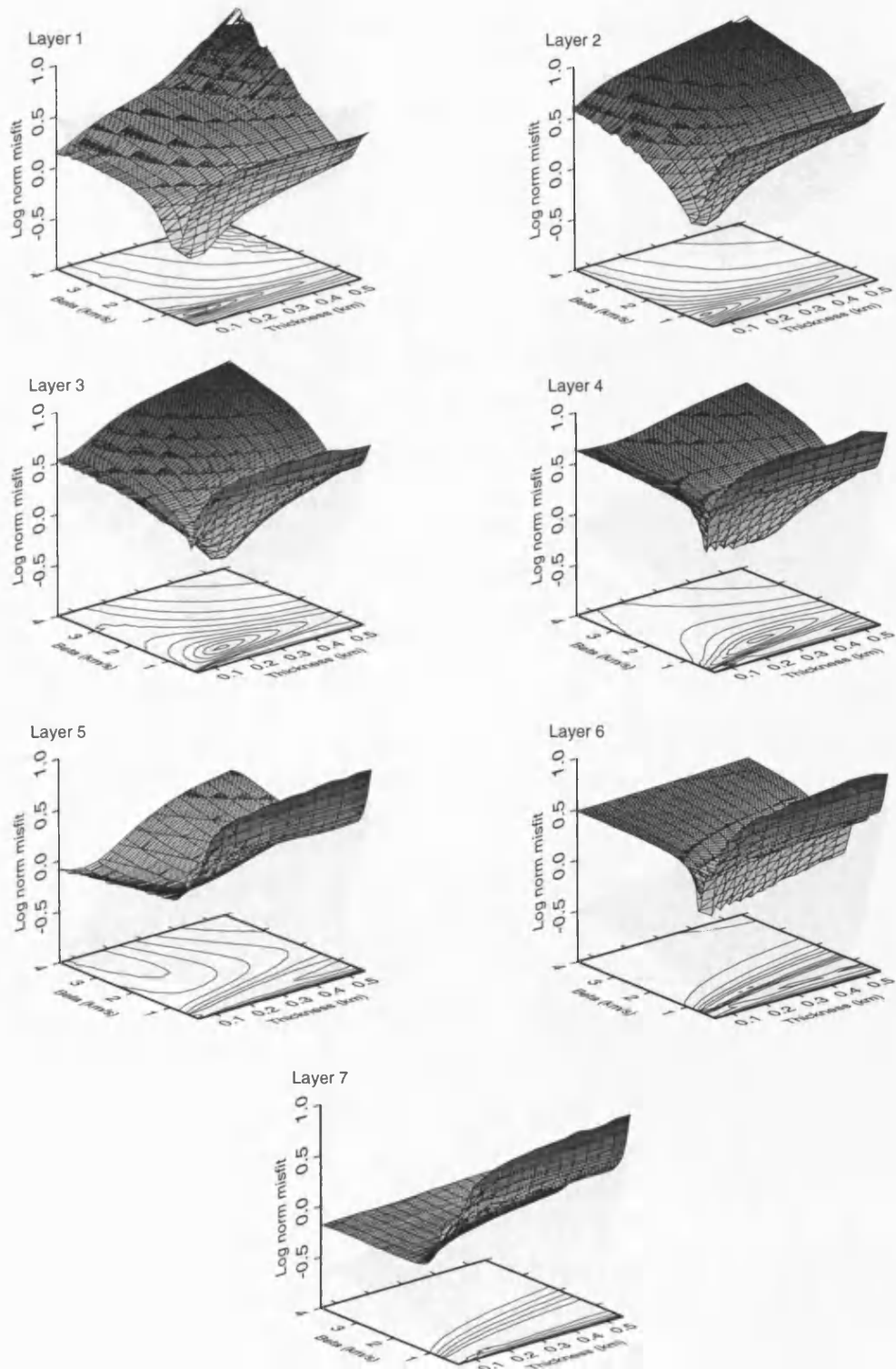


Figure 6.5: Layer misfit surfaces for the fundamental group dispersion curve recorded at E04 and corresponding to model F-E04.

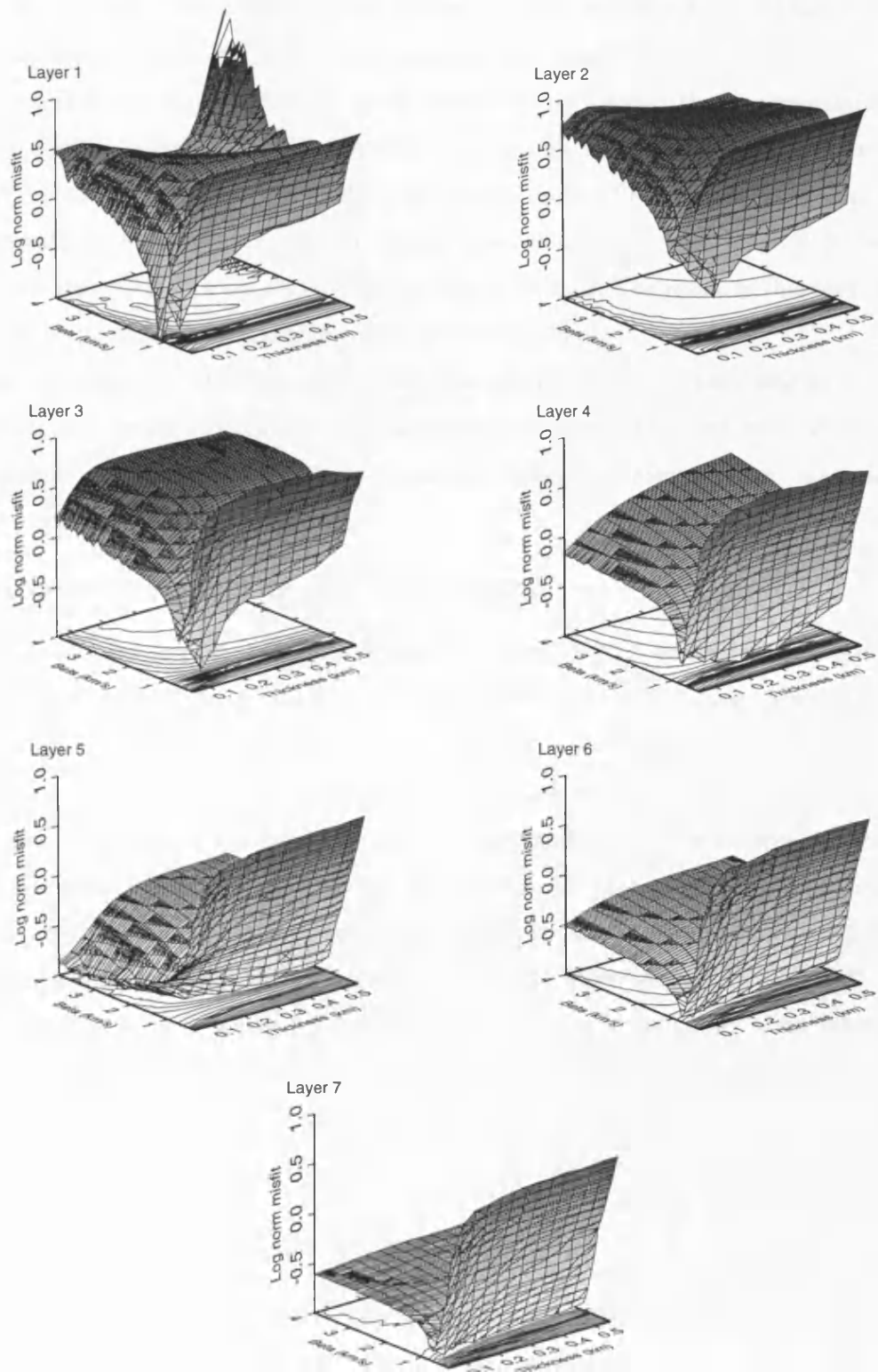


Figure 6.6: Layer misfit surfaces for the fundamental group dispersion curve recorded at E18 and corresponding to model D-E18.

two rather than three dimensional. Where it is relatively homogeneous then the average should approximate the true structure but where there are significant lateral variations then the models show features that do not represent true structure.

An example of this is model D-E18 whose path is across a region that is also sampled by the three paths D-E12, A-E12 and A-E18. The models for these paths are shown in Figure 6.7. It can be seen that the model A-E12 has a quite different structure from the other two with no high velocity layer underlain by a low velocity. Also in A-E18 these high and low velocity layers are slightly deeper than in D-E12. The result of this over the longer path is the apparent thickening of the low velocity layer.

Whilst the sediments are likely to be fairly homogeneous over the path lengths being investigated, any crater structure will probably include large variations over relatively short distances and so this effect will be important during the interpretation, especially for longer path lengths.

6.1.5 Summary of fundamental mode models

The 1-D shear wave velocity models obtained from optimization of fundamental group velocity are well resolved to depths of c. 0.7–1 km. Velocities for the upper few hundred metres are similar to those obtained using the half space approximations from interstation phase curves and confirm the presence of an inverted velocity structure across most of the region. This negative velocity gradient is not modelled across the central area. Forward modelling (Figure 6.8) shows that it is this change that results in the bi-modal characteristic of the fundamental group velocity dispersion curves observed above 2.5 Hz.

A high velocity layer of c. 200 m thickness and of shear wave velocity of $1.6\text{--}3\text{ km s}^{-1}$ is modelled varying between depths 0.5 km and 0.7 km. This is underlain by a low velocity layer whose thickness is poorly resolved but is likely to be around 200 m. Surficial velocities are slightly higher to the south of the array. The lowest surficial velocities are modelled on paths across the central area where the observed dispersion is of Group 1 type.

6.2 Inversion of higher modes

Following the inversion using only the fundamental modes, higher mode dispersion curves, where measured, were included in the inversion to constrain the deeper structure. The

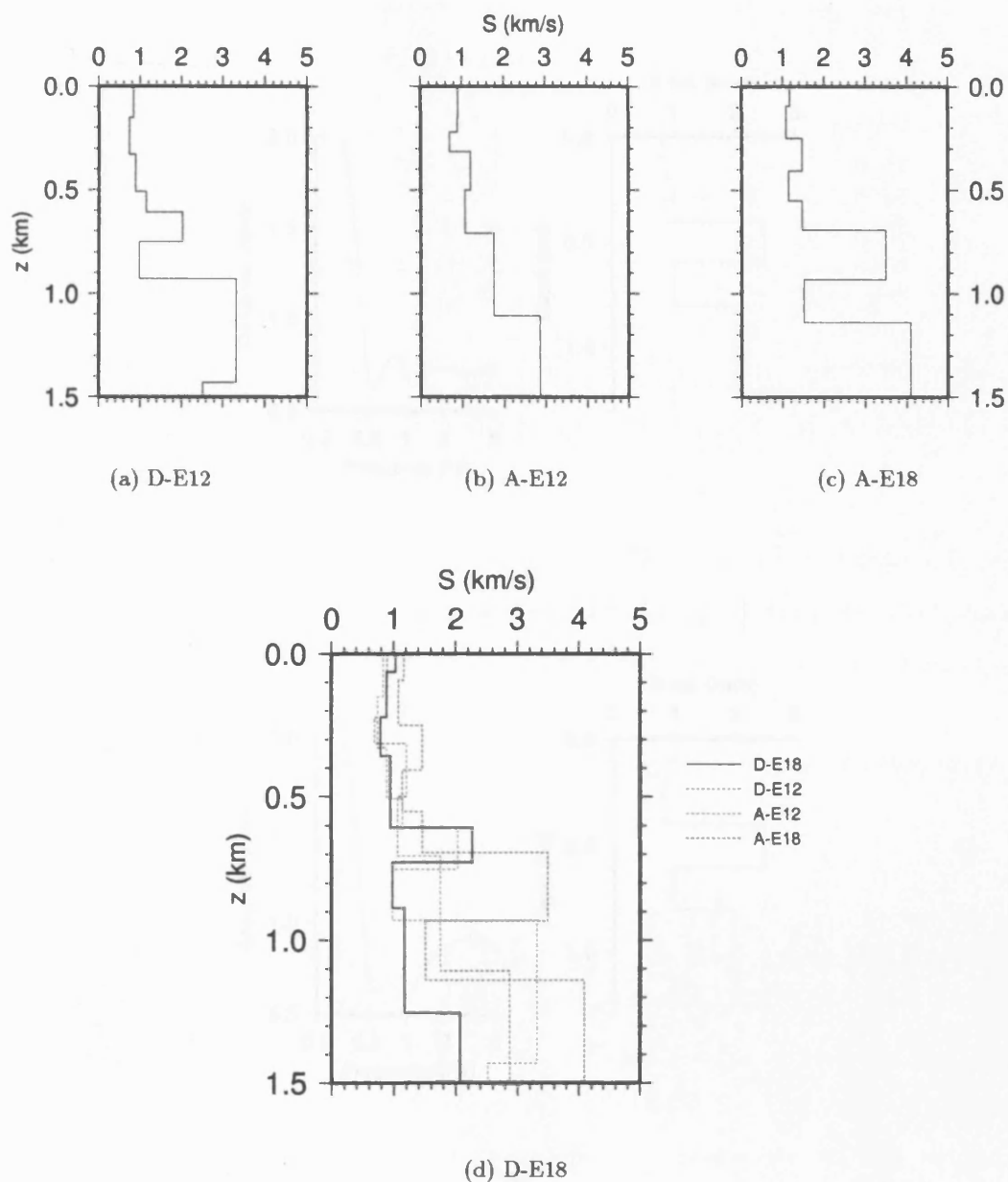
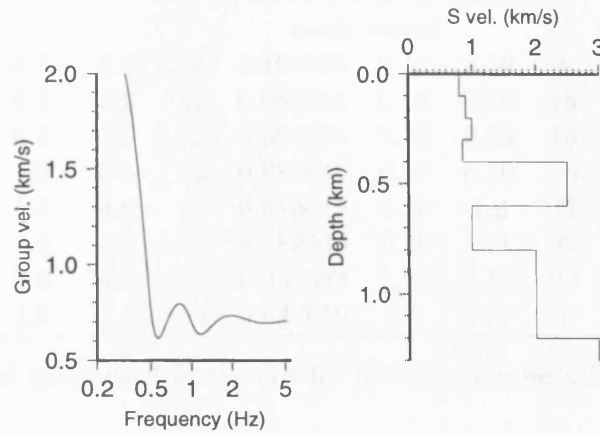
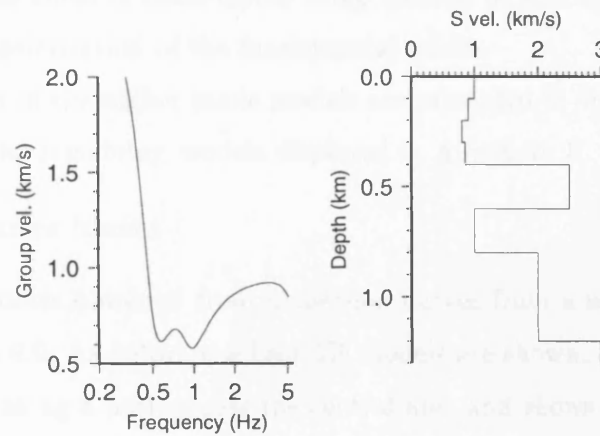


Figure 6.7: Illustration of the averaging effect in the 1-D model caused by lateral variations in velocity structure. The first three models (a–c) together cross approximately the same path as the final model (d). It can now be seen that the apparent thick low velocity zone from 0.6–1.2 km depth in D-E18 is in fact most likely an artifact caused by significant velocity variations along the path.



(a)



(b)

Figure 6.8: Synthetic fundamental mode group dispersion curves for two velocity models. (a) Normal velocity gradient and (b) inverted velocity gradient over the top 300 m. Bar the variation in velocities over the top 300 m the model parameters are identical in both situations.

Layer	β (kms ⁻¹)				Thickness (km)			
	Min	Max	N	Δ	Min	Max	N	Δ
1	<i>Constrained using fundamental mode model</i>							
2								
3	0.5	2.3	16	0.109375	0.10	0.20	8	0.014286
4	0.5	3.0	32	0.080645	0.10	0.50	16	0.026667
5	0.5	3.5	32	0.096774	0.10	0.50	16	0.026667
6	1.0	3.5	32	0.080645	0.10	0.50	16	0.026667
7	1.5	4.0	32	0.080645	0.10	1.0	32	0.060000
8	1.5	4.0	32	0.080645	0.20	1.0	32	0.025806
9	2.0	4.5	64	0.039683	0.20	2.50	32	0.074194
10	2.0	5.0	64	0.047619	0.0	0.0	1	0.000000

Table 6.2: Model space used in the GA for optimization including higher modes.

model space used is shown in Table 6.2

As the higher modes are unlikely to be very sensitive to shallow structure the top two layers were constrained using the models obtained from the fundamental modes with the velocities and thickness of these layers being allowed to vary by $\pm 10\%$ around those obtained from the optimization of the fundamental modes.

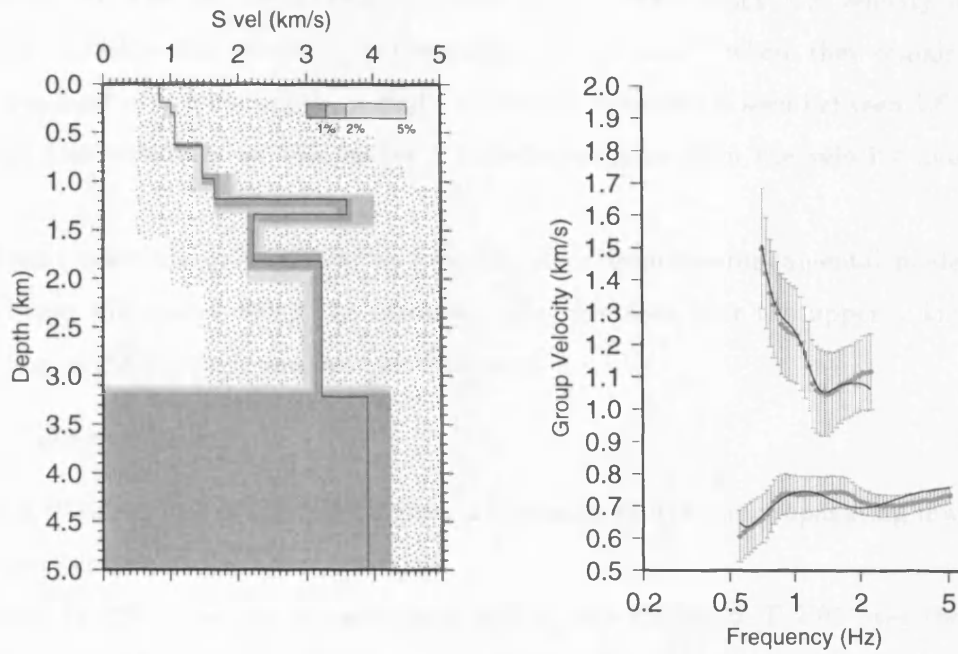
Several examples of the higher mode models are presented in the following section by source region with the remaining models displayed in Appendix F.

6.2.1 Flamboyanes blasts

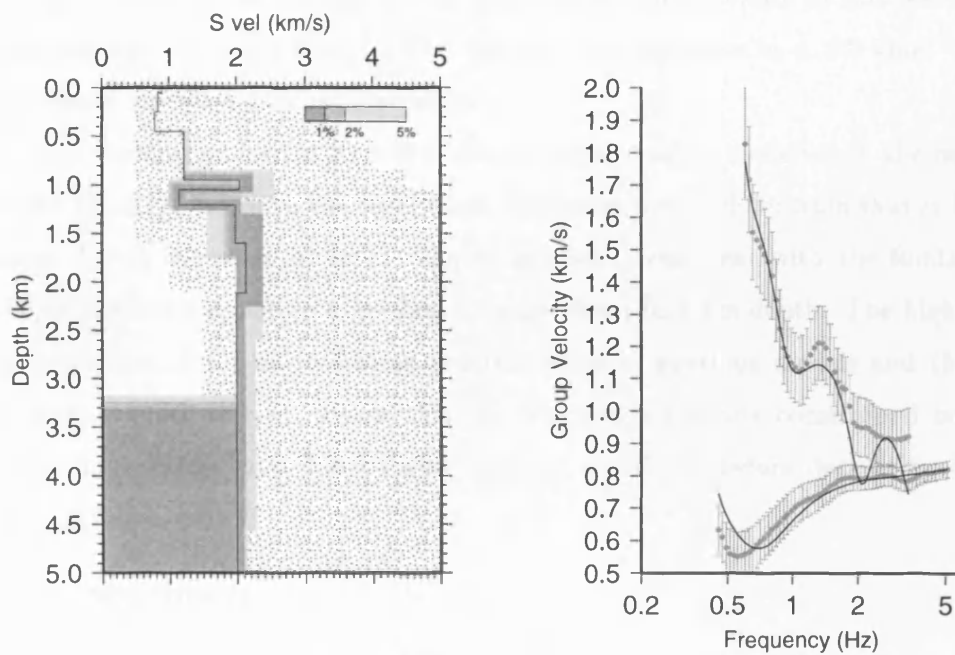
Two examples of models obtained from dispersion curves from a source at Flamboyanes are shown in Figure 6.9. As before the best 5% models are shown.

Model F-F05 is along a path across the central area and shows an increasing velocity structure from 0.8 kms⁻¹ to 1.7 kms⁻¹ over the top 1.2 km. A c. 200m thick high velocity layer of 3.5 kms⁻¹ is then modelled although from the variation of the best models this appears to be poorly constrained. This is underlain by a lower velocity layer of c. 2.1 kms⁻¹ down to c. 1.9 km depth before the velocity increases to c. 3.2 kms⁻¹. A further velocity increase is then modelled at 3 km depth although this shows large variations from the best models and resolution most probably only extends to 2.5–3 km depth.

Model F-D13 has a slightly higher surface velocity of 0.9 kms⁻¹ which decreases over the upper 450 m to 0.75 kms⁻¹. A thin (100 m) high velocity layer of c. 2.1 kms⁻¹



(a) F-F05



(b) F-D13

Figure 6.9: 1-D shear wave velocity models and modelled dispersion curves for joint inversion of fundamental and higher mode data for paths from Flamboyanes to stations F05 and D13.

is observed at 0.95 km depth and underlain by a c. 200m thick low velocity layer of c. 1 kms^{-1} . Below this velocities increase again to c. 2 kms^{-1} where they remain to the resolution limit of c. 3 km depth. A slight increase in velocities is seen between 1.6–2.1 km although the resolution on this makes it indistinguishable from the velocity above and below.

These models are quite similar to those obtained from the fundamental models with the primary differences being the increased structure seen over the upper 1 km and a deepening of the the high and low velocity zones.

6.2.2 Dzitya blasts

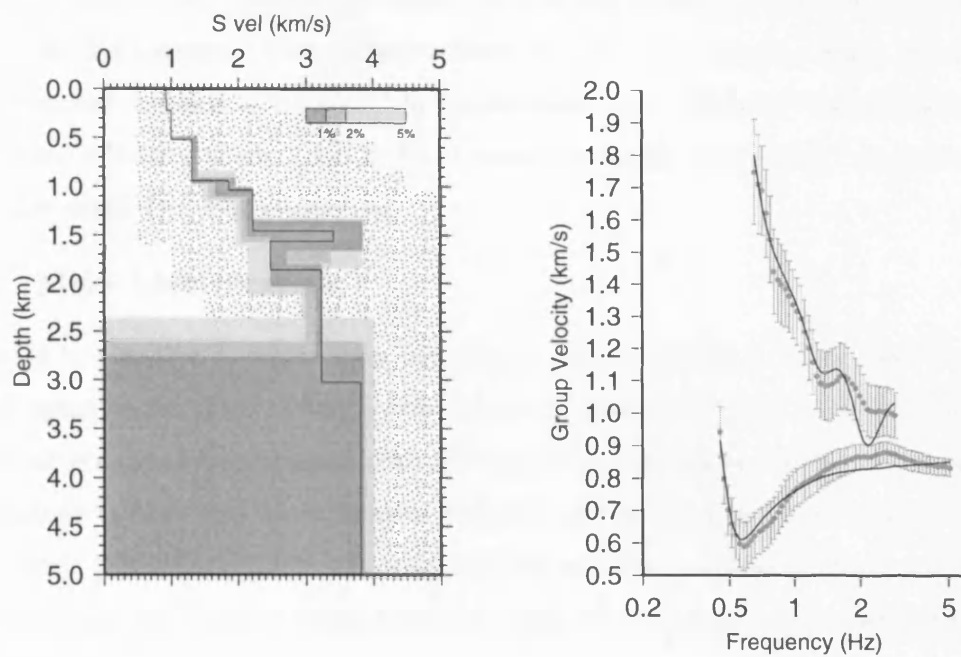
Figure 6.10 shows two of the models from a source at Dzitya one propagating inwards to the crater centre and the other outwards.

Model D-E7b is for the inwards path and is very similar to F-F05 over the crater centre. A slowly increasing velocity structure is modelled over the upper 1.5 km before an abrupt increase in shear wave velocity from 2.2 kms^{-1} to c. 3.4 kms^{-1} . As with F-F05 this thin high velocity layer is quite poorly constrained and underlain by a c. 300 m thick lower velocity zone of c. 2.3 kms^{-1} . The velocity then increases to c. 3.2 kms^{-1} with a second increase modelled but unconstrained.

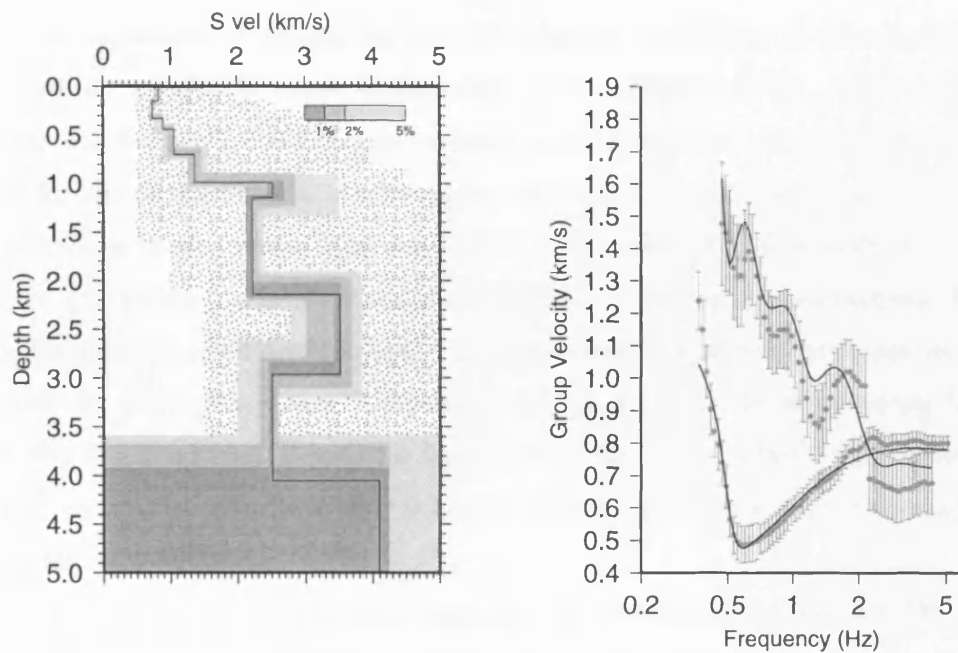
The high velocity underlain by a low velocity zone is again modelled in the outwards path model (D-E12) but both the deeper and shallow structure differ from that in D-E7b. The upper 300 m shows an inverted velocity gradient, consistent with the fundamental mode being of Group 2, before a gradual increase down to 1 km depth. The high to low velocity transition at 1.2 km is not as pronounced as in previous models and the lower velocity zone is much thicker. Below this the velocities are poorly constrained but show an increase in velocity from $2.3\text{--}3.4 \text{ kms}^{-1}$ at 2.2 km depth before decreasing back to 2.5 kms^{-1} at 3 km.

6.2.3 Airport blasts

Similar upper crustal structure is modelled from the airport blasts (Figure 6.11) with an initial inverted velocity gradient followed by a gradual increase. However the high velocity layer is not as distinct as in the previous models. A-E12 has two large velocity increases at 800 m and 1.3 km depth, both of which are underlain by lower velocity zones, although



(a) D-E7b



(b) D-E12

Figure 6.10: 1-D shear wave velocity models and modelled dispersion curves for joint inversion of fundamental and higher mode data for paths from Dzitya to stations E7b and E12.

the first of these is very poorly constrained. A-E18 also shows two large velocity increases at 1 km and 1.4 km depth with a lower velocity zone at 1.6 km depth. Below this at 2 km depth velocities increase to 4.5 kms^{-1} before decreasing to $< 2.8 \text{ kms}^{-1}$ below 3 km depth. In contrast velocities below 2 km in E-12 remain constant at 2.7 kms^{-1} to below 4 km where the model becomes unresolved.

6.2.4 Mode identification

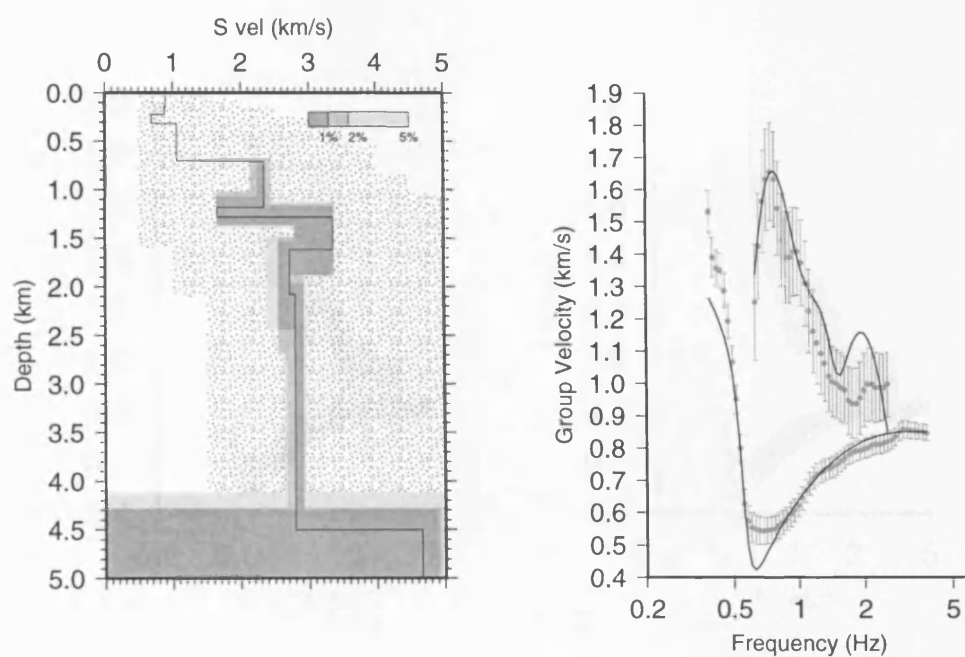
As stated in Chapter 4, where only one higher mode is visible it is believed to be the second higher mode. Mode identification was confirmed during the inversion process by optimizing several of the curves as both the first and second higher mode. In the majority of situations models with an acceptable fit could not be found for the curve as the first higher mode (Figure 6.12). The exceptions to this were for the cases of waves propagating southward from the Airport where inversion using the first higher mode was required to fit the curves.

6.2.5 Resolution

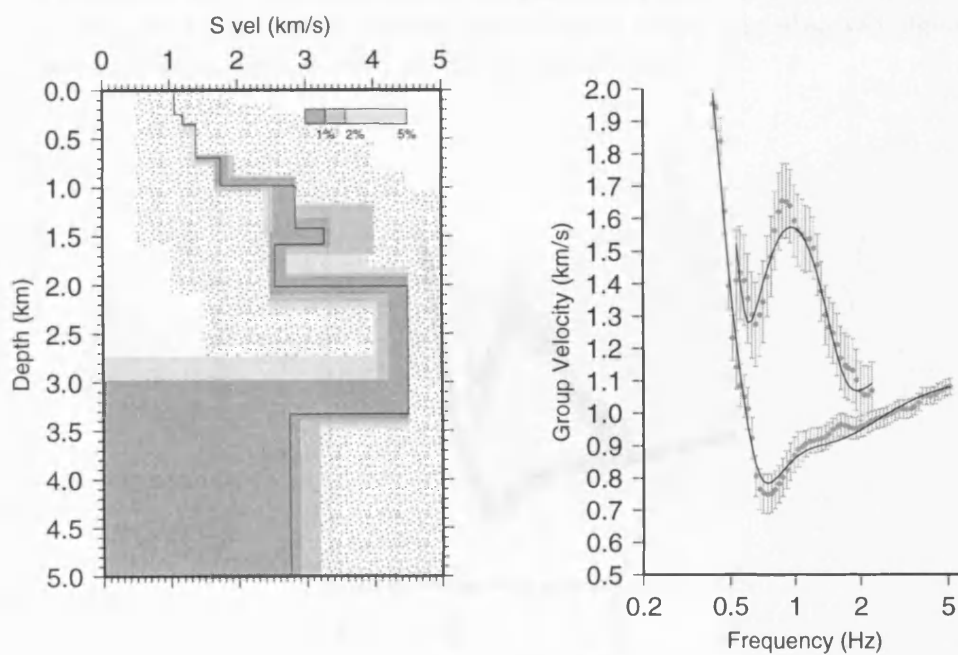
As with the fundamental modes, the top 5% solutions were taken as having the ability to generate an acceptable range of dispersion curves (Figure 6.13). Again parameter resolution was further investigated by varying layer parameters and graphing the misfit surfaces for one of the models. As the upper two layers were partially constrained from the fundamental mode models these layers were not considered in this analysis.

Figure 6.14 shows the misfit surfaces obtained from varying the parameters of model F-F05. Resolution is good down to layer 6 (at 1.2 km depth) with velocity resolution better than thickness resolution. Layer 7 is poorly resolved with a trade off occurring between the velocity and thickness. Below this layer the velocity remains fairly well resolved but thickness resolution is poor and layer 9 has no thickness resolution other than suggesting a lower limit of c. 600 m.

This corresponds to the resolution suggested by the variance in the best 5% models, confirming that, as with the fundamental mode, using the variance within the best 5% models is sufficient to judge model resolution.



(a) A-E12



(b) A-E18

Figure 6.11: 1-D shear wave velocity models and modelled dispersion curves for joint inversion of fundamental and higher mode data for paths from the airport to stations E12 and E18.

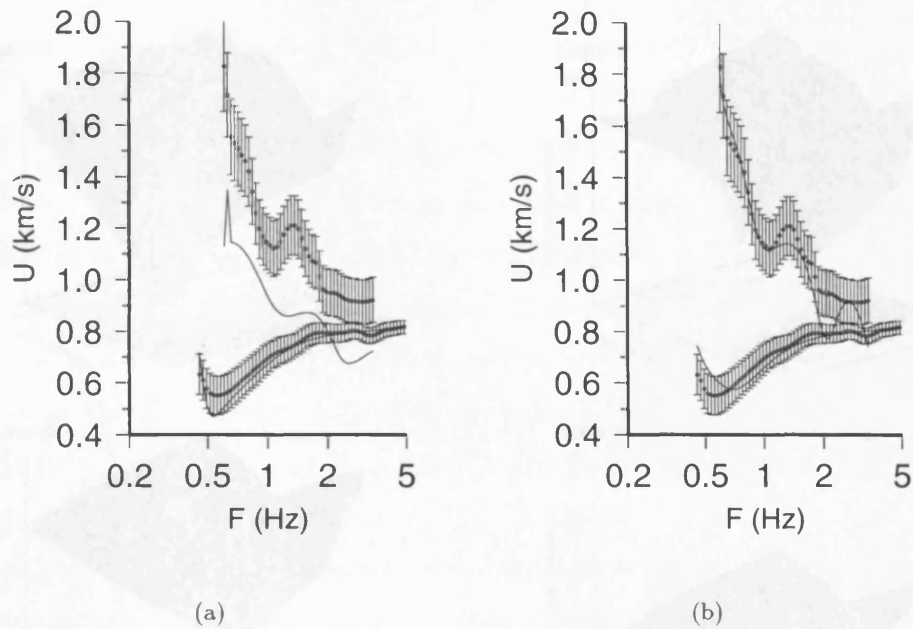


Figure 6.12: Best fitting dispersion curves for path F-D13. (a) Higher mode inverted as 1st higher mode, (b) higher mode inverted as 2nd higher mode. The observed higher mode data can not be adequately modelled as the 1st higher mode.

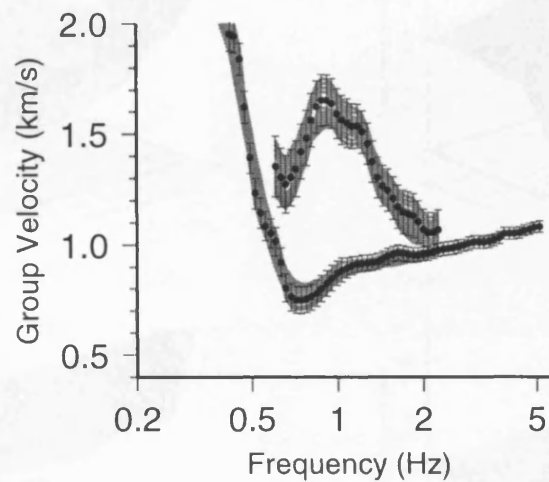


Figure 6.13: Range of dispersion curves generated by the top 5% velocity models for A-E18.

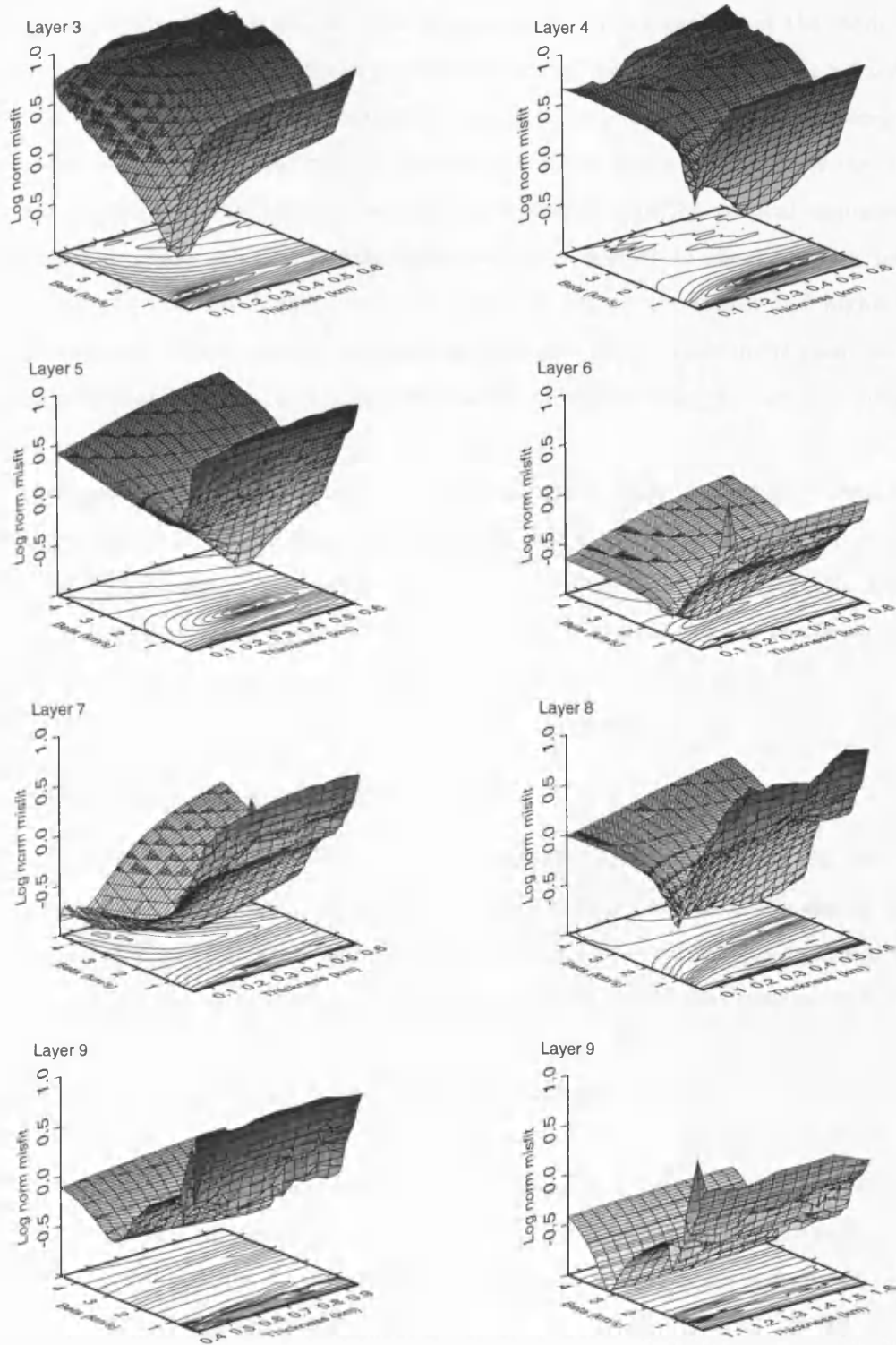


Figure 6.14: Layer misfit surfaces obtained from varying the parameters of model F-F05 using fundamental and second higher mode dispersion curves. Two ranges of layer thicknesses have been investigated for layer 9.

6.2.6 Mode sensitivity

The resolution analysis provides a means of examining the resolution of layer parameters but gives no information on which mode is constraining which regions of the model. As mentioned briefly in Chapter 4 the depth dependence of the various modes at a fixed frequency are different, with certain areas of the model influencing the modes independently. Examination of eigenvalues and velocity partial derivatives shows how sensitive the modes are at varying depths. Figure 6.15 show the depth variation of the vertical displacement eigenvalues and phase velocity partial derivatives with respect to shear velocity for the fundamental and first two higher modes for model F-F05 at the lowest and highest frequencies observed. Where layers independently influence part of each mode then the joint inversion of the fundamental and higher modes will provide a more reliable determination of model parameters.

It can be seen that the top two layers are primarily constrained by the higher frequencies of the fundamental mode justifying the constraint placed on the model space during the higher mode optimization. Between c. 0.2 km and 1.5 km all three modes are influenced by the layer velocities allowing increased resolution over this region than in the fundamental mode inversion. Below this the second higher mode is providing the majority of the model constraint thus increasing the non-uniqueness of the model at these depths.

6.2.7 Summary of higher mode models

Modelling of the higher modes has increased resolution to approximately 2.5 km depth and confirmed the identification of the majority of the higher modes as the second higher mode. The principal differences seen between these models and the fundamental mode models are within the upper kilometre, where more structure has now been modelled, and the variation in depth to the large increase in velocity. These result from the overlap of mode sensitivity within the 1.5 km which has increased the constraints on the model parameters.

A summary of models obtained by collapsing them radially onto Line E is shown in Figure 6.16. The models obtained are very similar to those obtained from the fundamental modes. Practically all the models exhibit a low-high-low velocity transition between 1–1.5 km depth which can easily be identified out to a radial distance of c. 30–40 km from

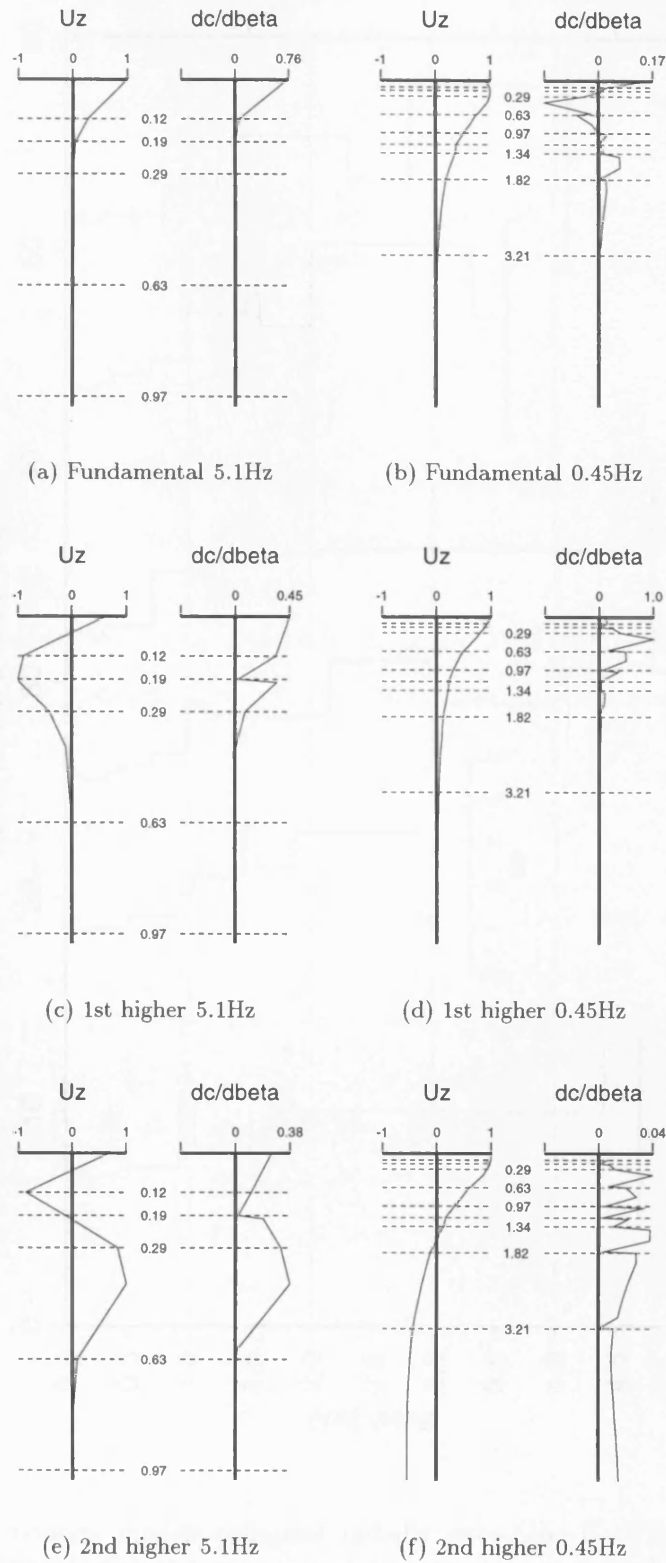


Figure 6.15: Variation of normalized vertical displacement eigenvalues, U_z , and phase velocity partial derivatives, $\partial c/\partial\beta$ with depth for the fundamental and first two higher Rayleigh wave modes at 0.45 and 5.1 Hz. Velocity model is F-F05.

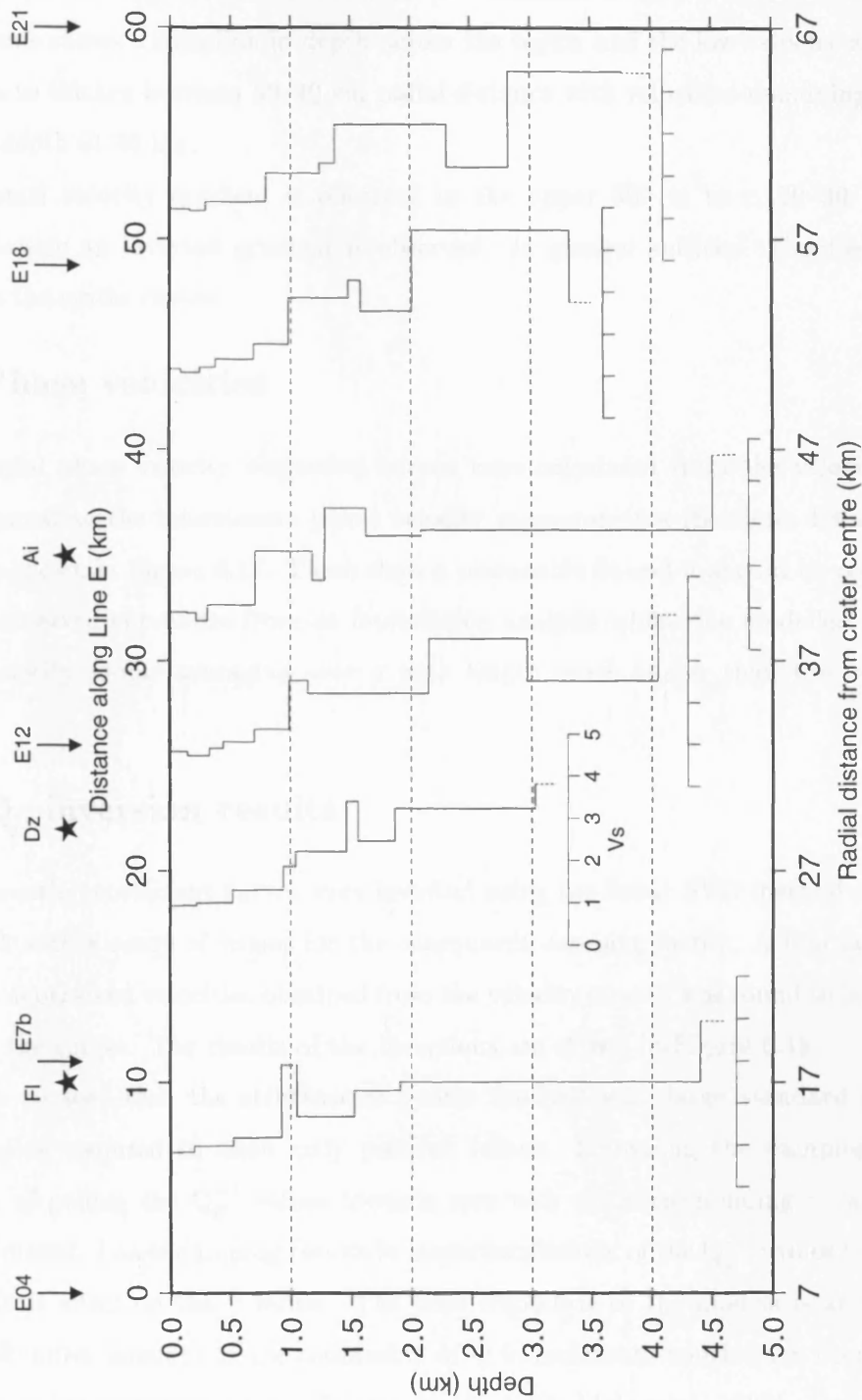


Figure 6.16: 1-D velocity models collapsed radially onto Line E. The velocity scale of all models is $0-5 \text{ km s}^{-1}$ with the midpoint of each station-event path at 0 km s^{-1} . F1 - Flamboyanes, Dz - Dzitya and Ai - airport.

the crater centre. Beyond this distance its identification is more ambiguous. The high velocity zone shows a variation in depth across the region and the low velocity zone below it appears to thicken between 30–40 km radial distance with velocities remaining low until <4.0 km depth at 40 km.

A normal velocity gradient is observed in the upper 300 m to c. 20–30 km radial distance where an inverted gradient is observed. In general surficial velocities decrease inward to the crater centre.

6.3 Phase velocities

Fundamental phase velocity dispersion curves were calculated from the velocity models and compared to the interstation phase velocity measurements (Sections 4.4 and 4.7.2). These are shown in Figure 6.17. These show a reasonable fit and it should be remembered that the observed curves are from an interstation analysis whilst the modelled curves are from a velocity model averaging over a path length much longer than the interstation distance.

6.4 Q_β inversion results

The attenuation coefficient curves were inverted using the linear SVD method outlined in Chapter 5 with a range of values for the Marquardt damping factor. A four layer model using the depths and velocities obtained from the velocity models was found to be sufficient to model the curves. The results of the inversions are shown in Figure 6.18.

It can be seen that the structure is poorly resolved with large standard deviations and damping required to allow only positive values. Increasing the damping also has the effect of pulling the Q_β^{-1} values towards zero with the corresponding γ values being underestimated. Lower damping results in larger oscillations of the Q_β^{-1} values but appears to have little effect on the γ values. The poor resolution of the models is an indication of the difficulties inherent in the estimation of Q in sediments which have been reported by several other researchers (e.g., Sarrate et al., 1993; Malagnini, 1996). Some of these problems arise from assumptions made during the measurement of γ (Chapter 4). A ripple blast from a quarry will not produce a circular radiation pattern but will result in amplitudes being higher in line with the ripple direction. If all the stations used were

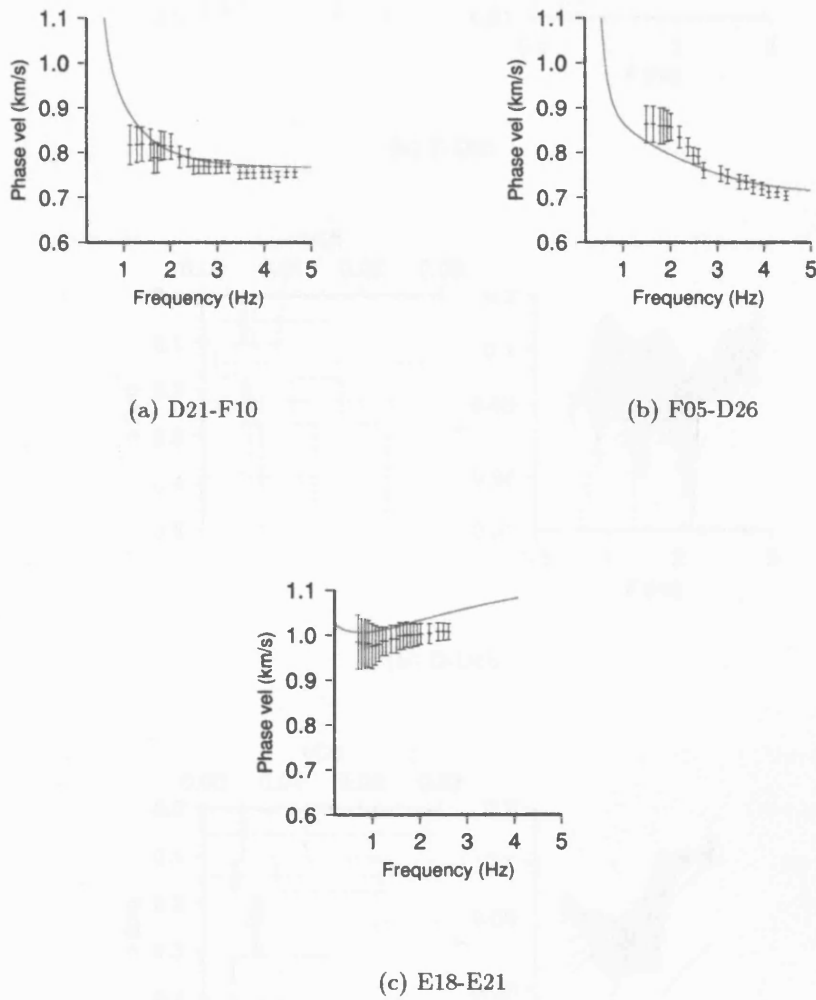
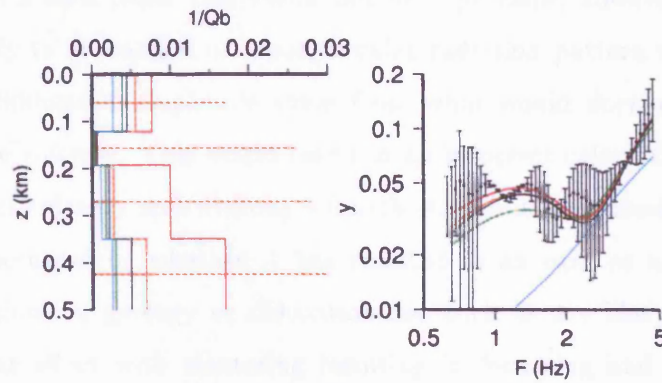
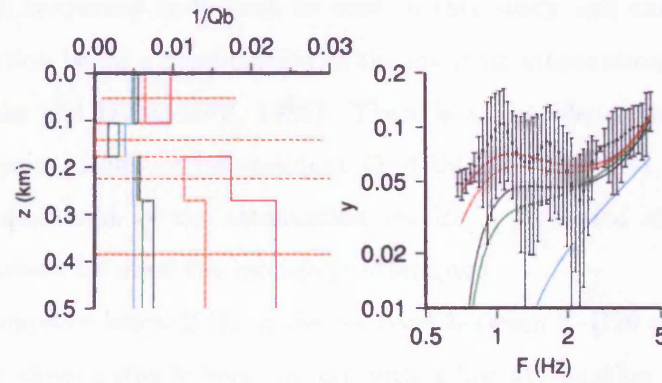


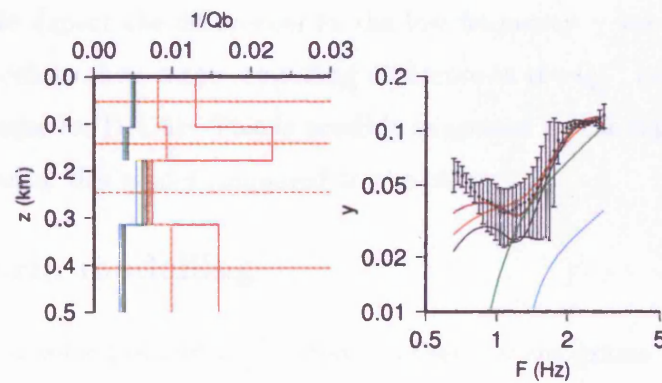
Figure 6.17: Interstation phase observations and modelled phase velocity dispersion curves (red) from 1-D velocity models derived from group velocity dispersion.



(a) F-D26



(b) D-D5b



(c) A-E25

Figure 6.18: $Q\beta^{-1}$ models from SVD inversion of γ values using a range of Marquardt damping values (red = 1, orange = 5, black = 10, green = 25, blue = 50). Horizontal bars are the standard deviations for a damping value of 5. Observed and calculated γ curves are shown on the right.

directly in line with each other this would not be a problem, however, the stations are only approximately in line and thus a non-circular radiation pattern will result in either an increased or diminished amplitude value from what would normally be expected at one or more of the stations. This would result in an incorrect calculation of γ during the linear regression calculation and without a fourth station it is impossible to say whether or not this has occurred or whether it has resulted in an over or under estimation of γ . Lateral variations in geology or discontinuities such as are likely across the crater will have a similar effect with scattering resulting in focussing and defocussing effects (Malagnini et al., 1995). Again without a fourth station it is not possible to state whether or not this is occurring. Elastic scattering from small scale inhomogeneities is especially a problem with high frequency coda such as used in this study and can also result in the measured attenuation being a combination of the intrinsic attenuation and the scattering attenuation (Menke and Dubendorff, 1985). There is also evidence for both a frequency dependent (Malagnini, 1996) or independent Q (Gibbs et al., 1994). For these reasons any quantitative discussion of the attenuation results is precluded although a tentative qualitative comparison between the models is attempted.

Despite the difference below 2 Hz in the γ curves between F-D26 and D-D5b the Q_β^{-1} structure for both these paths is very similar with a low attenuation zone at 100–200 m depth. In contrast the third model (A-E25) has a highly attenuating zone at this depth. This is almost certainly responsible for the high frequency differences observed in the γ curves. One would expect the differences in the low frequency γ values between D-D5b and the other models to show a corresponding difference in the Q_β^{-1} models with a deeper high attenuation zone for D-D5b. This is possibly suggested by the slight decrease of Q_β^{-1} in the bottom layer of this model compared to the others

6.5 Waveform modelling

Using the modelled velocities and Q_β^{-1} values synthetic seismograms were calculated for several of the event-station paths. The Q_β^{-1} models were then refined using forward modelling to improve the fit between the observed and synthetic waveforms.

Various source time functions have been used to generate synthetic seismograms from surface explosions. Mokhtar et al. (1988) found that that a delta function was necessary to

Model 1		Model 2	
Thickness (km)	Q_β	Thickness (km)	Q_β
0.05	60	0.02	2.5
0.10	200	0.05	60
	300		250

Table 6.3: Q_β models used to generate synthetic waveforms in Figures 6.20 and 6.21.

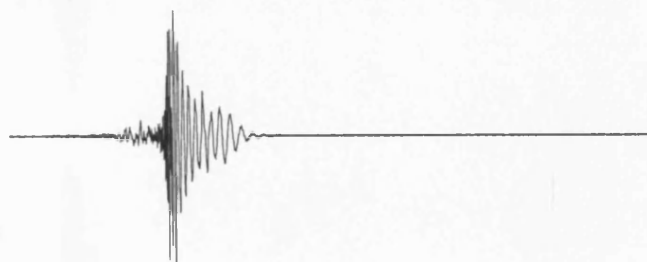
generate sufficient high frequency component but Hutchenson (1994) found a step function sufficient. Using the velocity model F-D13 and no attenuation structure, synthetics were calculated for both an impulse and step source time function (Figure 6.19). The step function appears to be sufficient and so was used. In reality the type of source function will probably vary depending on the orientation of the “ripple” of the blast in relation to the station azimuth.

The final Q_β models are shown in Table 6.5 with the synthetic waveforms in Figures 6.20 and 6.21. It was found that almost all of the waveforms could be modelled with one Q_β structure, the exception being for path A-E21. It can be seen that in most cases the fundamental mode has been well modelled with a reasonable fit obtained for both amplitude and velocity. Given the lack of knowledge of the phase of the source and data, the poor phase match in some of the models is not particularly surprising. Modelling of the higher modes however, has not been as successful. The inability to model the higher mode amplitudes suggests that the Q_β structure needs to be extended deeper. Another problem with the higher modes is the interaction of all higher modes in the actual data whilst the synthetics are modelled with only three higher modes as this was all that were successfully identified from the real data. This may also partially explain why many of the synthetic higher modes have a slight delay in their arrival compared to the observed data. Alternatively, this delay could also indicate differences between the modelled and actual velocities.

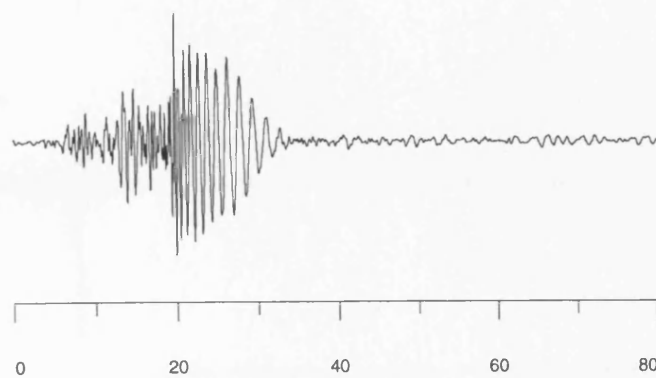
The values obtained from the waveform modelling are similar to those obtained in other studies of sedimentary basins e.g., Hutchenson (1994) obtained surficial Q_β ranging from 20–70 increasing to 200–300 at 400 m depth and Jongmans and Demanet (1993) values of 10–200 over the top few hundred metres.



(a)



(b)



(c)

Figure 6.19: Synthetic seismograms using velocity model F-D13 with no attenuation and two different source time functions. (a) Delta function (b) step function (c) actual waveform.

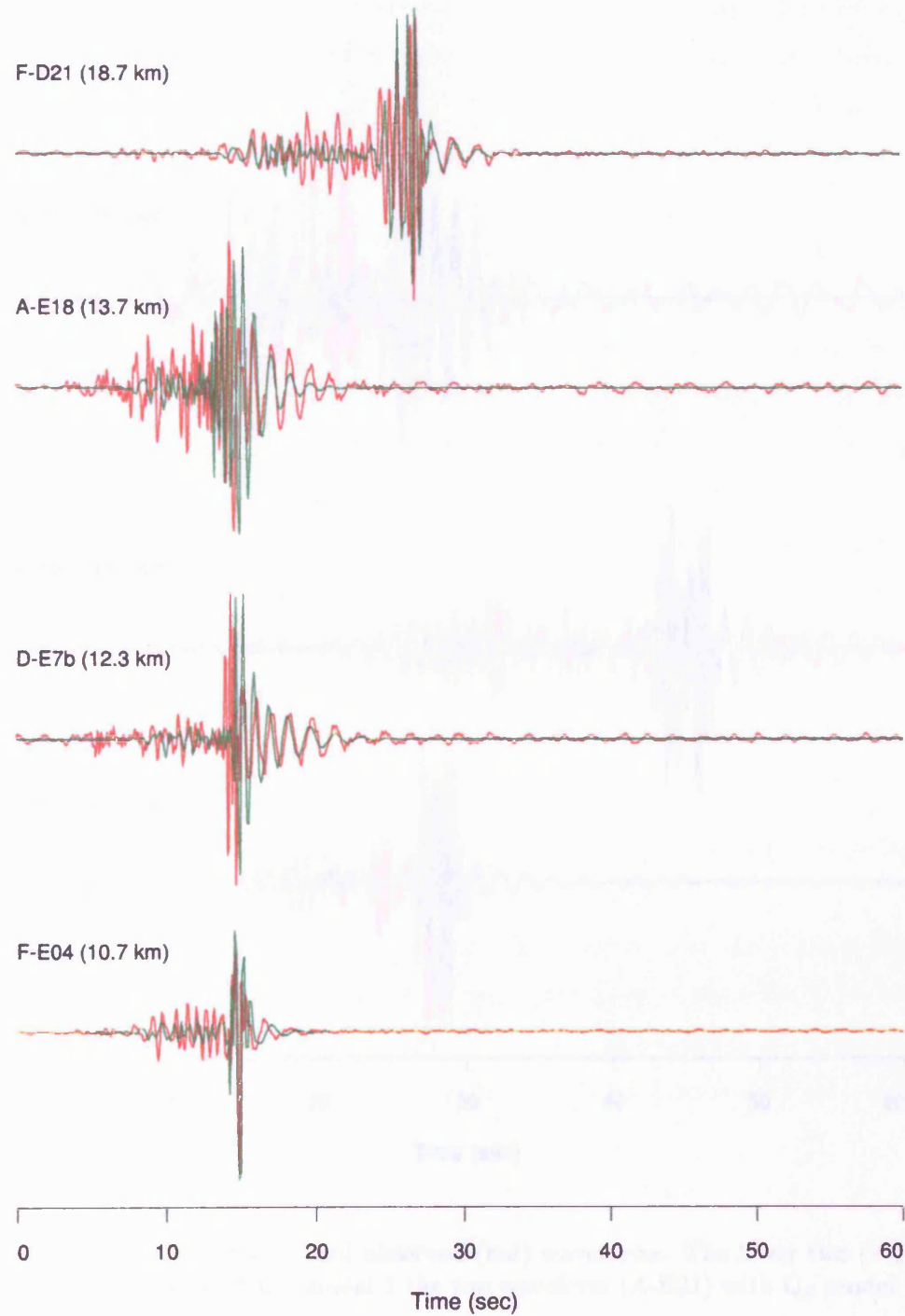


Figure 6.20: Synthetic (green) and observed (red) waveforms using Q_β model 1.

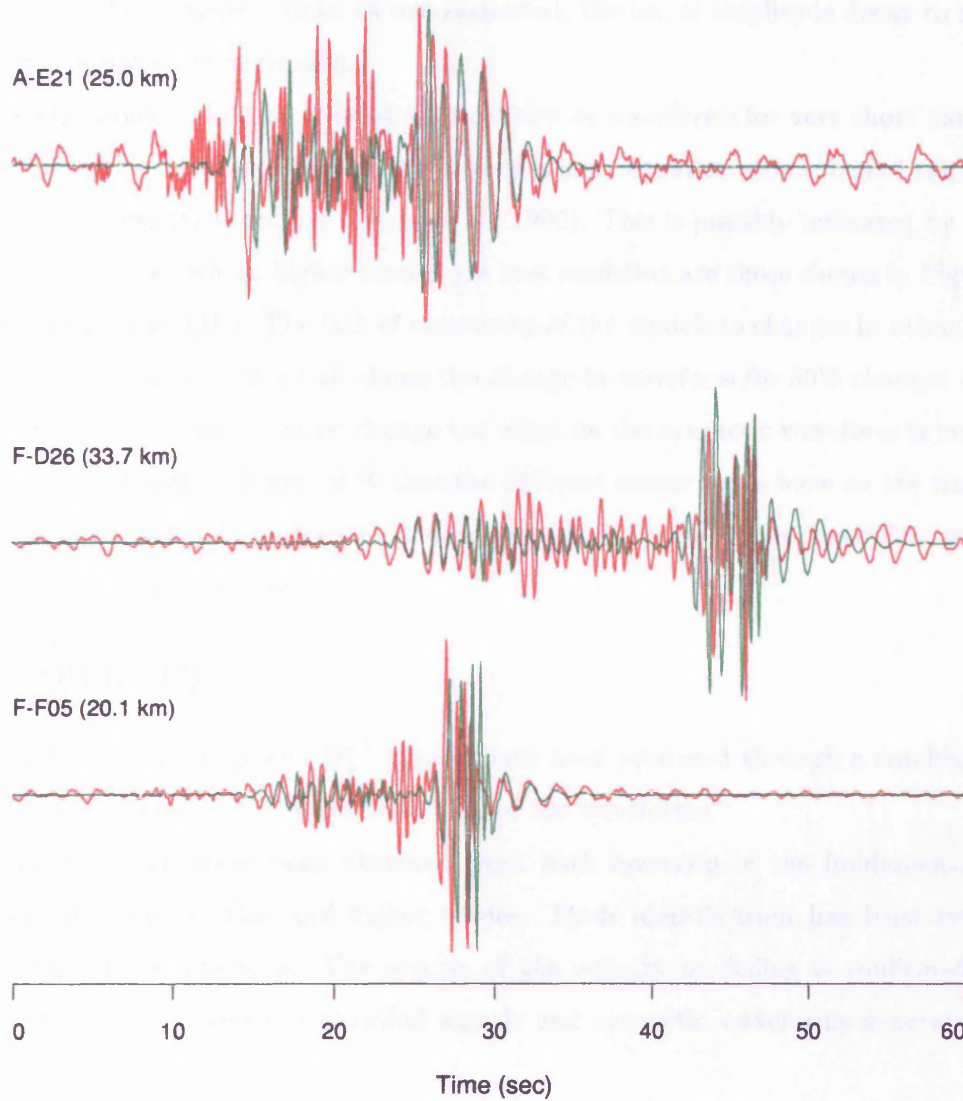


Figure 6.21: Synthetic (green) and observed (red) waveforms. The lower two (F-F05 and F-D26) are modelled with Q_β model 1 the top waveform (A-E21) with Q_β model 2.

Q_β values show an increase with depth with very low values for the top layer required to model A–E21. It is interesting to note that very low values of around 2 were suggested by the inversion of the γ curve for this path although at a much lower depth. However, this model could not generate a synthetic for A–E18 which was included in the calculation of this γ curve. This suggests that, as was suspected, the use of amplitude decay to measure Q_β in this situation is unreliable.

The Q_β values should be treated with caution as waveforms for very short paths have been shown to be relatively insensitive to changes in attenuation structure and the primary control is the velocity structure (Sakia et al., 1990). This is possibly indicated by the fact that the waveforms whose higher modes are best modelled are those shown in Figure 6.21 with longer path lengths. The lack of sensitivity of the models to changes in attenuation is highlighted in Figure 6.22 which shows the change in waveform for 50% changes of Q_β in each layer. Even for such a large change the effect on the synthetic waveform is negligible. Given the effect seen in Figure 6.19 that the different source types have on the waveforms it is quite probable that source effects dominate over attenuation in controlling waveform shape at such short distances.

6.6 Summary

One dimensional velocity and Q_β^{-1} models have been produced through a combination of inversion techniques and forward modelling of the waveforms.

Velocity models have been obtained from both inversion of the fundamental mode and joint inversion of this and higher modes. Mode identification has been verified in the process of the inversion. The success of the velocity modelling is confirmed by the match obtained between the recorded signals and synthetic waveforms generated using these models.

Attempts to model attenuation have proved to be extremely difficult. Inversion for Q_β^{-1} from the measurement of amplitude decay proved to be unreliable with large deviations in the final models. Waveform modelling using a simple trial and error approach produced values of Q_β equivalent to values measured elsewhere. However these results remain ambiguous as the waveforms are very insensitive to attenuation over such short path lengths and may be dominated by source effects. Whilst much more information is

required to confidently discuss the attenuation of the area, a high attenuation zone appears to correlate with the southern most region of the array. Elsewhere one model of decreasing attenuation with depth is sufficient to generate the synthetics.

A discussion of the geological interpretation of these 1-D models and their implication for previous hypotheses of the crater structure is presented in the next chapter.

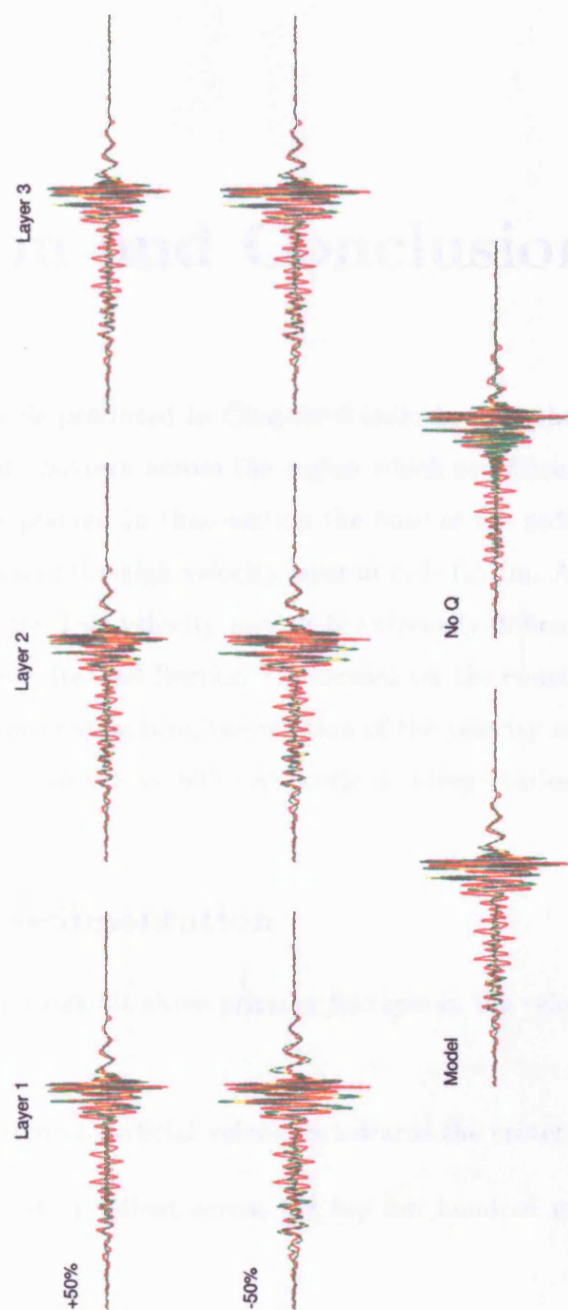


Figure 6.22: Effect on the synthetic waveform (green) of changing the Q_β values for each layer in Model 1 by $\pm 50\%$. Also shown is the synthetic waveform generated with no attenuation model. The observed (red) seismogram is for path F-D21.

Chapter 7

Discussion and Conclusions

The 1-D velocity models produced in Chapter 6 indicate that there are variations in the Cenozoic sedimentation pattern across the region which are discussed in Section 7.1. For reasons that will be explained in that section the base of the sediment sequence is interpreted as being the base of the high velocity layer at c. 1–1.5 km. A direct interpretation of crater structure from the 1-D velocity models is extremely difficult due to the significant lateral inhomogeneities. Instead Section 7.2 focuses on the constraints that the velocity models can place on crater structure, the relation of the velocity models to other geophysical data and comments on the viability of previous interpretations of crater morphology (see Chapter 1).

7.1 Cenozoic sedimentation

The Cenozoic sediments exhibit three primary features in the velocity models which need to be discussed:

- A general reduction of surficial velocities towards the crater centre.
- An inverted velocity gradient across the top few hundred metres outwith a central area.
- A thin high velocity layer at c. 1–1.5 km depth.

The reduction in surficial velocities towards the centre of the crater may be indicative of an infilling of the crater from the rim possibly with the youngest sediments at the centre. Whilst there is no direct evidence for this, it would seem the most likely scenario and

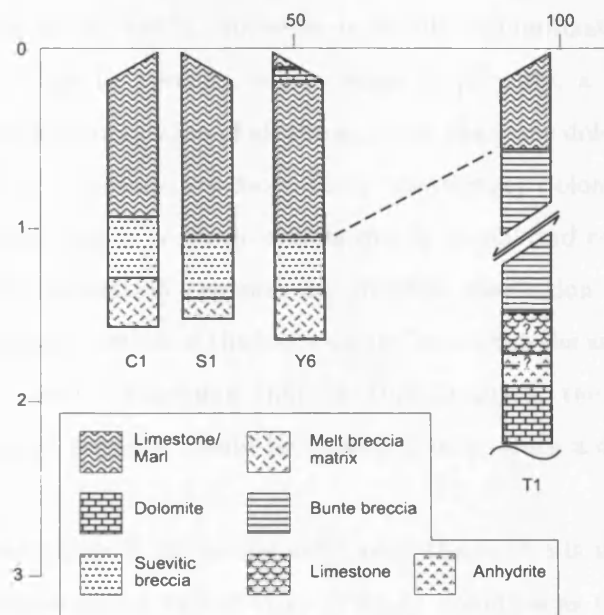


Figure 7.1: Well logs of wells C-1, S-1, Y-6 and T-1 arranged in radial distance from the crater centre (modified from Sharpton et al, 1996).

would agree with the offshore OBS and normal incidence data which show a progression of younger facies into the central area (Christeson et al., 1998).

Onshore, Pope et al. (1996) have advocated older Miocene sediments across the centre surrounded by a moat of younger (Pliocene) sediments on the basis of soil analysis. However it is unclear how they correlate soil differences to age and the observed surficial velocity changes do not match the complex soil patterns.

The observed velocity change may be a result of differences in weathering or surface cementation. The diagenesis of carbonates varies depending on the climate, environment and which mineralogical form of CaCO_3 has been deposited (Tucker and Wright, 1990), thus without samples of surface rocks it is difficult to produce any well defined conclusions.

The inverted velocity gradient that is modelled beyond 30–40 km radius over the top few hundred metres coincides with the existence of a dolomite layer at c. 200 m depth in well Y-6 that is absent in wells S-1 and C-1 over the central area (Figure 7.1) (Ward et al., 1995; Sharpton et al., 1996). The effect of dolomitization on the physical properties of rocks is variable and comparisons with other dolomites is impractical due to their highly individual nature. The replacement of calcium by magnesium should result in an increase in porosity, with a 32% replacement capable of producing a 12% increase

in porosity (Chilingar et al., 1985). However in reality dolomitization is in fact capable of resulting in a decrease in porosity, an increase in porosity, a redistribution of pre-existing pore spaces or a combination of all three within the same dolomitized body (Purser et al., 1994). Porosity increases are more likely in younger dolomites with subsequent porosity decreases occurring in older dolomites due to burial and consequent compaction and generation of dolomitization cements by pressure dissolution (Purser et al., 1994). Given the relatively shallow depth of the low velocity layer then the assumption of increased porosity is probably valid. Assuming that, in this situation, the pores have remained open then this increased porosity would be expected to produce a decrease in shear wave velocities.

The reason for the absence of the dolomite over the centre is unclear. The dolomite is almost certainly replacement rather than primary dolomite as the latter is extremely rare (Tucker and Wright, 1990) and unlikely to produce the c. 100 m thick layer seen in well Y-6 (J. Hudson pers. comm. 1999). Replacement dolomitization requires a source of Mg^{2+} ions and a process to drive the dolomitization fluid through the sediments. Seawater being Mg^{2+} rich is an obvious source and should easily allow $CaCO_3$ to be dolomitized. However kinetic obstacles related to the salinity, ionic ratios and temperatures (Tucker and Wright, 1990) prevent this and most models require some chemical modification to the seawater. The principal dolomitization model categories are evaporative, seepage-reflux, mixing zone, burial and sea water (Figure 7.2). Each involve a different fluid, mode of flow and geological setting but several can occur together and without knowledge of the dolomite geochemistry, petrography, distribution and palaeogeography it is not possible to distinguish which model should be applied (Tucker and Wright, 1990). Similarly to explain the absence of the dolomite over the centre would require knowledge of the method of dolomitization. Changes in ocean chemistry, climate, absence of a driving process or change in sedimentation are all possibilities.

Using the various models it is however possible to comment on several scenarios that could explain the dolomite formation and absence in the central area. A burial mechanism is unlikely as it is debatable that sufficient compaction would occur to overcome the kinetic obstacles to dolomitization and the two most likely models are those of seepage-reflux or a mixing zone.

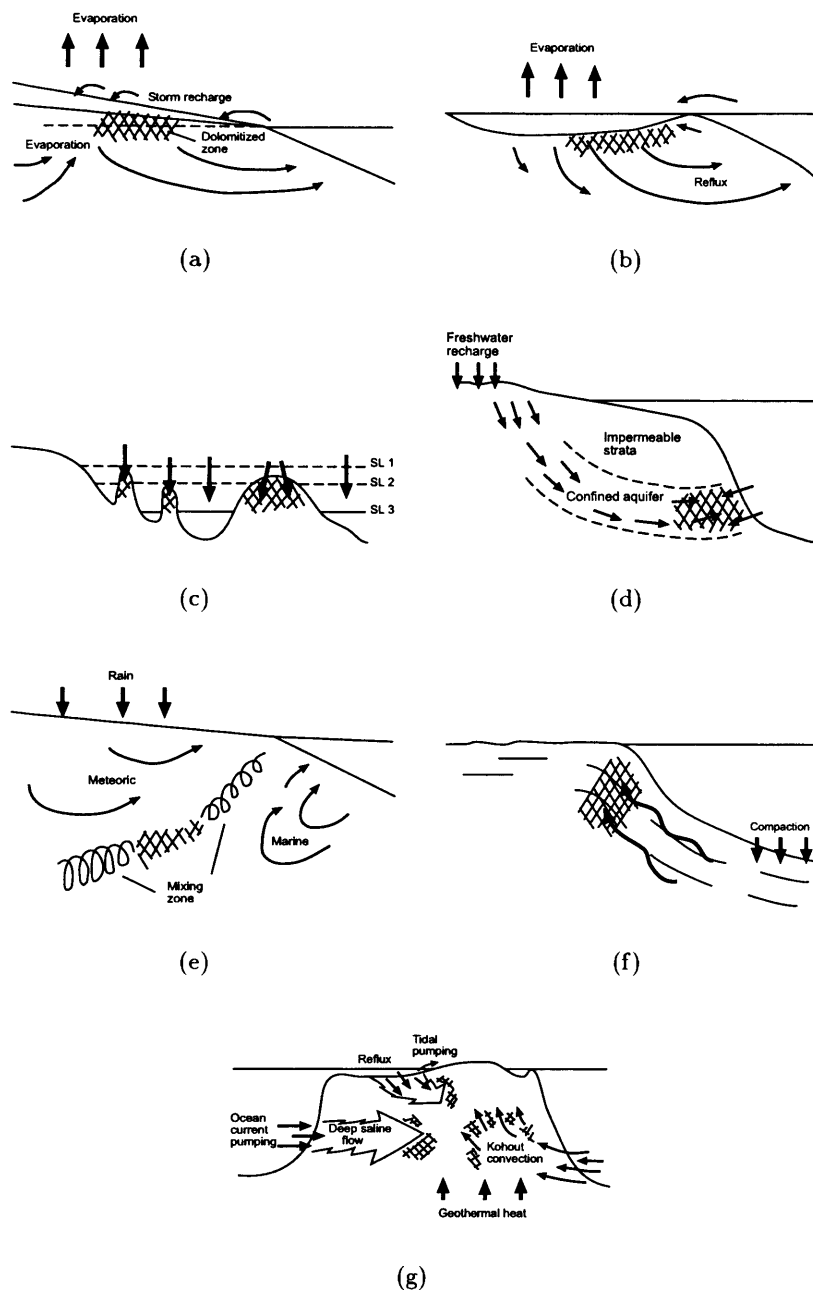


Figure 7.2: Models of dolomitization. (a) Evaporative model where storm recharge followed by evaporation induces an upward flow of Mg rich groundwater. Changes in pore water chemistry occur due to the evaporation and mixing of tidal and fresh water. The seepage-reflux (b) and evaporative drawdown (c) models are an extension of this with dolomitizing fluids generated through evaporation of lagoonal waters and then descending through the underlying carbonates. Mixing zone dolomitization (d & e) is based on the principle that dolomite is precipitated more easily from a dilute solution e.g., a mix of fresh water and sea water. The sea water provides the Mg^{2+} whilst the groundwater pumps the solution through the carbonates. Burial dolomitization (f) relies on the compactional dewatering of basinal mudrocks and the expulsion of Mg rich fluids into adjacent carbonates. Finally seawater dolomitization (g) relies purely on an efficient pumping mechanism to drive seawater that is chemically unchanged through the carbonate (after Tucker and Wright, 1990).

A seepage-reflux mechanism could be possible through the formation of coastal lagoons during a marine regression. Evaporation of the brine rich lagoonal waters and descent of the fluids into the carbonates could result in the dolomitization. The dolomitized zone would migrate seaward as the coastline and lagoonal areas regressed. Being deeper the central area may have remained a shallow marine environment throughout the regression and so dolomitization did not occur in this region. However this model would generally be expected to have an evaporite layer above the dolomite which is not reported in the well logs.

The lack of an evaporite layer would make a mixing zone mechanism more probable and has been widely used to explain dolomitization in the Caribbean and Bahamas region (e.g., Vahrenkamp and Swart, 1994). The absence of dolomites near the centre can be explained using this model and the formation of evaporites above the dolomite is not required. As with the seepage-reflux scenario, dolomitization would have occurred during a regression. Mixing zone dolomites can be expected to develop extensively during major regressions as the seaward migration of the shoreline is accompanied by a progradation of the mixing zone (Tucker and Wright, 1990). Since this model depends on the effective movement of fluids, the dolomites should be located in the landward parts of the carbonate platform. They may also relate to a more porous facies through which groundwater can flow, thus any further porosity increase would certainly explain the low shear wave velocities. Again, a halt in the dolomitization may be explained by a basin remaining over the central area throughout the regression. Alternatively a climate change may have reduced groundwater circulation removing the driving force for the dolomitizing solution.

If the dolomitization did occur during a marine regression then an approximate age for this low velocity layer can be suggested by examination of global sea level changes (Figure 7.3). Two major regressions occurred during the Tertiary, during the Oligocene and the late Miocene/early Pleistocene. The relatively shallow depths of the layer would support a formation during the late Miocene with a much thicker overlying sediment layer expected for formation during the earlier Oligocene regression.

Although the inverted velocity does coincide with the appearance of dolomite this could be coincidental and another effect may be responsible for the reduced velocities. One possibility is that some form of subsurface dissolution and collapse has occurred with

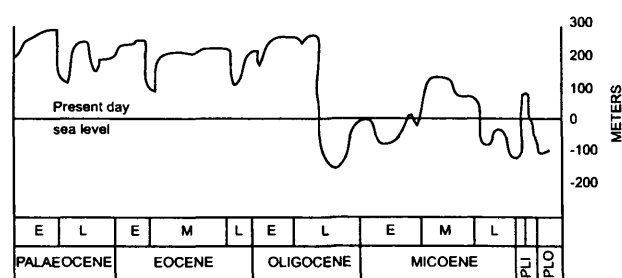


Figure 7.3: Eustatic sea level changes during the Tertiary (modified from Kennett, 1982).

the reduced velocities resulting from the increased fracturing. There are a number cenotes within this area which could be consistent with this. Similarly, the inverted zone that is visible in model A-E21 may be connected to the outer cenote ring and the corresponding increase in fracture density.

The formation of the central cenotes may be a result of slumping around the area of central uplift similar to the formation of the cenote ring at c. 80 km radius. However, this mechanism for formation would be expected to form a ring feature constrained to a narrow radial region analogous to the outer cenote zone. The central cenotes do not appear to show any form of radial symmetry and so this hypothesis may be inadequate to explain their formation. An alternative is that they are related to a change in subsurface geology. It is possible that the increased porosity of a dolomite layer is allowing increased groundwater flow and dissolution in this region. If so then the velocity decrease could be a result of the existence of these cenotes, the mechanism of their formation or a combination of both.

The final sequence of the Tertiary sediments is interpreted as the high velocity layer at c. 1–1.5 km depth. This depth is similar to the depths to the base of the Tertiary obtained from well log data and the layer almost certainly corresponds to a strong reflector that is imaged by the offshore normal incidence data immediately above the breccia sequence. These sediments are Danian in age and their fossil assemblages suggest a deep water (c. 200 m) neritic depositional environment (Sharpton et al., 1996). There is also a possibility that they may be dolomitic (V. Sharpton, pers. comm.). The high velocity associated with these sediments may be limited to an area of < 60 km radius as it does not appear to be present in model A-E21 and also seems to pinch out on the reflection data (see Morgan et al. (1997) Figure 2).

The difference between these earliest Tertiary and later sediments is perhaps not surprising. Some of the primary controls on sedimentation are climate, sea level and oceanic chemistry all of which would have been affected by the impact creating a unique depositional environment. Some portion of this layer may also be related to a backwash of material into the crater immediately after impact and its formation. What the effect of these conditions would have on the physical properties of these sediments is unclear but it could help explain some portion of the observed velocity increase. A velocity increase due to compaction is also to be expected as these are the oldest and deepest sediments although it is unlikely that compaction alone can explain the increase.

Another effect that should be considered is that resulting from the underlying melt sheet and breccia. The 9 km diameter Lake Mien impact is believed to have formed a thermal blanket that drove hydrothermal circulation for several thousand years (Åström, 1998) and a similar effect probably occurred at Chicxulub. Part of the effect of such a blanket may have been a dolomitization of the Danian sediments through an increase in temperature either diminishing the kinetic obstacles to dolomitization, or acting as a driving force for seawater, as in the Kohout convection model (Figure 7.2g). Subsequent compaction or pore cementation closing the pore spaces and reducing the porosity would explain the increased velocities in this dolomite compared to the shallower and younger dolomite layer. This may also explain why the high velocities appear limited to a region of c. 60 km radius which would be the approximate limit of the thermal blanket. However, the increased sulphate levels from the vaporization of the anhydrite layer in the target rock would be expected to hinder dolomitization. It should also be stressed that it is not known whether these sediments are definitely dolomitized. However, it is still possible that a thermal alteration may have affected these sediments as the higher temperatures could have resulted in the formation of aragonite rather than calcite which could explain the higher velocities.

7.2 Crater structure and models

7.2.1 Impact breccia

In almost all the models the high velocity Palaeocene sediments are underlain by a much lower velocity layer. This is interpreted as the impact breccia and the inverted velocity

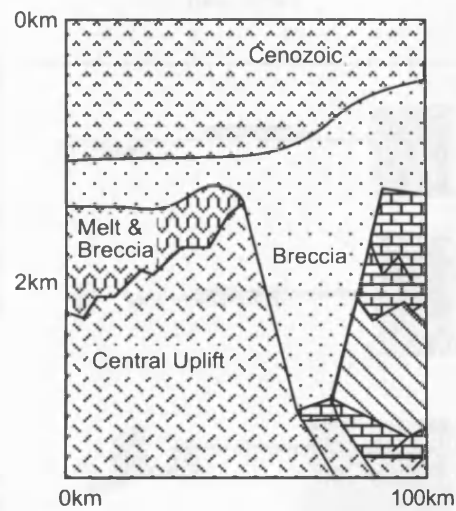
between it and the overlying sediments is in agreement with sonic measurements made on well samples (Urrutia-Fucugauchi et al., 1997). Samples of the suevitic impact breccia provided shear wave velocities of between $1.0\text{--}1.8\text{ km s}^{-1}$ which compare well with those obtained in the 1-D velocity models. The suevitic breccia layer varies between 1.1–1.6 km depth and 100–600 m in thickness. This variation is also identified from normal incidence reflection data and probably represents topography of the crater floor which can be explained in terms of the crater morphology e.g., the peak ring.

7.2.2 Central uplift

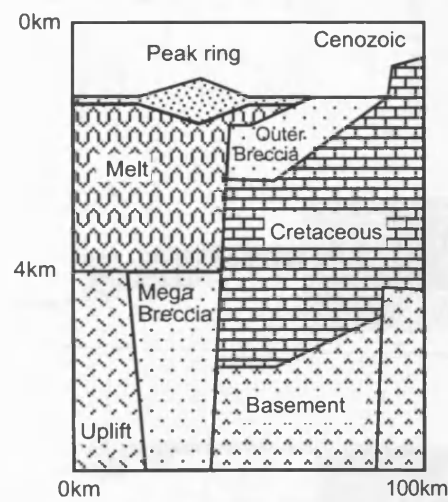
For an impact the size of Chicxulub a central uplift of basement material is to be expected. Due to the problems of modelling potential field data this has been the subject of various modelling efforts (Figure 7.4). The normal incidence reflection data is too far offshore to constrain the depth and radius of the top of the uplift and so these have remained ambiguous. Sharpton et al. (1996) suggest that the top of the uplift is between 1.5–2 km depth with a radius at its top of c. 50 km. This is overlain by a melt and breccia matrix at the centre (Figure 7.4a). Hildebrand et al. (1998) suggest a smaller, deeper structure, overlain by a melt sheet (Figure 7.4b) and offset from the centre of the crater to the southwest due to an oblique impact. Both these models would be expected to show a velocity increase between the impact breccia and melt followed by a second increase between the melt and basement.

Figure 7.5 summarizes the 1-D velocity models obtained across the central area. Between 1.5–3 km depth the models show shear wave velocities of $2\text{--}3.2\text{ km s}^{-1}$, consistent with compressional velocity measurements from samples of the melt matrix in Y-6 (V. Sharpton, pers. comm.) but less than would be expected for the central basement uplift. A poorly constrained increase to c. 4 km s^{-1} velocity is modelled at 3.1–4.1 km depth. The resolution of this layer is such that it is unclear whether the modelled increase represents true structure or is a modelling artifact. However, if it does represent an actual increase then it would be consistent with the top of the uplift proposed by Hildebrand et al. (1998).

This increase in velocity at $> 3\text{ km}$ depth is not seen in model F-D13 and the variation between the top 5% models suggests that its absence is not simply a problem with the model resolution. Whilst a simple 20 km radius uplift would explain this absence several problems exist with this solution. Assuming radial symmetry in the crater structure model



(a)



(b)

Figure 7.4: Schematic models of the central crater area by (a) Sharpton et al, 1996 and (b) Hildebrand et al, 1998.

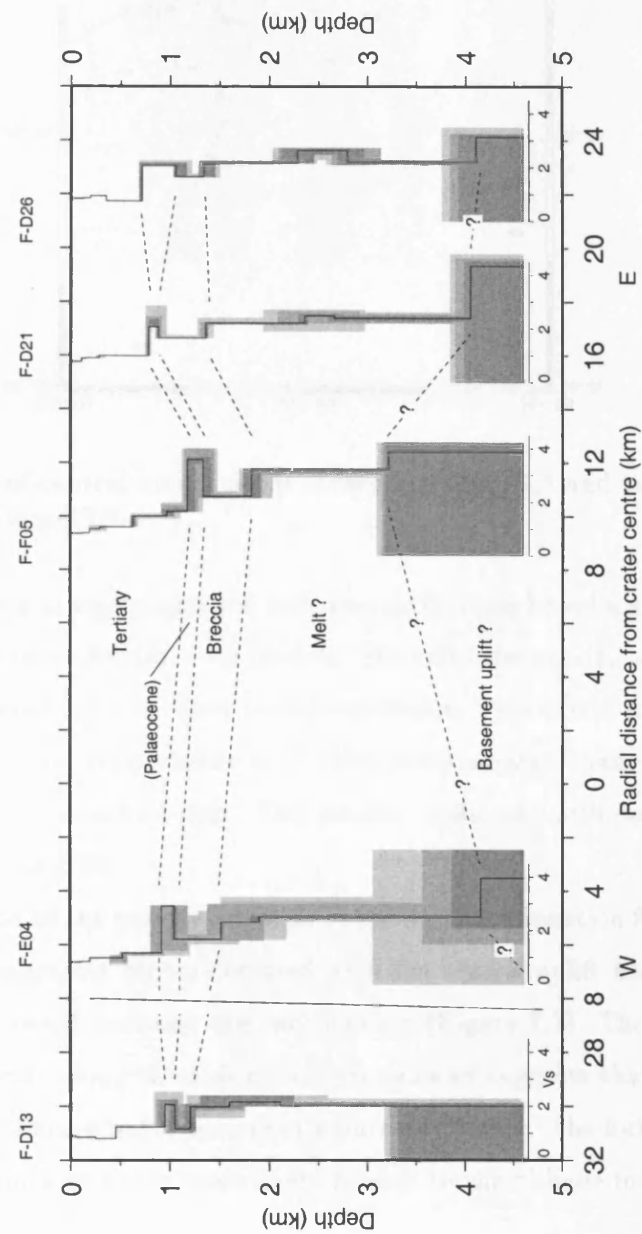


Figure 7.5: 1-D velocity models collapsed radially onto a transect parallel to the coast across the central crater area. Location of model paths are shown in Figure 7.6.

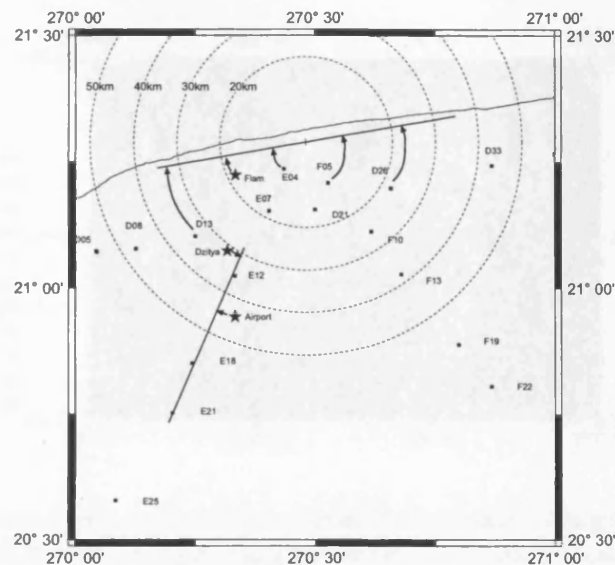


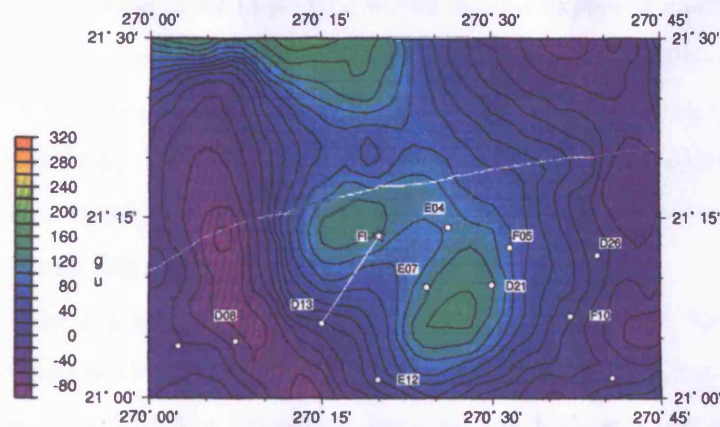
Figure 7.6: Location of central model paths shown in Figure 7.5 and the paths across the peak ring shown in Figure 7.8.

D-E7b covers an identical region and yet indicates an increase in velocity at 3.2 km depth, similar to that of the other central 1-D models. Secondly the gravity anomaly associated with the uplift suggests that it is offset to the southwest. This would require the uplift to have a radius of < 10 km to be absent in F-D13, much smaller than would be expected from a structure the size of Chicxulub. This smaller uplift also still does not explain the difference with model D-E7b.

Closer examination of the gravity anomaly suggests an explanation for the absence of a velocity increase. The gravity high associated with the central uplift has a twin peak with a southwest bearing trough between the two maxima (Figure 7.7). The path averaged by F-D13 is almost directly along the axis of this trough and suggests that the central uplift is not simply a radial feature but has more of a butterfly shape. The formation mechanism of such of feature is unclear but is most likely related to the oblique impact scenario.

7.2.3 Peak ring

One of the principal crater unknowns is the location, structure and formation of the peak ring. Pilkington et al. (1994) originally suggested a 35 km radius ring consisting of low density material detached from an underlying melt sheet and correlating to a gravity low. Sharpton et al. (1996) propose that the peak ring is the surficial expression of the



The extremely thin breccia layer in A-E12 would not be expected and if the peak ring is below D-E12 then the depth to the breccia layer would be expected to increase outwards from the ring. The velocity structure below 3 km depth is also not easily explained, although the decrease in velocity could perhaps be the result of mega-breccia below the melt sheet. Despite these problems however, the models are not well enough constrained to be able to rule out this form of a peak ring.

Figure 7.9 shows a portion of the offshore reflection data across the peak ring and a schematic illustration of the formation mechanism suggested by Brittan et al. (1998). The dipping interface caused by the transition between the high and low velocity zones will result in most paths across the region sampling both high and low velocities at the same depth making interpretation of 1-D models difficult.

Possible velocity models that such a structure may be expected to produce are shown in Figure 7.10. A path propagating inwards from outwith the peak ring will sample the high velocity sediments, low velocity breccia and low velocity material beneath the breccia. As it propagates further across the peak ring, slightly higher velocities should start to become apparent beneath the breccia. Similarly any path propagating outwards will sample the sediment and breccia and a high velocity layer. As it propagates across the ring the lower velocities should begin to appear below the high velocity.

These expected velocity models match the observed ones quite well with model A-E12 representing the path propagating from outside the peak ring inwards and D-E12 a path propagating outwards. A thinning of the breccia layer may be expected across the top of the peak ring, which is observed in A-E12 whilst the thickened layer in D-E12 may represent a thickening of the same layer interior of the ring. If this model is correct it would place the peak ring at c. 40 km (mid-way between the airport and station E12).

The similarity between models MD-D21 and D-E12 (Figure 7.11) would suggest that these are sampling approximately the same region, despite being at different radii from the crater centre. This could imply that the peak ring may be closer to the crater centre on the eastern side, possibly around 25–30 km radius. This asymmetry would be consistent with an oblique impact from the southwest (Figure 7.12).

Several of the central models also suggest a high velocity layer at c. 1.5–2.5 km depth but from Figure 7.10 any increase would be expected directly below the breccia. These

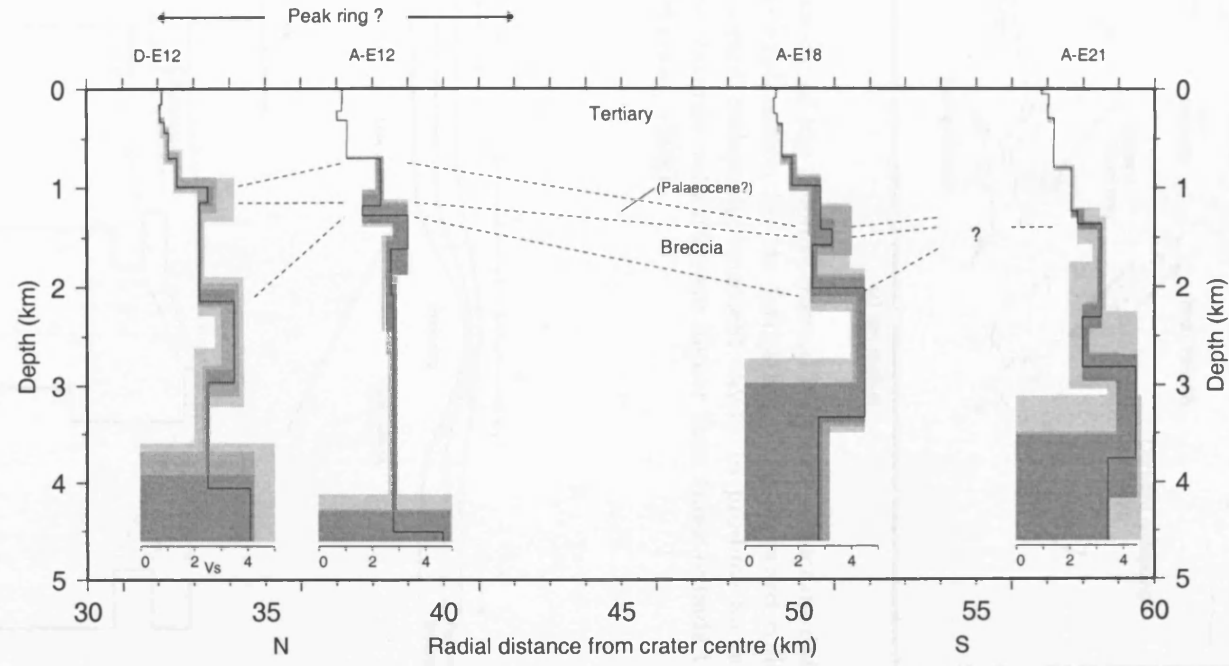


Figure 7.8: 1-D velocity models along Line E from 30-60 km radius.

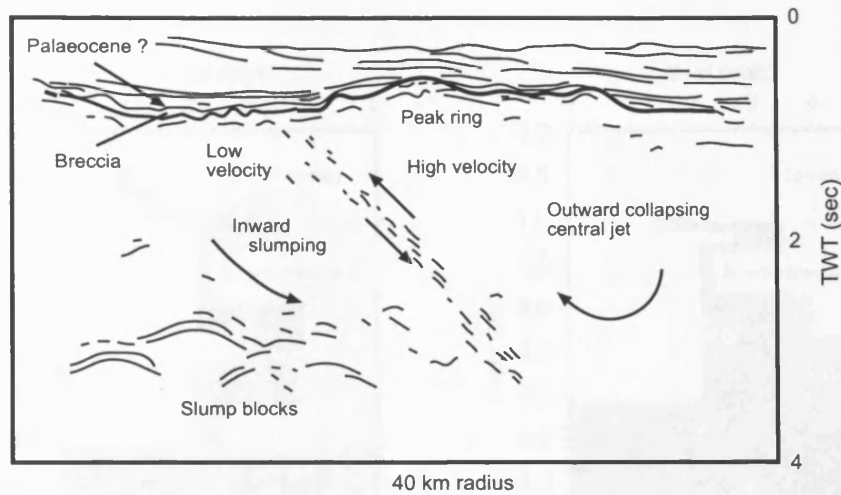


Figure 7.9: Line drawing of the offshore normal incidence reflection data across the peak ring with a possible explanation for its formation. The outward collapsing central jet interacts with the inward collapsing transient cavity to produce an inward dipping low angle transition zone. Interior velocities are higher than those outside the transition zone (after Morgan and Warner, 1998).

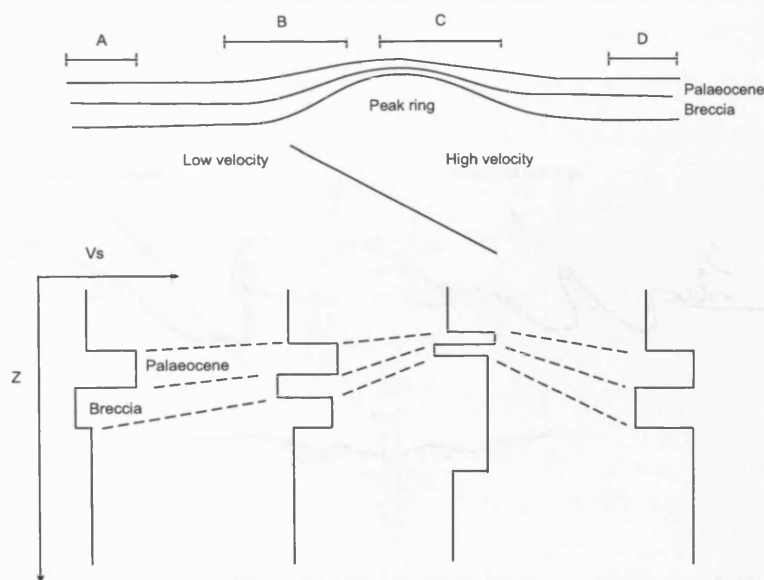


Figure 7.10: Expected 1-D velocity models arising from the structure proposed by Brittan et al, 1998. The dipping high-low velocity interface will produce a transition in models from those with high velocities to those with lower velocities below the breccia layer.

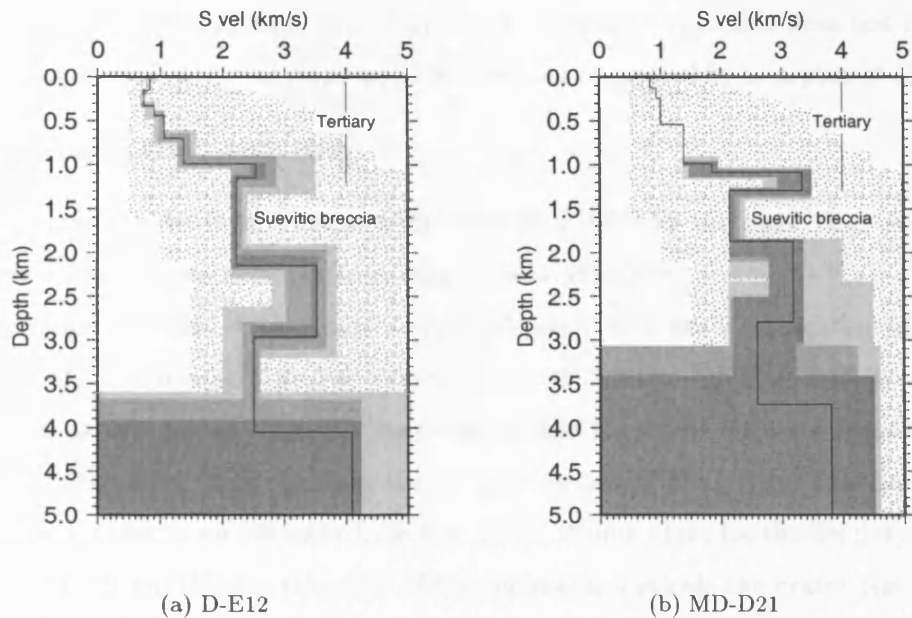


Figure 7.11: Comparison of models D-E12 and MD-D21. MD-D21 is centred at c. 25 km from the crater centre whilst D-E12 is c. 35 km suggesting asymmetries in the location of the peak ring, possibly consistent with an oblique impact from the southwest.

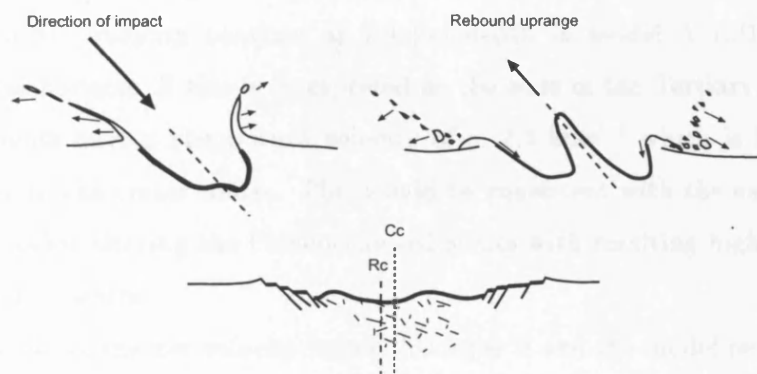


Figure 7.12: Formation of an off-centre peak ring from an oblique impact. The central jet rebounds up and towards the impact direction before collapsing to form the peak ring. The resultant crater has a peak ring centred at R_c , offset uprange from the overall crater centre, C_c .

slightly lower velocities between the breccia and this depth may suggest that some form of a melt and breccia matrix exists, overlying the collapsed central jet. The variation in depth and discontinuity of this layer may be an indication that this does not exist as a continuous sheet but rather as small pods as has been suggested by Sharpton et al. (1996).

7.2.4 Outside the peak ring

Only two models have been obtained for the region beyond the peak ring, A-E18 and A-E21 providing information out to c. 70 km radial distance.

The primary problem with model A-E21 (Figure 7.8) is the identification of the base of the Tertiary sediments. The low velocity layer at 2.5 km depth is unlikely to be the breccia layer as this would require a deepening of the layer with distance from the crater centre well below that expected from simply passing over a peak ring. This deepening is also unlikely as there is no evidence from any of the offshore data for the Tertiary sequence to be so thick. If anything a thinning of the sediments towards the crater rim would be expected. A possible explanation is a pinching out of the suevitic impact breccia towards the crater rim (Figure 7.4b). Breccia recovered from well T-1 at c. 90 km radius is of bunte rather than suevitic type. This is composed predominantly of only lightly shocked or unshocked target material and is more carbonate rich than the suevitic breccia which consists of shock melted material. Urrutia-Fucugauchi et al. (1997) reported that similar breccia in well U-6 had a higher velocity than the suevitic breccia. Given this fact then it is likely that the velocity contrast at 1.4 km depth in model A-E21 represents the Tertiary-breccia horizon. If this is interpreted as the base of the Tertiary then the oldest Tertiary sediments have a shear wave velocity of c. 2.3 km s^{-1} which is lower than that modelled closer to the crater centre. This would be consistent with the earlier hypothesis of a thermal blanket altering the Palaeocene sediments with resulting higher velocities for this layer near the centre.

It is unclear what the low velocity below this layer is and the model resolution is poor. It is noted that a low velocity layer is also modelled in A-E18 at 3.5 km depth (the first low velocity layer at 1.5 km begin interpreted as the suevitic breccia). Whilst any correlation is tenuous, this deepening could be a result of possible slumping during collapse of the transient cavity. Morgan et al. (1997) and Hildebrand et al. (1998) model a slump zone from $> 45 \text{ km}$ radius so this explanation could be possible.

7.3 Conclusions

High frequency crustal Rayleigh wave velocity dispersion across the Chicxulub impact crater has been studied to investigate the sedimentary infill and the near surface structure of the crater. The main conclusions are:

- Fundamental group velocity dispersion curves from 0.2–5 Hz were successfully obtained from quarry blasts using a multiple filter technique. These were refined and isolated from the waveform allowing identification of higher modes using a phase matched filter although amplitude spectra were distorted during the application of this filter. Interstation phase velocity curves were used to identify the correct 2π multiple of the curves. Simple half space modelling of the curves allowed a number of statements to be made on the nature of the velocity structure of the upper few hundred metres.
- A genetic algorithm was applied to produce 1-D shear wave velocity models resolving the upper kilometre of the crust using only the fundamental mode Rayleigh waves. The application of a GA overcame the bias associated with the use a starting model in other methods of optimization e.g., SVD and provided a full exploration of the model space. Variations within a best percentage of models were shown to be sufficient to give an immediate determination of model resolution. Inclusion of higher mode dispersion curves improved the depth range of the models and increased the accuracy and reliability of the model in the upper regions. Prior to its use, the GA was tested to find the optimal parameters to maximize its performance.
- Sedimentary features have been relatively well resolved by the 1-D velocity models, however the deeper structure relating to crater morphology is poorly modelled and features cannot be unequivocally identified. Moreover the wide station spacing and the restrictions of 1-D modelling limit the lateral resolution and the uniqueness of the modelled features. These restrictions have a greater effect on interpretations of crater structure where large lateral velocity inhomogeneities are present, than on interpretations of the sediments.
- The models highlight a radial infilling of the Chicxulub crater which has occurred during the Tertiary. The youngest sediments possibly correspond to the lower veloc-

ities seen near the centre of the crater although this cannot be confirmed without better geological control.

- An inverted velocity gradient is modelled within the upper 300 m of the Tertiary sediments over most of the region. The exception to this is a central region c. 30–40 km in radius where the velocity gradient is normal. The inverted gradient zone corresponds to where a dolomitic layer is seen to occur from borehole data. This layer is not present in wells drilled over the central area. The dolomitization may explain the inverted velocities as a result of increased porosity. A mixing zone formation during a late Miocene regression would best explain the dolomite formation. Alternatively the velocity structure may be a result of increased carbonate dissolution beyond a radius of 40 km from the crater centre.
- An abrupt increase in velocity is modelled for the Palaeocene sediments. The increased velocities are not obvious at radii of >60 km suggesting that the high velocities may be restricted to the area within the transient cavity. One explanation of this restriction may be the effect of a thermal blanket consisting of the melt sheet and breccia within the transient cavity. This may have driven hydrothermal alteration, including possible dolomitization or the preferential formation of aragonite rather than calcite. Combined with subsequent compaction this could produce the higher velocities.
- The boundary between the base of the Tertiary sediments and suevitic impact breccia is clearly visible at c. 1–1.5 km depth as a c. 30% decrease in shear wave velocities. Velocities in the Palaeocene sediments range from 2.2–3.2 kms^{-1} with the suevitic breccia velocities between 0.9–2.4 kms^{-1} . The suevitic breccia also appears to be limited to within a 60 km radius. Beyond this radius a higher velocity is imaged beneath the suspected base of the sediments. This is most likely a result of a pinching out of the suevitic breccia and the introduction of a less shocked bunte breccia with a greater composition of unaltered carbonate clasts from the target rock.
- A decrease in depth to the breccia layer from 1.5 to 1.1 km depth is modelled between c. 30–40 km radius. This is interpreted as the result of the existence of a peak ring occurring as a topographic high above the crater floor. The velocity models

are explained best by this being formed by the interaction between the outwardly collapsing central jet and and inwardly collapsing transient cavity. However, a low velocity ring composed of impact breccia overlying a melt sheet cannot be disproved. A peak ring composed of basement material at c. 50 km diameter fails to match the models and is considered unlikely. The radius to the peak ring may be less on the southeast side of the crater than on the southwest, consistent with a central jet rebounding uprange following an oblique impact from the southwest.

- Any central uplift of basement material cannot have an upper surface shallower than 3 km depth. The central uplift also appears to be split into two sections along a southwest trending axis with each side associated with a maxima in the gravity anomaly.

7.4 Further work

The models produced have helped identify and constrain several features but still leave many areas open to further research . Future studies can be divided into two sections: further field investigations and the extension of studies of existing data.

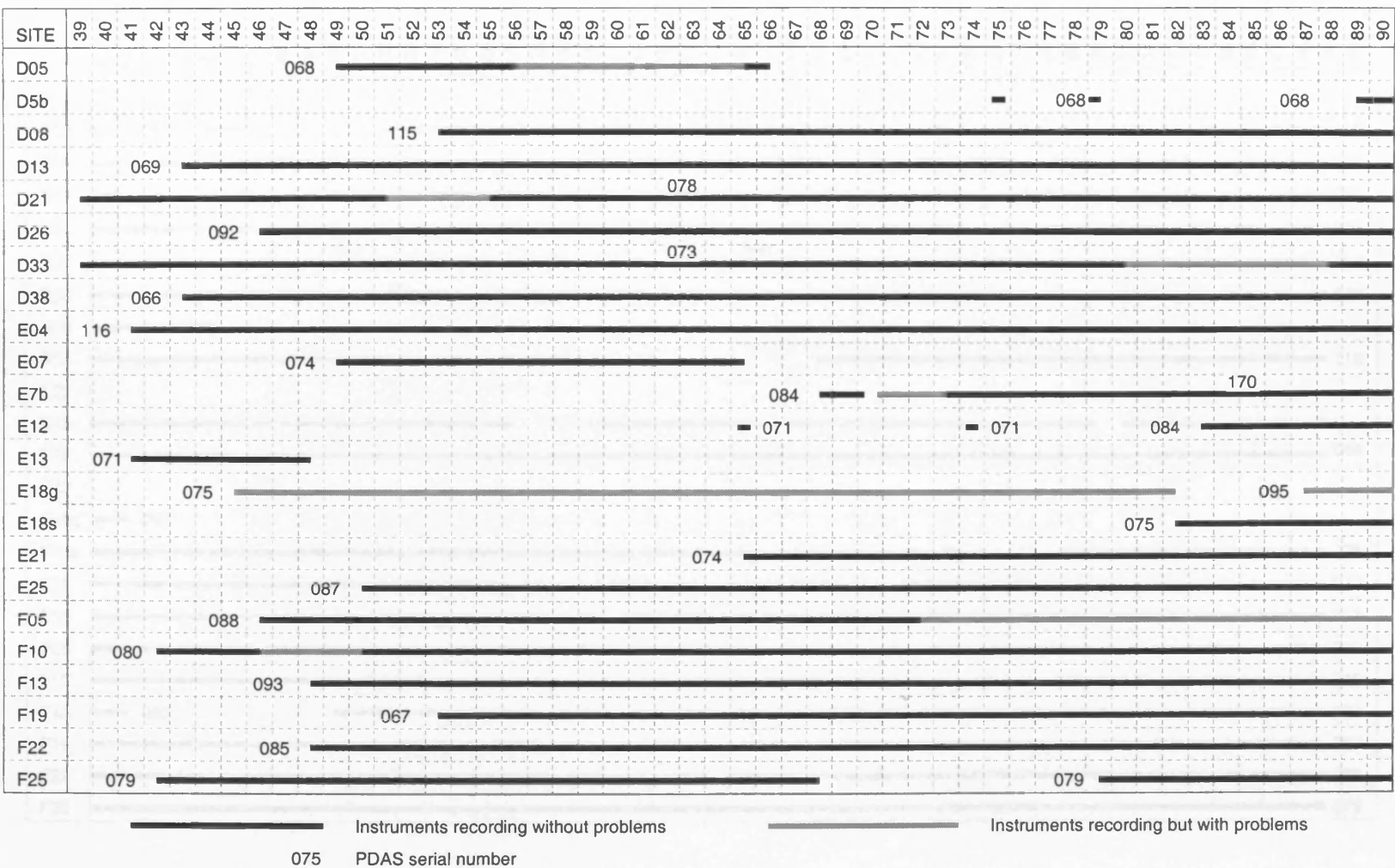
- Additional surface wave measurements could be made using an array specifically designed for such a study. This would include smaller recorder spacings and stations in line with sources thus allowing interstation phase and γ measurements to be made. A recording site situated at the quarry would also remove all origin time error. Such a study could incorporate a refraction/reflection study.
- In situ measurements of Q_β from the existing boreholes would enable causal effects to be considered and also allow investigations into the frequency dependence of Q_β .
- A proper waveform inversion for Q_β structure could be attempted; however it is debatable whether the waveforms are sensitive enough to attenuation to make this worthwhile. Any such study would need to include an investigation into the effect the source function has on waveform shape over short path lengths.
- An examination of the dispersion from regional events may allow the deeper structure across the array to be modelled. Towards the end of this project a very brief

examination was made of an event occurring beneath the Campeche bank. Whilst this appeared to be extremely complex including higher mode interference and little fundamental mode energy, the use of different filter widths could possibly improve the signal. Also other regional events would not contain any possible effects resulting from the oceanic–continental transition which occurs on this path and so may be better suited for any such study.

- Shear wave modelling and an examination of the V_p/V_s ratio could be made from the onshore recordings of the wide angle data. This could help constrain the 1-D shear wave models obtained from the dispersion curves and should also provide evidence to support or disprove any thermal blanket effect within the central area of the crater.
- Numerical modelling of crater formation would allow testing of several of the models of peak ring formation. This modelling should also include the effects of an oblique impact, especially in relation to the formation of a central uplift to help understand the reason for the interpreted asymmetries.

Appendix A

Recording Schedule



SITE	91	92	93	94	95	96	97	98	99	100	101	102	103	104	105	106	107	108	109	110	111	112	113	114	115	116	117	118	119	120	121	122	123	124	125	126	127	128	129	130	131	132	133	134	135	136	137	138	139	140
D05																																																		
D5b		068								068																																								
D08																																																		
D13																																																		
D21																																																		
D26										092																																								
D33																																																		
D38																																																		
E04																																																		
E07																																																		
E7b																																																		
E12																																																		
E13																																																		
E18g																																																		
E18s																																																		
E21																																																		
E25																																																		
F05																																																		
F10																																																		
F13																																																		
F19																																																		
F22																																																		
F25																																																		

Table A.2: Recording schedule Julian Days 91–140.

Station	Days deployed	Problems Days (%)	Down Time Days (%)
D05	17	7 (41.2)	
D5b	64		21 (32.8)
D08	86		
D13	96	4 (4.2)	
D21	100		
D26	93		1 (1.1)
D33	100	8 (8)	
D38	96		2 (2.1)
E04	98		8 (8.2)
E07	17		
E7b	70	8 (11.4)	5 (7.1)
E12	74		18 (24.3)
E13	7		
E18 G	47	42 (89.4)	5 (10.6)
E18 S	57		
E21	74	10 (13.5)	
E25	89		
F05	93	18 (19.4)	
F10	97	5 (5.2)	
F13	91	7 (7.7)	
F19	86		
F22	91		
F25	97		10 (10.3)
TOTAL	1724	101 (5.9)	70 (4.1)

Table A.3: Summary of station recording statistics.

Appendix B

Teleseismic and Regional Events

Regional and teleseismic events recorded by the Chicxulub array are listed in the following pages and shown in Figure B.1. Hypocentral details were obtained from earthquake information lists produced by the USGS.

Date	Time	Location	Depth	Mag.	Region
10-Feb-96	07:48:27	15.2N 92.6W	33	MB=3.8	MEXICO-GUATEMALA BORDER
12-Feb-96	09:08:12	11.0S 118.9E	33	MS=5.7	S OF SUMBAWA, INDONESIA
14-Feb-96	21:26:56	29.2N 140.4E	139	MB=5.9	SOUTH OF HONSHU, JAPAN
16-Feb-96	15:22:58	37.5N 142.4E	33	MB=6.2	OFF E CST OF HONSHU, JAPAN
16-Feb-96	16:53:33	15.6N 93.6W	33	MB=4.5	NEAR COAST OF CHIAPAS, MEX
17-Feb-96	05:59:30	1.0S 136.9E	33	MS=8.0	IRIAN JAYA REG, INDONESIA
17-Feb-96	10:23:42	14.0N 91.2W	33	MB=5.2	NEAR COAST OF GUATEMALA
21-Feb-96	12:51:04	9.7S 79.7W	33	MS=6.7	OFF COAST OF NORTHERN PERU
21-Feb-96	13:47:20	9.5S 80.2W	33	MB=5.6	OFF COAST OF NORTHERN PERU
22-Feb-96	08:38:36	8.6N 83.2W	33	MB=5.0	COSTA RICA
22-Feb-96	13:40:53	33.6S 71.3W	44	MB=5.9	NEAR COAST OF CEN CHILE
25-Feb-96	03:08:16	16.0N 97.9W	33	MS=6.8	NEAR COAST OF OAXACA, MEX
25-Feb-96	04:00:08	16.0N 97.9W	33	MB=4.0	OAXACA, MEXICO
25-Feb-96	04:17:09	15.9N 97.9W	33	MB=5.3	NEAR COAST OF OAXACA, MEX
25-Feb-96	04:49:13	16.0N 97.8W	33	MB=3.8	OAXACA, MEXICO
25-Feb-96	05:07:08	15.5N 98.0W	33	MB=4.4	NEAR COAST OF OAXACA, MEX
25-Feb-96	05:34:28	15.9N 97.8W	33	MB=4.9	NEAR COAST OF OAXACA, MEX
25-Feb-96	05:40:29	16.1N 97.6W	33	MB=4.8	OAXACA, MEXICO
25-Feb-96	05:53:12	16.4N 97.8W	33	MB=4.1	OAXACA, MEXICO
25-Feb-96	06:10:25	16.0N 97.8W	33	NO MAG	OAXACA, MEXICO
25-Feb-96	06:24:35	15.9N 98.0W	33	MB=4.4	NEAR COAST OF OAXACA, MEX
25-Feb-96	06:31:07	15.9N 97.4W	33	MB=4.2	NEAR COAST OF OAXACA, MEX
25-Feb-96	07:50:50	15.7N 97.7W	33	MB=4.3	NEAR COAST OF OAXACA, MEX
25-Feb-96	08:44:50	16.6N 97.6W	33	MB=4.6	OAXACA, MEXICO
25-Feb-96	09:07:26	16.3N 97.8W	33	MB=4.4	OAXACA, MEXICO
25-Feb-96	09:17:59	16.1N 97.9W	33	MB=5.7	OAXACA, MEXICO
25-Feb-96	10:20:57	15.7N 97.7W	33	MB=4.4	NEAR COAST OF OAXACA, MEX
25-Feb-96	12:18:39	16.2N 97.8W	33	MB=4.2	OAXACA, MEXICO
25-Feb-96	14:17:20	12.9N 91.0W	33	MB=5.5	OFF COAST OF CEN AMERICA
25-Feb-96	14:27:30	16.1N 97.7W	33	MB=5.3	OAXACA, MEXICO
25-Feb-96	14:44:12	16.1N 97.7W	33	MB=4.8	OAXACA, MEXICO
25-Feb-96	14:46:59	16.0N 97.6W	33	MB=4.5	OAXACA, MEXICO
25-Feb-96	14:47:54	16.1N 97.7W	33	MB=4.6	OAXACA, MEXICO
25-Feb-96	14:51:57	15.8N 97.8W	33	MB=5.2	NEAR COAST OF OAXACA, MEX
25-Feb-96	14:54:12	16.1N 97.8W	33	MB=5.0	OAXACA, MEXICO
25-Feb-96	15:02:32	16.1N 97.7W	33	MB=4.6	OAXACA, MEXICO
25-Feb-96	15:04:13	15.9N 97.9W	33	MB=4.9	NEAR COAST OF OAXACA, MEX
25-Feb-96	15:08:37	16.0N 97.7W	33	MB=4.7	OAXACA, MEXICO
25-Feb-96	15:09:20	15.9N 97.7W	33	MB=4.5	NEAR COAST OF OAXACA, MEX
25-Feb-96	15:48:14	16.5N 97.8W	33	MB=4.5	OAXACA, MEXICO
26-Feb-96	01:37:33	15.8N 97.7W	33	MB=5.1	NEAR COAST OF OAXACA, MEX
26-Feb-96	02:32:15	16.0N 97.8W	33	MB=4.0	OAXACA, MEXICO

26-Feb-96	07:33:38	15.7N 97.6W	33	MB=5.0	NEAR COAST OF OAXACA, MEX
26-Feb-96	12:00:28	15.9N 97.7W	33	MB=4.5	NEAR COAST OF OAXACA, MEX
26-Feb-96	12:56:59	16.2N 97.7W	33	MB=4.4	OAXACA, MEXICO
26-Feb-96	22:01:23	16.3N 97.9W	33	MB=4.7	OAXACA, MEXICO
26-Feb-96	22:02:30	15.8N 98.1W	33	MB=4.9	OFF COAST OF GUERRERO, MEX
28-Feb-96	04:38:51	11.8N 87.5W	33	MB=4.6	NEAR COAST OF NICARAGUA
28-Feb-96	19:41:37	15.9N 97.9W	33	MB=4.6	NEAR COAST OF OAXACA, MEX
29-Feb-96	16:58:40	4.2N 83.9W	10	MB=4.9	OFF COAST OF CEN AMERICA
03-Mar-96	14:55:06	10.9N 86.7W	33	MS=6.4	OFF COAST OF COSTA RICA
03-Mar-96	14:58:53	11.1N 86.8W	33	MB=5.5	NEAR COAST OF NICARAGUA
03-Mar-96	16:37:26	11.1N 86.7W	33	MS=6.6	NEAR COAST OF NICARAGUA
04-Mar-96	12:39:40	13.7N 93.0W	33	MB=4.7	OFF COAST OF CHIAPAS, MEX
05-Mar-96	19:48:23	11.2N 86.9W	33	MB=5.2	NEAR COAST OF NICARAGUA
07-Mar-96	04:27:50	10.8N 86.1W	33	MB=4.9	OFF COAST OF COSTA RICA
07-Mar-96	05:29:10	11.4N 87.1W	33	MB=4.4	NEAR COAST OF NICARAGUA
10-Mar-96	06:19:59	16.4N 98.2W	33	MB=4.4	NR COAST OF GUERRERO, MEX
10-Mar-96	10:03:39	17.6N 94.4W	33	MB=4.4	CHIAPAS, MEXICO
12-Mar-96	05:24:19	16.0N 97.6W	33	MB=4.7	OAXACA, MEXICO
13-Mar-96	21:04:19	16.8N 98.8W	33	MB=5.2	NR COAST OF GUERRERO, MEX
14-Mar-96	09:12:11	19.3N 91.9W	33	MB=4.4	BAY OF CAMPECHE
15-Mar-96	23:33:55	16.7N 98.1W	33	MB=4.3	NR COAST OF GUERRERO, MEX
16-Mar-96	22:04:06	29.0N 138.9E	476	MW=6.6	SOUTH OF HONSHU, JAPAN
17-Mar-96	14:48:56	14.7S 167.2E	164	MS=6.0	VANUATU ISLANDS
19-Mar-96	15:31:36	24.9N 109.4W	10	MB=4.9	GULF OF CALIFORNIA
19-Mar-96	17:12:42	15.8N 97.2W	33	MB=5.8	NEAR COAST OF OAXACA, MEX
20-Mar-96	04:44:50	16.4N 97.1W	33	MB=4.3	OAXACA, MEXICO
20-Mar-96	04:53:26	15.8N 97.2W	33	MB=5.4	NEAR COAST OF OAXACA, MEX
20-Mar-96	18:08:41	15.8N 97.2W	33	MB=5.3	NEAR COAST OF OAXACA, MEX
22-Mar-96	03:24:21	51.3N 178.6E	33	MS=6.7	RAT ISL, ALEUTIAN ISLANDS
22-Mar-96	10:30:26	16.1N 97.9W	33	MB=4.8	OAXACA, MEXICO
23-Mar-96	03:05:53	8.3N 72.7W	199	MB=4.9	VENEZUELA
27-Mar-96	12:34:49	16.4N 98.0W	33	MB=5.5	OAXACA, MEXICO
27-Mar-96	20:52:06	11.7N 88.0W	33	MB=5.6	NEAR COAST OF NICARAGUA
28-Mar-96	23:03:49	1.1S 78.6W	33	MB=5.7	ECUADOR
30-Mar-96	13:05:17	52.4N 168.8W	33	MS=6.2	FOX ISL, ALEUTIAN ISLANDS
01-Apr-96	03:43:02	16.6N 95.7W	58	MB=5.1	OAXACA, MEXICO
01-Apr-96	05:06:09	14.6N 93.5W	33	MB=5.2	NEAR COAST OF CHIAPAS, MEX
01-Apr-96	06:10:52	14.5N 93.4W	33	MB=5.3	NEAR COAST OF CHIAPAS, MEX
03-Apr-96	23:00:48	14.7N 93.4W	33	MB=5.1	NEAR COAST OF CHIAPAS, MEX
09-Apr-96	01:29:23	16.4N 98.8W	33	MB=4.7	NR COAST OF GUERRERO, MEX
09-Apr-96	03:00:13	16.2N 98.6W	33	MB=4.7	NR COAST OF GUERRERO, MEX
10-Apr-96	04:05:29	16.3N 98.0W	33	NO MAG	OAXACA, MEXICO
10-Apr-96	23:24:13	13.0S 76.0W	70	MB=5.0	NEAR COAST OF PERU
10-Apr-96	23:51:31	10.0N 70.1W	33	MB=4.9	VENEZUELA

11-Apr-96	21:57:46	13.6N 90.9W	33	MB=4.5	NEAR COAST OF GUATEMALA
12-Apr-96	18:45:50	6.0S 154.5E	33	MS=5.9	SOLOMON ISLANDS
13-Apr-96	19:49:41	16.4N 98.9W	26	MB=4.3	NR COAST OF GUERRERO, MEX
16-Apr-96	00:30:54	24.1S 177.2W	110	MS=6.8	SOUTH OF FIJI ISLANDS
19-Apr-96	00:19:31	23.8S 70.0W	49	MS=6.1	NORTHERN CHILE
23-Apr-96	06:53:35	17.3N 101.3W	33	MB=5.3	NR COAST OF GUERRERO, MEX
24-Apr-96	17:06:36	8.1S 74.3W	150	MB=5.6	PERU-BRAZIL BORDER REGION
24-Apr-96	18:56:22	18.8N 70.4W	80	MB=5.2	DOMINICAN REPUBLIC REGION
27-Apr-96	08:40:46	3.0N 79.3W	10	MS=5.9	SOUTH OF PANAMA
29-Apr-96	14:40:41	6.5S 154.9E	44	MS=7.5	SOLOMON ISLANDS
29-Apr-96	22:31:15	8.1N 39.0W	10	MB=5.0	CENTRAL MID-ATLANTIC RIDGE
02-May-96	02:32:35	6.4S 154.6E	33	MS=6.0	SOLOMON ISLANDS
03-May-96	04:04:22	47.8N 121.9W	5	MB=5.4	WASHINGTON
07-May-96	08:44:36	1.6N 126.6E	33	MS=5.9	NORTHERN MOLUCCA SEA
07-May-96	18:25:59	16.2N 97.4W	33	MB=4.5	OAXACA, MEXICO
07-May-96	21:43:41	14.9S 69.7W	242	MB=5.1	PERU-BOLIVIA BORDER REGION
07-May-96	23:20:00	43.7N 147.6E	49	MB=6.2	KURIL ISLANDS
08-May-96	01:24:40	16.5N 100.0W	33	MB=4.3	NR COAST OF GUERRERO, MEX
09-May-96	21:54:13	18.8N 104.3W	33	MB=4.9	NEAR COAST OF JALISCO, MEX
10-May-96	00:33:01	14.1N 91.9W	33	MB=4.2	GUATEMALA
10-May-96	10:19:38	13.9S 74.3W	101	MB=5.3	CENTRAL PERU
11-May-96	13:43:45	6.5S 154.8E	33	MS=6.4	SOLOMON ISLANDS
13-May-96	04:53:47	7.2N 76.9W	27	MB=5.1	NORTHERN COLOMBIA
15-May-96	14:07:54	13.6N 91.0W	33	MB=4.4	NEAR COAST OF GUATEMALA
16-May-96	10:24:14	14.8N 93.1W	33	MB=4.0	NEAR COAST OF CHIAPAS, MEX
17-May-96	05:54:07	15.8N 91.8W	224	MB=4.5	MEXICO-GUATEMALA BDR REG

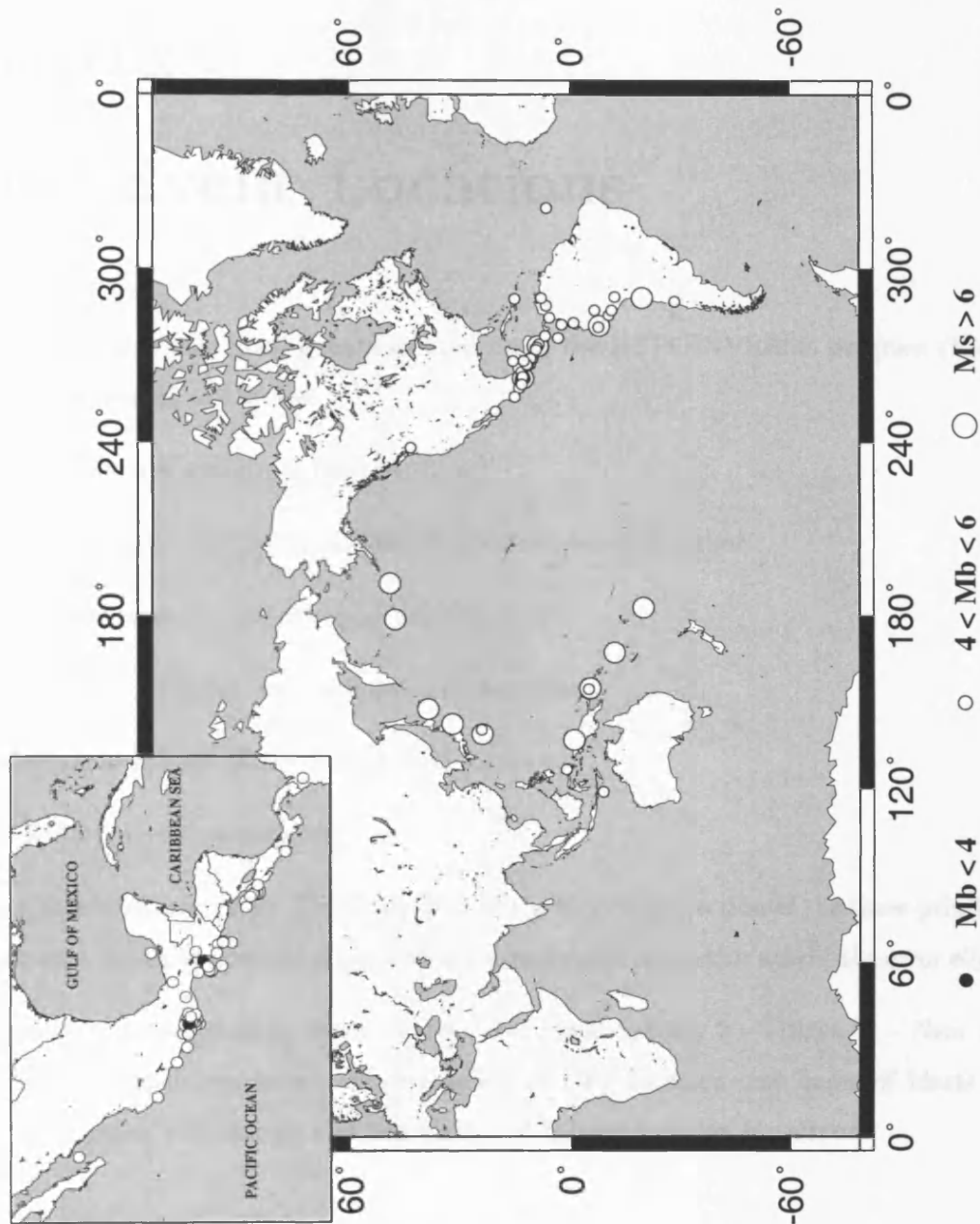


Figure B.1: Locations of teleseismic and regional events.

Appendix C

Local Event Locations

The following table lists local events located using the HYPOINVERSE program (Klein, 1990). The format is as follows:

Date - Year, month and day of event

Time - Hour minute and decimal second of calculated origin time

Lat - Latitude, degrees and decimal minutes North

Lon - Longitude, degrees and decimal minutes West

Dep - Depth in metres (fixed during final location)

RMS - RMS travel time residual

ERH - Horizontal error, km. This is defined as the largest projection of the three principal errors onto the horizontal plane and is approximates the major axis of the error ellipse.

Q - Identified as originating from quarry: 1 - Flamboyanes, 2 - Dzitya, 3 - Near airport. Identification based on correlation of GPS location and dates of blasts for Flamboyanes and Dzitya and correlation of believed location for airport.

Date	Time	Lat (N)	Lon (W)	Depth (m)	RMS	ERH	Q	
96- 2-12	2034	53.64	21 4.95	89 40.66	5	0.31	1.06	2
96- 2-13	2037	36.29	21 6.81	89 47.38	5	1.20	6.00	
96- 2-15	1613	29.07	21 2.50	89 30.18	5	0.12	1.48	
96- 2-16	1806	25.05	21 14.10	89 40.55	10	0.11	0.85	1
96- 2-16	2320	59.80	20 56.45	89 39.79	5	0.11	0.56	3
96- 2-17	1811	44.79	21 2.38	89 39.56	10	0.12	0.45	
96- 2-17	1903	46.78	21 10.02	89 38.14	5	0.14	1.12	
96- 2-17	2013	50.33	21 5.00	89 40.93	5	0.09	0.60	2
96- 2-21	1735	44.77	20 56.04	89 39.98	5	0.13	0.39	3
96- 2-21	1813	40.78	21 10.21	89 38.63	5	0.12	0.51	
96- 2-21	2345	6.25	21 6.80	89 41.28	5	0.20	0.81	2
96- 2-22	1818	54.99	21 2.54	89 44.41	10	0.15	0.39	
96- 2-23	1656	34.33	21 3.24	89 30.79	5	0.24	0.64	
96- 2-23	1905	45.38	20 56.31	89 40.37	5	0.14	0.37	3
96- 2-24	1710	18.09	21 13.36	89 39.96	10	0.14	0.76	1
96- 2-26	1804	37.75	21 4.02	89 41.09	5	0.13	0.89	2
96- 2-26	1904	46.21	20 57.22	89 39.79	5	0.14	0.44	3
96- 2-28	2045	18.73	21 5.08	89 41.56	5	0.25	0.99	2
96- 2-28	2323	48.81	21 12.41	89 40.01	10	0.13	0.57	1
96- 2-29	1913	35.63	21 3.56	89 31.09	5	0.19	0.63	
96- 3-06	0008	4.52	21 4.60	89 41.04	5	0.10	0.40	2
96- 3-06	1700	47.42	20 57.31	89 40.96	5	0.14	0.36	3
96- 3-07	1649	5.00	20 56.91	89 40.67	5	0.09	0.48	3
96- 3-09	1728	12.37	20 56.85	89 40.25	5	0.20	0.51	3
96- 3-09	2041	29.64	21 4.94	89 40.95	5	0.14	0.99	2
96- 3-12	2142	40.34	21 4.98	89 41.66	5	0.24	1.18	2
96- 3-13	1916	44.76	21 4.21	89 31.85	5	0.29	0.86	
96- 3-13	2343	33.34	21 13.71	89 40.17	10	0.10	0.51	1
96- 3-14	2116	15.77	21 11.46	89 19.69	5	0.10	0.32	
96- 3-15	1642	53.69	20 56.93	89 40.17	5	0.20	0.51	3
96- 3-16	1825	59.74	21 13.76	89 39.88	10	0.10	0.57	1
96- 3-16	1912	37.79	21 1.84	89 39.58	10	0.12	0.35	
96- 3-19	2007	14.34	21 10.00	89 38.07	5	0.12	0.81	
96- 3-21	1931	58.99	21 13.74	89 40.00	10	0.15	0.61	1
96- 3-22	2331	51.88	21 4.50	89 40.95	5	0.13	0.83	2
96- 3-26	0023	7.64	21 4.63	89 31.59	5	0.16	0.72	
96- 3-26	1724	11.14	21 4.89	89 41.13	5	0.08	0.49	2
96- 3-27	1924	58.04	20 56.25	89 40.47	5	0.12	0.48	3
96- 3-27	2024	2.60	21 8.46	89 45.60	10	0.23	0.70	
96- 3-28	1738	39.19	20 56.37	89 40.23	5	0.22	0.52	3
96- 3-28	1825	34.08	21 13.88	89 40.45	10	0.08	0.48	1
96- 3-28	2216	1.43	20 56.26	89 40.16	5	0.12	0.39	3
96- 3-28	2301	22.47	21 5.05	89 40.87	5	0.10	0.61	2
96- 3-30	1751	42.04	20 56.09	89 40.48	5	0.17	0.43	3
96- 3-30	2332	36.14	21 5.43	89 41.05	5	0.27	0.61	2
96- 4-04	1617	35.53	21 3.43	89 41.85	5	0.08	0.49	
96- 4-09	1609	32.53	21 4.02	89 41.36	5	0.14	0.56	2
96- 4-09	1928	23.50	21 4.99	89 41.14	5	0.13	0.44	
96- 4-10	1830	35.57	20 57.62	89 40.53	5	0.16	0.46	3
96- 4-10	2109	59.76	21 4.45	89 41.08	5	0.12	0.51	2

Date	Time	Lat (N)	Lon (W)	Depth (m)	RMS	ERH	Q			
96- 4-11	1428	19.63	21	13.43	89	40.07	10	0.05	0.93	1
96- 4-12	2300	8.74	21	4.74	89	41.15	5	0.11	0.44	2
96- 4-13	1414	48.77	21	13.53	89	40.31	10	0.08	0.92	1
96- 4-16	2017	44.59	21	4.84	89	40.89	5	0.12	0.45	2
96- 4-18	2302	30.96	21	4.61	89	41.09	5	0.09	0.41	2
96- 4-18	2141	30.41	21	1.90	89	43.85	10	0.07	0.53	
96- 4-19	1559	37.43	21	4.10	89	41.35	5	0.11	0.51	
96- 4-20	1719	28.15	21	1.67	89	39.22	10	0.12	1.45	
96- 4-20	1746	39.19	21	12.84	89	39.86	10	0.12	0.87	1
96- 4-22	1850	41.04	20	55.96	89	39.66	5	0.20	0.53	3
96- 4-22	2303	54.87	21	4.73	89	40.75	5	0.16	0.57	2
96- 4-23	2040	27.90	21	3.24	89	44.89	10	0.13	0.83	
96- 4-24	1649	52.35	20	55.90	89	34.34	5	0.07	0.37	
96- 4-24	1757	51.79	20	56.16	89	40.25	5	0.17	0.42	3
96- 4-24	1819	2.77	21	12.66	89	39.74	10	0.15	0.59	1
96- 4-25	1442	43.42	20	55.76	89	32.54	5	0.19	0.38	
96- 4-25	1852	16.63	20	55.98	89	40.08	5	0.10	0.33	3
96- 4-26	1630	16.00	21	9.91	89	38.63	5	0.10	0.90	
96- 4-26	1806	25.23	20	56.46	89	40.21	5	0.11	0.30	3
96- 4-26	2257	39.96	21	4.86	89	40.75	5	0.13	0.45	2
96- 4-27	1624	59.98	21	13.16	89	40.24	10	0.11	0.58	1
96- 4-27	1726	47.20	21	2.24	89	39.85	10	0.08	0.30	
96- 4-29	1643	35.89	20	55.80	89	34.41	5	0.18	0.50	
96- 4-29	2256	43.46	21	4.59	89	40.99	5	0.11	0.43	2
96- 5-02	1712	17.33	21	3.99	89	41.54	5	0.12	0.47	
96- 5-06	1553	59.66	21	3.72	89	41.48	5	0.17	0.60	
96- 5-06	2256	4.42	21	4.63	89	40.88	5	0.14	0.45	2
96- 5-08	2110	54.21	21	13.81	89	40.23	10	0.11	0.50	1
96- 5-10	1739	3.82	21	3.20	89	41.79	5	0.21	0.45	
96- 5-10	1816	21.86	20	56.48	89	40.10	5	0.11	0.36	3
96- 5-10	1851	16.83	21	10.69	89	38.50	5	0.10	0.50	
96- 5-10	1956	4.69	21	5.32	89	40.93	5	0.11	0.34	2
96- 5-11	1405	30.02	21	13.76	89	39.88	10	0.13	0.45	1
96- 5-11	1731	4.51	20	56.72	89	40.14	5	0.11	0.39	3
96- 5-13	1823	20.03	20	55.35	89	34.18	5	0.08	0.31	
96- 5-14	1542	56.39	20	56.46	89	30.62	5	0.59	1.47	
96- 5-14	1755	14.84	20	56.68	89	40.24	5	0.13	0.39	3

Appendix D

Instrument Details

The equipment used in Mexico consisted of PDAS recorders and three types of seismometers. The details of these, their responses and associated intrinsic problems are given within this Appendix.

D.1 Seismometers

Three type of seismometers, the Teledyne Geotech S13, Guralp CMG-40T and Guralp CMG-3T were used. The S13 is a short period instrument with a natural frequency of 1Hz and a velocity response which is flat above this frequency (Figure D.1). Both Guralps are broadband instruments, the CMG-3T with a frequency band of 0.01–50 Hz and the CMG-40T from 30 seconds–50 Hz. Within these ranges the instruments have a flat response (Figure D.2).

The seismograms obtained are a convolution of the actual ground response and the

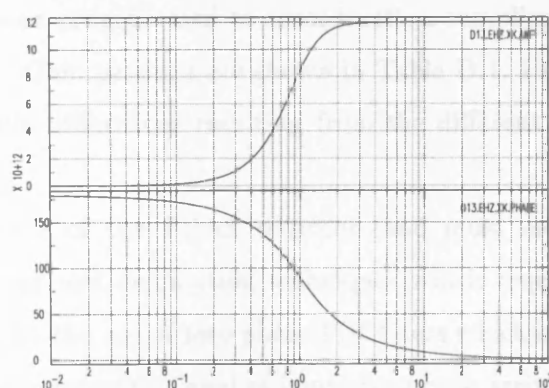


Figure D.1: Amplitude and phase response for the Teledyne Geotech S13.

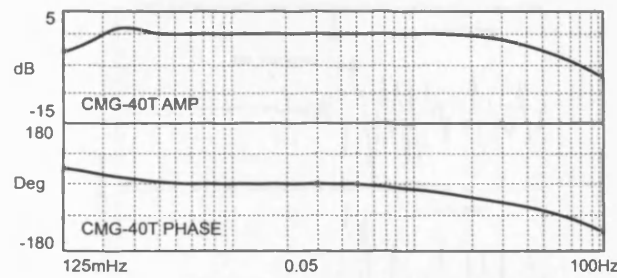


Figure D.2: Amplitude and phase response for the Guralp CMG-40T. The response of the CMG-3T is similar but with a flat response over a wider frequency range.

Seismometer	Pre-amp gain	External gain	Full scale reading	Sensitivity
S13	1	High	± 1 V	629 V/m/s
Guralp	1	Low	± 20 V	800 V/m/s (40T) 1400 V/m/s (3T)

Table D.1: Gain settings for the seismometers used and their associated maximum reading.

sensor responses (in the time domain). Prior to the surface wave analysis the traces had to be corrected for the instrument responses. These were removed using SAC and the pole-zero values of the instruments (in the case of the S13s the theoretical values for a damping constant of 0.7 and for the Guralps the manufacturers values).

Differences in the instrument sensitivities were corrected for at the same time as the corrections for the recorder gain settings (Table D.1).

D.2 The PDAS recorder

The PDAS recorders were programmed to record with a sampling rate of 100 s/sec in 32 bit gain ranged format. Gain settings are shown in Table D.1. Prior to the calculation of γ , the relative amplitude differences resulting from the different gain settings had to be accounted for.

The high performance of the PDAS recorder (and most modern digital recorders) results from oversampling and decimation techniques which require very steep anti-alias filters. This is achieved by the use of zero phase FIR filters which cause no phase distortion but can result in a false precursory signal of impulsive phase arrivals (Figure D.3). This is a result of the steepness of the filter which causes a “ringing” of the filter response (Gibb’s

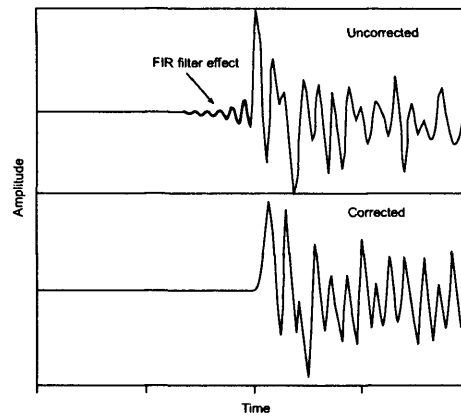


Figure D.3: Observed and true P arrival showing precursor generated by the internal FIR filter (after Scherbaum, 1996).

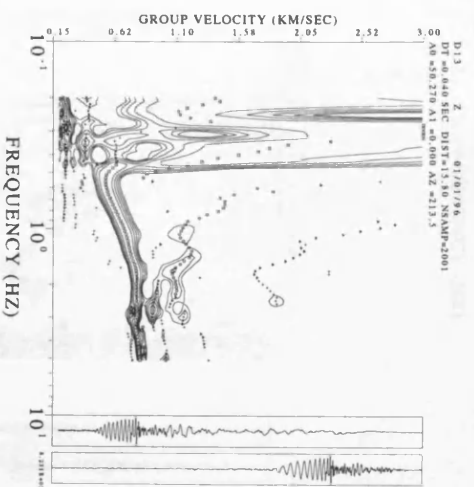
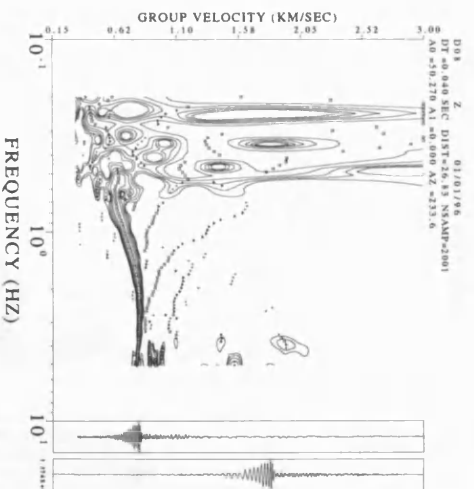
phenomenon) (Scherbaum, 1996; Scherbaum and Bouin, 1997; Scherbaum, 1997).

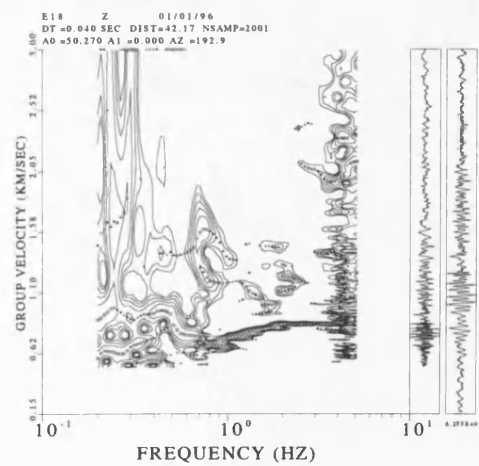
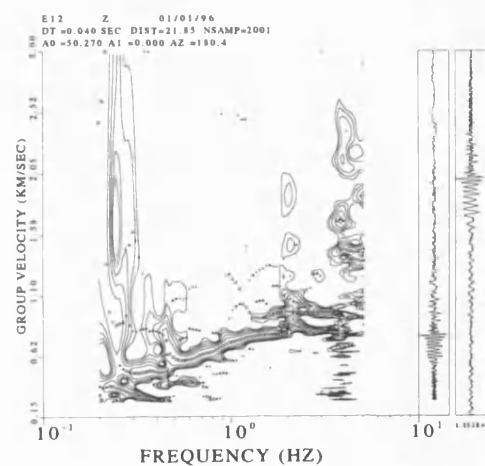
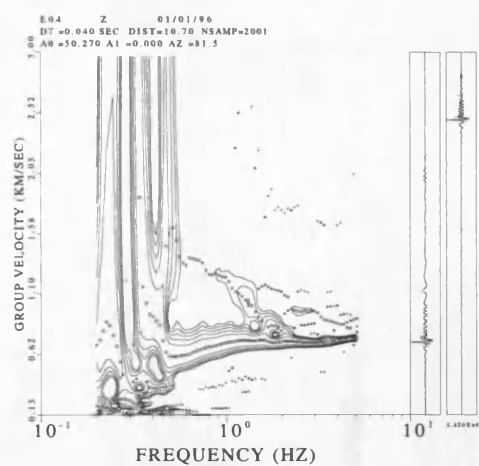
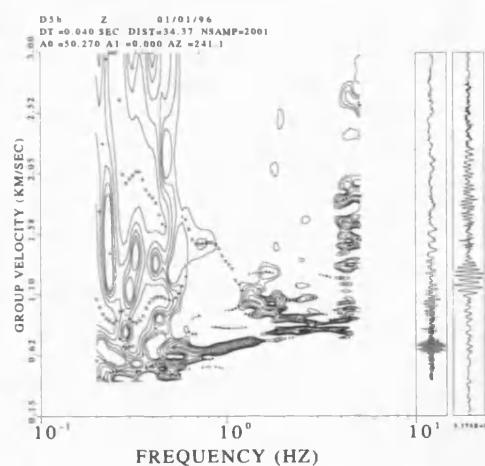
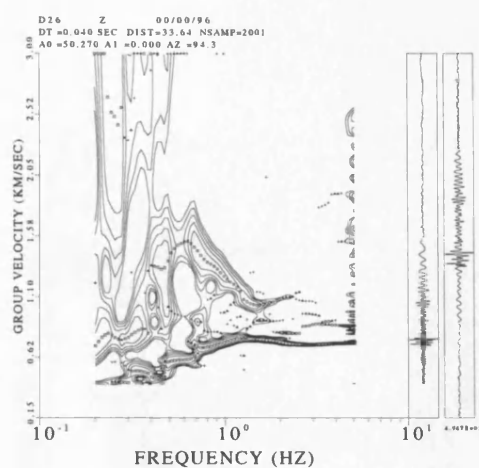
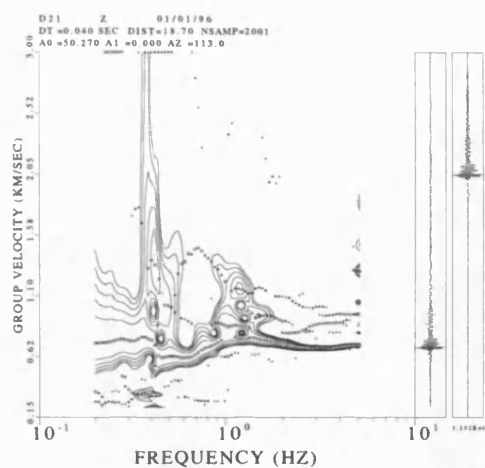
It is advised to remove this effect prior to any analysis requiring onset time or polarity by replacing the maximum phase portion of the filter by a minimum phase equivalent (Scherbaum, 1996). However in order to do this the FIR filter coefficients must be known and for the PDAS instrument these are unavailable from the manufacturers (F. Scherbaum, pers. comm.). It is generally believed that these precursors can be recognized by the monochromatic nature however it has been shown that they can in fact be complex making them impossible to distinguish unless compared to a corrected signal (Scherbaum and Bouin, 1997). It is therefore unknown whether or not this problem exists with this data set however it is unlikely as the only time this has been observed to be a problem with the PDAS recorder was during the recording of controlled source data at very short ($< 1\text{km}$) path lengths (P. Denton, pers. comm.).

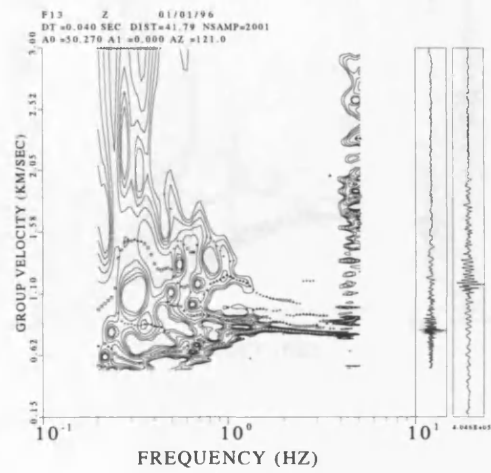
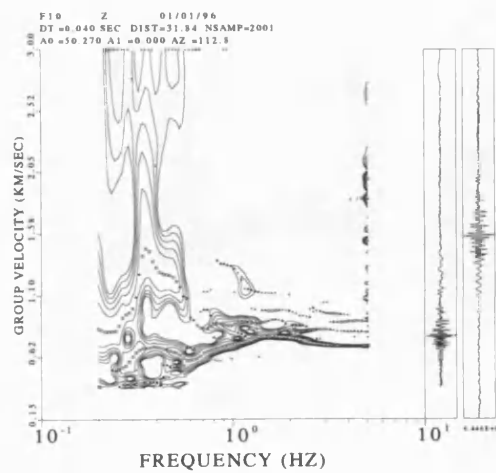
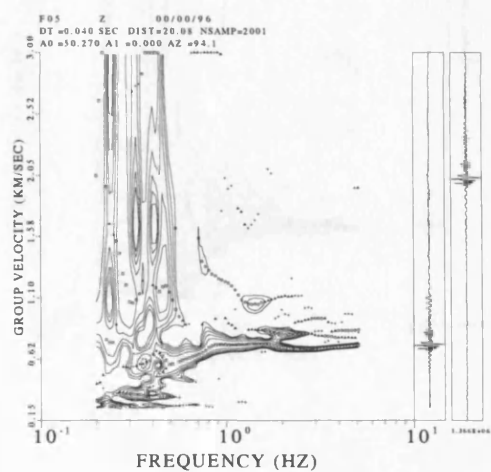
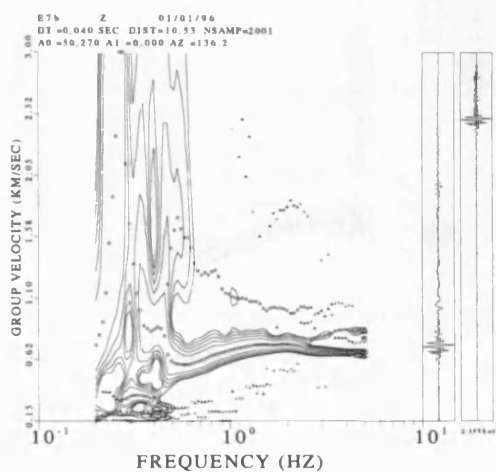
Appendix E

Stacked MFT Plots

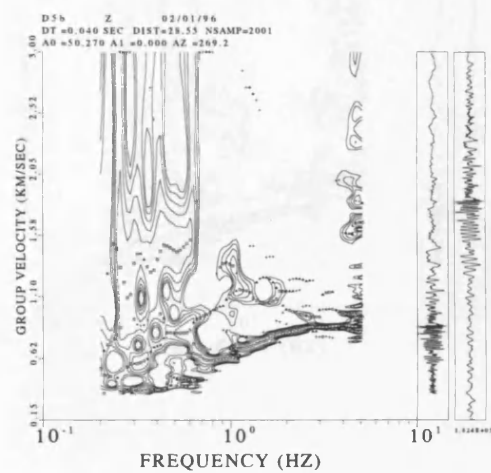
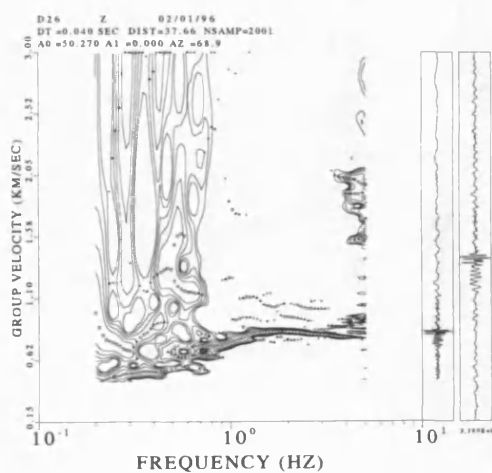
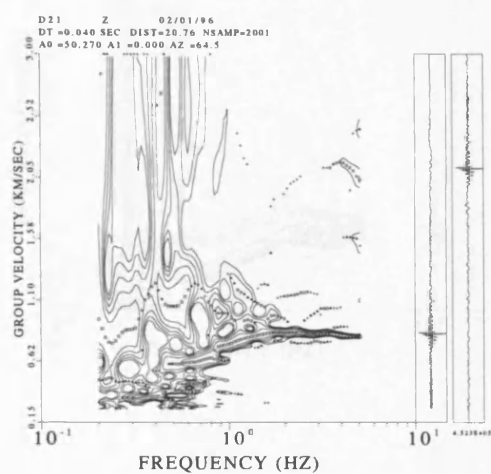
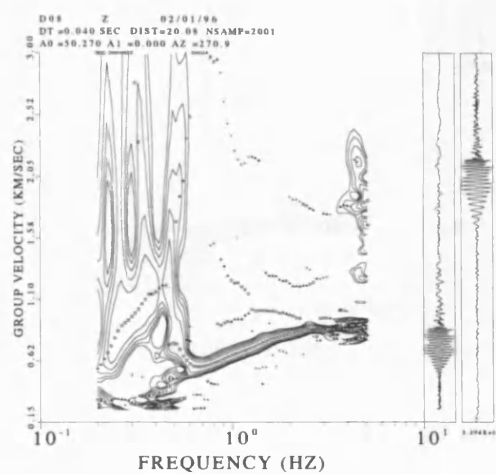
E.1 Flamboyanes Quarry

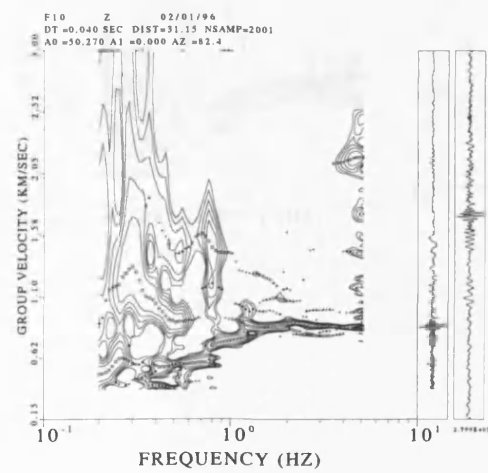
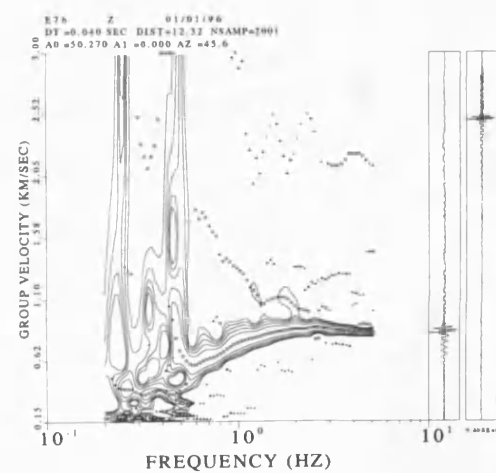
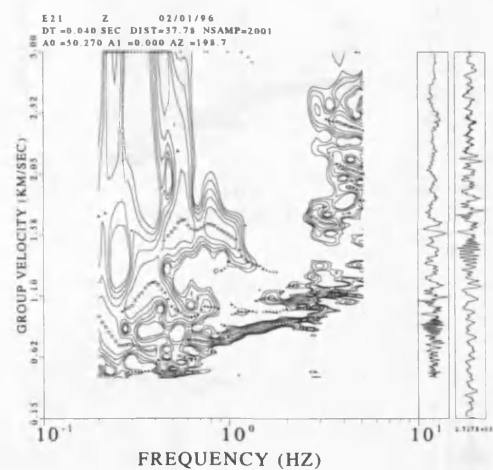
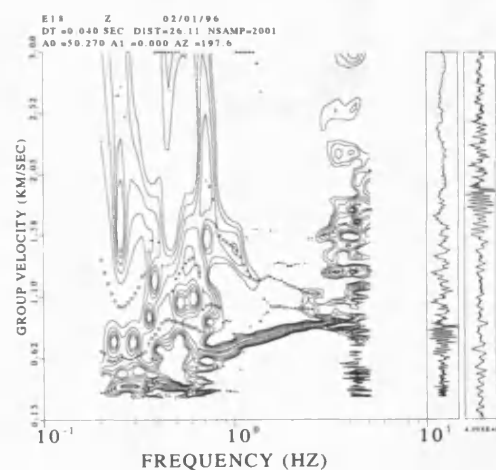
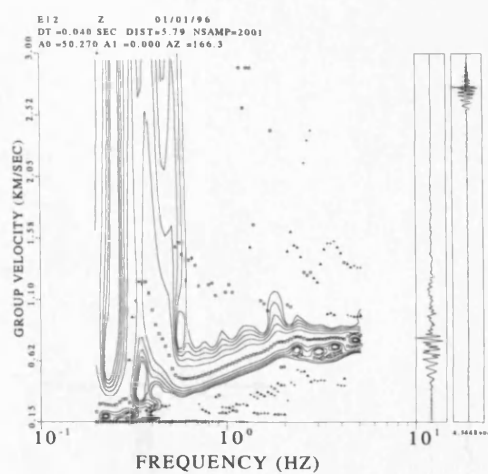
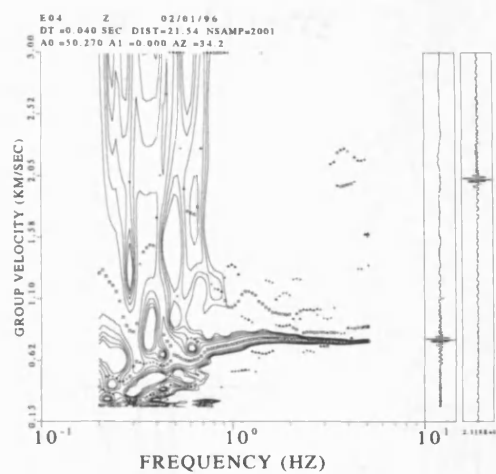




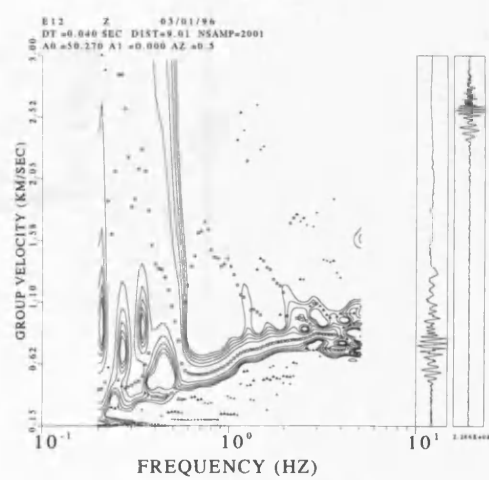
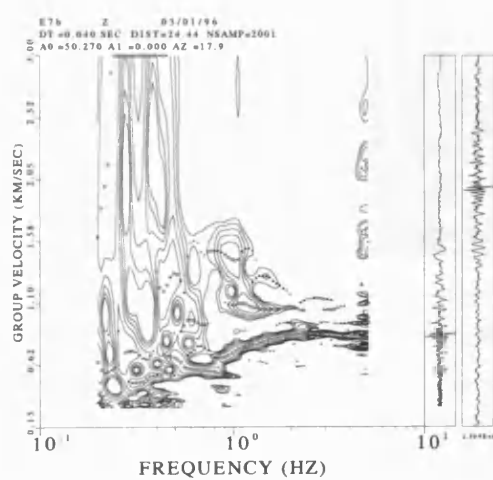
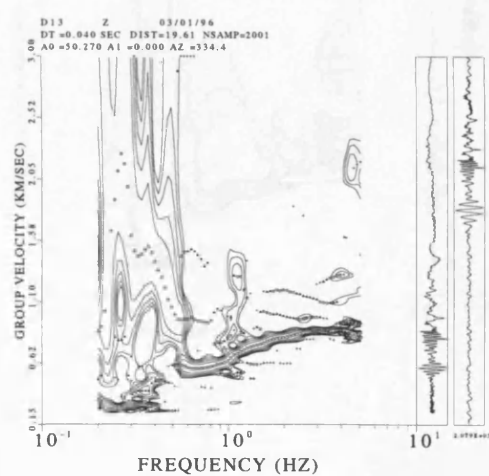
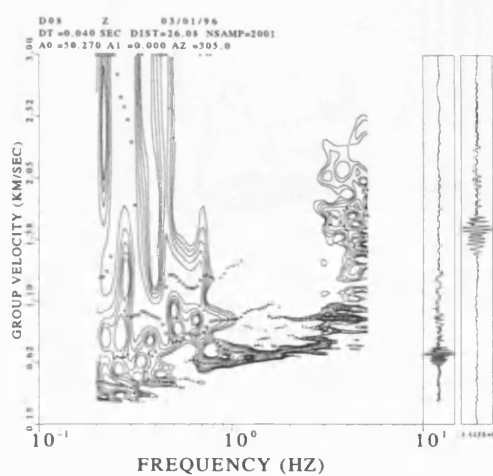


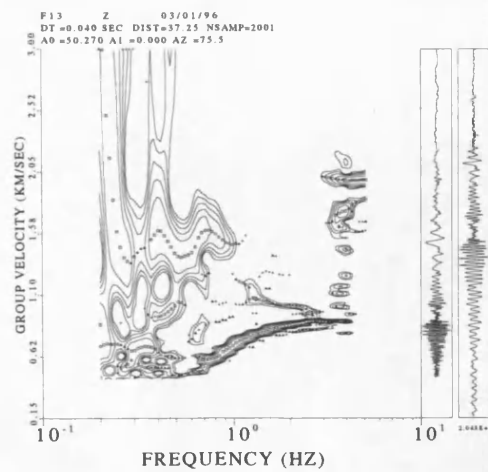
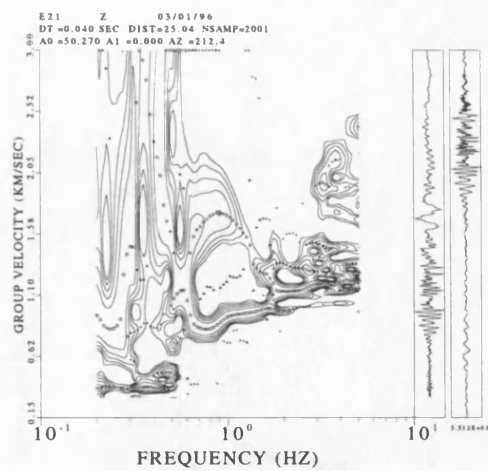
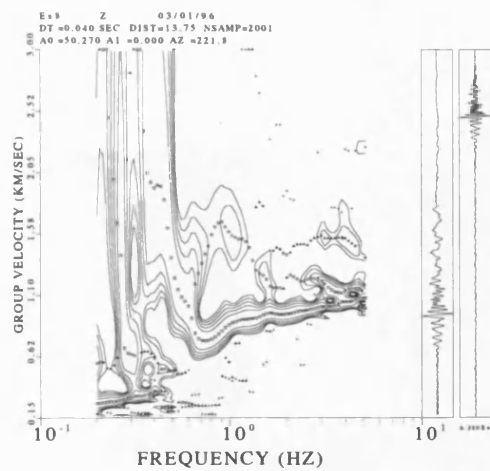
E.2 Dzitya Quarry



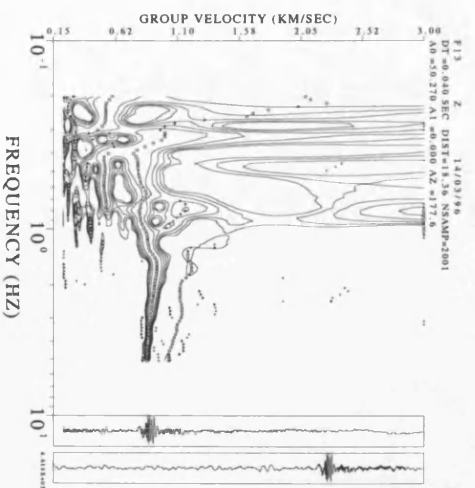
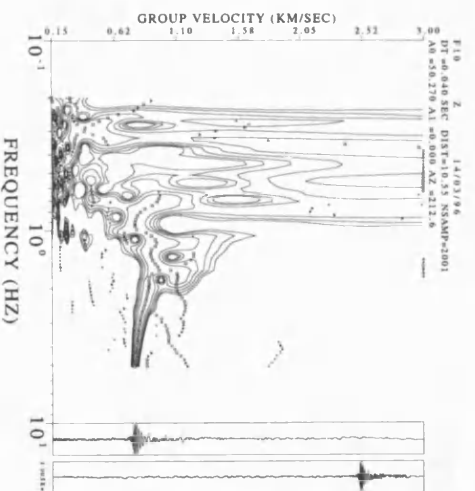
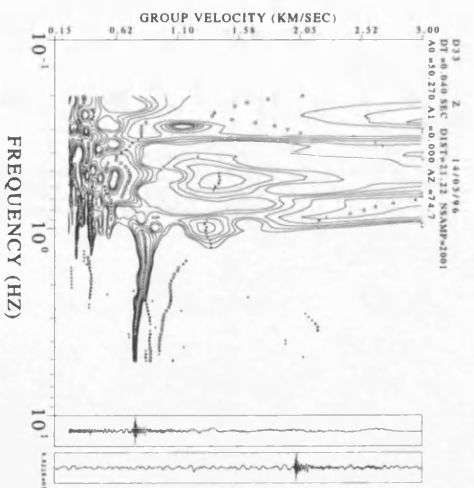
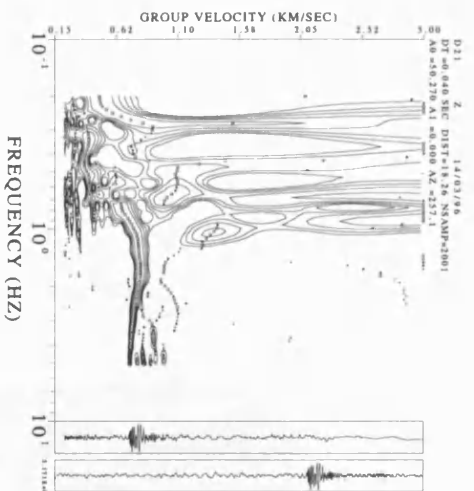


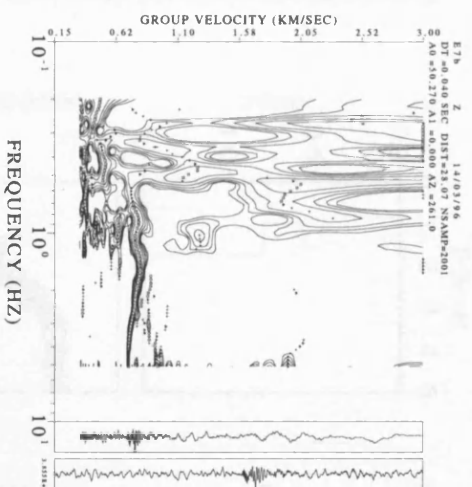
E.3 Airport Quarry





E.4 Near D26

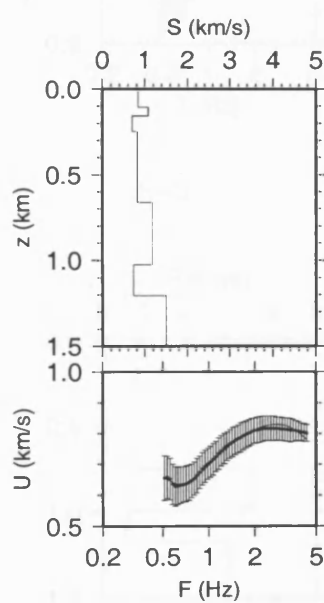




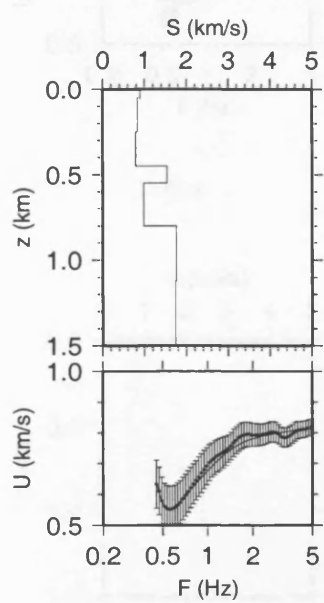
Appendix F

Models

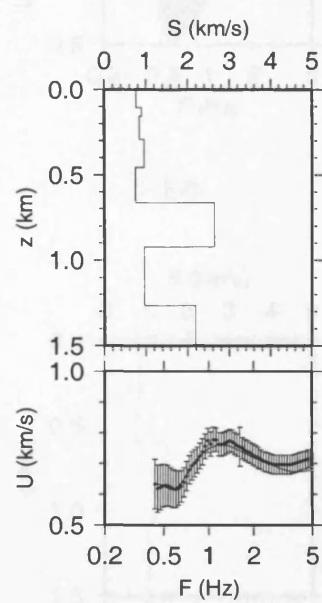
F.1 Fundamental mode models



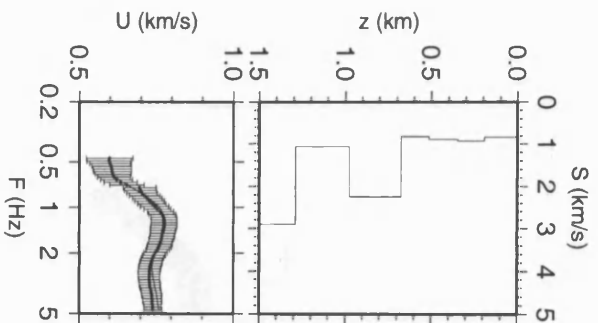
F-D08



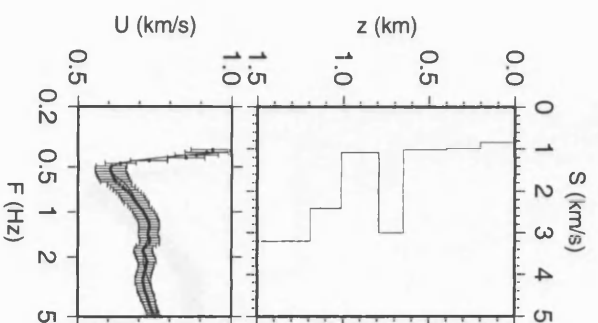
F-D13



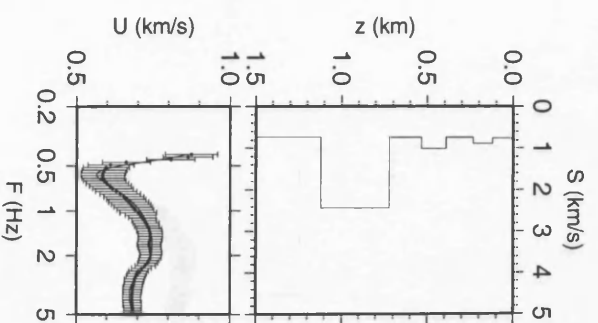
F-D21



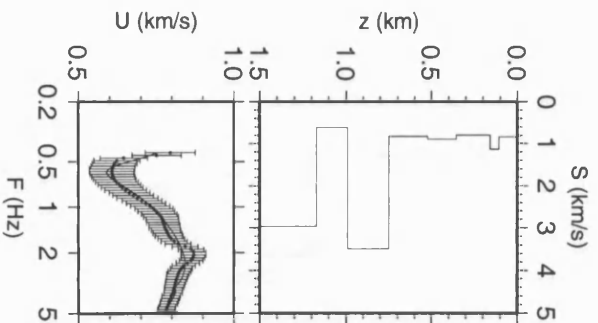
F-D26



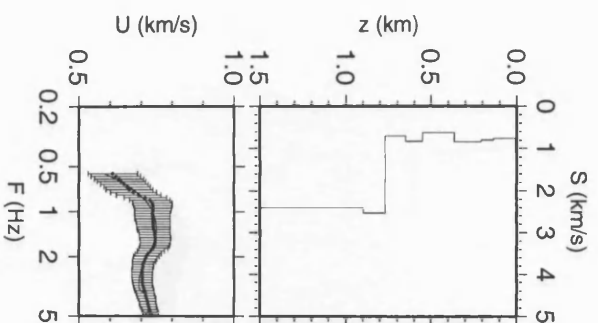
F-E04



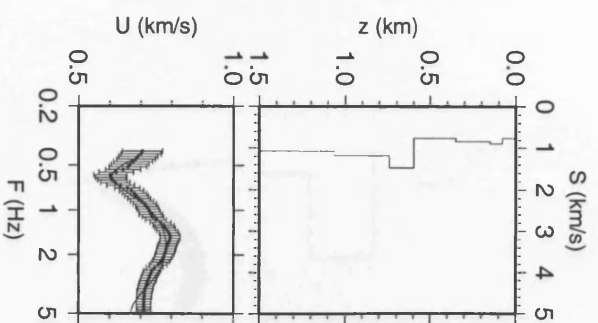
F-E7b



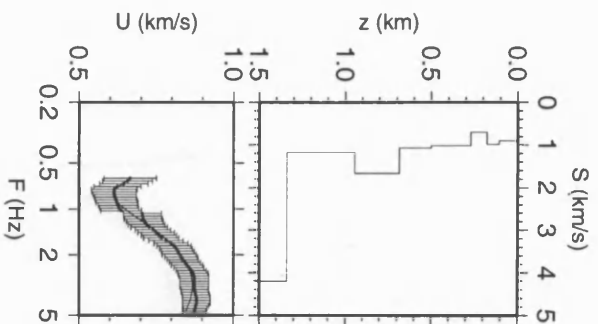
F-E12



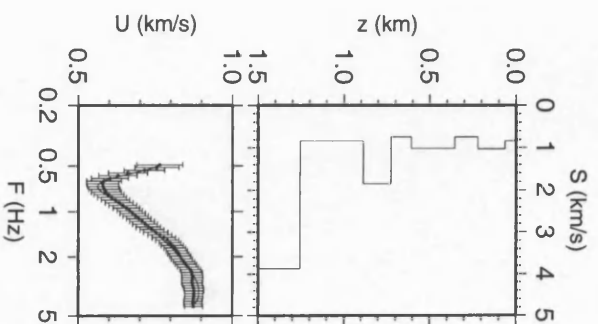
F-F05



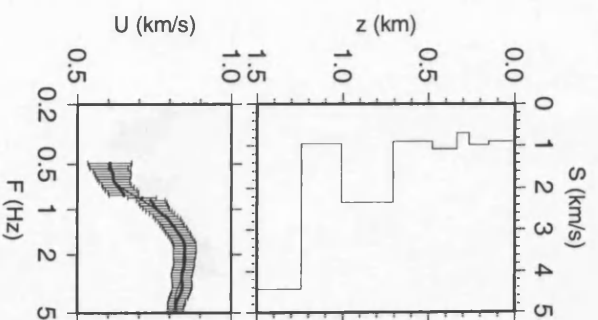
F-F10



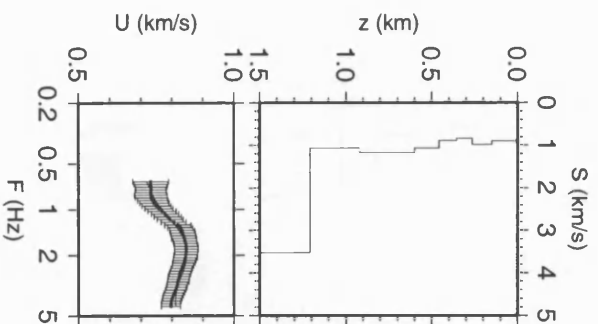
D-D5b



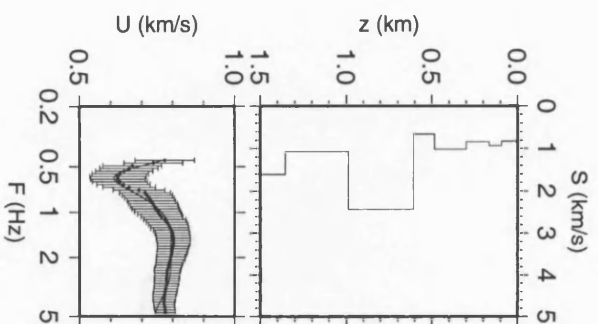
D-D08



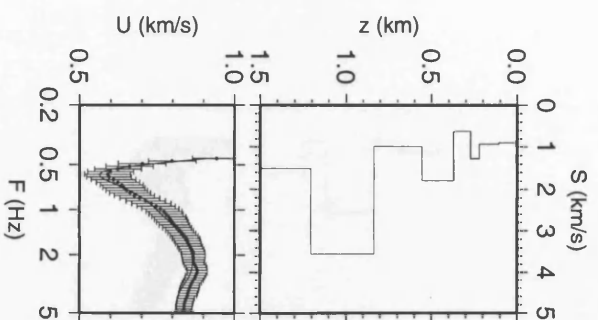
D-D21



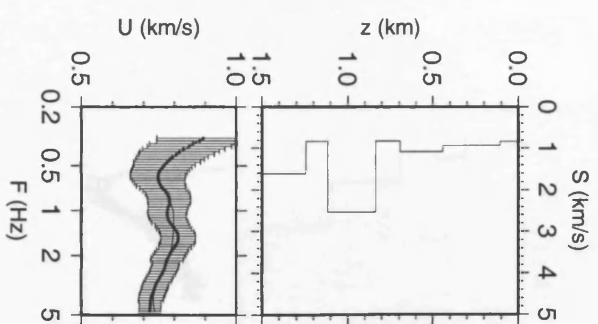
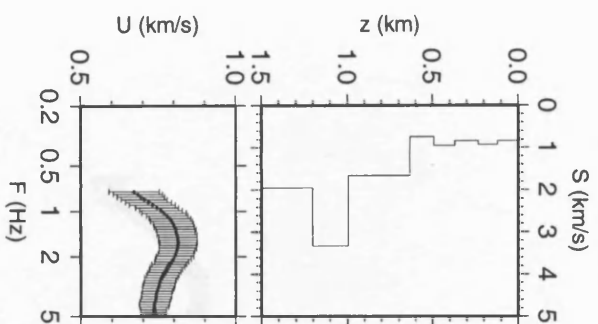
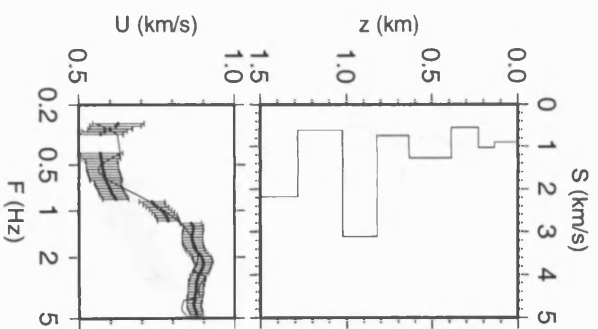
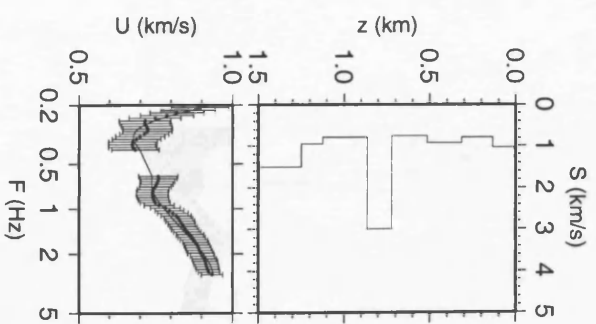
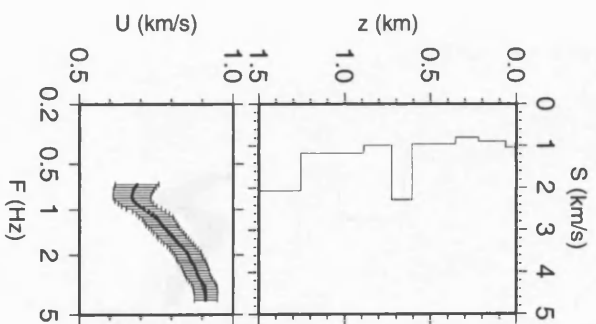
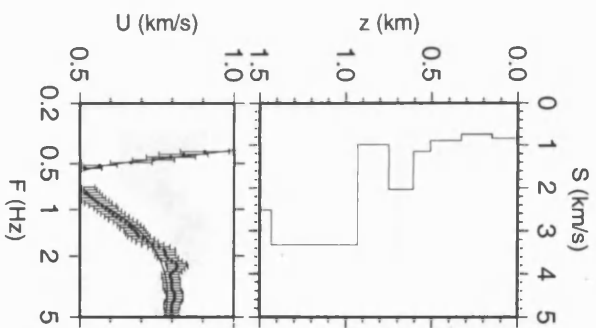
D-D26

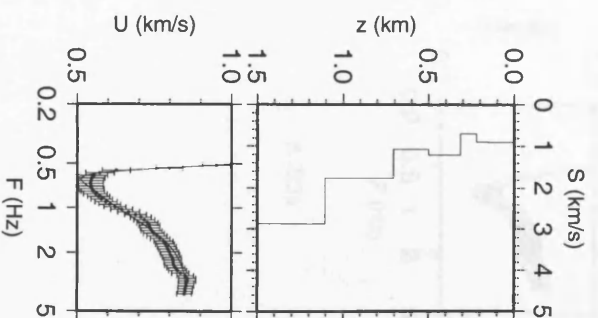
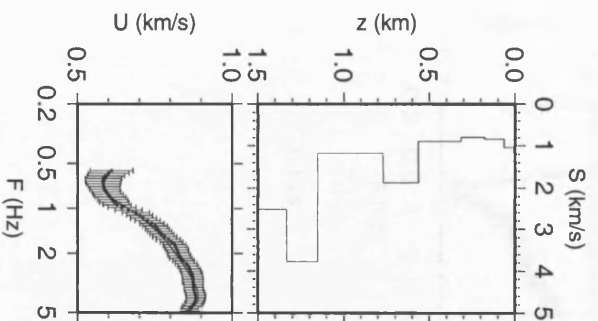
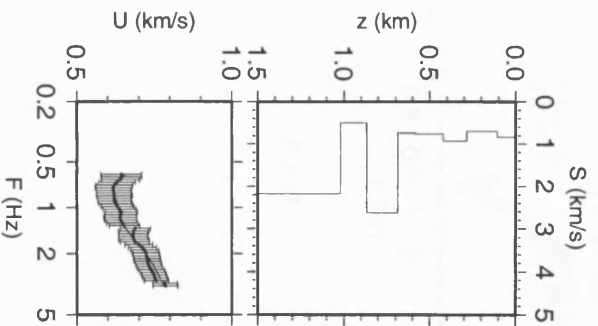
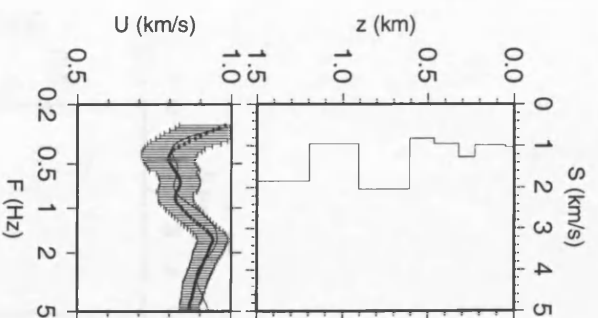
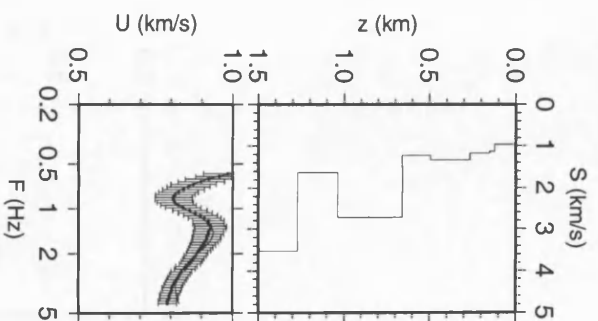
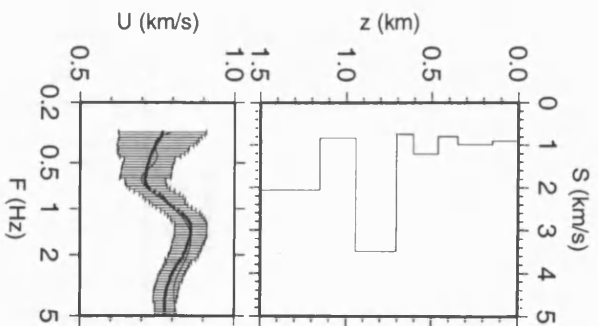


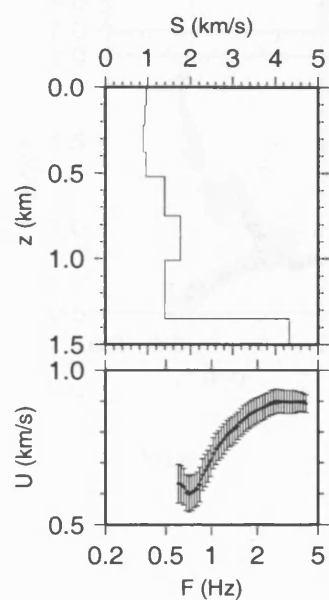
D-E04



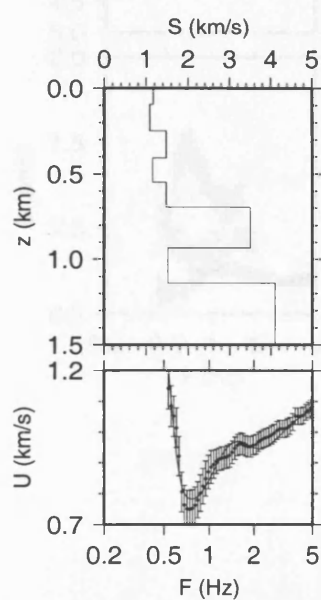
D-E7b



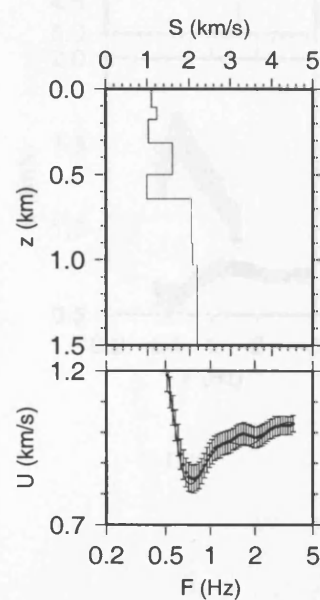




A-F13

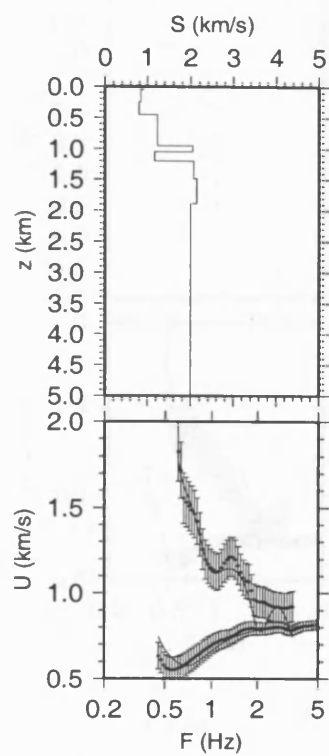


A-Es8

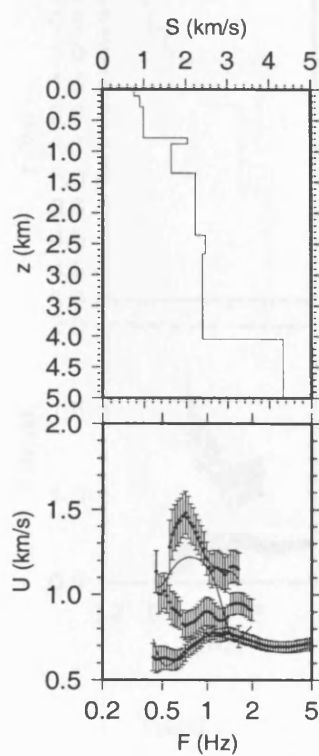


A-E21

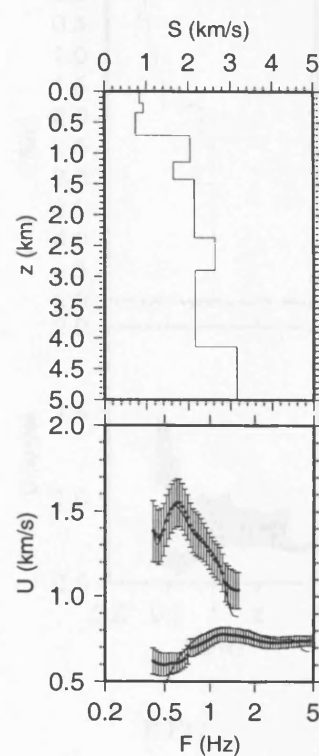
F.2 Higher mode models



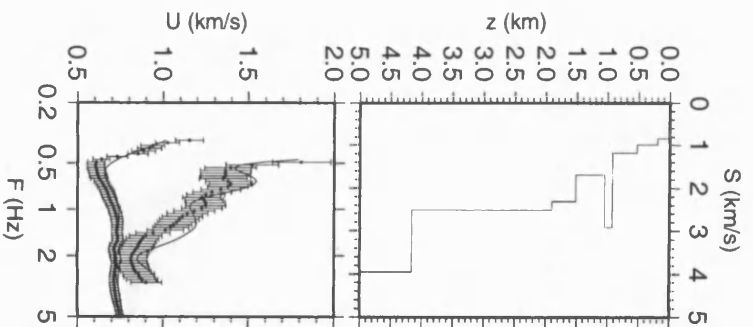
F-D13



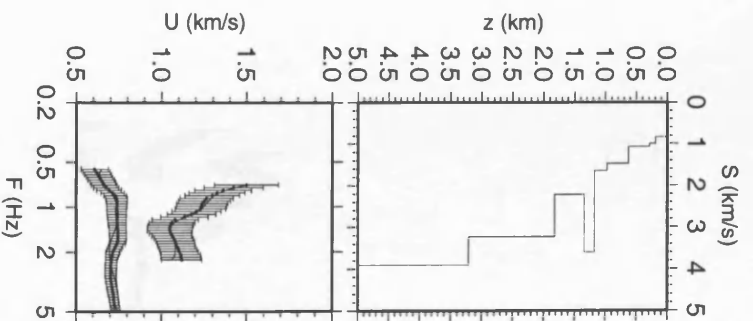
F-D21



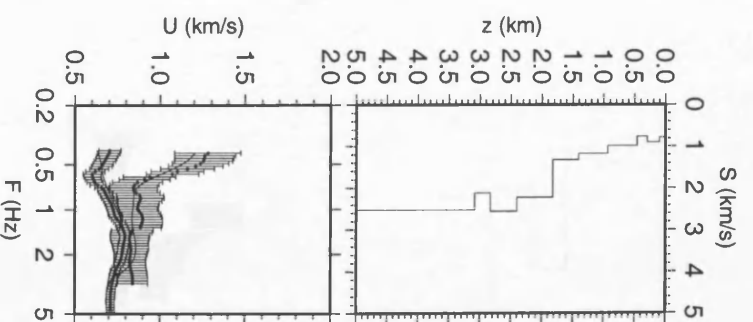
F-D26



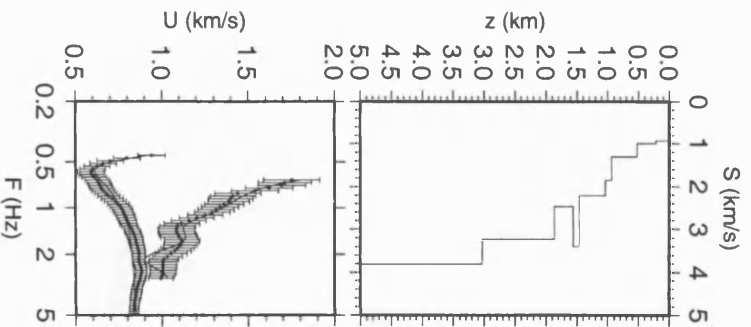
F-E04



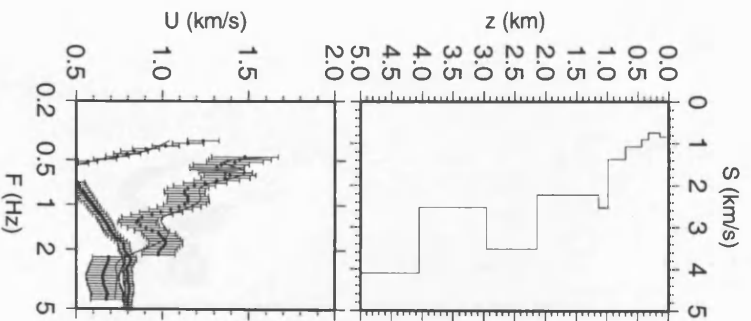
F-F05



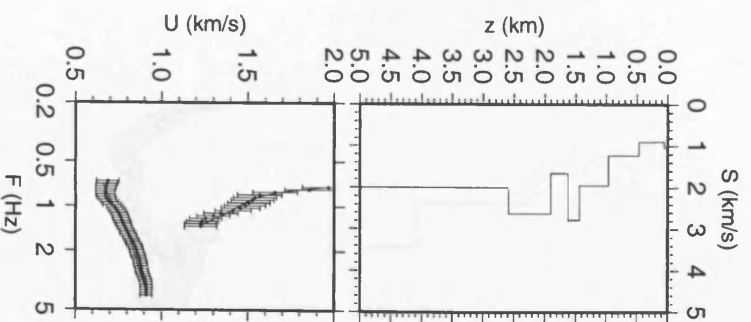
F-F10



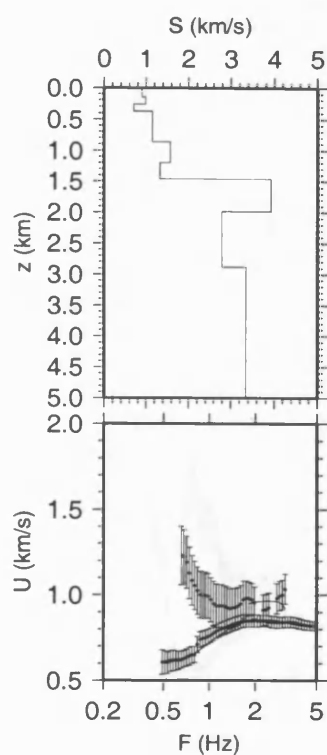
D-E7b



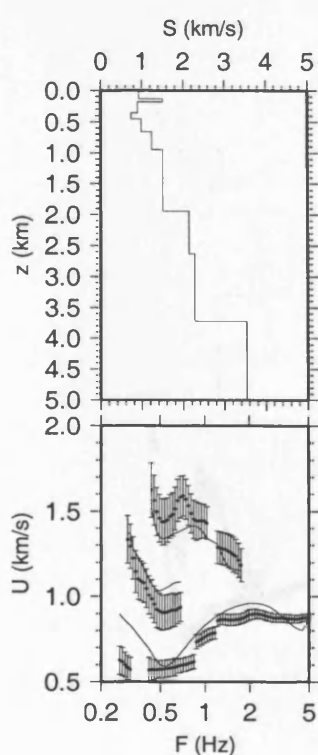
D-E12



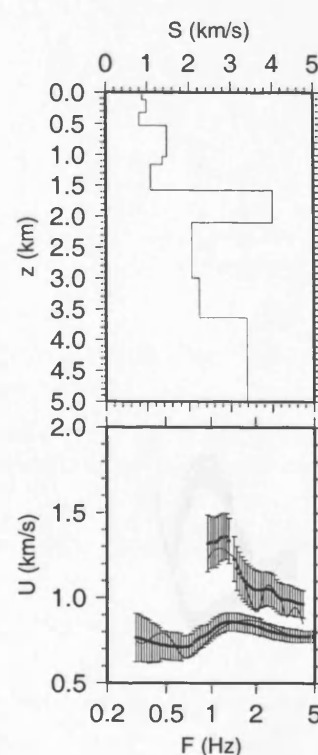
D-E18



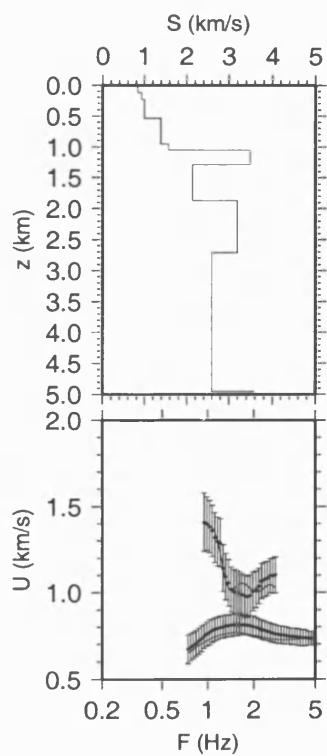
D-D21



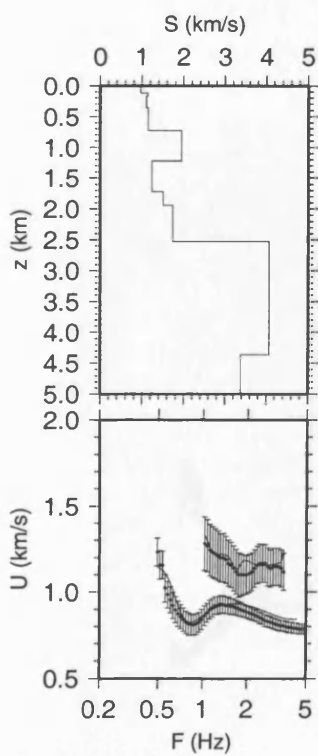
D-F10



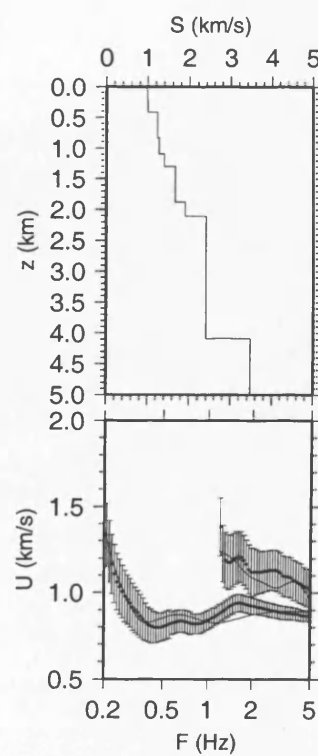
MD-D33



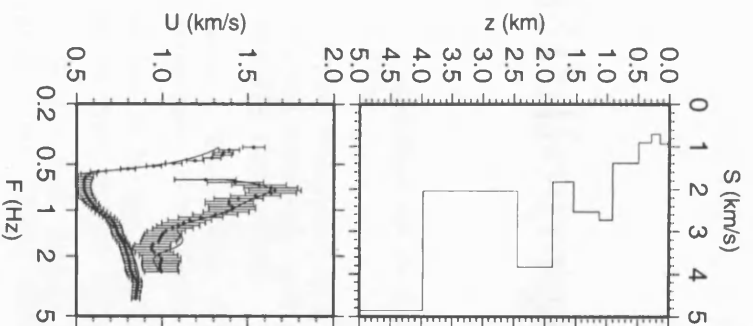
MD-D21



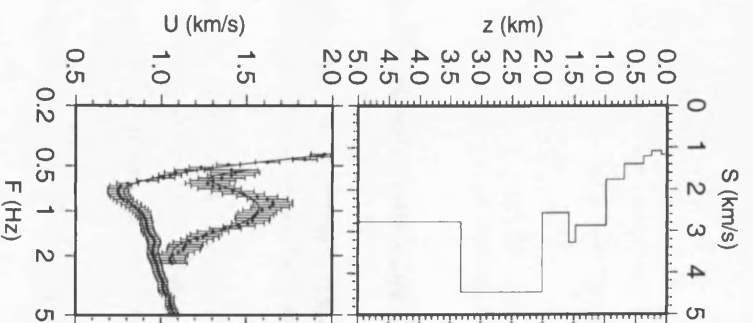
MD-F10



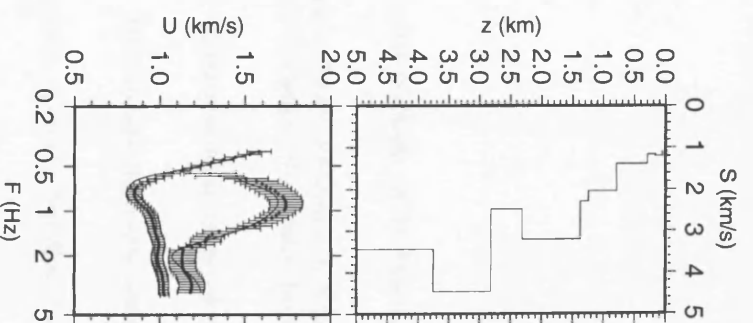
MD-F13



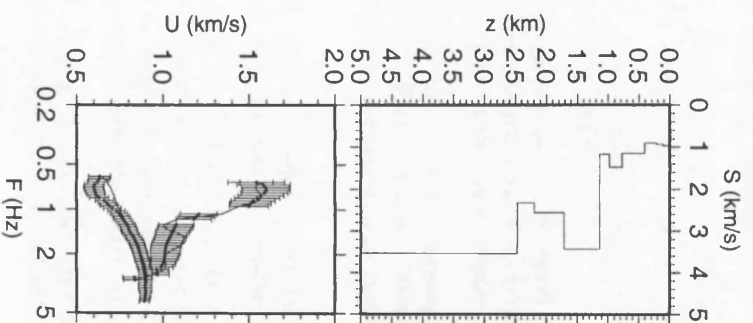
A-E12



A-Es8



A-E21



A-F13

Bibliography

- Aki, K. and Richards, P. G. (1980). *Quantitative seismology. Theory and methods*. W.H. Freeman and Co.
- Alsina, D., Woodward, R. L., and Snieder, R. K. (1996). Shear wave velocity structure in North America from large scale waveform inversions of surface waves. *J. Geophys. Res.-Solid Earth*, **101**(B7), 15969–15986.
- Alvarez, L. W., Alvarez, W., Asaro, F., and Michel, H. V. (1980). Extraterrestrial cause of the Cretaceous-Tertiary extinction. *Science*, **208**, 1095–1108.
- Anderson, D. L., Ben-Menahem, A., and Archambeau, C. B. (1965). Attenuation of seismic energy in the upper mantle. *J. Geophys. Res.*, **70**(6), 1441–1448.
- Åström, K. (1998). Seismic signature of the Lake Mien impact structure, southern Sweden. *Geophys. J. Int.*, **135**(1), 215–231.
- Bache, T. C., Rodi, W. L., and Harkrider, D. G. (1978). Crustal structure inferred from Rayleigh wave signatures of NTS explosions. *Bull. Seism. Soc. Am.*, **68**, 1399–1413.
- Backus, G. E. and Gilbert, J. F. (1967). Numerical applications of a formalism for geophysical inverse problems. *Geophys. J. R. astr. Soc.*, **13**, 247–276.
- Berry, M. J. and Fuchs, K. (1973). Crustal structure of the Superior and Grenville provinces of the north-eastern Canadian shield. *Bull. Seism. Soc. Am.*, **63**, 1393–1432.
- Bloch, S. and Hales, A. L. (1968). New techniques for the determination of surface wave phase velocities. *Bull. Seism. Soc. Am.*, **58**(3), 1021–1034.
- Blum, J. D., Chamberlain, C. P., Hingston, M. P., Koeberl, C., Marin, L. E., Schuraytz, B. C., and Sharpton, V. L. (1993). Isotopic comparison of K/T boundary impact glass with melt rock from the Chicxulub and Manson impact structures. *Nature*, **364**, 325–327.
- Bohor, B. F. (1990). Shocked quartz and more; Impact signatures in Cretaceous/Tertiary boundary clays. In V. L. Sharpton and P. D. Ward, editors, *Global catastrophes in Earth history; An interdisciplinary conference on impacts, volcanism and mass mortality*, Special Paper 247, pages 335–342. Geol. Soc. Am.
- Booker, L. (1987). Improving search in genetic algorithms. In L. Davis, editor, *Genetic Algorithms and Simulated Annealing*, Chapter 5, pages 61–73. Pitman Publishing.
- Boslough, M. B., Chael, E. P., Trucano, T. G., Crawford, D. A., and Campbell, D. L. (1996). Axial focusing of impact energy in the Earth's interior; A possible link to flood basalts and hotspots. In G. Ryder, D. Fastovsky, and S. Gartner, editors, *The Cretaceous-Tertiary event and other catastrophes in Earth history*, Special Paper 307, pages 541–550. Geol. Soc. Am.
- Brittan, J., Morgan, J., Warner, W., Marin, L., and the Chicxulub Working Group. (1998). Chicxulub seismic experiment: the first two seconds. Submitted to Sudbury 1997 Proceedings Volume.

- Brune, J. and Dorman, J. (1963). Seismic waves and Earth structure in the Canadian shield. *Bull. Seism. Soc. Am.*, **53**(1), 167–210.
- Brune, J. N. (1969). Surface waves and crustal structure. In P. J. Hart, editor, *The Earth's crust and upper mantle*, Geophysical Monograph 13, Chapter 3, pages 230–241. Am. Geophys. Un.
- Bullen, K. E. (1939). On Rayleigh waves across the Pacific Ocean. *Mon. Not. Roy. astr. Soc. Geophys. Suppl.*, **4**, 579–582.
- Bunch, T. E. (1968). Some characteristics of selected minerals from craters. In B. M. French and N. M. Short, editors, *Shock metamorphism of natural materials*, pages 413–432. Mono Book Corp.
- Burkhardt, H. and Vees, R. (1976). Seismic signals from quarry blasts. In P. Giese, C. Prodhel, and A. Stein, editors, *Explosion seismology in central Europe.*, Chapter 3.2, pages 62–72. Springer-Verlag.
- Burton, P. W. (1974). Estimations of Q_{γ}^{-1} from seismic Rayleigh waves. *Geophys. J. R. astr. Soc.*, **36**, 167–189.
- Camargo-Zanoguera, A. and Suárez-Reynoso, G. (1994). Evidencia sísmica del cráter de impacto de Chicxulub. *Boletín de la Asociación Mexicana de Geofísicos de Exploración*, **34**(1), 1–28.
- Campos-Enríquez, J. O., Arzate, J. A., Urrutia-Fucugauchi, J., and Delgado-Rodríguez, O. (1997). The subsurface structure of the Chicxulub crater (Yucatán, Mexico): Preliminary results of a magnetotelluric study. *The Leading Edge*, **16**(12), 1774–1777.
- Campos-Enríquez, J. O., Morales-Rodríguez, H. F., Domínguez-Méndez, F., and Birch, F. S. (1998). Gauss's theorem, mass deficiency at Chicxulub crater (Yucatan, Mexico), and the extinction of the dinosaurs. *Geophys.*, **63**(5), 1585–1594.
- Carmichael, R. S. editor (1982). *Handbook of physical properties of rocks*. CRC Press.
- Chavez-Garcia, F. J., Ramos-Martinez, J., and Romeroji-Menez, E. (1995). Surface-wave dispersion analysis in Mexico City. *Bull. Seism. Soc. Am.*, **85**(4), 1116–1126.
- Chilingar, G. V., Zenger, D. H., Bissell, H. J., and Wolf, K. H. (1985). Dolomites and dolomitization. In G. Larsen and G. V. Chilingar, editors, *Diagenesis in sediments and sedimentary rocks*, Developments in Sedimentology 25A, Chapter 7, pages 423–536. Elsevier Science.
- Christeson, G. L., Buffer, R. T., Nakamura, Y., and the Chicxulub Working Group (1998). Structure of the Chicxulub impact crater from wide-angle ocean bottom seismograph data. Submitted to Sudbury 1997 Proceedings Volume.
- Chunduru, R. K., Sen, M. K., and Stoffa, P. L. (1997). Hybrid optimization methods for geophysical inversion. *Geophys.*, **62**(4), 1196–1207.
- Claeys, P. (1995). When the sky fell on our heads: identification and interpretation of impact products in the sedimentary record. *Rev. Geophys.*, **33**(Pt 1. SS), 95–100.
- Connors, M., Hildebrand, A. R., Pilkington, M., Ortiz-Aleman, C., Chavez, R. E., Urrutia-Fucugauchi, J., Graniel-Castro, E., Camara-Zi, A., Vasquez, J., and Halpenny, J. F. (1996). Yucatan karst features and the size of Chicxulub crater. *Geophys. J. Int.*, **127**(3), F11–F14.
- Cué, V. A. (1953). Determinación de velocidades sísmicas en el pozo Chicxulub No. 1. *Boletín de la Asociación Mexicana de Geólogos Petroleros*, **5**, 285–290.
- Davis, J. C., (1973) *Statistics and Data Analysis in Geology*. Wiley International.
- Davis, L., editor (1996). *Handbook of Genetic Algorithms*. International Thomson Computer Press.

- De Laubenfels, M. W. (1956). Dinosaur extinction: one more hypothesis. *J. of Palaeontology*, **30**, 207–218.
- DeJong, K. A. (1975). *Analysis of the behaviour of a class of genetic adaptive systems*. Ph.D. thesis, University of Michigan.
- Dence, M. R., Grieve, R. A. F., and Robertson, P. B. (1977). Terrestrial impact craters: Principal characteristics and energy considerations. In D. J. Roddy, R. O. Pepin, and R. B. Merrill, editors, *Impact and explosion cratering*, pages 247–275. Pergamon Press.
- Denny, M. O. and Chin, R. C. Y. (1976). Gaussian filters for determining group velocity. *Geophys. J. R. astr. Soc.*, **45**, 495–525.
- Der, Z. A. (1986). Comments on the paper “Estimation of scalar moments from explosion-generated surface waves” by Jeffrey L. Stevens. *Bull. Seism. Soc. Am.*, **76**(6), 1822–1824.
- D’Hondt, S., Pilson, M. E. Q., Sigurdsson, H., Hanson, A. K., and Carey, S. (1994). Surface-water acidification and extinction at the Cretaceous-Tertiary boundary. *Geology*, **22**(11), 983–986.
- Dietz, R. S. (1968). Shatter cones in cryptoexplosion structures. In B. M. French and N. M. Short, editors, *Shock metamorphism of natural materials*, pages 267–285. Mono Book Corp.
- Donofrio, R. R. (1981). Impact craters: Implications for basement hydrocarbon production. *J. Petroleum Geol.*, **3**(3), 279–302.
- Drijkoningen, G. G. and White, R. S. (1995). Seismic velocity structure of oceanic-crust by inversion using genetic algorithms. *Geophys. J. Int.*, **123**(3), 653–664.
- Dunkin, J. W. (1965). Computation of modal solutions in layered, elastic media at high frequencies. *Bull. Seism. Soc. Am.*, **55**(2), 335–358.
- Dziewonski, A. M., Bloch, S., and Landisman, M. (1969). A technique for the analysis of transient seismic signals. *Bull. Seism. Soc. Am.*, **59**, 427–444.
- Espindola, J. M., Mena, M., De la Fuente, M., and Campos-Enriquez, J. O. (1995). A model of the Chicxulub impact structure (Yucatan, Mexico) based on its gravity and magnetic signatures. *Phys. Earth Planet. Inter.*, **92**(3–4), 271–278.
- Evans, A. C. (1981). *Propagation and dissipation of VHF Rayleigh waves in Scotland*. Ph.D. thesis, University of Edinburgh.
- Everett, M. E. and Schultz, A. (1993). 2-dimensional nonlinear magnetotelluric inversion using a genetic algorithm. *J. Geomagnetism Geoelectricity*, **45**(9), 1013–1026.
- Evernden, J. F. (1953). Direction of approach of Rayleigh waves and related problems (Part I). *Bull. Seism. Soc. Am.*, **43**, 335–374.
- Evernden, J. F. (1954). Direction of approach of Rayleigh waves and related problems (Part II). *Bull. Seism. Soc. Am.*, **44**, 159–184.
- Ewing, J. I., Edgar, N. T., and Antoine, J. W. (1970). *The Sea*, Volume 4: New Concepts of Sea Floor Evolution, Part II, Chapter 10: Structure of the Gulf of Mexico and Caribbean Sea, pages 321–358. Wiley.
- Ewing, M. and Press, F. (1954). An investigation of mantle Rayleigh waves. *Bull. Seism. Soc. Am.*, **44**, 127–148.
- Ewing, W. M., Jardetsky, W. S., and Press, F. (1957). *Elastic waves in layered media*. McGraw Hill.
- Fix, J. E. (1975). The crust and upper mantle of central Mexico. *Geophys. J. R. astr. Soc.*, **43**, 453–500.

- Forrest, S. (1993). Genetic algorithms: Principles of natural selection applied to computation. *Science*, **261**(5123), 872–878.
- Friedman, G. M. (1996). Yucatan subsurface stratigraphy: Implications and constraints for the Chicxulub impact: Discussion. *Carbonates and Evaporites*, **11**(1), 141–142.
- Friedman, G. M. (1997). Dissolution-collapse breccias and paleokarst resulting from dissolution of evaporite rocks, especially sulfates. *Carbonates and Evaporites*, **12**(1), 53–63.
- Gallagher, K. (1995). Evolving temperature histories from apatite fission-track data. *Earth Planet. Science Lett.*, **136**(3–4), 421–435.
- Gallagher, K. and Sambridge, M. (1994). Genetic algorithms: A powerful tool for large-scale nonlinear optimization problems. *Computers & Geosciences*, **20**, 1229–1236.
- Gault, D. E., Quaide, W. L., and Oberbeck, V. R. (1968). Impact cratering mechanics and structures. In B. M. French and N. M. Short, editors, *Shock metamorphism of natural materials*, pages 87–99. Mono Book Corp.
- Gibbs, J. F., Boore, D. M., Joyner, W. B., and Fumal, T. E. (1994). The attenuation of seismic shear waves in Quaternary alluvium in Santa Clara valley, California. *Bull. Seism. Soc. Am.*, **84**(1), 76–90.
- Gilbert, F. and Backus, G. E. (1966). Propagator matrices in elastic wave and vibration problems. *Geophys.*, **31**(2), 326–332.
- Gilmour, I. (1998). Geochemistry of carbon in terrestrial impact processes. In M. M. Grady, R. Hutchison, G. J. H. McCall, and D. A. Rothery, editors, *Meteorites: flux with time and impact effects*, Special Publication 140, pages 205–216. Geological Society, London.
- Glass, B. P. (1990). Tektites and microtektites: key facts and inferences. *Tectonophysics*, **171**, 393–404.
- Glikson, A. Y. (1995). Asteroid/comet mega-impacts may have triggered major episodes of crustal evolution. *Eos*, **76**(6), 49,54–55.
- Goldberg, D. E. (1987). Simple genetic algorithms and the minimal, deceptive problem. In L. Davis, editor, *Genetic algorithms and simulated annealing*, Chapter 6, pages 74–88. Pitman Publishing.
- Goldberg, D. E. (1989). *Genetic Algorithms in Search, Optimization, and Machine Learning*. Addison-Wesley.
- Gomberg, J. S. and Masters, T. G. (1988). Waveform modelling using locked mode synthetic and differential seismograms: application to determination of the structure of Mexico. *Geophys. J. Int.*, **94**(2), 193–218.
- Gomberg, J. S., Priestley, K. F., Masters, T. G., and Brune, J. N. (1988). The structure of the crust and upper mantle of northern Mexico. *Geophys. J. Int.*, **94**(1), 1–20.
- Green, R. W. and Chetty, P. (1990). Seismic refraction studies in the basement of the Vredefort structure. *Tectonophysics*, **171**, 105–113.
- Grieve, R. A. F. (1987). Terrestrial impact structures. *Ann. Rev. Earth Planet. Sci.*, **15**, 245–270.
- Grieve, R. A. F. (1998). Extraterrestrial impacts on earth: the evidence and the consequences. In M. M. Grady, R. Hutchison, G. J. H. McCall, and D. A. Rothery, editors, *Meteorites: flux with time and impact effects*, Special Publication 140, pages 105–131. Geological Society, London.
- Grieve, R. A. F., Dence, M. R., and Robertson, P. B. (1977). Cratering processes: As interpreted from the occurrence of impact melts. In D. J. Roddy, R. O. Pepin, and R. B. Merrill, editors, *Impact and explosion cratering*, pages 791–814. Pergamon Press.

- Hallam, A. and Wignall, P. B. (1997). *Mass extinctions and their aftermath*, Chapter 9, pages 184–222. Oxford University Press.
- Harkrider, D. G. and Anderson, D. L. (1966). Surface wave energy from point sources in plane layered Earth models. *J. Geophys. Res.*, **71**, 2967–2980.
- Hartzell, S. and Liu, P. C. (1995). Determination of earthquake source parameters using a hybrid global search algorithm. *Bull. Seism. Soc. Am.*, **85**(2), 516–524.
- Haskell, N. A. (1953). The dispersion of surface waves on multilayered media. *Bull. Seism. Soc. Am.*, **43**, 17–34.
- Haskov, J. (1995). *The SEISAN earthquake analysis software*. University of Bergen, 5th edition.
- Hedlin, M. A. H., Minster, J. B., and Orcutt, J. A. (1989). An automatic means to discriminate between earthquakes and quarry blasts. *Bull. Seism. Soc. Am.*, **80**(6), 2143–2160.
- Herrin, E. and Goforth, T. (1977). Phase-matched filters: Application to the study of Rayleigh waves. *Bull. Seism. Soc. Am.*, **76**(6), 1739–1754.
- Herrmann, R. B. (1969). The structure of the Cincinnati Arch as determined by short-period Rayleigh waves. *Bull. Seism. Soc. Am.*, **59**, 399–407.
- Herrmann, R. B. (1973). Some aspects of band-pass filtering of surface waves. *Bull. Seism. Soc. Am.*, **63**(2), 663–671.
- Herrmann, R. B. (1987). *Computer programs in seismology*. St. Louis University.
- Herrmann, R. B. and Mitchell, B. J. (1975). Anelastic attenuation data for stable interior of North America. *Bull. Seism. Soc. Am.*, **65**, 1115–1128.
- Hildebrand, A. R., Penfield, G. T., Kring, D. A., Pilkington, M., Camargo, A., Jacobsen, S. B., and Boynton, W. V. (1991). Chicxulub crater - a possible Cretaceous Tertiary boundary impact crater on the Yucatan peninsula, Mexico. *Geology*, **19**, 867–871.
- Hildebrand, A. R., Connors, M., Pilkington, M., Ortiz-Aleman, C., and Chavez, R. E. (1994). Size and structure of the Chicxulub crater. *Revista de la Sociedad Mexicana de Paleontologia*, **7**(1), 59–68.
- Hildebrand, A. R., Pilkington, M., Connors, M., Ortiz-Aleman, C., and Chavez, R. E. (1995). Size and structure of the Chicxulub crater revealed by horizontal gravity gradients and cenotes. *Nature*, **376**(6539), 415–417.
- Hildebrand, A. R., Pilkington, M., Halpenny, J. F., Cooper, R. V., Connors, M., Ortiz-Aleman, C., Chavez, R. E., Urrutia-Fucugauchi, J., Graniel-Castro, E., Camara-Zi, A., and Buffler, R. T. (1997). The Chicxulub crater as revealed by gravity and seismic surveys. *Eos Trans. AGU*, **78**(46), F398. Fall Meet. Suppl.
- Hildebrand, A. R., Pilkington, M., Ortiz-Aleman, C., Chavez, R. E., Urrutia-Fucugauchi, J., Halpenny, J. F., and Niehaus, D. (1998). Mapping Chicxulub crater structure with gravity and seismic reflection data. In M. M. Grady, R. Hutchison, G. J. H. McCall, and D. A. Rothery, editors, *Meteorites: flux with time and impact effects*, Special Publication 140, pages 155–176. Geological Society, London.
- Holland, J. H. (1975). *Adaptation in Natural and Artificial Systems*. University of Michigan Press.
- Holland, J. H. (1992). Genetic algorithms. *Scientific American*, **267**(1), 44–50.
- Hörz, F. (1982). Ejecta of the Ries crater, Germany. In L. T. Silver and P. H. Shultz, editors, *Geological implications of impacts of large asteroids and comets on the Earth*, Special Paper 190, pages 39–53. Geol. Soc. Am.

- Hutchenson, K. D. (1994). *Shallow structure of the Illinois basin from fundamental and higher-mode regional surface wave dispersion*. Ph.D. thesis, St. Louis University.
- Israelsson, H. (1990). Correlation of waveforms from closely spaced regional events. *Bull. Seism. Soc. Am.*, **80**(6), 2177–2193.
- Ivany, L. C. and Salawitch, R. J. (1993). Carbon isotopic evidence for biomass burning at the K–T boundary. *Geology*, **21**(6), 487–490.
- Jackson, D. D. (1972). Interpretation of inaccurate, insufficient and inconsistent data. *Geophys. J. R. astr. Soc.*, **28**, 97–109.
- Jeffreys, H. (1925). On the surface waves of earthquakes. *Mon. Not. Roy. astr. Soc. Geophys. Suppl.*, **1**, 282–292.
- Jeffreys, H. (1961). Small correction in the theory of surface waves. *Geophys. J. R. astr. Soc.*, **6**, 115–117.
- Jongmans, D. and Demanet, D. (1993). The importance of surface vibration study and the use of Rayleigh waves for estimating the dynamic characteristics of soils. *Eng. Geol.*, **34**, 105–113.
- Kafka, A. L. and Dollin, M. F. (1985). Constraints on lateral variation in upper crustal structure beneath southern New England from dispersion from Rg waves. *Geophys. Res. Lett.*, **12**(5), 235–238.
- Kennett, J. P. (1982). *Marine Geology*. Prentice Hall.
- Kido, M., Yuen, D. A., Cadek, O., and Nakakuki, T. (1998). Mantle viscosity derived by genetic algorithm using oceanic geoid and seismic tomography for whole-mantle versus blocked-flow situations. *Phys. Earth Planet. Inter.*, **107**(4), 307–326.
- Kieffer, S. W. (1977). Impact conditions required for formation of melt by jetting in silicates. In D. J. Roddy, R. O. Pepin, and R. B. Merrill, editors, *Impact and explosion cratering*, pages 751–769. Pergamon Press.
- King, S. D. (1995). Radial models of mantle viscosity - results from a genetic algorithm. *Geophys. J. Int.*, **122**(3), 725–734.
- Kisslinger, C. and Engdahl, E. R. (1973). The interpretation of the Wadati diagram with relaxed assumptions. *Bull. Seism. Soc. Am.*, **63**, 1723–1736.
- Klein, F. W. (1990). Users guide to HYPOINVERSE, a program for VAX computers to solve for earthquake locations and magnitudes. USGS Open File Report 89-314.
- Knopoff, L. (1964). *Q. Rev. Geophys.*, **2**(4), 625–660.
- Knopoff, L. and Schwab, F. A. (1968). Apparent initial phase of a source of Rayleigh waves. *J. Geophys. Res.*, **73**, 755–760.
- Koch, K. and Stump, B. W. (1996). Constraints for upper mantle shear-wave models of the Basin and Range from surface-wave inversion. *Bull. Seism. Soc. Am.*, **86**(5), 1591–1607.
- Koeberl, C., Sharpton, V. L., Schuraytz, B. C., Shirey, S. B., Blum, J. D., and Marin, L. E. (1994). Evidence for a meteoritic component in impact melt rock from the Chicxulub structure. *Geochimica Et Cosmochimica Acta*, **58**(6), 1679–1684.
- Kring, D. A. (1995). The dimensions of the Chicxulub impact crater and impact melt sheet. *J. Geophys. Res. -Planets*, **100**(E8), 16979–16986.
- Krogh, T. E., Kamo, S. L., Sharpton, V. L., Marin, L. E., and Hildebrand, A. R. (1993). U-Pb ages of single shocked zircons linking distal K/T ejecta to the Chicxulub crater. *Nature*, **366**, 731–734.

- Kyte, F. T. (1998). A meteorite from the Cretaceous/Tertiary boundary. *Nature*, **369**, 237–239.
- Lamb, H. (1903). On the propagation of tremors over the surface of an elastic solid. *Phil. Trans.*, **203**, 1–42.
- Lange, M. A. and Ahrens, T. D. (1982). The evolution of an impact-generated atmosphere. *Icarus*, **51**, 96–120.
- Lanzcos, C. (1961). *Linear differential operators*, Chapter 3, pages 665–679. Van Nostrand.
- Lawson, C. L. and Hanson, R. J. (1974). *Solving least squares problems*. Prentice Hall.
- Lee, W. B. and Solomon, S. C. (1978). Simultaneous inversion of surface waves phase velocity and attenuation: Love waves in western North America. *J. Geophys. Res.*, **83**, 3389–3400.
- Lee, W. H. K. and Stewart, S. W. (1981). *Principles and Applications of Microearthquake Networks*. Advances in Geophysics 2. Academic Press.
- Levenberg, K. (1944). A method for the solution of certain non-linear problems in least squares. *Quart. Appl. Math.*, **2**, 164–168.
- Lines, L. R. and Treitel, S. (1984). Tutorial: A review of least-squares inversion and its applications to geophysical problems. *Geophys. Prospecting*, **32**, 159–186.
- Lomax, A. and Snieder, R. (1994). Finding sets of acceptable solutions with a genetic algorithm with application to surface-wave group dispersion in Europe. *Geophys. Res. Lett.*, **21**(24), 2617–2620.
- Lomax, A. and Snieder, R. (1995). The contrast in upper mantle shear-wave velocity between the East European platform and tectonic Europe obtained with genetic algorithm inversion of Rayleigh-wave group dispersion. *Geophys. J. Int.*, **123**(1), 169–182.
- Lopez Ramos, E. (1975). Geological summary of the Yucatan platform. In A. E. M. Nairn and F. G. Stehli, editors, *The Ocean Basins and Margins*, Volume 3: The Gulf of Mexico and the Caribbean, Chapter 7, pages 257–282. Plenum Press.
- Love, A. E. H. (1911). *Some problems of Geodynamics*. Cambridge University Press.
- Macbeth, C. (1983). *Propagation and attenuation of seismic Rayleigh waves along single paths in Scotland*. Ph.D. thesis, University of Edinburgh.
- Maguire, P. K. H., Mackenzie, G. D., Denton, P., Trejo, A., Kind, R., and members of the Chicxulub Working Group (1998). Preliminary results from a passive seismic array over the Chicxulub impact structure in Mexico. In M. Grady, R. Hutchinson, G. J. H. McCall, and D. A. Rothery, editors, *Meteorites: flux with time and impact effects*, Special Publication 140, pages 177–193. Geological Society, London.
- Malagnini, L. (1996). Velocity and attenuation structure of very shallow soils: Evidence for a frequency dependent Q. *Bull. Seism. Soc. Am.*, **86**(5), 1471–1486.
- Malagnini, L., Herrmann, R. B., Biella, G., and de Franco, R. (1995). Rayleigh waves in Quaternary alluvium from explosive sources : Determination of shear-wave velocity and Q structure. *Bull. Seism. Soc. Am.*, **85**(3), 900–922.
- Marquardt, D. W. (1963). An algorithm for least squares estimation of non-linear parameters. *J. Soc. Ind. appl. Math.*, **11**, 431–441.
- Marrow, P. C. and Walker, A. B. (1988). Llyn earthquake of 1984 July 19: aftershock sequence and focal mechanism. *Geophys. J.*, **92**, 487–493.
- McEvelly, T. V. and Stauder, W. (1965). Effect of sedimentary thickness on short-period Rayleigh wave dispersion. *Geophys.*, **30**(2), 198–203.

- McKinnon, W. B. (1982). Impact into the Earth's ocean floor: Preliminary experiments, a planetary model and possibilities for detection. In L. T. Silver and P. H. Schultz, editors, *Geological Implications of Impacts of Large Asteroids and Comets on the Earth*, Special Paper 190, pages 129–142. Geol. Soc. Am.
- Meju, M. (1994a). A general program for linear parameter estimation and uncertainty analysis. *Computers & Geosciences*, **20**(2), 197–220.
- Meju, M. A. (1994b). *Geophysical data analysis: Understanding inverse problem theory and practice*, Course Notes Volume 6. Society of Exploration Geophysicists.
- Melosh, H. J. (1977). Crater modification by gravity: A mechanical analysis of slumping. In D. J. Roddy, R. O. Pepin, and R. B. Merrill, editors, *Impact and explosion cratering*, pages 1245–1260. Pergamon Press.
- Melosh, H. J. (1982). A schematic model of crater modification by gravity. *J. Geophys. Res.*, **87**(B1), 371–380.
- Melosh, H. J. (1983). Acoustic fluidization. *Am. Scientist*, **71**(2), 158–165.
- Melosh, H. J. (1989). *Impact Cratering: A Geologic Process*. Oxford Monographs on Geology and Geophysics 11. Oxford University Press.
- Menke, W. (1984). *Geophysical data analysis: Discrete inverse theory*. Academic Press.
- Menke, W. and Dubendorff, B. (1985). Discriminating intrinsic and apparent attenuation in layered rock. *Geophys. Res. Lett.*, **12**(10), 721–724.
- Meyerhoff, A. A., Lyons, J. B., and Officer, C. B. (1994). Chicxulub structure: a volcanic sequence of late Cretaceous age. *Geology*, **22**(1), 3–4.
- Miller, G. H. (1998). Jetting in oblique, asymmetric impacts. *Icarus*, **134**, 163–175.
- Mitchell, B. J. (1975). Regional Rayleigh wave attenuation in North America. *J. Geophys. Res.*, **80**(35), 4904–4916.
- Mokhtar, T. A., Herrmann, R. B., and Russell, D. R. (1988). Seismic velocity and Q model for the shallow structure of the Arabian shield from short-period Rayleigh waves. *Geophys.*, **53**(11), 1379–1387.
- Morgan, J. and Warner, M. (1998). Chicxulub: The third dimension of a multi-ring impact basin. Submitted to *Geology*.
- Morgan, J., Warner, M., Brittan, J., Buffler, R., Camargo, A., Christeson, G., Denton, P., Hildebrand, A., Hobbs, R., MacIntyre, H., Mackenzie, G., Maguire, P., Marin, L., Nakamura, Y., Pilkington, M., Sharpton, V., Snyder, D., Suarez, G., and Trejo, A. (1997). Size and morphology of the Chicxulub impact crater. *Nature*, **390**, 472–476.
- Oliver, J. and Ewing, M. (1957). Higher modes of continental Rayleigh waves. *Bull. Seism. Soc. Am.*, **47**, 187–204.
- O'Neill, M. E. and Hill, D. P. (1979). Causal absorption: its effect on synthetic seismograms computed by the reflectivity method. *Bull. Seism. Soc. Am.*, **69**, 17–25.
- Parker, R. L. (1994). *Geophysical inverse theory*. Princeton University Press.
- Penfield, G. T. and Camargo-Zanoguera, A. (1981). Definition of a major igneous zone in the central Yucatan platform with aeromagnetism and gravity. In *Technical Program, Abstracts and Bibliographies, 51st Annual Meeting, Society of Exploration Geophysicists, Tulsa, OK*, page 37.

- Perry, E., Swift, J., Gamboa, J., Reeve, A., Sanborn, R., Marin, L., and Villasuso, M. (1989). Geological and environmental aspects of surface cementation, north coast, Yucatan, Mexico. *Geology*, **17**(9), 818–821.
- Perry, E., Marin, L., McClain, J., and Velázquez, G. (1995). Ring of cenotes (sinkholes), northwest Yucatan, Mexico: its hydrogeologic characteristics and possible association with the Chicxulub impact crater. *Geology*, **23**(1), 17–20.
- Pestel, E. C. and Leckie, F. A. (1963). *Matrix methods in elastomechanics*. McGraw Hill.
- Pike, R. J. and Spudis, P. D. (1987). Basin ring spacing on the Moon, Mercury and Mars. *Earth, Moon and Planets*, **39**, 129–194.
- Pilkington, M. and Grieve, R. A. F. (1992). The geophysical signature of terrestrial impact craters. *Rev. Geophys.*, **30**(2), 161–181.
- Pilkington, M., Hildebrand, A. R., and Ortiz-Aleman, C. (1994). Gravity and magnetic-field modeling and structure of the Chicxulub crater, Mexico. *J. Geophys. Res. -Planets*, **99**(E6), 13147–13162.
- Pilon, J. A., Grieve, R. A. F., and Sharpton, V. L. (1991). The subsurface character of Meteor Crater, Arizona, as determined by ground probing radar. *J. Geophys. Res.*, **96**, 15563–15576.
- Pope, K. O., Ocampo, A. C., and Duller, C. E. (1991). Mexican site for K/T impact crater. *Nature*, **351**, 105.
- Pope, K. O., Ocampo, A. C., and Duller, C. E. (1993). Surficial geology of the Chicxulub impact crater, Yucatan, Mexico. *Earth Moon Planets*, **63**(2), 93–104.
- Pope, K. O., Ocampo, S. C., Kinsland, G. L., and Smith, R. (1996). Surface expression of the Chicxulub crater. *Geology*, **24**(6), 527–530.
- Premo, W. R. and Izett, G. A. (1992). Isotopic signatures of black tektites from the K–T boundary on Haiti: Implications for the age and type of source material. *Meteoritics*, **27**, 413–423.
- Press, F. (1966). Seismic velocities. In S. P. Clark, editor *Handbook of physical constants*, Section 9, pages 195–218. Geological Society of America.
- Purser, B. H., Brown, A., and Aissaoui, D. M. (1994). Nature, origins and evolution of porosity in dolomites. In B. Purser, M. Tucker, and D. Zenger, editors, *Dolomites*, Special Publication of the Int. Ass. Sediment. 21, pages 283–308. Blackwell Scientific.
- Ramos-Martinez, J., Chavez-Garcia, F. J., Romeroji-Menez, E., Rodriguez-Zuniga, J. L., and Gomez-Gonzalez, J. M. (1997). Site effects in Mexico City: constraints from surface wave inversion of shallow refraction data. *J. Applied Geophys.*, **36**(4), 157–165.
- Rampino, M. R. (1987). Impact cratering and flood basalt volcanism. *Nature*, **327**, 478.
- Rampino, M. R., Haggerty, B. M., and Pagano, T. C. (1997). A unified theory of impact crises and mass extinctions: Quantitative tests. *Ann. New York Acad. Sci.*, **822**, 403–431.
- Rayleigh, L. (1885). On waves propagated along the plane surface of an elastic solid. *Proc. London Math. Soc.*, **17**, 4–11.
- Riolo, R. L. (1992). Survival of the fittest bits. *Scientific American*, **267**(1), 89–91.
- Rivière-Barbier, F. and Grant, L. T. (1993). Identification and location of closely spaced mining blasts. *Bull. Seism. Soc. Am.*, **83**(5), 1527–1546.
- Sakia, C. K. (1992). Numerical study of quarry generated Rg as a discriminant for earthquakes and explosions : Modeling of Rg in southwestern New England. *J. Geophys. Res.*, **97**(B7), 11057–11072.

- Sakia, C. K., Kafka, A. L., Gnewuch, S. C., and McTigue, J. W. (1990). Shear velocity and intrinsic Q structure of the shallow crust in southeastern New England from Rg wave dispersion. *J. Geophys. Res.*, **95**(B6), 8527–8541.
- Sambridge, M. and Drijkoningen, G. (1992). Genetic algorithms in seismic wave-form inversion. *Geophys. J. Int.*, **109**, 323–342.
- Sambridge, M. and Gallagher, K. (1993). Earthquake hypocenter location using genetic algorithms. *Bull. Seism. Soc. Am.*, **83**, 1467–1491.
- Sanchez-Sesma, F. J., Perez-Rocha, L. E., and Reinoso, E. (1993). Ground motion in Mexico City during the April 25, 1989, Guerrero earthquake. *Tectonophysics*, **218**, 127–140.
- Sandvol, E., Seber, D., Calvert, A., and Barazangi, M. (1998). Grid search modeling of receiver functions: Implications for crustal structure in the Middle East and North Africa. *J. Geophys. Res.*, **103**(B11), 26899–26917.
- Sarrate, J., Canas, J. A., Pujades, L., Badal, J., Corchete, V., and Payo, G. (1993). Shallow structure of part of northwestern Iberia from short-period Rayleigh-wave observations. *Tectonophysics*, **221**, 95–105.
- Scherbaum, F. (1996). *Of poles and zeros : Fundamentals of digital seismology.*, Modern Approaches in Geophysics 15. Kluwer Academic.
- Scherbaum, F. (1997). Zero phase FIR filters in digital seismic acquisition systems: Blessing or curse? *Eos*, **78**(33), 343–344.
- Scherbaum, F. and Bouin, M. P. (1997). FIR filter effects and nucleation phases. *Geophys. J. Int.*, **130**(3), 661–668.
- Schultz, A., Kurtz, R. D., Chave, A. D., and Jones, A. G. (1993). Conductivity discontinuities in the upper-mantle beneath a stable craton. *Geophys. Res. Lett.*, **20**(24), 2941–2944.
- Schultz, P. H. and D'Hondt, S. (1996). Cretaceous-Tertiary (Chicxulub) impact angle and its consequences. *Geology*, **24**(11), 963–967.
- Schuraytz, B. C., Sharpton, V. L., and Marín, L. E. (1994). Petrology of impact-melt rocks at the Chicxulub multiring basin, Yucatan, Mexico. *Geology*, **22**(10), 868–872.
- Schuraytz, B. C., Lindstrom, D. J., Marin, L. E., Martinez, R. R., Mittlefehldt, D. W., Sharpton, V. L., and Wentworth, S. J. (1996). Iridium metal in Chicxulub impact melt: forensic chemistry on the K-T smoking gun. *Science*, **271**, 1573–1576.
- Sen, M. and Stoffa, P. L. (1995). *Global optimization methods in geophysical inversion.* Advances in Exploration Geophysics 4. Elsevier.
- Sen, M. K. and Stoffa, P. L. (1992). Rapid sampling of model space using genetic algorithms: examples from seismic wave-form inversion. *Geophys. J. Int.*, **108**(1), 281–292.
- Shapiro, N. M., Campillo, M., Paul, A., Singh, S. K., Jongmans, D., and Sánchez-Sesma, F. J. (1997). Surface-wave propagation across the Mexican Volcanic Belt and the origin of the long-period seismic-wave amplification in the Valley of Mexico. *Geophys. J. Int.*, **128**, 151–166.
- Sharpton, V. L. (1997). Surface expression of the Chicxulub crater: Comment. *Geology*, **25**(6), 567–568.
- Sharpton, V. L., Dalrymple, G. B., Marín, L. E., Ryder, G., Schuraytz, B. C., and Urrutia-Fucugauchi, J. (1992). New links between the Chicxulub impact structure and the Cretaceous/Tertiary boundary. *Nature*, **359**, 819–821.

- Sharpton, V. L., Burke, K., Camargo-Zanoguera, A., Hall, S. A., Lee, D. S., Marín, L. E., Suárez-Reynoso, G., Quezada-Muñeton, J. M., Spudis, P. D., and Urrutia-Fucugauchi, J. (1993). Chicxulub multiring impact basin: size and other characteristics derived from gravity analysis. *Science*, **261**, 1564–1567.
- Sharpton, V. L., Marín, L. E., Carney, C., Lee, S., Ryder, G., Schuraytz, B. C., Sikora, P., and Spudis, P. (1996). A model of the Chicxulub impact basin based on evaluation of geophysical data, well logs and drill core samples. In G. Ryder, D. Fastovsky, and S. Gatner, editors, *The Cretaceous-Tertiary event and other catastrophes in Earth history*, Special Paper 307, pages 55–74. Geol. Soc. Am.
- Shibutani, T., Sambridge, M., and Kennett, B. (1996). Genetic algorithm inversion for receiver functions with application to crust and uppermost mantle structure beneath eastern Australia. *Geophys. Res. Lett.*, **23**(14), 1829–1832.
- Sileny, J. (1998). Earthquake source parameters and their confidence regions by a genetic algorithm with a ‘memory’. *Geophys. J. Int.*, **134**(1), 228–242.
- Singh, S. K., Quass, R., Ordaz, M., Mooser, F., Almora, D., Torres, M., and Vasquez, R. (1995). Is there truly a ‘hard’ rock in the Valley of Mexico. *Geophys. Res. Lett.*, **22**, 481–484.
- Smith, A. T. (1989). High-frequency seismic observations and models of chemical explosions: Implications for the discrimination of ripple-fired mining blasts. *Bull. Seism. Soc. Am.*, **79**(4), 1089–1110.
- Spray, J. G. and Thompson, L. M. (1996). Friction melt distribution in a multi-ring impact basin. *Nature*, **373**, 130–132.
- Steinich, B. and Marín, L. E. (1996). Hydrogeological investigations in northwestern Yucatan, Mexico, using resistivity surveys. *Ground Water*, **34**(4), 640–646.
- Stevens, J. L. (1986). Reply to Z. Der’s “Comments on the paper ‘Estimation of scalar moments from explosion-generated surface waves’”. *Bull. Seism. Soc. Am.*, **76**(6), 1825–1829.
- Stevenson, D. J. (1987). Origin of the moon – the collision hypotheses. *Ann. Rev. Earth Planet. Sci.*, **15**, 271–315.
- Stoffa, P. L. and Sen, M. K. (1991). Nonlinear multiparameter optimization using genetic algorithms: Inversion of plane-wave seismograms. *Geophys.*, **56**(11), 1794–1810.
- Stoneley, R. (1931). The thickness of continental layers of Europe. *Mon. Not. Roy. astr. Soc. Geophys. Suppl.*, **2**, 429–433.
- Stuart, G. W., Douglas, A., and Blamey, C. (1976). A computer program for the determination of the phase velocity of seismic surface waves between pairs of stations. AWRE Report O 8/76, MOD Procurement Executive.
- Sutherland, F. L. (1994). Volcanism around K/T boundary time — its role in an impact scenario for the K/T extinctions. *Earth Sci. Rev.*, **36**, 1–26.
- Swisher, C. C., Grajalesnishimura, J. M., Montanari, A., Margolis, S. V., Claeys, P., Alvarez, W., Renne, P., Cedillopardo, E., Maurrasse, F. J. M. R., Curtis, G. H., Smit, J., and McWilliams, M. O. (1992). Coeval $^{40}\text{Ar}/^{39}\text{Ar}$ ages of 65.0 million years ago from Chicxulub crater melt rock and Cretaceous-Tertiary boundary tektites. *Science*, **257**, 954–958.
- Thurber, C. H. (1993). Local earthquake tomography: velocities and V_p/V_s - theory. In H. M. Iyer and K. Hirahara, editors, *Seismic tomography: Theory and practice*, Chapter 20, pages 563–583. Chapman & Hall.
- Toksöz, M. N. and Ben-Menahem, A. (1963). Velocities of mantle Love and Rayleigh waves over multiple paths. *Bull. Seism. Soc. Am.*, **53**, 741–764.

- Toon, O. B., Zahnle, K., Morrison, D., Turco, R. P., and Covey, C. (1997). Environmental perturbations caused by the impacts of asteroids and comets. *Rev. Geophys.*, **35**(1), 41–78.
- Tucker, M. E. and Wright, V. P. (1990). *Carbonate sedimentology*. Blackwell Scientific Publishing.
- Twomey, S. (1977). *An introduction to the mathematics of inversion in remote sensing and indirect measurements*. Elsevier Scientific Publ. Co.
- Urey, H. (1973). Comet collisions and geological periods. *Nature*, **242**, 32–33.
- Urrutia-Fucugauchi, J., Marín, L., and Trejo-García, A. (1996a). Initial results of the UNAM scientific drilling program on the Chicxulub impact structure: rock magnetic properties of UNAM-7 Tekax borehole. *Geofis. Intern.*, **35**(2), 125–133.
- Urrutia-Fucugauchi, J., Marín, L., and Trejo-García, A. (1996b). UNAM scientific drilling program of Chicxulub impact structure - Evidence for a 300 kilometer crater diameter. *Geophys. Res. Lett.*, **23**(13), 1565–1568.
- Urrutia-Fucugauchi, J., Sharpton, V. L., and Marin, L. (1997). Geophysical properties of impact breccias and Tertiary carbonate sequence - Chicxulub crater, Yucatan, Mexico. *Eos Trans. AGU*, **78**(46), F398. Fall Meet Suppl.
- Vahrenkamp, V. C. and Swart, P. K. (1994). Late Cenozoic dolomites of the Bahamas: metastable analogues for the genesis of ancient platform dolomites. In B. Purser, M. Tucker, and D. Zenger, editors, *Dolomites*, Special Publication of the Int. Ass. Sediment. 21, pages 133–153. Blackwell Scientific.
- Viniegra, O. F. (1981). Great carbonate bank of Yucatan, southern Mexico. *J. Petroleum Geol.*, **3**(3), 247–278.
- Wadati, K. (1933). On the travel time of earthquake waves. Part II. *Geophys. Mag.*, **7**, 101–111.
- Ward, W. C. (1996). Yucatan subsurface stratigraphy: Implications and constraints for the Chicxulub impact: Reply. *Carbonates and Evaporites*, **1**(11), 142.
- Ward, W. C., Keller, G., Stinnesbeck, W., and Adatte, T. (1995). Yucatan subsurface stratigraphy: implications and constraints for the Chicxulub impact. *Geology*, **23**(10), 873–876.
- Weidie, A. E. (1985). Geology of the Yucatan platform. In W. C. Ward, A. E. Weidie, and W. Back, editors, *Geology and Hydrogeology of the Yucatan and Quaternary Geology of Northeastern Yucatan Peninsula*, Chapter 1. New Orleans Geological Society.
- Wessel, P. and Smith, W. H. F. (1995). *The Generic Mapping Tools technical reference and cookbook*, 3rd edition.
- Whitley, D. (1994). A genetic algorithm tutorial. *Statistics & Computing*, **4**(2), 65–85.
- Wiggins, R. A. (1972). The general inverse problem: Implications of surface waves and free oscillations for earth structure. *Reviews of Geophysics and Space Physics*, **10**(1), 251–285.
- Winkler, K. W. and Murphy III, W. F. (1995) Acoustic velocity and attenuation in porous rocks. In T. J. Ahrens, editor, *Rock physics and phase relations: A handbook of physical constants*, AGU Reference Shelf 3, pages 20–34. American Geophysical Union.
- Wu, J., Milkereit, B., and Boerner, D. E. (1995). Seismic imaging of the enigmatic Sudbury structure. *J. Geophys. Res.*, **100**(B3), 4117–4130.
- Xie, Z., Spencer, T. W., Rabinowitz, P. D., and Fahlquist, D. A. (1996). A new regional hypocenter location method. *Bull. Seism. Soc. Am.*, **86**(4), 946–958.
- Yamanaka, H. and Ishida, H. (1996). Application of genetic algorithms to an inversion of surface-wave dispersion data. *Bull. Seism. Soc. Am.*, **86**(2), 436–444.

-
- Young, P. A. V. (1989). *A local earthquake study near Lake Bogoria in the Kenya rift*. Ph.D. thesis, University of Leicester.
- Zelt, C. A. and Smith, R. B. (1992) Seismic travel time inversion for 2-D crustal velocity structure. *Geophys. J. Int.*, **108**, 16–34.